

Electrochemical processes for design and modification of interfaces and surfaces of electronic devices



A Dissertation Presented for the Degree of
Doctor of Natural Sciences
(Dr. rer. nat.)

At the Natural Sciences Faculty IV
Chemistry and Pharmacy
University of Regensburg

Edmund Riedl

Regensburg 2014

Official Registration: 18.06.2014

Defence: 22.07.2014

Supervisor: Prof. Dr. H. J. Gores

Adjudicators: Prof. Dr. R. M. Gschwind; chair
Prof. Dr. H. J. Gores
Prof. Dr. W. Kunz
Prof. Dr. J. Daub

For Martina, Johanna and Theresa

**Schreite beschwingt voran
und akzeptiere kein „Geht nicht“.
Rechne mit wunderbaren Lösungen.
Mystique**

Acknowledgements

This work was only possible with the continuous help and support of many people.

First I want to thank Prof. Dr. Heiner-Jacob Gores for his never ending encouragement on the structuring of this work and document. He basically was the bridge between academic approach and industrialization of the described technologies and the heart of this dissertation within the workgroup “Electrochemistry and Electrolytes” at the University of Regensburg.

Prof. Dr. Werner Kunz, chair of the Institute of Physical and Theoretical Chemistry, offered me a place to work in his laboratories and enabled a lot of results from University of Regensburg in addition to the vast amount of data gained within Infineon AG in nearly one dozen of successful cooperation projects with his organisation.

As the father of the industrialization of this works and the soul of the technology I want to thank Dr. Helmut Strack from Infineon AG with his never ending hunger for discussions and the continuous believe in my success.

Finally I want to thank all the colleagues at University of Regensburg and at Infineon worldwide for their support and cooperation, my colleagues! Steve T., Tobias S., Franz W., Franz K., Steffen J., Johannes L., Arno Z., Robert B., Loo EH, Wong FH, Badrol H., Mohtar, Jagen, Lit HK, Rudolf S., Karl M., Andreas R, Josef M. and all the others. Thank you for guiding me through the ups and downs of this work.

And finally the most thanks I have to give to my ever supporting family Martina, Johanna and Theresa always putting a smile on my face at each time of the work. I love you.

Abstract

This work describes several approaches and two major advances obtained by numerous studies on the areas of semiconductor packaging technologies including adhesion promotion technology and copper surface design for interconnect technologies. This work was partially performed during the last decade in collaboration with the workgroup “Electrochemistry and Electrolytes” at the University of Regensburg, Institute of Physical and Theoretical Chemistry, chair Prof. Dr. W. Kunz. All analytical work and investigations on processes and manufacturing technologies was done at Infineon AG at different locations worldwide.

In the first main part both the design and development of adhesion promoter technologies for semiconductor devices is reviewed. The focus is put on electrochemical deposition of nanostructured adhesion promoters.

The results of this work were the industrialization of the deposition of a Zn-Cr alloy as a nanoporous adhesion promoter after assembly of the semiconductor device right before encapsulation. As an important innovation, the deposition of the adhesion promoter was successfully performed on all metallic surfaces of the chip and the package including aluminium chip metallisation, leadframe, solder and interconnect wires. Particularly activation of aluminum for the subsequent electrochemical deposition of Zn-Cr alloy was a major resolved challenge besides various aspects of the deposition process itself.

Results are reported on deposition mechanisms for obtaining a nanoporous layer by electrochemical deposition.

In addition, respective process investigations are described to gain a best-in-class adhesion promoter technology for highly reliable power semiconductor devices including finally the integration of this technology into the manufacturing process flow.

As further major developments new electrolytes were obtained by these works enabling the withdrawal of unwanted and environmentally detrimental chromium-VI species in the process and improving plating homogeneity as well. These novel examples include electrolytes for Zn-Mo and Zn-V alloys.

In the second part presented as an addendum, the surface design of copper with organic molecules is reported. These organic coatings are preventing uncontrolled oxidation of copper and are therefore prerequisites for processing copper surfaces during soldering or during copper wirebonding. A short review of the copper oxidation kinetics is given as well. The efficiency of oxidation protection of copper coated with 1H-benzotriazole, mercaptobenzimidazole, decanethiole, poly(1-vinylimidazole), poly(4-vinylimidazole) and poly(benzimidazole) is discussed. The application to either soldering processes or copper wirebonding was shown and an outlook is given for the usage of organic molecules as Cu passivations in these applications.

To sum up, various advances have been reached some have already been included in current production processes. Suffice it to mention that also several novel aspects were studied that may be useful for future progress.

Table of content:

1	Motivation for interface and surface design for electronic devices	17
1.1	Introduction.....	17
1.2	Basic fatigue mechanisms within a power semiconductor device	19
1.3	Fatigue of the chip.....	21
1.4	Fatigue of the package.....	23
1.5	Measures to prevent fatigue in a power semiconductor device	30
1.5.1	Chip related measures.....	31
1.5.2	Package related measures	33
1.6	Focus of this work.....	41
2	Analytical and experimental methods.....	42
2.1	Field emission scanning electron microscope (FESEM): Surface morphology	42
2.2	Energy dispersive x-ray spectroscopy (EDX).....	47
2.3	Transmission electron microscopy (TEM).....	48
2.4	Button shear test.....	49
2.5	Tape adhesion test	50
2.6	A2 dip test.....	53
2.7	Auger electron spectroscopy (AES).....	54
2.8	X-ray photoelectron spectroscopy (XPS).....	58
2.9	Time of flight secondary ion mass spectroscopy (TOF-SIMS).....	61
2.10	Scanning acoustic microscopy	64
2.11	Solder wetting balance for measuring wetting force-time-graphs	66
3	Adhesion promoter: Identification of A2 process as the target technology for adhesion in a MOSFET package.	68
4	Theoretical background and models for the understanding of dendritic depositions	76
4.1	Activation of metal surfaces	76
4.1.1	Properties and states of the different surfaces prior to activation	76
4.1.2	Activation of Cu surfaces.....	83

4.1.3	Activation of Ni and NiP surfaces	87
4.1.4	Activation of Pb-2Sn-2.5Ag solder surfaces.....	95
4.1.5	Activation of aluminium chip surfaces	101
4.1.5.1	Reactions of the aluminium metallisation: Oxidation and corrosion	101
4.1.5.2	Activation of Al ₂ O ₃ with an Ar/CF ₄ plasma process.....	108
4.1.5.3	Activation of Al ₂ O ₃ with aqueous HF / MSA chemistry.....	109
4.2	Theory of the electrochemical deposition of a porous layer.....	115
4.2.1	Basics for electrochemical deposition	115
4.2.1.1	Electrode potential and overpotential	115
4.2.1.2	Kinetic mechanism of deposition with reaction control.....	122
4.2.1.3	Kinetic mechanism with mass transport control	126
4.2.1.4	Deposition of alloys.....	130
4.2.1.5	Current efficiency and concurring reactions	134
4.2.2	Electrolyte chemistry for A2 deposition and comparison to other electrolytes	135
4.2.3	The deposition of zinc.....	136
4.2.4	The chemistry of chromates and the deposition of chromium.....	141
4.2.5	Chromate conversion coatings (CCCs) on zinc	143
4.2.6	The deposition of Zinc - chromium alloy	144
4.2.7	Chemistry and function of silicate: Co-deposition of SiO ₂	148
4.2.8	Mechanisms of deposition kinetics for porous and dendritic electrodeposits.....	149
4.2.8.1	Dendritic growth via mass transport controlled deposition	150
4.2.8.2	Dendritic growth via surface inhibition followed by mass transport controlled deposition	156
4.2.8.3	Dendritic growth via surface topology and mass transport controlled deposition	156
4.2.8.4	Dendritic growth by electrophoretic deposition with silicate carrier.	157
5	Deposition of A2 layer: Experimental results of the development of an industrial process	160
5.1	Overview on the A2 process and technology.....	160
5.2	Activation process	163

5.2.1	Investigation of activation with H ₂ SO ₄ and MSA (er81 and er98)	163
5.2.2	Investigation of the influence of oxidation during chip soldering on deposition of A2 (er175)	166
5.2.3	Argon / CF ₄ plasma process for activation of the Al chip metallization (er265)..	169
5.2.4	Integration of Ar / CF ₄ plasma process for activation of the Al chip metallization in the process flow (er269, er270).....	186
5.2.5	Aluminium activation in A2 process with HF chemistry and Ar / O ₂ plasma conditioning of wafer.....	195
5.2.6	Further work and development of fluorine free alternative conditioning of Al-1Si-0.5Cu.....	199
5.2.7	Summary of activation procedures.....	201
5.3	Deposition of A2 with constant current.....	203
5.3.1	Overview on deposition parameters	203
5.3.2	A2 layer characterization and properties	204
5.3.3	Electrolyte for A2 process and chemical interactions	207
5.3.3.1	Preparation of the electrolyte for A2 deposition.....	207
5.3.3.2	Characterization of the electrolyte	209
5.3.4	Influence of the concentration of the various electrolyte species on the morphology of A2 deposit.	210
5.3.5	Influence of deposition current density	217
5.3.6	Hydrodynamic influence: Electrolyte flow and transport belt speed	224
5.3.7	Cell design for A2 deposition	230
5.3.7.1	Cathode shield tube: Design of geometry and flow of electrolyte for TO220 leadframe (er228).....	230
5.3.7.2	A2-Cell: Design of geometry of plating cell for TO263 leadframe (er309)...	232
5.3.8	Summary on A2 deposition.....	239
5.4	Environmental measures for A2 technology.....	241
5.4.1	Wastewater treatment to prevent chromium-VI emission	241
5.4.2	New chromium-VI free electrolytes for A2 process in the future.....	243
5.4.2.1	Chromium-VI free alkaline zincate electrolytes for A2 deposition.....	244
5.4.2.2	Chromium-VI free acidic zinc electrolytes for A2 deposition.....	265

5.4.3	Summary and outlook on Cr-VI free electrolytes for A2 deposition.....	270
6	Addendum - Organic coatings of surfaces for prevention of copper oxidation.....	272
6.1	Applications of copper and its limitations due to oxidation	272
6.2	The Oxidation of copper	274
6.3	Organic materials for copper passivation	277
6.3.1	Application of benzotriazole for copper passivation of semiconductor device terminals for PCB soldering	277
6.3.2	Application of poly(vinylimidazole) for copper passivation for copper wirebonding on copper metallisation	285
7	Summary, publications and outlook.....	295
7.1	Main part: Nanoporous adhesion promoter in semiconductor packages - A2 technology.....	295
7.2	Addendum: Organic coatings of surfaces for prevention of copper oxidation.....	300
8	Abbreviations and acronyms.....	303
9	Curriculum Vitae.....	305
10	Literature.....	307

1 Motivation for interface and surface design for electronic devices

1.1 Introduction

Looking at the past decade it can be seen that the effort in semiconductor industry is undergoing a shift towards systems with high energy efficiency driven by miniaturization of products. Miniaturization of power semiconductor devices means for example shrinking energy stores for the individual device that reduces switching losses. Besides energy efficiency there is an increasing demand for electric power management of electronic for automotive, industrial and commodity products. A booming area in this field is the renewable energy technology including wind-powered generators, photovoltaic devices (solar cells), and see water-powered generators; all are demanding of highly reliable and efficient power semiconductor products. These requests speed up the trend to miniaturization and reliability as key drivers for power semiconductor devices. Example given, Figure 1 shows the dramatic advances of technology of MOSFET (metal oxide semiconductor field effect transistor) devices in the first half of the past decade taking one technology step every two years and a chip size approximately halved each step. In addition production volume of power semiconductor devices has increased, too.

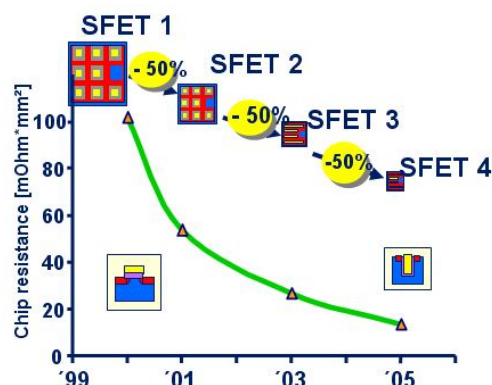


Figure 1 : Shrink path for power semiconductor technology: From year 2000 until 2005 three technology steps have been accomplished in contrast to the time before 2000 (source: Infineon MOSFET roadmap).

Also the realization of environmental directives like the RoHS (Restriction of hazardous substances) and WEEE (Waste of electrical and electronic equipment) directives by mainly the switch from Pb-Sn PCB (printed circuit board) solder with melting temperatures of $T_m=179^\circ\text{C}$ to Sn-Ag or Sn-Ag-Cu alloys with melting temperatures of $T_m=221^\circ\text{C}$ is addressing higher reliability to devices. It brings up much higher PCB soldering temperatures of up to 260°C peak temperatures of course with some consequences to semiconductor device stressing during manufacturing of the application on PCB. The increased thermal stress at PCB soldering is leading to a much higher pre-damage to power devices and bringing the risk of lower lifetime reliability.

From this point of view the environmental laws such as the WEEE- and RoHS-directives and product requirements have enforced innovations and brought out next generation product reliability for power semiconductor devices needed for further high temperature applications for future applications. In figure 2 the benefit of electronic devices within cars can be seen. Shown are safety improvements in comparison to the increasing number of cars within the last decades. The increasing complexity of electronic components is increasing efforts for reliability of the individual device in order to make the complete system more reliable. If the complete system in the car has to be highly reliable the individual devices for building the system require zero defect density to minimize multiplication of defects. In order to develop and to manufacture a highly reliable device a couple of failure mechanisms need to be understood first to identify the major fatigue chain in a power semiconductor device. This chain will show that there are major approaches possible to design interfaces and surfaces via electrochemical processes to help to design reliable electronic devices.

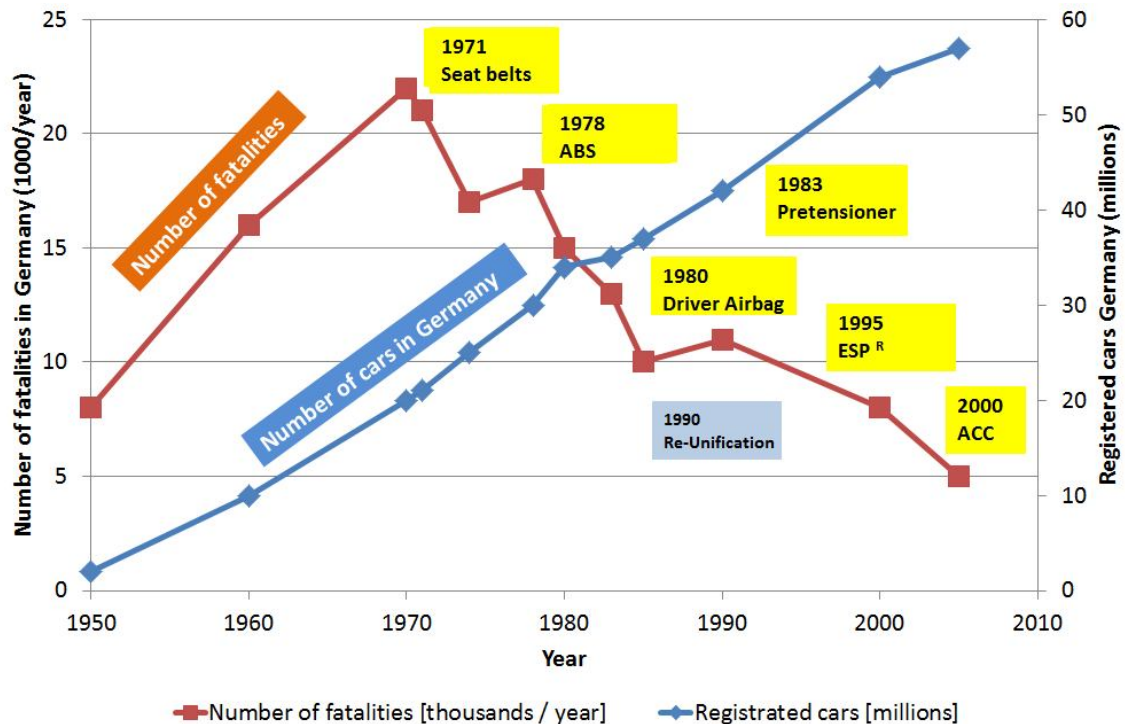


Figure 2: Overview of development of deathly casualties from 1950 until 2005[1].

1.2 Basic fatigue mechanisms within a power semiconductor device

To understand the basic failure mechanisms within a power semiconductor device first the simplified structure of a device is explained. The package of a power semiconductor device consists of many different materials and interfaces as shown in figure 3 . Almost every device uses polymer based mold compounds and metal based leadframes, common is the use of Cu with different plating such as Ag, Ni or NiP alloys (nickel/phosphorus). The top of the semiconductor chip is coated with an Al based metallization and by the isolating passivation, mostly SiN (silicon nitride), opened at the bond windows to get an Al surface towards the package. Underneath the Al layer there are other layers depending on the semiconductor device. For a MOSFET device BPSG (boron-phosphorus-silicon-glass), polycrystalline silicon and finally the gate oxide (SiO₂) is located there on top of the silicon substrate of the chip.

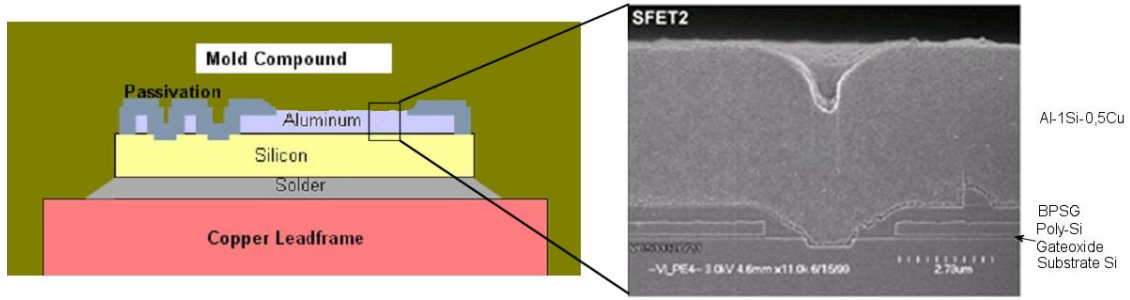


Figure 3: Structure of a power semiconductor device which shows the geometry and the different interfaces.

The device is undergoing various process temperatures during specific manufacturing processes. For example two major thermal budgets are applied during chip soldering at $\theta=400^{\circ}\text{C}$ and during the molding of the device with mold compound at $180\text{-}200^{\circ}\text{C}$. Cooling down the device to room temperature after the individual process already implies stress due to CTE (Coefficients of linear thermal expansion) mismatch of the different materials within the device. Table 1 shows the differences of the CTE and elastic modules (E) of the used materials.

Material	α [10^{-6} K^{-1}]	E [$10^9 \text{ N}\cdot\text{m}^{-2}$] = [GPa]	Note
Silicon Si, [2]	2.9 (273-1673K),	112	298.15 K
Copper Cu, [2]	16.5	128	298.15 K
Aluminium Al, [2]	23.0	70.3	298.15 K
Mold compound KMC 2110G-7, [3]	$\alpha_1=13$	E1=18.5	α_1 at $\theta < \theta_G=133^{\circ}\text{C}$ E1 at $\theta=25^{\circ}\text{C}$
Mold compound KMC 2110G-7, [3]	$\alpha_2=51$	E2=1.5	α_2 at $\theta > \theta_G=133^{\circ}\text{C}$ E2 at T=150°C

Table 1: CTE (Coefficients of linear thermal expansion) and elastic modulus (E) of different materials used within a semiconductor device, mold compound data also in [4].

The different CTE cause a lateral stress at various interfaces. For example during cooling down a device from a molding process temperature of 180°C to -55°C during cold testing of the device in the production line the geometrical mismatch between mold compound and silicon is already $4 \mu\text{m}$ per 1 mm length of interface (0.4%). The residual stress is concentrated at the interfaces between the specific materials, hence interface damage due to CTE mismatch during temperature cycling is one very common fatigue mechanism in a semiconductor device. This interface fatigue is generating secondary fatigue mechanisms. Primarily the interface fatigue can be detected as a delamination

between two subsequent materials which is analysed by SAM (scanning acoustic microscopy).

1.3 Fatigue of the chip

As the molding compound has more than 5 times the CTE of Si below the glass transition temperature (T_g) the polymer brings a high stress on the chip top during heating and cooling. Additionally the mechanical properties of the molding compound are changing dramatically below T_g and at lower temperatures which can be seen in table 1. The elastic modulus increases by more than factor 10 comparing $E_{1, 25^\circ\text{C}} = 18,5$ GPa and $E_{2, 150^\circ\text{C}} = 1,5$ GPa. Hence the stiffness of the molding compound is increasing strongly during cooling. Together with the high CTE this leads to deformation of metal lines and to a even complete removing of metal lines after several temperature cycles, finally to electrical fail through shortages or cracks. Figure 4 shows a FESEM (field effect scanning electron microscopy) picture of this fatigue on a device which is having an aluminium metallisation without passivation. Results will be shown later how this fatigue can be prevented.

For the passivation of the frontside metallisation of the chip and structures usually a silicon nitride layer (SiN) is used. The above mentioned shift of aluminium metal layers below the SiN happens with a high plastic deformation rate during applying temperature cycles. This can lead to SiN passivation cracks which then are starting points for corrosion giving a path for humidity to diffuse down to the aluminum layer [5]. In figure 5 an example is given, a FESEM picture is shown with a 800nm SiN layer on aluminium lines showing cracks which can go deeper into layers underneath the metal layers leading to immediate electrical fails.

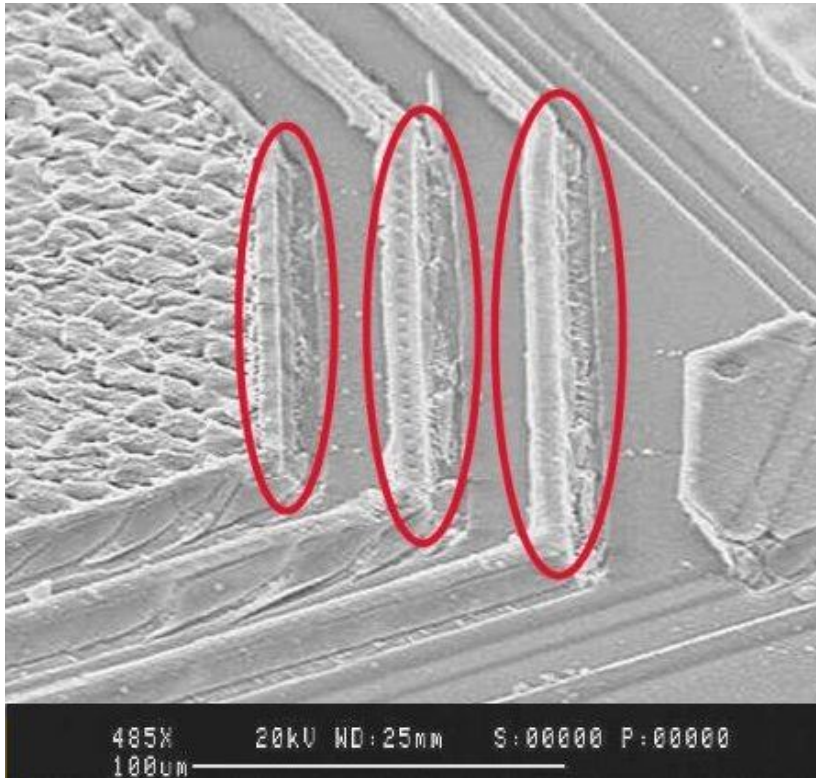


Figure 4: Shifted aluminium metal lines after 1000 TC (temperature cycles) from -55 °C to 150 °C on a MOSFET power device in a TO263-3 package.

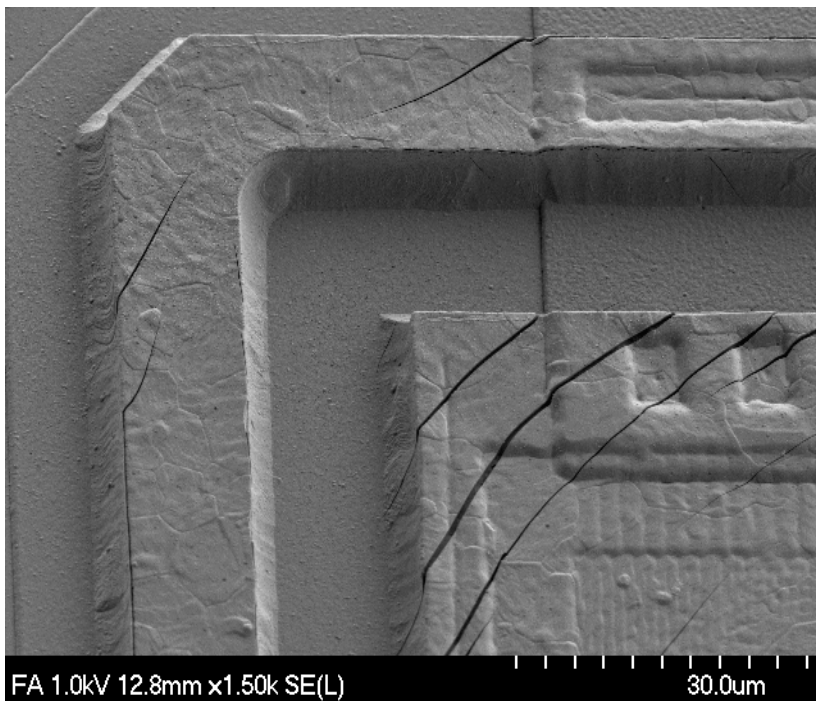


Figure 5: Passivation cracks over metal areas after 1000 temperature cycles (-55°C to 150 °C)

1.4 Fatigue of the package

Not only the chip but also the package of a device has several interfaces, especially critical interfaces are those between polymers and metals. These interfaces are so critical as polymers are not chemically bonded strongly to metals as compared to a crystalline interface between two metals forming for example intermetallic phases. Therefore, those polymer to metal interfaces are the weak link in the system. Damage of these interfaces, which is basically called delamination and popcorn cracking in the package leads to several secondary fatigue mechanisms, some of them are shown in figure 6. This delamination occurs already during the hot PCB soldering process which is done for example at temperatures of 245°C up to 260°C.

In addition to major fatigue of the chip front side the chip backside interconnect fails through solder- or glue cracking. Cracking of the wire interconnects happens toward the chip frontside as well as toward the package on the leads. Finally all these effects lead to drift or fail of electrical parameters and therefore entail an unstable or failed device. In the following section some examples will be given showing that the major problem in plastic packages is the adhesion of the molding compound to the rest of the device. In figure 6 some examples of fatigues can be seen which all are primarily generated by a delamination of the molding compound.

Chip backside interconnect fatigue (e.g. solder)

Solder fatigue can be differentiated into two modes:

- a. Melting of the solder alloy due to temperature overstress.
- b. Cracking of the solder due to thermo-mechanical stress.

The mechanism of melting can easily be explained for alloys which are unsuitable for high PCB soldering temperatures. An example is shown in figure 7, Sn-25Ag-10Sb (alloy-J) is melting during 260°C board soldering resulting in big voids in the solder layer. These voids reduce the thermal coupling of the chip to the package heatsink and lead to overheating of the device during operation.

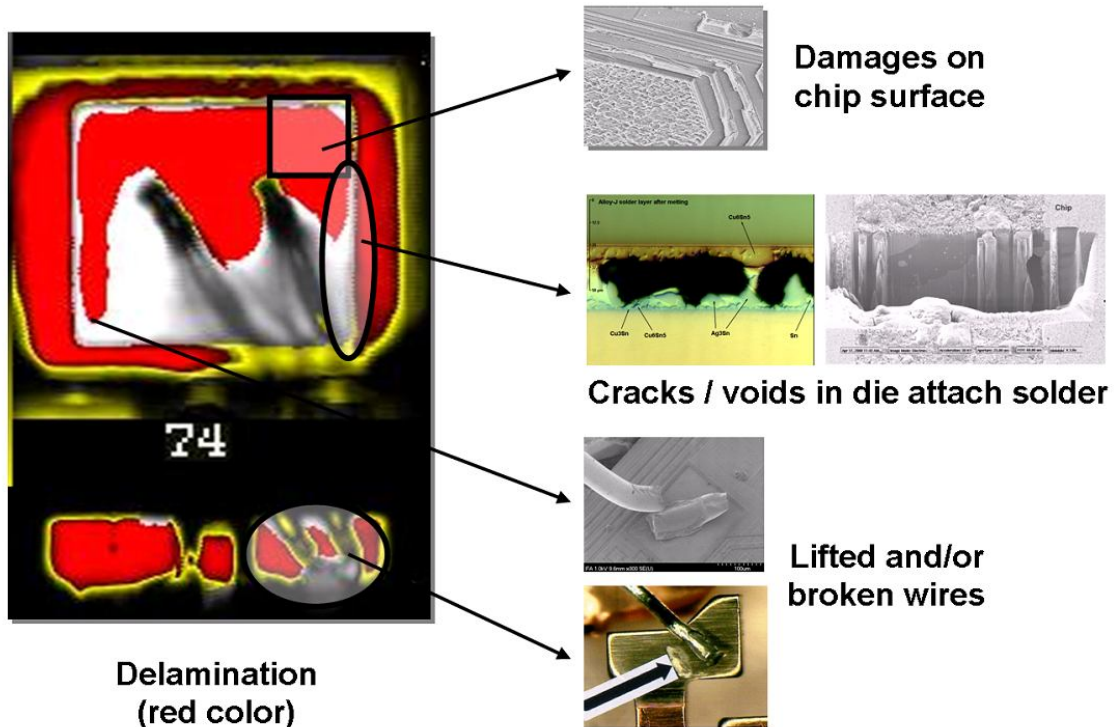


Figure 6: Failure mechanisms in a strongly delaminated package leading to electrical failures during lifetime of a product.

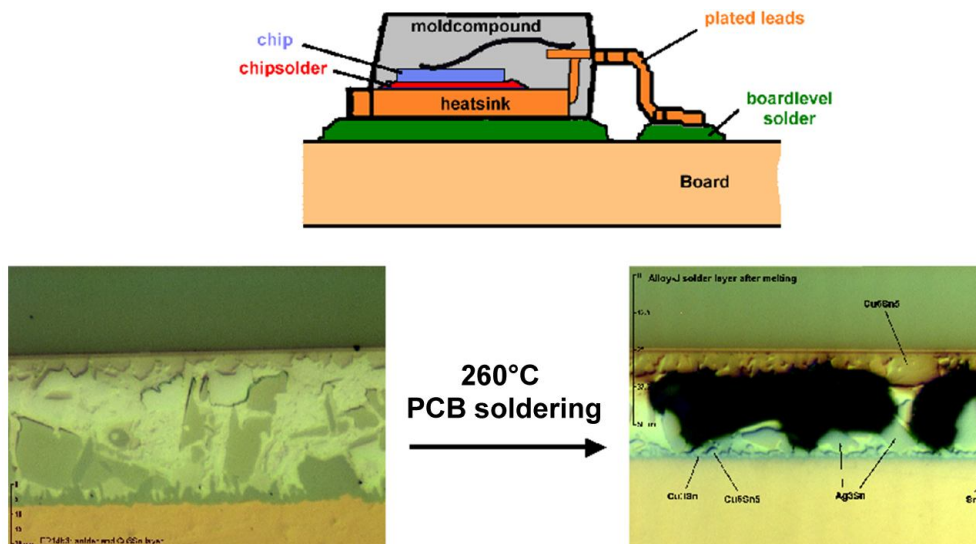


Figure 7: The solder alloy Sn-25Sn-10Sb (“alloy-j”) melts at a temperature of $\Theta_m=228^\circ\text{C}$ leading to voids. This is a consequence of the high PCB soldering temperature of 260°C .

The mechanism of solder cracking is explained first by thermomechanical stress during temperature cycling. Due to the CTE mismatch the chip and the heatsink are enforcing

creeping in the softer solder alloy. This creeping is additionally enforced by the molding compound especially in asymmetric packages with strong delamination. There the molding compound can apply forces to the chip leading to creep in the solder.

Looking at the available solder materials and the prerequisite from metallurgy for the requirement of 260°C PCB soldering from industry Pb-Sn-Ag (Pb content >90 weight %) alloys are offering a high melting temperature with the disadvantage of a lower creep resistance especially at higher temperature. During temperature cycle stress the creeping of the alloy leads to formation of voids at the grain boundaries which finally leads to crack propagation from void to void along the grain boundaries. For those soft solder alloys this weakness is a technological limitation which can be compensated in the package only by supporting the chip with a high adhesion of the molding compound so that plastic deformation of the solder is minimized during lifetime of the device.

Void formation during thermomechanical stress is already degrading the thermal connection of the chip backside to the package heatsink leading to drift of parameters. Figure 8 shows a FIB (focused ion beam) cut through a solder layer after a thermomechanical stress of 1000 temperature cycles from -55°C to 150°C. Voids between the grains of the solder are located especially besides the chip and its backside metallisation.

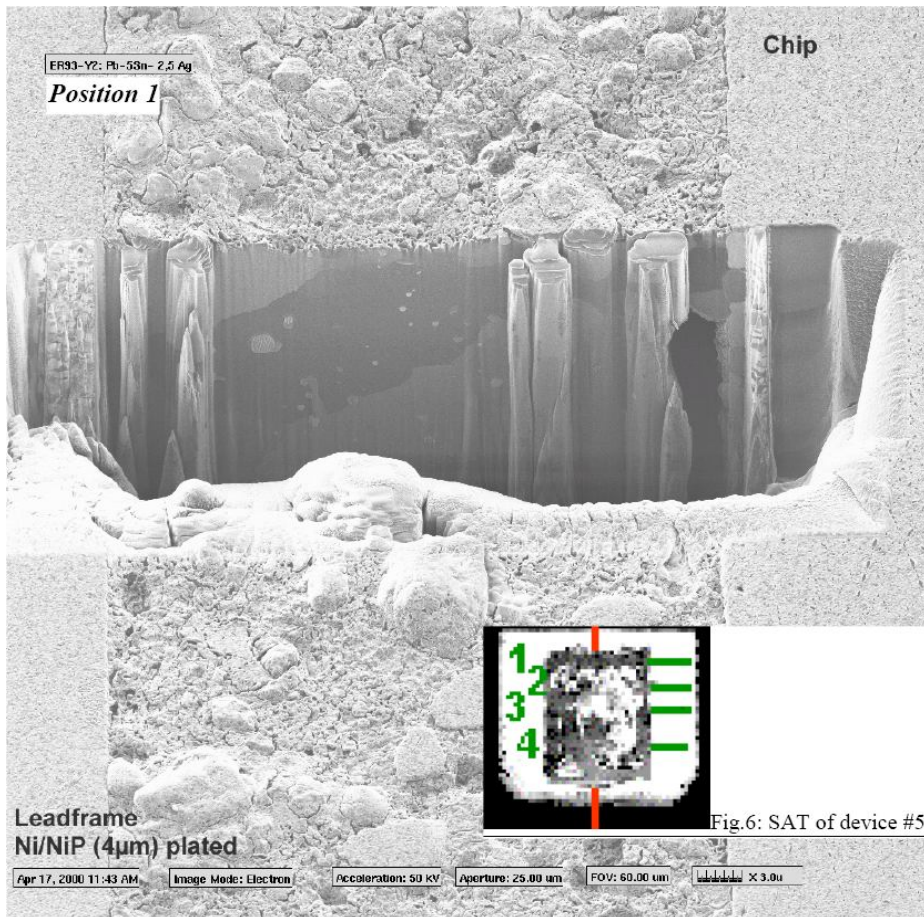


Fig.6: SAT of device #5.

Figure 8: FIB (focused ion beam) cut on a cross section of a solder layer which shows solder crack after TC500 (-55 to 150°C) already. The analysis shows voids between the different crystallites of the solder. The x-section was done along the red line in the SAM picture below, the FIB cut was done on position 1 in the SAM picture.

The behavior of such degrading devices is shown in figure 9. During several package evaluations stress tests were done on standard devices and on devices with an adhesion promoter technology. The groups with low adhesion along the stress tests shows strong delamination of the molding compound and huge void formation within the solder layer in the SAM. Related to the voids also the electrical parameter measured in this experiments show strong drift after the respective stress tests proving the degradation of the thermal connection between chip backside and package heatsink.

Stability of electrical parameter: DVSD in Robust Package

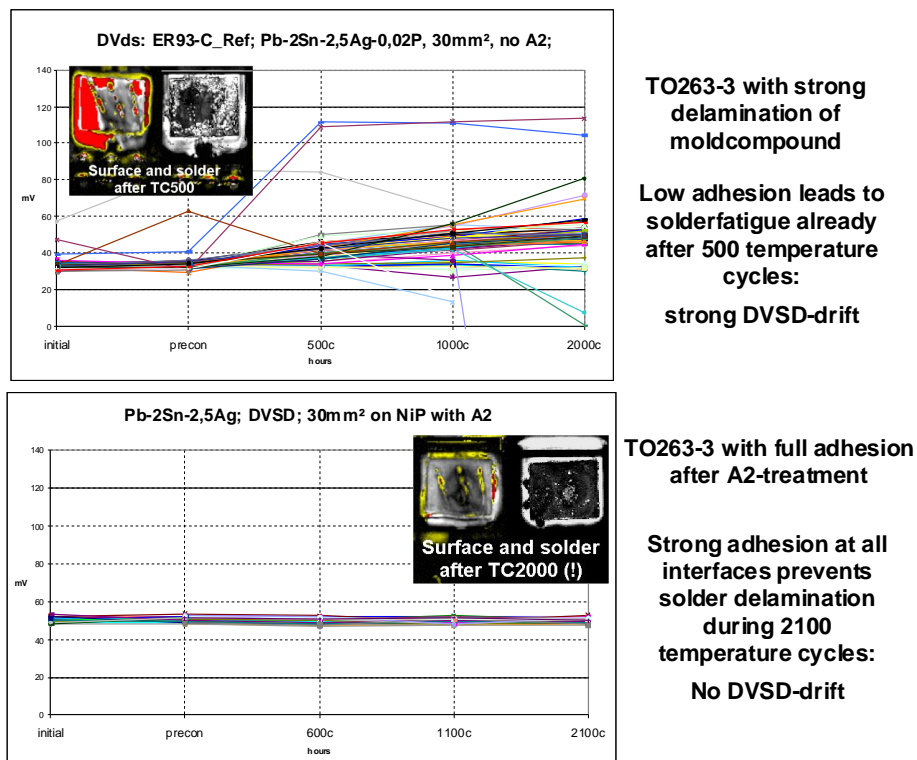


Figure 9: Top: Interface degradation leads to fatigue of the solder and therefore to a fail of the thermal contact between chip and package. This leads to a electrical drift of the DVSD parameter. Bottom: No solder degradation, no drift of the electrical DVSD parameter.

Wire-Interconnect fatigue

Besides the chip solder the delamination of molding compound also affects the wire interconnects at the frontside of the chip. There are basically two categories of wire interconnects in power semiconductor packages:

- a. Homogenous systems such as Al/Al, Au/Au or Cu/Cu.
- b. Heterogeneous systems such as Al/NiP; Au/Al; Cu/Al.

Within the homogenous systems the metal-to-metal adhesion is only driven by interdiffusion, there are no metallurgical reactions running as both partners consist of identical metals even if there are slight differences in doping. Therefore interconnects with homogenous systems do not show metallurgical degradation mechanisms.

In contrast, heterogeneous systems can form several intermetallic phases which in some cases are not favored due to degradation, in some cases are favored as they offer a very

strong crystalline interconnect. Contacts of Au wires on Al metallisation for example show a decrease of the mechanical strength of the interconnect during formation of several intermetallic phases such as Au_4Al , Au_5Al_2 , Au_2Al , AuAl and AuAl_2 especially at a temperature above 150°C [6].

In addition to metallurgical degradation mechanisms of wire interconnects, a additional failure mode specifically for heterogeneous systems is corrosion. As different metals are in contact to each other contact corrosion together with humidity leads to ion movement and fast oxidation of the less noble partner (e.g. Al dissolution in the system Al/NiP). This can happen during the manufacturing of the device in wet chemical processes and also during the lifetime of the device. Delamination of molding compound is the starting point which leads to open paths between ambient humidity and the interconnect.

Finally, in addition to metallurgical and electrochemical degradation mechanisms which mainly lead to a decrease of the mechanical strength of the interconnect one of the major fatigue risks for all bond interconnects is mechanical stress due to delamination of the molding compound to the device. This leads to shear and pull stresses on wires and finally to breaking of the already weakened bond contact. Figure 6 shows two example pictures.

Also for the interconnects on the chip frontside adhesion of the molding compound is an important factor to maintain stable wire bond contacts.

Degradation of package interfaces

A pure polymer (either duromer or thermoplast) has only a weak interaction to inorganic surfaces (e.g. metals, oxides, nitrides) by Van-der-Waals forces or via hydrogen bridges. Therefore most molding compounds are coming with bifunctional additives engaging a stronger bonding towards inorganic surfaces (e.g. tri-ethoxysilyl functions). There is a high number of adhesion enhancing technologies either intrinsically inside the molding compound with bifunctional molecules as well as dedicated adhesion promoters or primers which are applied to the surfaces of the chip and the leadframe prior to molding.

Fatigue at the interface can happen at the leadframe, for example through cracking inside a Cu(I)-oxide/Cu(II)-Oxide interface and fatigue can happen by cracking of the

molding compound along the interface. Finally also the chemical bonds at the interface can disintegrate. The latter happens especially together with water. Water at high temperature is acting as a nucleophilic agent reacting with carbonyls and other electrophilic groups which are responsible for the interconnect. Water from ambient humidity diffuses into the molding compound towards the interface. Applying PCB solder heat is increasing the reactivity of water, its vapor pressure increases and that can lead to a sudden cracking of the interfaces which is known as popcorn cracking [7] within a semiconductor device.

Degradation of molding compounds

The major parts of a molding compound are the resin and the fillers. Typically epoxy resins with SiO₂ filler are used. The most frequent is an orthocresolnovolac resin (OCN). Catalysts accelerate the polyaddition of the oligomers during molding at temperatures of 170°C - 180°C. Elastifiers maintain elasticity in order to keep thermo mechanical tensions in the package low. Adhesion promoter molecules improve the adhesion of the molding compound.

Waxes are used to enable the release of the molded units from the mold tool. Carbon black lowers the resistivity of the molding compound which works against electrostatic loading and gives it its black color. Flame retardants like metal hydroxides, phosphonates or red phosphorous lower the flammability. The tuning of all these components for processability and reliability of the molding compound is the challenge for compound and semiconductor manufacturers.

Increasing temperature on the molding compound is leading to several reactions. For instance 175°C with conventional molding compounds leads to accelerated decomposition of the flame retarding components, for example brominated aromatic substances. They form decomposition products which by themselves can act as nucleophilic and electrophilic reagents (Br⁺, Br radicals and Br⁻) for further decomposition. Corrosive products, e.g. bromine ions, can develop which lead to corrosion on bonds and chip metallizations [8]. Due to health restrictions such brominated aromatics are not used anymore since the semiconductor world has converted electronic devices to "green" products in 2006.

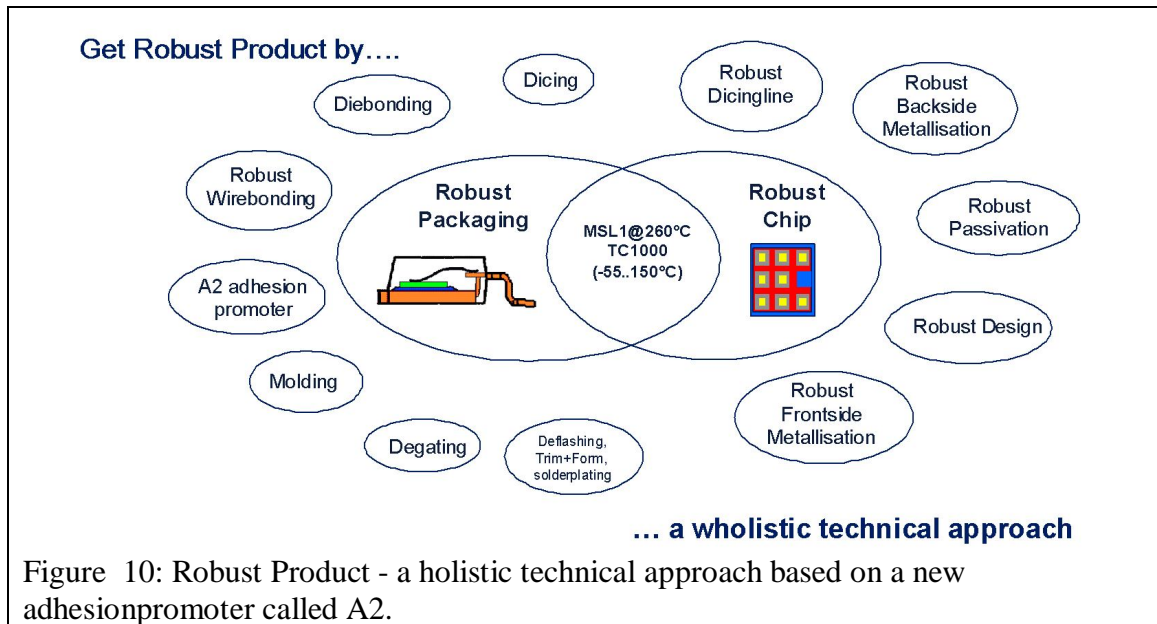
An important property is the glass transition temperature, which for most molding compounds lies within the range of 100°C to 200°C. The biphenyl systems are similar to the epoxy resin systems showing glass transition temperature within the range of 100°C to 130°C, the OCN (orthocresol novolac) molding compounds within the range of 130°C to 160°C, and multifunctional molding compounds such as naphthalene based resins in the range of 180°C to 200°C [4].

Also CTE rises once the temperature exceeds the glass transition temperature of a molding compound which leads to increase of the stress at the interfaces to the metals and ceramics of the device. Adhesion at the interfaces is weakened and molecular adhesion is thermally cracked.

1.5 Measures to prevent fatigue in a power semiconductor device

Current requirements on especially automotive semiconductor devices are high already and due to the increase of electric complexity in cars future requirements will be further increasing. Lead-free soldering application brought in higher PCB reflow soldering temperatures of 260°C at high humidity (260°C@MSL1/85/85%rel.hum.) already in 2006 which required the design of a robust product as described in this work. High temperature application will furthermore apply high thermal and thermomechanical stress to the package as well as to the chip.

To overcome this challenge only a holistic strategy turned out to be successful in designing a robust product which is prepared to withstand also future stress. Figure 10 describes the elements within a semiconductor device and its manufacturing process which have to be addressed in order to make a product robust.



1.5.1 Chip related measures

Chip related counter measures can be divided into three categories:

- a. Material design of metallization
- b. Material design of passivation
- c. Geometrical layout of metallization

The interaction between metallization and passivation is mainly described by thermomechanical parameters like CTE and mechanical parameters mainly represented by yield strength. The yield strength indicates the change from the elastic mode to the plastic mode of the mechanical deformation. Increasing the yield strength of a metal line means to withstand higher stress without a plastic deformation, only elastic deformation happens which means that after the mechanical stress the metal line turns back to the initial shape.

As a metallization for aluminium technologies state of the art is to use Al-1Si-0,5Cu alloy. The requirements for this alloy are coming from the semiconductor itself and from manufacturing constrains as aluminium for frontside metallizations is mainly sputtered. For technologies with diffusion barriers also Al-0,5Cu is established as there is no requirement to add Si to the Al in order to prevent spiking between Si of the chip bulk material and the adjacent Al metallization. Therefore there are not very much possibilities to change the mechanical properties of the Al bulk material in the

metallization. Sputter parameters and annealing steps within the manufacturing process do have specific other constrains for other sections of the chip (cell geometry and edge coverage) so that a specific optimization of the Al bulk properties is very difficult. Some semiconductor technologies are going the way towards sandwich structures sputtering several recurring Al and Ti layers in order to increase yield strength of the metallization. The more recent semiconductor technologies move completely away from Al and go for Cu based frontside metallizations. During development of the current robust product the alloy composition was not changed, but there were specific optimization regarding the sputtering of the Al metallization especially regarding minimization of Si precipitates in order to get a homogeneous distribution of Si grains within the metallization rather than a accumulation at any interface. This was basically reached by optimization of the sputter temperature profile during the whole process.

Major work has also been done on the design of the surface of the Al metallization, but the motivation here was not to increase the yield strength of the layer but to prepare the Al surface for the further adhesion promoter process which will be discussed in the individual section later.

For optimizing the material of the passivation there were two ways evaluated, the first way is to apply a silicon-oxy-nitride (SiON) instead of a SiN as SiON has a higher yield strength and therefore is not prone to cracking as what figure 11 shows. Increase of the yield strength by 50% showed no crack within this evaluation group.

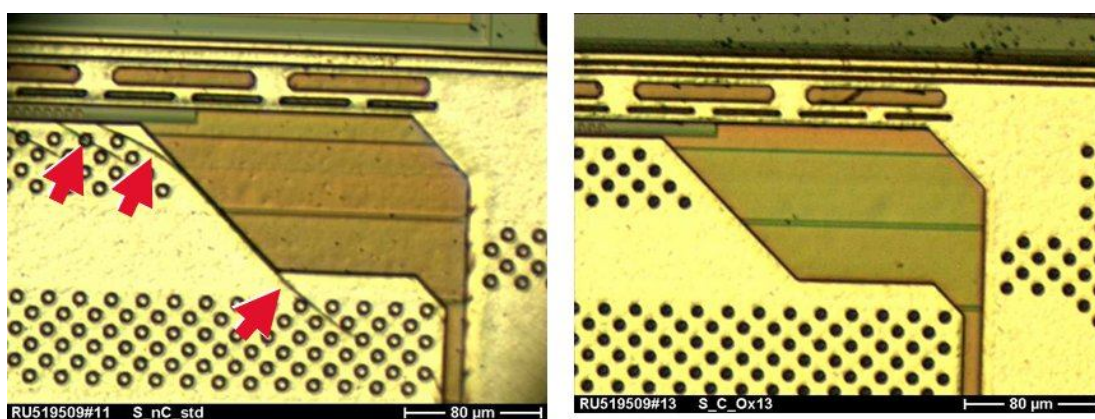


Figure 11: Comparison of crack formation with passivation layers with a yield strength of $0,04 \text{ MPa}\cdot\text{m}^2$ (left side, SiN) and $0,06 \text{ MPa}\cdot\text{m}^2$ (right side, SiON).¹

¹ : Investigations done by Josef Maerz, Karl Mayer, Zechmann Arno, Kleinbichler Franz and the team.

The second preferred option was to use a very thin SiN layer (40nm instead of 400nm) and cover this SiN with a 5 μ m polyimide layer. This system showed up the best reliability of the device and can be manufactured on standard equipment and processes. Figure 12 shows the difference of the crack behavior of a standard 400nm SiN passivation with huge cracks and of a stack of 40nm SiN and 5 μ m Polyimide where there are only minor small cracks visible after a thermomechanical stress of 1000 temperature cycles (-55°C to 150°C).

Besides the change of the mechanical behavior of the different materials the geometrical layout of the layers also has a big influence on crack formation. It is well known that the stress on the chip surface is highest at the chip corners. New design rules were applied in order to avoid damage of chip surface also in chip edges and chip corners. Limits for maximum width and minimum distances of metal lines are one of the major rules. In case of multi layer metallization technologies the overlap of the different metal lines was fixed.

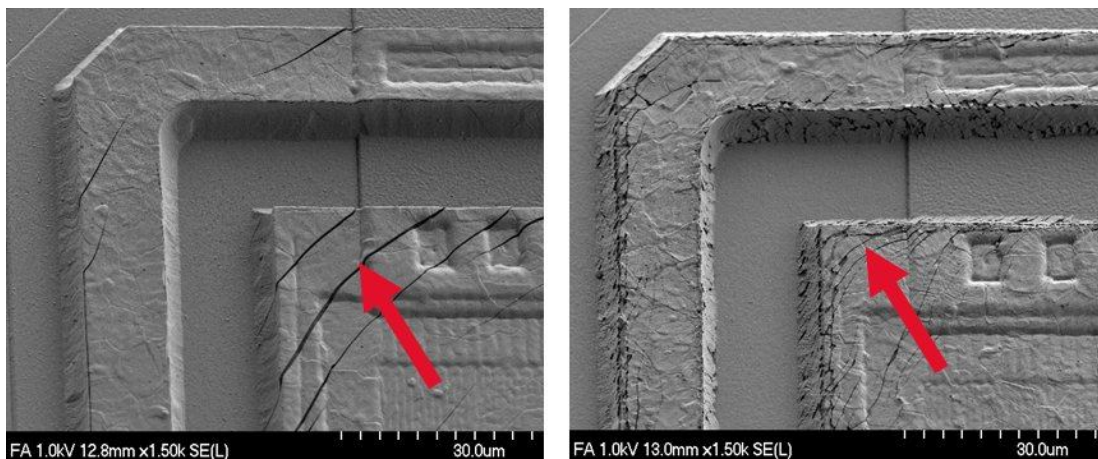


Figure 12: Comparison of crack formation between chips with 400 nm (left side) and 25 nm Silicon Nitride (right side). In order to investigate the SiN layer during opening and decapsulation of the device also the complete polyimide layer was removed. FESEM pictures only show the surface of the SiN and the Al metallization.¹

1.5.2 Package related measures

¹ : Investigations done by Josef Maerz, Karl Mayer, Zechmann Arno, Kleinbichler Franz and the team.

Chip-backside interconnect

Besides the optimization of the backside metallisation, which was moved from a vapor deposition process to a sputter process in order to get a highly reproducible single wafer process, choosing of the correct solder alloy was one key factor.

One major criterion was the melting point which had to be above 260°C with a safety margin of at least 10°C. Technological standard today is to use high Pb containing Pb-Sn-Ag alloys with melting points between 280-310°C dependent on composition. The composition chosen was Pb-2Sn-2.5Ag as a compromise between wetting of the solder and reliability. Moving to higher Sn concentration is reducing reliability of the solder, voids are formed much earlier during thermomechanical stress. Reducing the Sn-concentration on the other hand side is decreasing the wetting of the solder as Sn is the reactive species on the used substrates like Cu or Ni. The chosen alloy offers a melting point of $T_m=300^\circ\text{C}$, figure 13 shows a cross section of this solder in a device soldered on a Cu heatsink.

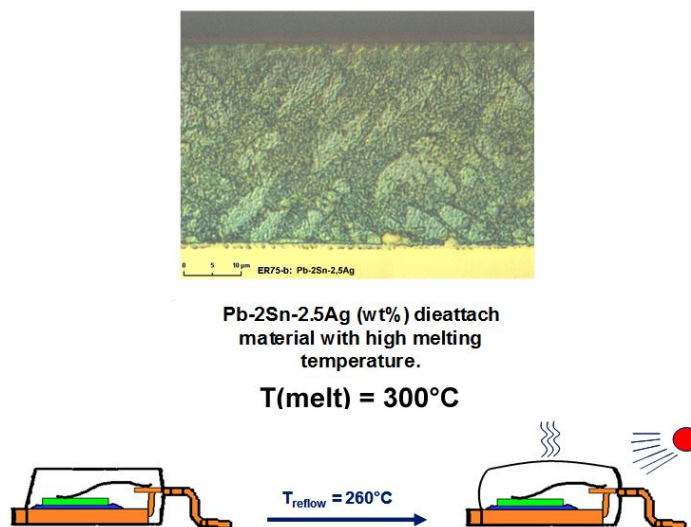


Figure 13: Ternary alloys are used for high temperature melting solders with $T_{\text{melt}}=300^\circ\text{C}$. These alloys withstand a soldering temperature on PCB of up to 260°C.

Currently these high melting Pb-based alloys are the only solders worldwide which are suitable for being used for 260°C PCB soldering temperatures. All alloys with high Sn content which are used in PCB industry (e.g. Sn-3.5Ag; $T_m=221^\circ\text{C}$) are melting below 260°C and therefore are unsuitable. There is still huge effort ongoing from the whole semiconductor industry to get a substitute for that Pb-alloy.

The known weakness of these solders is due to their soft mechanical properties, they easily undergo creep fatigue especially during temperature cycling stress. This technological limitation of the used solder alloy can currently only be compensated by minimizing shear stress to the chip and finally to the solder and to minimize creepage. In order to achieve this, the package has to have a hermetic encapsulation without any delamination of molding compound. This makes sure that the molding compound stiffness around the chip is also stiffening the solder layer. At this point it can be seen that an adhesion promoter is required on all surfaces interacting with the molding compound to achieve this stiffness.

Wire-interconnect

Besides the chip backside interconnect and the chip frontside metallisation also the interconnect from the package to the chip frontside plays an important role for a robust and reliable package. Furthermore besides the reliability of the interconnect it is important to make sure that through the interconnect processes the chip frontside is not damaged. In a power semiconductor device active structures are directly underneath the aluminium metallisation at the chip frontside which is a risk for wire bonding. Running wirebonding with very soft bondforce to the chip reduces the quality of the formed bond. Increased bond forces increases impact to the chip with the risk of getting a damaged chip frontside metallisation. During adhesion promoter deposition after wirebonding chemicals are able to penetrate into the semiconductor leading to parameter drifts.

In most cases the metal on the chip frontside is only 5 μm thick or even thinner down to 3 μm in power semiconductors. Besides this, the topology of the metallisation is defined by the structure underneath the metal. Figure 14 shows a comparison of three different, MOSFET devices. The sealing of the contact hole and the robustness for wirebonding is defined by the edge coverage of the aluminium which is defined by the contact hole geometry and sputter parameters for the aluminium deposition.

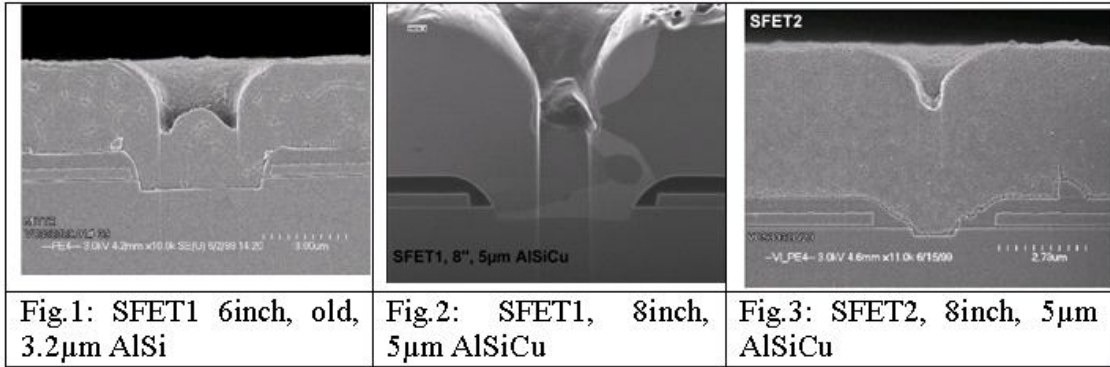


Figure 14: Comparison of contact holes in terms of metallization sealing. New technology platforms show excellent edge covering of the metallization.

The sealing of the chip towards ambient conditions is important to prevent corrosion and penetrating of ions into the semiconductor. After contact hole metal coverage optimization also the wirebonding processes have been adjusted in order to prevent further damage of the chip. From assembly side this issue was solved by a new generation of wirebonding parameters and by installing a new process control to make sure that the bond process results remains stable. In order to trace cracks in the frontside metallisation after wirebonding a reactive-ion-etch (RIE) analysis was established on sample base which decorates any cracks into the underneath Si oxide. Figure 15 shows an example of a 50µm Al wirebond with a very high penetration into the Al metallisation of the chip.

For power devices mainly Al wirebonding is applied as the interconnects on chip (Al/Al) and on lead (Al/NiP) are known to be metallurgically reliable up to 175°C and offer high current interconnects for MOSFET devices, therefore the focus in this work is on devices with Al wirebonding technology.

Recently in the last decade also Cu wire is used for power devices offering higher conductivity. In addition new semiconductor chip technologies are built with a Cu metallisation instead of the Al, using a Cu wire to directly bond on this Cu metallisation has the advantage of having the same metal for both partners and therefore no unfavoured metallurgical transformations.

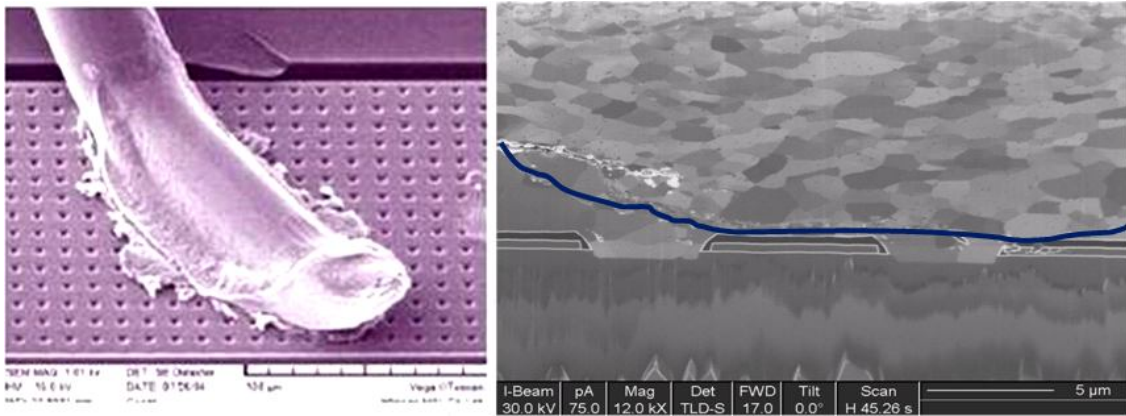


Figure 15 : Example of an Al interconnect with too strong bonding parameters leading to a high penetration depth and damage of the chip metallisation. The blue line indicates the crack direction.¹

Adhesion promoter

Throughout the different fatigue mechanisms which can be found in a power semiconductor device the primary defect in most cases is delamination of the molding compound. In a package the metal to molding compound interface is the dominating one and is present on all critical positions like at the chip surface, around the chip, on the solder and around the bondwires. Out of the learning of the different failure mechanisms it was claimed to have an adhesion promoter which covers the full device surface in order not to exclude any position in this system from proper adhesion. This claim consequently means application of the adhesion promoter just before molding process in order to cover all surfaces and therefore prevent the formation of weak interfaces. Strong adhesion on all interfaces minimizes internal friction and plastic deformation within the whole device and is therefore minimizing secondary fatigue mechanisms, as for example shown in figure 16 for the chip frontside. With a thermomechanical stress of up to 2000 temperature cycles (-55°C until 150°C) no shift of metal lines can be found in this example of a MOSFET device in a TO263 package.

¹ : Investigation done by Khalil Hosseini as an example of an Al wire bond interconnect

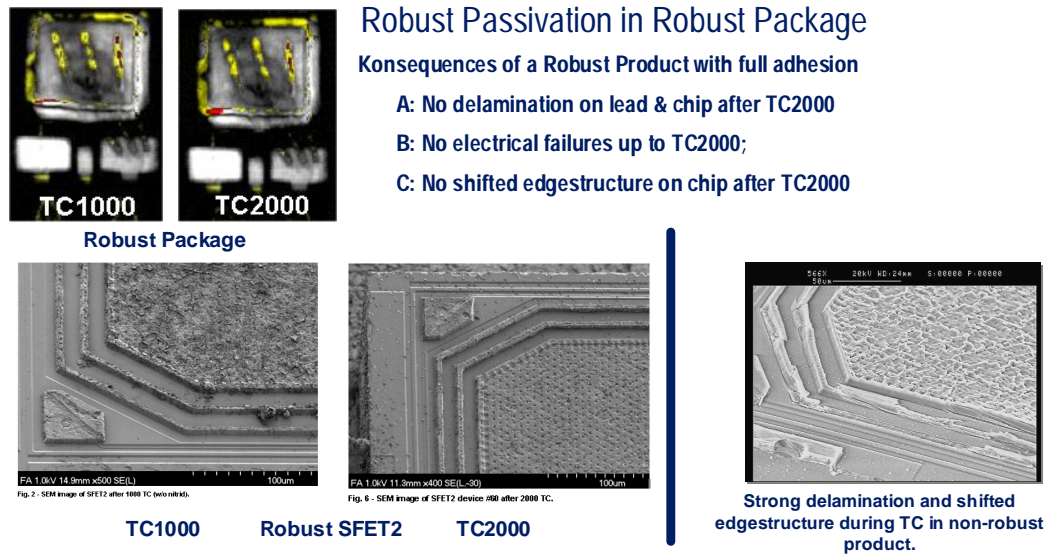
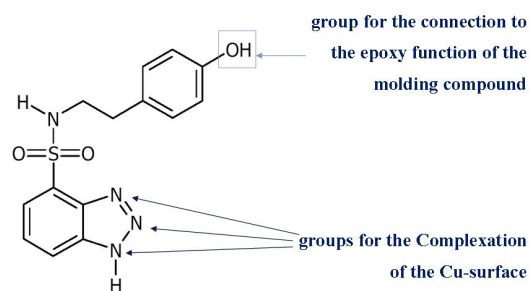


Figure 16: Reliability results after 2000 TC (-55 °c to 150 °C) within a TO263-3 package with a 30mm² MOSFET chip. Ultrasonic microscopy images show no delamination after this stress and this corresponds with metal lines which are still in good order (left). In the non-robust product (right) without A2 strong shift of the metal lines is seen.

On the other hand applying the adhesion promoter in assembly requires effort of applying a specific layer on the device within an assembly line under clean room conditions. Choosing the suitable candidate of adhesion promoter and developing a manufacturing process for mass production was one of the challenges of this work. Basically there are several adhesion promoters known which can mainly be categorized into two sections:

- a. Promoters acting on molecular level.
- b. Promoters acting on mechanical level.

For example primers are acting on molecular level and require a proper preparation of the surface chemistry to be able to form the relevant chemical bonds. In many cases these reactions are very specific and limited to certain metal oxides and metals. The deposition of that species can be done by dipping or spraying. The surface preparation has to be specifically generating a surface chemistry which fits to the functional groups of the primer. Figure 17 shows a molecule of a benzotriazole-derivative which is designed specifically to fit to Cu surfaces due to the triazo-group. The aromatic hydroxyl-function is reactive towards the oxiran function of common epoxy resins of molding compounds.



Remark: "Designed" especially for Cu-surfaces

Figure 17: Example of a primer working on molecular level. In this case these triazolium type system are dedicated to Cu surfaces and the hydroxyl group is linking to oxiranes of epoxy resins.

The second category are adhesion promoters acting on mechanical level. Mechanical adhesion promoters are mainly adhering through mechanical interlocking. There are always also chemical or physical forces working like van-der-Waals forces or hydrogen bridges, but those are not the dominating forces and therefore the surface chemistry compatibility to the resin is not that crucial as with molecular adhesion promoters. On the other hand mechanical adhesion promoters are performing only effectively if the morphology is fitting to the used polymer. In the section 3 identification of suitable candidates will be deeper discussed, Figure 27 shows two examples of mechanical adhesion promoters with their specific pore size.

Encapsulation - Molding compounds

Regarding reliability of molding compounds it was described above already that there are a couple of resin systems available to manufacture molding compounds with high T_g and with specific properties. Target properties achieve minimized stress level for the package, an optimum processability during molding, and full compatibility to all surfaces. There are many orders of freedom in designing a molding compound since there are more than 10 different ingredients in modern molding compounds which have specific chemical and geometrical properties like the filler size, shape and filler material. Table 2 shows an overview of components required for the formulation of a molding compound. The composition of this material formulation defines how the material behaves in the manufacturing processes and in the product.

Component	Examples	Content [wt%]
Basic resin	Ortho cresole novolac, dicyclopetadienyl, biphenyl	10-20
Hardener	Components similar to the base resins, hydroxylated multi-aromates	
Filler	Cristallin silica, sherial cristallin silica, AlN, BN	80-90
Catalyst	substituted triphenylphosphines	<5
Flame retardant	Al ₂ O ₃ , MoO ₃ , B ₂ O ₃ , Al(OH) ₃ , Mg(OH) ₂ , Zinc Borate, Zinc Molybdate, Zinc Stannate, red phosphorus, phosphates, phosphonates, Melamine, Guanidine, Silicone Polymer, Polyphosphazene	
Adhesion promotor	Triethoxysilyl groups included in the epoxy matrix, mercapto silane	
Releasing agent (wax)	Acts as a mold release agent, but decreases adhesion; carnauba wax; polyethylenwax	
Flexibiliser and coupling agent	Aliphatic dicarboxylic acidester, polyester, phosphoricacidester, fattyacidester Hydroxycarboxylacidester, epoxy and sulfoxide/sulfon	
Ion catcher	Catches free ions in the molding compound like Na ⁺ ; Cl ⁻ in order to prevent corrosion, BiO(OH) _{0.74} (NO ₃) _{0.15} (HSiO ₃) _{0.11} ; MgAl _{0.45} O _{1.67}	
Coloring agent	Optical purpose and dissipates electrostatic charges; carbon black	

Table 2 : Overview on different substances used for molding compound formulation.

The molding process has to be fast due to high equipment investment, so the polymerisation kinetics defined by the resin, hardener and catalyst is optimized by the supplier of the molding compound. On the other hand during the injection of the material into the moldtool the viscosity has to be limited, the viscosity increase of the liquid resin needs a specific delay until the full injection is over and then a fast hardening is required. Especially for packages with nanoporous adhesion promoters the selection of suitable polymerisation kinetics is important to be able to fully penetrate into the adhesion promoter layer.

Finally, after resin hardening the product needs to be released from the moldtool. Due to the volume shrinkage of the epoxy matrix during hardening this is no big problem for molding compounds with low volume fraction of fillers as the overall shrinkage is quite high. Unfortunately those molding compounds do have a higher CTE as the average

CTE of the molding compound is defined by the mixture of resin with a very high CTE and the filler particles with a quite low CTE.

Besides processability there are some reliability aspects to consider for choosing molding compounds.

In order to reduce the stress to the chip surfaces molding compounds with advanced filler contents have been developed. In order to adapt the average CTE of the molding compound to silicon filler loading, type and shape has been optimized. There are materials which reach CTE very close the CTE of silicon (Example: Shinetsu KMC2110-7G: $\alpha_1 = 6 \cdot 10^{-6} \text{ K}^{-1}$ ($T < T_G$); $\alpha_2 = 36 \cdot 10^{-6} \text{ K}^{-1}$ ($T > T_G$); Silicon: $\alpha_{Si} = 2,9 \cdot 10^{-6} \text{ K}^{-1}$). There are other factors arising with those low CTE materials especially with semiconductors manufactured with aluminium metallisation. The CTE of aluminium ($\alpha_{Al} = 23 \cdot 10^{-6} \text{ K}^{-1}$) is much higher compared to the CTE of those molding compounds which leads to an increase of thermomechanical stress towards the aluminium metallisation.

1.6 Focus of this work

Several process steps and materials have to be optimized to get a highly reliable power semiconductor device. One important understanding out of the fatigue mechanisms in such a device is, that delamination of the molding compound is responsible for several fatigue mechanisms. Solving this adhesion problem is the crucial element to get a robust product. There are many approaches to increase adhesion. The focus of this work is the identification of a suitable adhesionpromoter and the development of this candidate up to mass production. The target with this technology was set to achieve 260°C PCB solder heat resistance at MSL1 (85°C/85%rel.hum) and TC2000 (-55 to 150°C) with full adhesion and stable electrical parameters over these stress tests.

The second focus of this work is the surface design of copper surfaces with organic molecules. This is applied for soldering and for bonding of Cu wire to the Cu metallisation of power semiconductor chips. To prevent oxidation of the Cu surfaces different passivation concepts have been worked out to enable the broad usage of this metal for power semiconductor devices.

2 Analytical and experimental methods

In the following sections the discussion of the experimental results will be made based on various analytical and experimental methods. Therefore in this chapter these methods are briefly described first. All experimental and analytical results that are being discussed are structured in a similar way using a specific number for the individual experiment, such as er265, and for each experiment specific sub-experiments are named as groups with specific numbers or characters, such as er265-1 or er265-A. The experimental matrices with the specific group numbering are given in the various experimental sections.

2.1 Field emission scanning electron microscope (FESEM): Surface morphology

Most of the analysis of deposited layers in terms of surface topology has been done with field emission scanning electron microscopy (FESEM). The basic principal of SEM imaging is the scanning of a surface with a focused primary electron beam (EB) consisting of a energy of up to 15keV. The generation of the EB within a FESEM is done with a cold field emission gun which is for example a tungsten needle within a very high electric field $E > 10^9 \text{ V}\cdot\text{m}^{-1}$. Under these conditions, in a high vacuum of about 10^{-7} mbar, electrons are emitted into the vacuum by tunnelling through the tungsten oxide barrier of the tungsten cathode. They are then accelerated by a voltage of 1-50kV between cathode and anode forming a very fine EB which offers a resolution for example of 0.4nm at an acceleration voltage of 30kV and of 1.2nm at 1kV [9]. A similar generation of the EB is done with a Schottky field emission source which offers the advantage of higher beam current while still maintaining good resolutions for example of 1.0 nm at an acceleration voltage of 15kV and 1.6nm at 1kV [10].

During the collision of the EB with the surface various interactions with the sample material happen as illustrated in figure 18. For FESEM mainly the signal of the low energy secondary electrons (SE) generated directly by the EB is detected. Depending on the angle of the sample, the amount of SE is varying and the signal variation during scanning of the surface by the electron beam enables the generation of a sharp 3-

dimensional image of the topology of the surface. SEs are released out of a depth of the first 10nm of the sample.

In addition modern FESEM equipment has a back scattering electron (BSE) detector. BSE are generated through elastic scattering of the primary electrons with the atomic nuclei of the sample and due to the elastic scattering they do not lose very much energy in comparison to the primary electron beam. Therefore, the BSE can come out of a depth of several hundred nanometres. In addition, the yield of BSE is strongly dependent on the atomic number, which is related to the atomic mass of the material. Therefore the BSE signal offers a material contrast which gives an indication of the chemical composition of the sample [11].

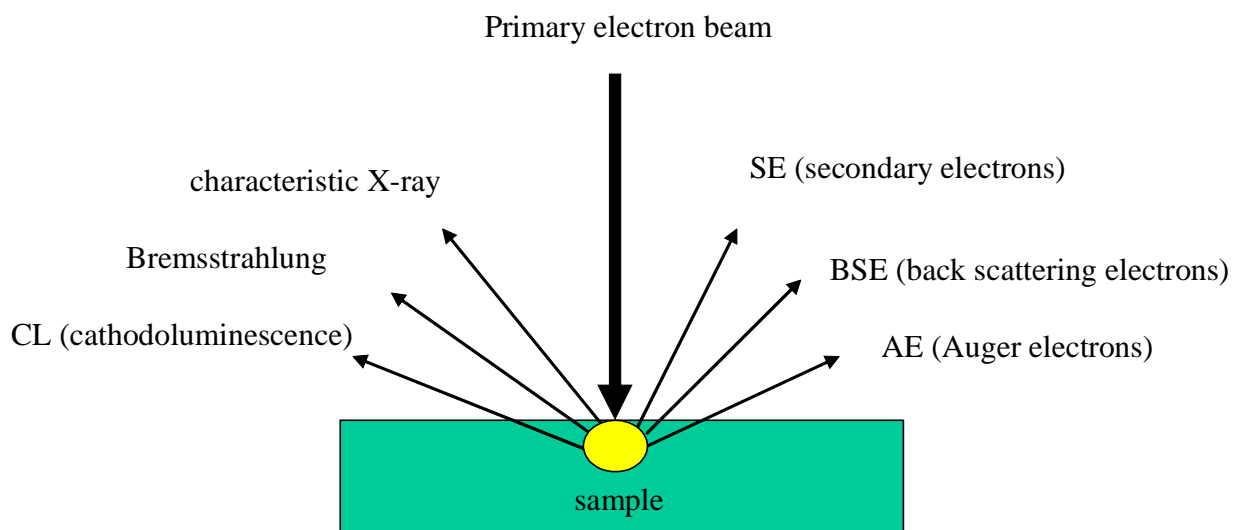
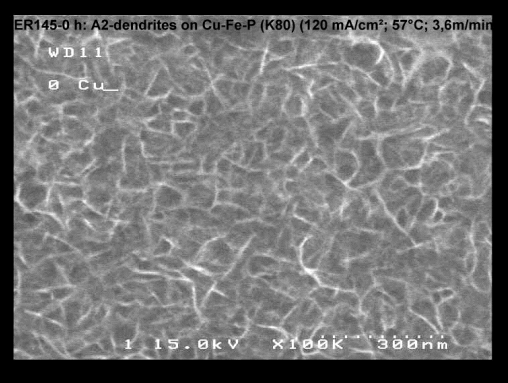
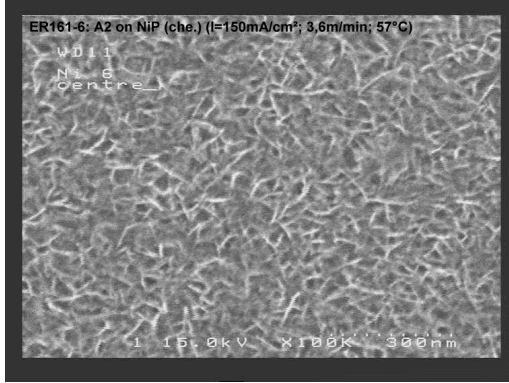
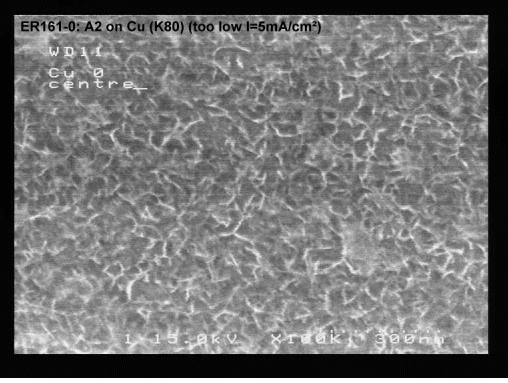
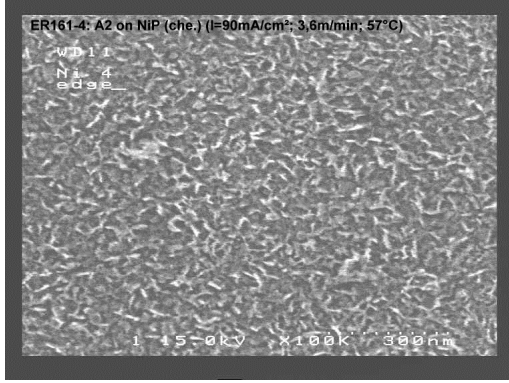


Figure 18: Interactions between an electron beam with a material.

An additional interaction between EB and the samples is generating Auger electrons explained later in chapter "2.7 Auger electron spectroscopy (AES)". Furthermore cathodoluminescence is an emission of light in the visible range of the electromagnetic spectrum ($\lambda=400-700\text{nm}$) generated by the primary electron beam, but the information based on this interaction is of less importance for FESEM and only important for specific semiconducting materials in analysis of for example doping concentrations [11]. Finally, emission of radiation in the lower wave length region as characteristic X-ray or as Bremsstrahlung is observed which is not discussed in this section. However, the former one is important for energy dispersive X-ray (EDX) analysis that is discussed in chapter "2.2 Energy dispersive x-ray spectroscopy (EDX)".

Specifically for the sponge structure of the A2-layer FESEM analysis was mostly done at 15kV acceleration voltage and a magnification of 100k. Since the most important property of the A2-layer is the surface morphology, enabling a mechanical interlocking function to the molding compound, the surface analysis with FESEM became a major part of the characterization of the deposition process together with the adhesion tape test described in chapter "2.5 Tape adhesion test". For the purpose of characterizing various morphologies on the various surfaces, a morphology catalog was defined based on FESEM results to assess the quality of the various deposits in 4 categories which are shown in table 3 for Cu and NiP and in table 4 for the Al chip metallisations and the solder surface.

Morphology catalogue of A2-coating for different adhesion performances		
Category	Cu surface	NiP surface
A		
B		

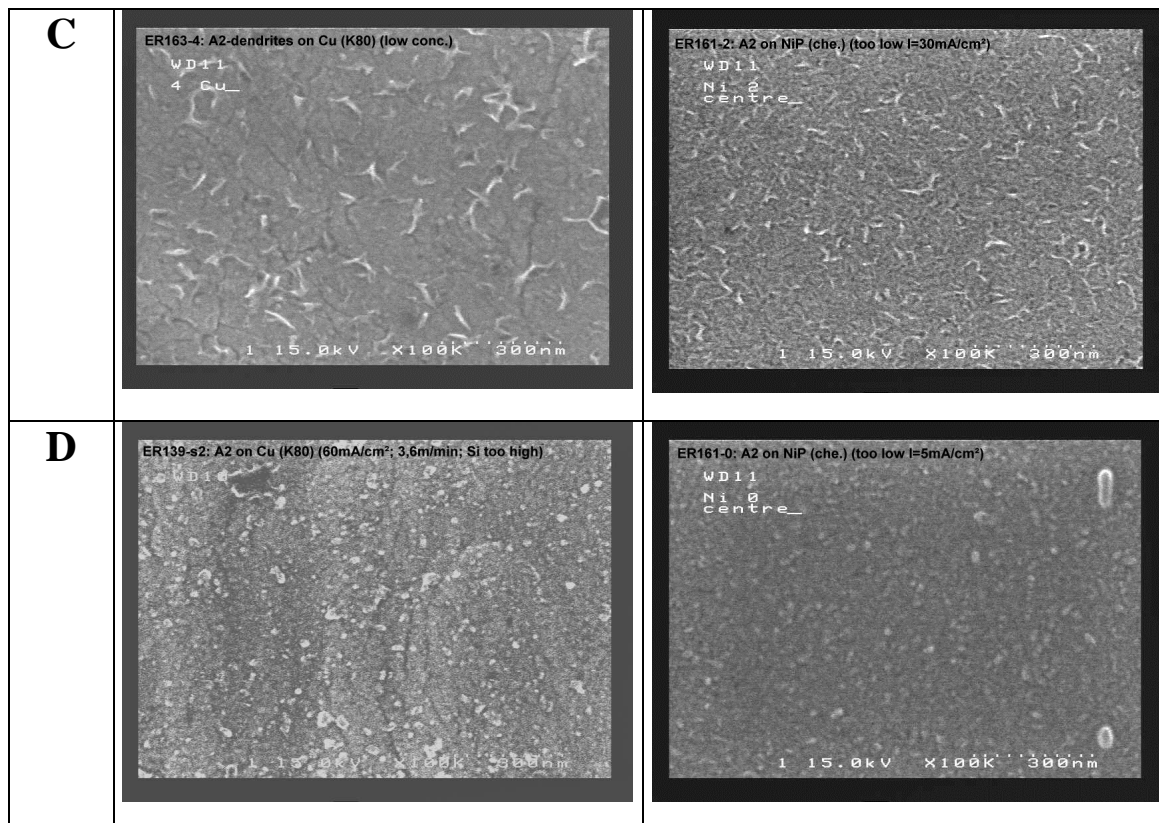


Table 3: FESEM based catalogue of various A2 dendrite morphologies on Cu and NiP surfaces rated A to D.

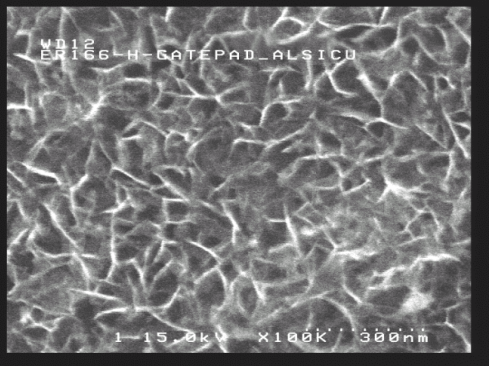
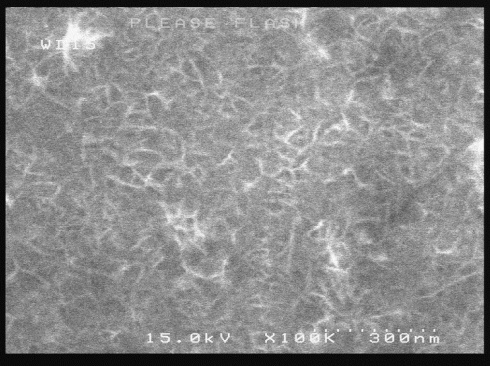
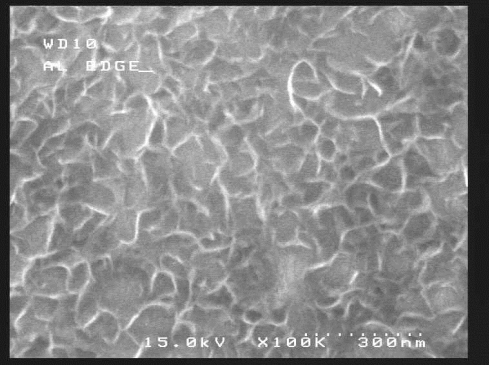
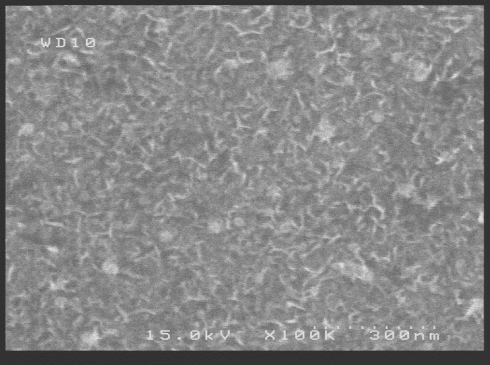
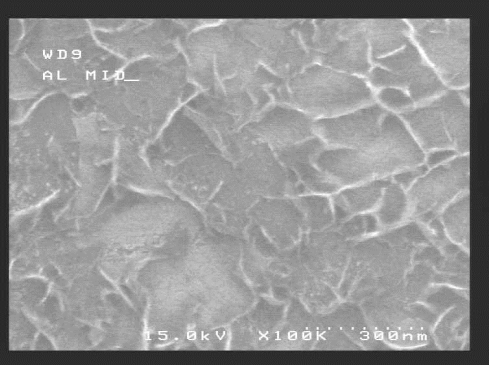
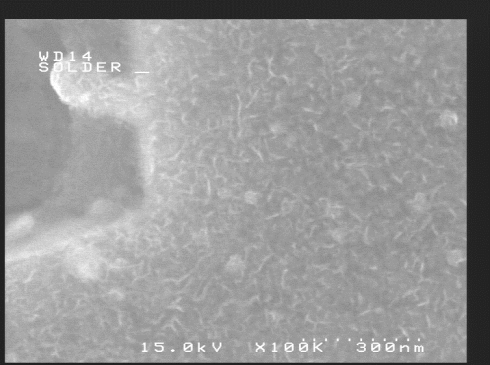
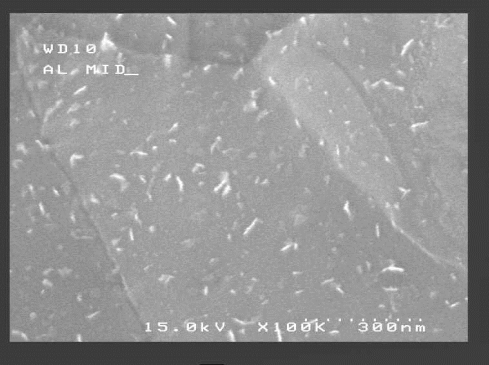
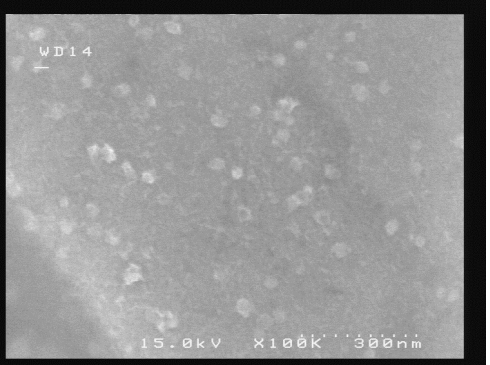
Category	Al chip metallisation (Al-1Si and Al-1Si-0.5Cu)	Pb-2Sn-2.5Ag solder
A		
B		
C		
D		

Table 4: FESEM based catalogue of various A2 dendrite morphologies on Al chip metallisation (Al-1Si and Al-1Si-0.5Cu) and Pb-2Sn-2.5Ag solder surface rated A to D.

For each substrate having the A2-layer, the categories A-D were defined with the following observations in the FESEM with 100k magnification:

Category A: Dense, homogenous sponge structure

Category B: Dense sponge structure with single spots without a A2 layer where the flat substrate is visible.

Category C: Sponge structure with bigger areas in between where the flat substrate is visible.

Category D: None or only single needles can be observed, mostly the flat substrate morphology is present.

These categories were used in the respective experiments to distinguish between the results of the specific process conditions.

2.2 Energy dispersive x-ray spectroscopy (EDX)

In the previous chapter the interaction of an electron beam with a material was described and two important interactions leading to the emission of radiation with lower wavelength ($\lambda \leq 400\text{nm}$) given. For the case of Bremsstrahlung a continuous spectrum is emitted, in addition x-rays with characteristic wavelength for the specific material are emitted. The latter one is generated through the excitation of an atom via x-ray or via the electrons of an electron beam. Excitation means the striking out of an electron from the orbital of an atom of the specific material which leads to a shift of electrons with higher energy from higher orbitals within the atom shell towards lower energy orbitals. The energy difference for this shift is equal to a characteristic wave length for a specific atom for a specific line which is given by equation (1). In this equation h is the Planck constant ($6.626 \cdot 10^{-34} \text{ J}\cdot\text{s}$), ν is the frequency of the radiation (s^{-1}), c is the light speed ($2.997 \cdot 10^8 \text{ m}\cdot\text{s}^{-1}$) and λ is the wavelength (nm).

$$E = h \cdot \nu = h \cdot \frac{c}{\lambda} \quad (1)$$

For example the interaction of an electron beam with Cu atoms leads to the following characteristic wavelengths which will be emitted from the sample: $\lambda_{K,\alpha 1, \text{Cu}} = 1.5406 \text{ \AA}$

10^{-10} m, $\lambda_{K,\alpha 2,Cu} = 1.5444 * 10^{-10}$ m, $\lambda_{K,\beta 1,Cu} = 1.3922 * 10^{-10}$ m, $\lambda_{L,\alpha 1,Cu} = 15.286 * 10^{-10}$ m, $\lambda_{L,\beta 1,Cu} = 13.053 * 10^{-10}$ m [2]. In energy dispersive x-ray spectroscopy (EDX) the characteristic energies are measured to detect the elements within the sample, the detectors are mostly combined with a SEM (scanning electron microscopy), FESEM (field emission scanning electron microscopy) or a TEM (transmission electron microscope). The characteristic radiation is generated within a depth of several micrometres depending on acceleration voltage and on the sample material. Hence, as a surface analysis tool EDX has limited application. More details are described for example from Oettel [11] and from Martin [15].

2.3 Transmission electron microscopy (TEM)

In contrast to SEM described above TEM requires very thin samples that are in the thickness range of 10 to 100nm. Preparation of the sample requires higher effort as the material has to be first encapsulated in epoxy and then thinned mechanically and polished to the necessary thickness with an ion milling equipment. Ion milling is done with 1-5keV Ar^+ low energy ions at low incident angle of $<5^\circ$ on mechanically cut foils that consist of the sample embedded in a resin.

Samples that are chemically and mechanically more stable, like materials from semiconductor devices, often are prepared through generation of a lamella via focus ion beam cutting (FIB)¹.

Then the sample is placed in a vacuum chamber and percolated from an electron beam.

The electron source used for TEM is working similarly as with FESEM/EDX using energies of 80 to 400keV. Due to the low thickness of the sample the electron beam intensity is decreasing only to some extent moving through the sample and the remaining primary beam intensity is detected. Depending on the material the electron

¹ : Focused ion beam method (FIB) uses Gallium ion beams (30keV) to cut into the surface and sputter material off the surface. A sharp cut edge is forming at the cutting crater. With this method thin slices for TEM can be cut out of the bulk material and mounted onto the TEM holder. The final sample thickness of <100 nm is reached by application of low energy ion beams, such as Gallium ions with 5 keV or Argon ions with <1 keV energy.

beam is scattered. Via special apertures the unscattered electrons are collected in the primary beam direction, the intensity detected depends on the atomic number of the elements in the samples. Similar to SEM an area in the x/y plane is scanned and a contrast picture can be obtained. Thick areas of the samples and areas with heavy atoms will appear dark and a bright contrast is obtained with thinner sample areas and material consisting of lighter atoms.

In addition with specific detector positions the back scattered electrons and the electrons that are undergoing diffraction are collected. More complex information can be gained concerning the crystallographic properties in the specific sample position

Besides the detection of electron intensities the combination with x-ray detectors is common enabling the collection of EDX spectra for elemental analysis as with SEM/EDX. For deeper information on TEM and sample preparation see Lee [12] who gives a brief review. An overview on methods for local chemical analysis of materials is given by Martin [15] and Schumann and Oettel [11].

2.4 Button shear test

Copper plates with the NiP plating ($A = 2 \times 10 \text{ cm}^2$) and the deposited A2 structure are subjected to a molding press (LHMS-28M equipment from Laufer GmbH & Co KG) where five molding compound buttons in one row are moulded onto the plates via a dedicated molding tool. These molding compound buttons have exactly the same size as the molding compound of a TO263-3 device (Area = $9.25 \times 10 \text{ mm}^2$; height = 3.1mm). After molding, the plates are further processed with post molding curing to get similar properties of the polymerized epoxy as within the real product. After their manufacturing, the molding buttons can be destructively sheared off in parallel to the Cu plate with a shear tester measuring the respective shear force at breakage of the buttons from the plate. This test is done for specific samples after specific stress test on the plate such as MSL1/260°C soldering or temperature cycling (TC) to simulate degradation effects that may result in interface adhesion deterioration which then are measured by the shear tester.

2.5 Tape adhesion test

The tape test was developed as a quick and simple method to test the coverage of a surface with an adhesion promoting layer, for example the A2 layer. Two different types of Scotch tape™ from 3M were used, Scotch 600 (No.:07457-8) and Scotch 800. Both types are suitable, but the Scotch 600 tape shows a slightly better reproducibility. During the testing the tape is first pressed upon the sample and smoothly rubbed onto the surface with the thumb to remove all enclosed air and to ensure a proper penetration of the glue into the structure of the surface, i.e. the sponge structure of the A2-layer. Then the tape is peeled off slowly from the surface. During the peeling of the tape two different cases can take place as it is shown in figure 19:

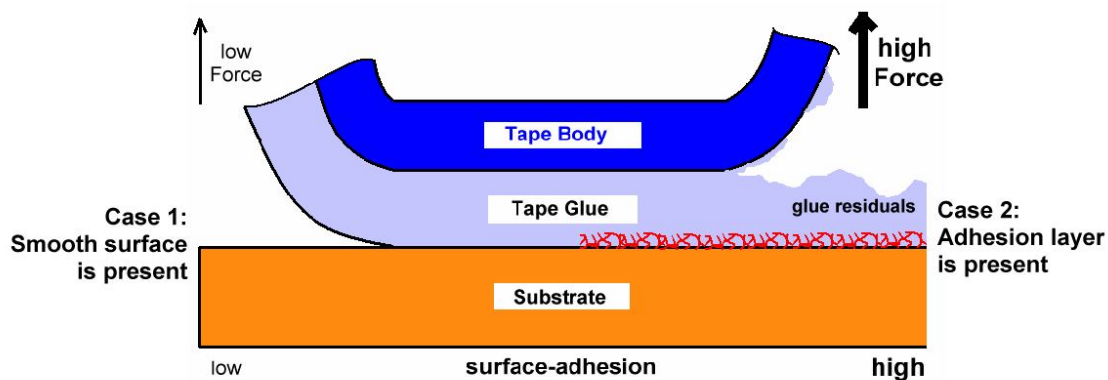


Figure 19: Schematic of the tape test and the two different results for the following surfaces: A smooth surface on the left and a surface consisting of an adhesion promoting layer as deposited by the A2 process on the right.

Case 1: If a smooth surface is present with a low adhesion towards the tape glue only a low force is required to peel off the tape. The separation happens at the interface between the substrate and the tape glue, no glue is sticking on the substrate and after the peeling no glue residuals can be seen on the surface (figure 19 left side).

Case 2: If an adhesion layer is present on the substrate which has a high adhesion to the glue, i.e. the sponge structure of the A2 layer, a high force is required to peel off the tape. The adhesion strength of the glue to the surface in this case is much higher than the adhesion strength to the tape body or the overall mechanical strength of the tape glue. Separation now occurs mainly between tape body and glue and sometimes inside

the glue. A layer of the tape glue is sticking to the substrate which can be easily optically observed with eye or with a microscope (figure 19 right side).

The major advantage of the tape test when compared to other methods is the analysis of a larger area of the substrate. This allows an estimation of the coverage of a surface with an adhesion promoting layer with a much broader statistics when compared to FESEM, which offers only a spot analysis and also gives no indication of the adhesion of the layer on the substrate. An estimation of the area of glue residuals covering the substrate was done as a qualitative test method on a standardized sample, a TO263 heat sink at the backside. In table 5 the glue residuals are shown for Cu and NiP substrates which are completely covered with an adhesion layer in comparison to the reference surfaces which are not covered with the adhesion layer. The coverage with glue after the tape test is 100% of the observed area of a TO263 heatsink backside.

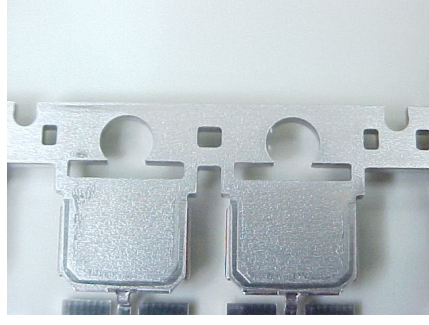
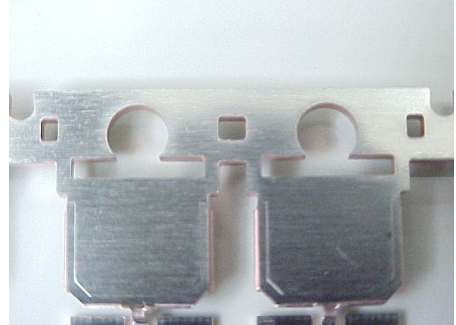
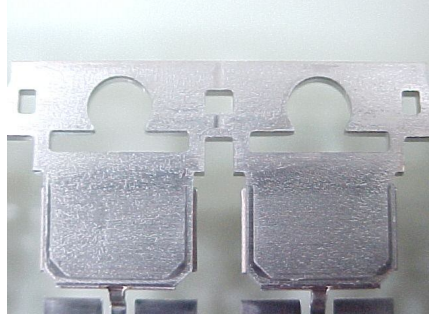
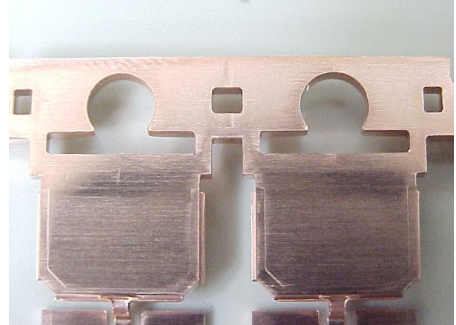
	NiNiP with A2 layer	Reference: pure NiNiP surface
Category A: Complete A2 layer coverage 100 % glue residuals		
	Cu with A2 layer	Reference: pure Cu surface
Category A: Complete A2 layer coverage 100 % glue residuals		

Table 5: Tape test results at completely A2-coated Cu and NiP on a TO263 heatsink backside and comparison to the non-treated surfaces as a reference. The coverage with glue residuals is 100% (category A).

Table 6 shows the tape test results on samples with lower coverage of the area with an adhesion layer and therefore fewer amounts of glue residuals distributed over the surface. The following categories and areas of glue residuals on a TO263 heatsink


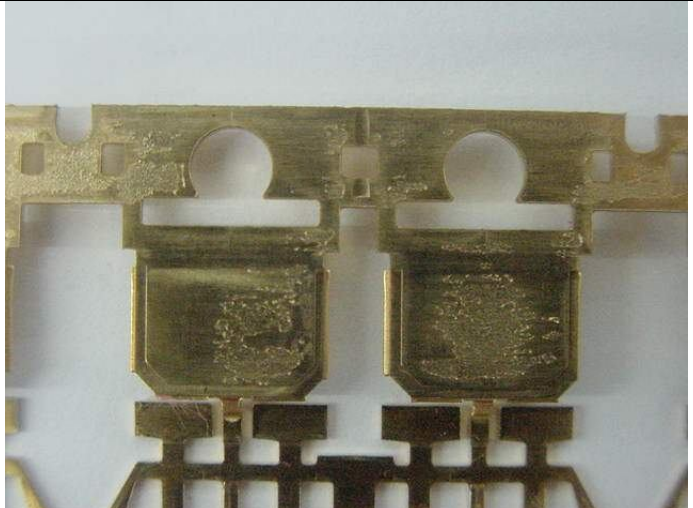
backside have been defined to measure the coverage of a surface with an adhesion layer, i.e. the sponge structured A2 layer:

Category A: 90-100% glue residuals, complete A2 layer coverage

Category B: 70-90% glue residuals, reduced A2 layer coverage

Category C: 50-70% glue residuals, poor A2 layer coverage

Category D: <50% glue residuals, insufficient A2 layer coverage

<p>Category B:</p> <p>Reduced A2 layer coverage</p> <p>70-90 % glue residuals</p>	
<p>Category C:</p> <p>Poor A2 layer coverage</p> <p>50-70 % glue residuals</p>	

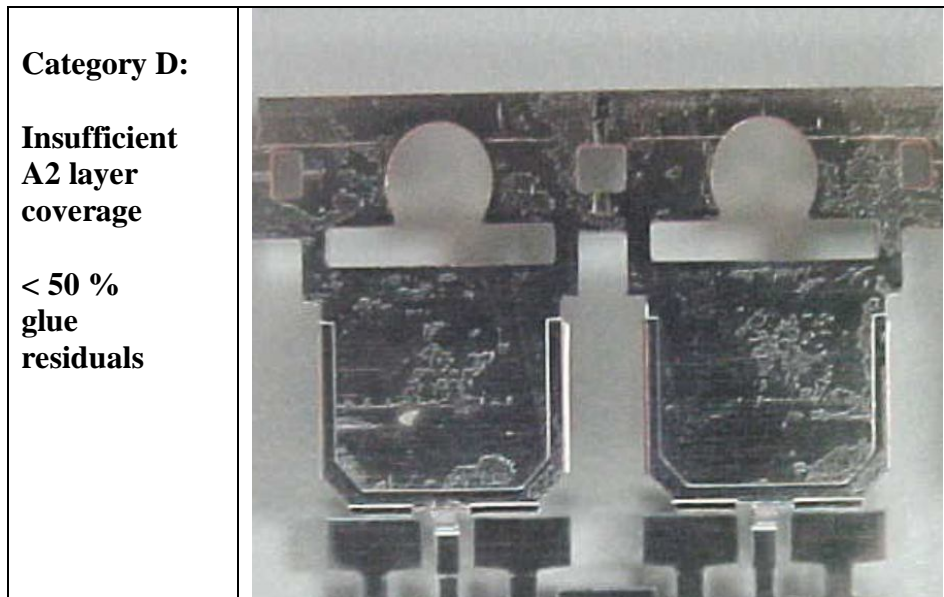


Table 6: Tape test results on A2-coated NiP on a TO263 heatsink backside with different A2 layer coverage from <50% (category D) to 70-90% (category B)

Unfortunately, no direct correlation to the adhesion in the final package can be made. This limits the value of this test for the final product. It is only suitable for the quantification of the surface area covered with the adhesion layer, but not for the quantification of the adhesion strength of the adhesion layer to the substrate.

2.6 A2 dip test

For characterising the reactivity of Al metallisation of a semiconductor chip within the electrolyte of the A2-plating processes a fast test was used as a dip test in the electrolyte solution used for A2 deposition.

During the standard A2-plating process the A2 layer is deposited electrochemically on all metallic surfaces. For Al surfaces this deposition also takes place without application of a current but only by dipping the Al sample into the A2 electrolyte. This happens by chemical exchange between Zn and Al according to equation (2). The reaction is also known as "zincate activation process" of Al surfaces described for example by Jelinek [13].



This chemical deposition also is forming a similar morphology of the deposit with sponge and dendritic shape. The condition for this reaction to take place is the absence of any barriers such as pure Al₂O₃ or organic barriers like residuals of resins from lithography within the wafer manufacturing. Surface reactivity of different Al chip metallisations can be monitored with this test by analysing the obtained surface with FESEM and rating the observed morphology as it is described with the morphology catalogue from chapter 2.1.

Procedure:

In a 300ml flask 200ml of A2 electrolyte are stirred smoothly with a magnetic stirrer at room temperature (25°C). Then the sample chip or the Al specimen is dipped into the electrolyte with tweezers for 15 s. Thereafter, this sample is taken off, rinsed with water, dried in a drying locker (80-100°C) and then inspected by FESEM at 100k x magnification. Rating of the obtained pictures is done according to the morphology catalogue from chapter 2.1.

For a simple pre-sampling, the deposition reaction time can be extended to 60 s. A slight discolouration can be seen optically already as a dark grey discolouration of the Al surface, which can be interpreted as a positive deposition result. The 15 s sample is used for the final check of dendrites in the FESEM.

For the sample handling, Teflon tweezers are used since a metallic contact to the metallisation would strongly influence the electrochemistry and therefore would produce misleading results.

2.7 Auger electron spectroscopy (AES)

Auger spectroscopy is also one important method to investigate a surface regarding the chemical composition. Similar to EDX discussed in chapter 2.2 the principle of Auger spectroscopy relies on the material interaction with a primary electron beam. But different from EDX, where the electron beam is generating photons as X-rays, within Auger spectroscopy a primary electron beam generated by an electron gun is leading to secondary relaxation behaviour as shown in figure 20.

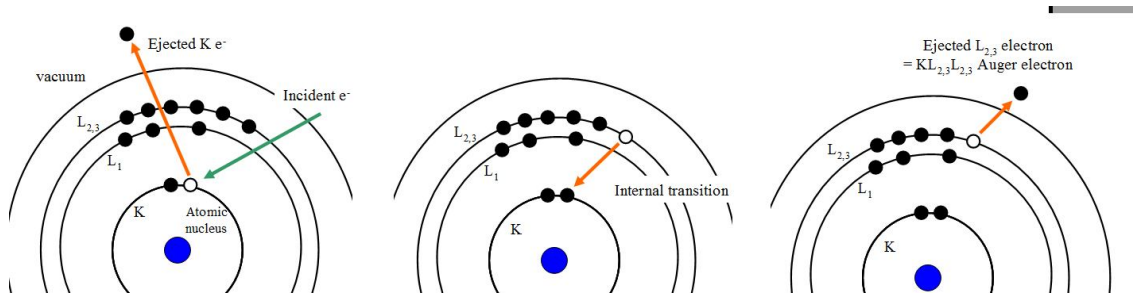


Figure 20: Auger electron generation via an interacting electron beam.

For example, the primary electron beam ejects an electron from the K level of an atom. The K shell vacancy formed is filled up with an electron from shells of a higher energy level such as the $L_{2,3}$ shell via an internal transition. To maintain the energy balance in the system the energy difference of this internal transition leads to the ejection of another electron from the atom, i.e. an electron from the $L_{2,3}$ shell. This electron is then called the $KL_{2,3}L_{2,3}$ Auger electron. The kinetic energy of this electron is characteristic for the atom and therefore for the material independent from the primary beam energy or type of beam, i.e. an electron beam. For XPS in this case an X-ray beam is applied, but that will be discussed in section 2.8.

Moving on with this example of a $KL_{2,3}L_{2,3}$ Auger electron the kinetic energy is approximately equal to the energy of the K shell minus the energy levels of the two $L_{2,3}$ electrons given in equation (3) given by Watts et al. [14]:

$$E_{KL_{2,3}L_{2,3}} \approx E_K - E_{L_{2,3}} - E_{L_{2,3}} \quad (3)$$

As a fine focussed electron beam is used as the primary source a high lateral resolution can be achieved in the range of 10 to 15 nm as described by Watts et al. [14]. Therefore, similar to EDX, surface mapping of the elements present is also possible. In addition the information depth of the measured Auger electrons is only a few nanometres as only a few layers of atoms is enough to filter out those electrons, hence Auger electrons are emitted only from the first few nanometres of the sample. This means that 65% of the signal of the Auger electrons will come from a depth of $<\lambda$ with λ being the attenuation length of the electrons [14]. For the presented work in table 7 the Auger energies for the analysed elements are summarized. For those elements besides the K, L and M lines also the character V is used representing the respective valence electrons within the

element. For example for Cr a L_3 electron is ejected first leading to the internal transition of an M_{23} electron to fill up this L_3 gap. The resulting energy of this internal transition leads to the ejection of a valence electron as a V Auger electron.

Element	Auger energy [eV]	Auger electron
Cr	527.20	$L_3M_{23}V$
Cr_2O_3	511.00	KVV
Zn	992.50	$L_3M_{45}M_{45}$
ZnO	988,90	$L_3M_{45}M_{45}$
$Zn(OH)_2$	986.50	$L_3M_{45}M_{45}$
Si	1616.20	$KL_{23}L_{23}$
SiO_2	1607.80	$KL_{23}L_{23}$

Table 7: Auger electron energies for selected species. Values are taken from National Institute of Standards and Technology (NIST) [171]

Auger spectra are mostly recorded in the differential mode as shown in a typical spectrum given in figure 21. The quantification of the specific elements out of the spectrum is done either by peak integration and the subtraction of the background signal or by a peak-to-peak measurement of the specific peak in the differentiated spectrum (figure 21 left). Sensitivity factors F for each individual element are used for the calculation of the concentration x of specific elements. Similar as for XPS data the concentration of an element A within an alloy is calculated via equation (5) as shown in chapter 2.8. I_A and I_i are the intensities measured for element A and for the elements i respectively.

All intensity data recorded with commercially available Auger equipment¹ are already corrected with sensitivity factors for the individual element based on a single element matrix and covering the equipment specific prerequisites, such as detector characteristic or electron beam. This sensitivity factors are sufficient for most analytical problems. For higher quantitative accuracy or complex chemical matrixes separate sensitivity factors have to be determined by recording sample standards with known concentrations.

¹ : For most of the results obtained in this work a Scanning-Auger-Multiprobe PHI600 from Perkin-Elmer with its internal sensitivity factors was used. Therefore all intensity values presented are corrected intensities including those sensitivity factors.

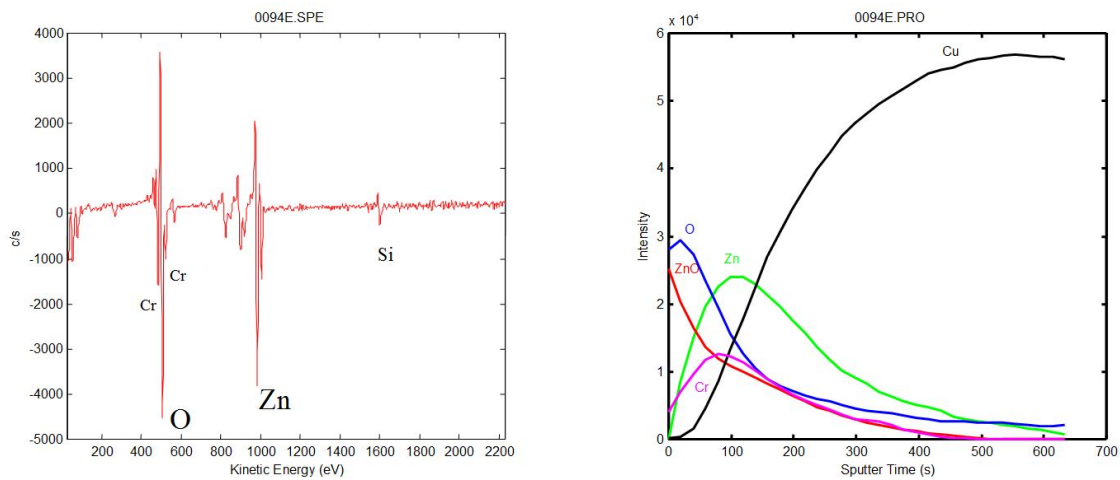


Figure 21: Typical example of an Auger analysis of a Zn/Cr A2 layer on a Cu substrate. On the left the differential spectrum is shown for the first surface spectrum and on the right the depth profile through the A2 layer is given (sample taken from experiment er82-5).

In addition to the surface sensitive analysis it is possible with most Auger spectrometers to perform a depth profile through several hundreds of micrometres; one example is given in figure 21 on the right side. This is achieved by a cyclic analysis consisting of the recording of a spectrum followed by a cycle of sputtering the surface with various elements such as noble gases (Ar, He) or Ga. Especially with the latter one very small beam sizes can be achieved below $<50\text{nm}$ and therefore very small sample areas can be sputtered with high sputter rates. After each sputter cycle a spectrum is recorded, and then another sputter cycle follows. This cycling is done until the required depth of the sample is reached. Specific signals of the spectra are combined to a depth profile which shows the relative distribution of the specific elements in dependence of the sputtered depth. Typically, plots are given with intensity over the sputter time. For obtaining real depth values rather than relative values a calibration of the sputter time versus thickness can be done with known standards, but the standard has to consist of the identical matrix similar to the sample to allow a comparison of the sputter rates on the sample and on the standard. Further information can be obtained from Watts et al. [14], Bard and Faulkner [105] or Martin [15].

2.8 X-ray photoelectron spectroscopy (XPS)

In several experiments XPS was used as a method to analyze the surface chemistry of specific samples. This method was used in addition to Auger electron spectroscopy (AES) described above mainly for the reason of equipment availability, but for some cases also due to advantages not available by AES. Because the signal of both the XPS and the AES is very similar in terms of the chemical shifts the description of XPS here is started with a short comparison. XPS and AES basically can be made on the same equipment. Whereas for AES the excitation of the material is done with a focused electron beam, in XPS excitation is done via X-ray exposure of the sample. X-ray anodes range from energies of $E=132.3\text{eV}$ (Y M-line) over $E=1486.6\text{ eV}$ (Al K_{α}) to $E=5417.0\text{ EV}$ (Cr K_{α}). In figure 22 the basic principle of a XPS experiment is shown.

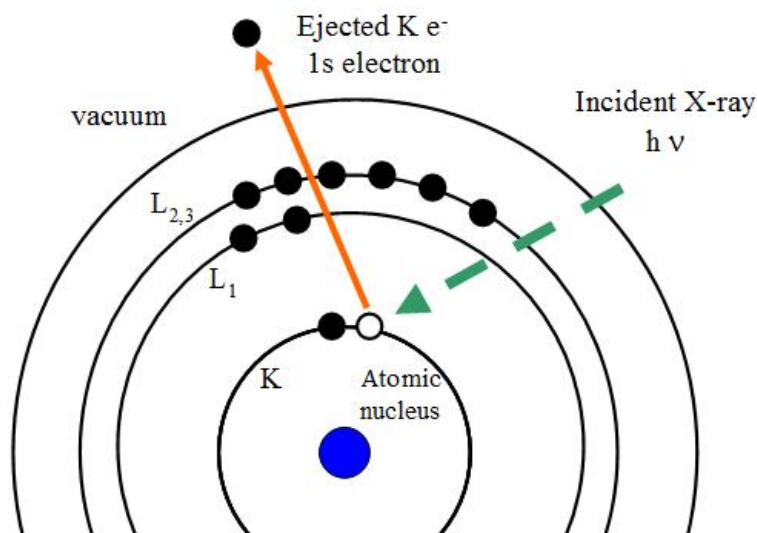


Figure 22: Schematic drawing of the XPS photo ionization.

The detection of the respective signal electrons is done similarly with electron multipliers. In contrast the interpretation of the lines in terms of the electron energies and the quantum numbers is done differently: In XPS notation the electron quantum numbers such as $1s_{1/2}$ or $2s_{1/2}$ are used while in Auger spectroscopy the X-ray notation such as K, L_1 or M_1 is used.

XPS is very specific regarding the chemical environment of an element. For example the chemical shift of the C1s signal is increasing with number and electronegativity of

substitutes of H in CH₃. For CH₂F the shift is 2.9eV, with CHF₂ and CF₃ a shift of 5.9eV and 7.7eV is observed, respectively. This strong differentiation in chemical environment and the fact, that also Auger electrons can be recorded with XPS is one advantage which has to be bought by a larger analysis area. Small area XPS equipment have a vertical resolution of about 10μm as compared to AES equipments that reaches a lateral resolution of about 10nm. This is one of the reasons why AES is mainly applied for very small structures specifically in semiconductor industry and XPS is very often seen in industries relying on more detailed chemical information of the surface, such as catalyst development.

Recording of an XPS spectrum is done in a similar way as with an Auger spectrum, the intensity is shown over the binding energy of the photoelectrons typically given from 0 to 1100eV, one example given in figure 23.

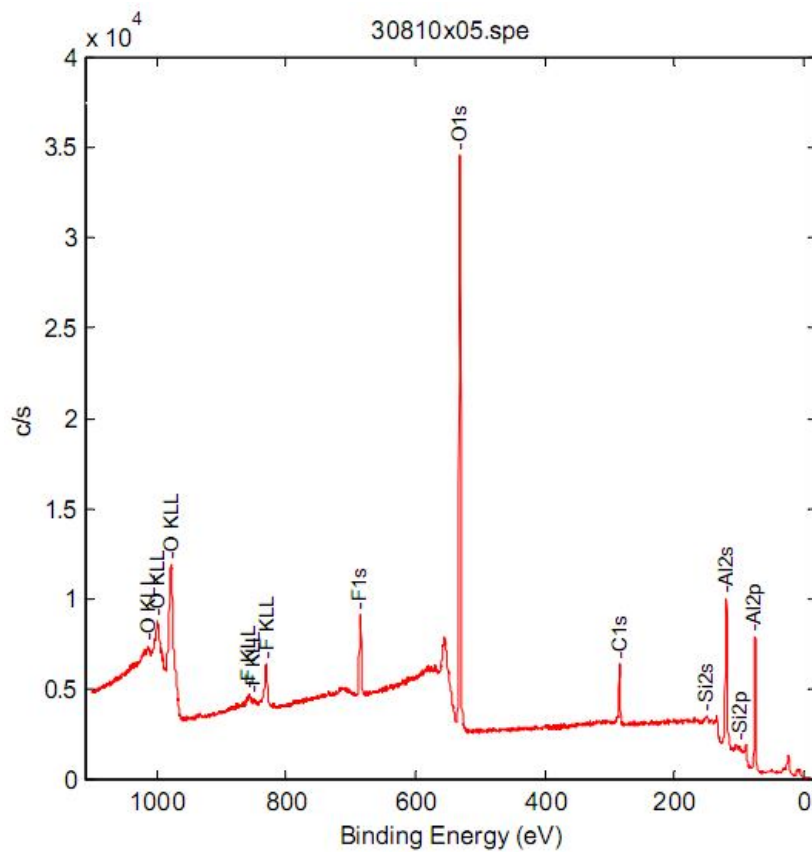


Figure 23: Example of an XPS spectrum of a fluorinated aluminium surface (sample taken out from experiment er265-r-ref).

The kinetic energy of the ejected electron, such as the 1s electron shown in figure 22, is the experimental quantity obtained by the spectrometer. But this kinetic energy is not independent on the energy of the incident x-ray. To get the final binding energy of a specific ejected electron at least three factors have to be considered including the X-ray energy, the kinetic energy as measured and the spectrometer specific work function [14]. The binding energy can be calculated with equation (4) with E_B being the binding energy of the ejected electron, $h \cdot \nu$ being the X-ray energy, E_K the kinetic energy of the ejected electron that is measured and W being the spectrometer work function. The work function is characteristic to the electron source used in the specific equipment such as a thermionic emitter ($W = 4.5$ eV), a LaB_6 emitter ($W = 2.7$ eV) or a cold field emitter ($W = 4.5$ eV) as presented by Watts and Wolmstenholm [14]. The work function is defined as the minimum energy required to remove an electron from the emitter device, such as a tungsten needle for the case of a thermionic emitter, into the vacuum and therefore release it from the needle surface. For this example the required energy is gained from the heating of the tungsten needle. Further details on emitter technologies are published from Watts and Wolmstenholm [14] and will not be discussed further here.

$$E_B = h \cdot \nu - E_K - W \quad (4)$$

All electrons within the measured sample surface with an energy below the X-ray energy will be excited which gives the background noise of the spectrum seen in figure 23. Only those electrons from the first few atom layers are able to escape without energy loss and form the characteristic peaks in the spectrum, i.e. the C1s peak in figure 23. Electrons from deeper layers suffer inelastic scattering and loose energy forming the background of the spectrum. Similar to AES the information depth of XPS is only a couple of nanometers depending on the analyzed material and the attenuation length of the electrons in this material. As the atoms have a shell vacancy due to the ejection of the electron also secondary relaxation takes place such as the formation of an Auger electron explained in section 2.7 or the emission of an X-ray quantum. The former mechanism is called XAES (X-ray induced Auger spectroscopy) and the latter one is called X-ray fluorescence, both methods are not further discussed here.

The quantification of the specific elements out of the spectrum is done by peak integration and the subtraction of the background signal. For refinement sensitivity factors are sometimes measured to get spectrometer specific refinement of the individual intensities according to equation (5), where x_A is the concentration of the specific element A, I_A and I_i are the intensities measured for element A and for the elements i respectively. F_A and F_i are the sensitivity factors of the element A and the elements i.

$$x_A[\text{atomic}\%] = \frac{\frac{I_A}{F_A}}{\sum_i \frac{I_i}{F_i}} \cdot 100\% \quad (5)$$

To obtain information on layer compositions by XPS also the mode of destructive sputtering can be applied to obtain depth profiles down to a depth of 1000 nm, the principle is basically the same as discussed for AES in section 2.7. It has to be mentioned here that there is also the possibility of a non-destructive method of getting depth profiles down to a depth of 10 nm via angle resolved electron spectrometry. This method was not applied in this work and is not further discussed here; the interested reader may for example refer to Watts et al. [14] who give a brief overview on theory and equipment of electron spectroscopy in general.

2.9 Time of flight secondary ion mass spectroscopy (TOF-SIMS)

Unlike the electron spectroscopy methods discussed above TOF-SIMS is a relatively new method being established in the 1970s [16]. Today it is a very sensitive method for detecting all elements and isotopes in traces down to ppm level with a lateral resolution of about 60nm and a information depth of one monolayer (<1nm), in contrast to XPS and Auger which integrate several monolayers [17].

The treatment of the sample to analyze the surface in TOF-SIMS is done by destructive sputtering of the surface with a primary beam of ions such as O_2^+ , Cs^+ , Ga^+ or Ar^+ . During short pulses of for example 10 ns with some keV of energy, for example 15 to 25keV for Ga^+ ions an evaporation of secondary ions into the vacuum chamber of the

TOF-SIMS equipment happens. Newest TOF-SIMS equipments like that specified by IONTOF company reach pulse length down to 1 ns [17]. Besides ions from elements also charged clusters are generated carrying some additional chemical information of the surface elements such as ligands or fractals of organic molecules from contaminants. The generation of secondary ions happens at the first monolayer of the sample material corresponding to an ion dosis of 10^{13} ions/cm² of the primary ion beam as reported by Grams [16].

The detection of those secondary ions is done via a very fast time resolved detector. In a conventional mass spectrometer the charged ions are accelerated in an electric field first and then separated according to their mass charge ratio m/z by a magnetic field. The ions are guided to the detector by sweeping the magnetic field over the m/z range which takes a long time to obtain a complete mass spectrum.

In a TOF-SIMS detector the determination of m/z is done via measurement of the flight time of the secondary ions. The ions are also accelerated in an electric field where they gain a kinetic energy specific to their charge $z \cdot e_0$ and the voltage of the electric field U where e_0 is the elementary electric charge ($e_0 = 1.602 \cdot 10^{-19}$ A·s). There they gain a velocity v specific to their mass m as figured out in equations (6) and (7).

$$E_{kin} = z e_0 \cdot U \quad (6)$$

$$E_{kin} = \frac{1}{2} m \cdot v^2 \quad (7)$$

With $v = \frac{s}{t}$ and combination of (6) and (7) equation (8) is obtained showing that m/z is proportional to the square of the flight time t .

$$t^2 = \left(\frac{s}{2U} \right)^2 \cdot \frac{m}{z} \quad (8)$$

The accelerated ions are guided through a drift zone where they get their specific distances due to the different velocities and are finally guided to a fast detector. The sampling frequency at the detector is in the range of 10^4 mass spectra per second and is

limited by the highest mass to be detected which means by the highest flight time. In figure 24 the main features of a TOF-SIMS analysis is shown.

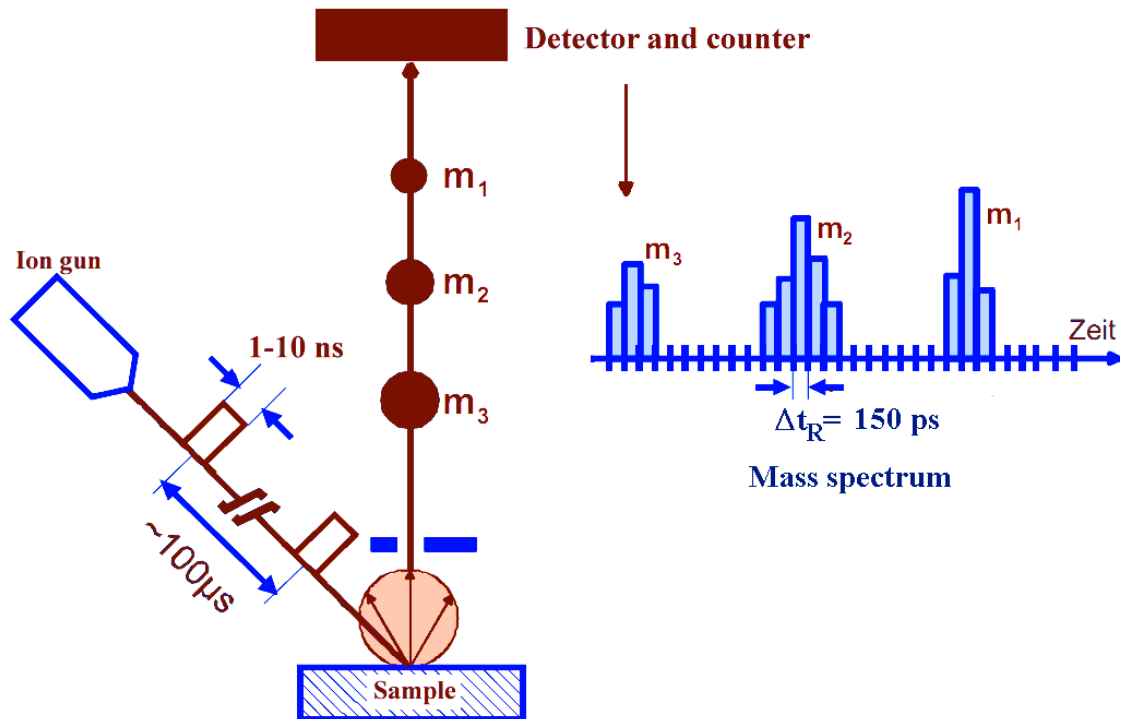


Figure 24: Principal of TOFSIMS

Between two measurement pulses with high energy ions for surface analysis a sputter cycle of low energy ions and higher current can be applied leading to an abrasion of the surface. This mode, known as sputter mode, offers the measurement of a depth profile similar to that obtained by AES and XPS. A typical sample area is about $200 \times 200\text{ }\mu\text{m}^2$ for the measurement cycle and about $400 \times 400\text{ }\mu\text{m}^2$ for the depth profiling. Through the specific selection of various species of the mass spectrum depth profiles of cluster and fractals can be analyzed regarding their distribution within the top layers.

A recent brief overview on TOFSIMS and its trends was published by Grams [16] or by Vickerman and Briggs [18].

2.10 Scanning acoustic microscopy

The reliability of the multiple interfaces and bulk materials in complex material combinations such as semiconductor devices is often characterized using scanning acoustic microscopy (SAM). SAM is an important non-destructive method to analyse fatigue mechanisms at interfaces of bulk materials such as delamination, cracks or voids.

Sonic waves have the property of continuous distribution within one homogenous medium. In the SAM method ultrasonic waves in the frequency range from 10 to 500 MHz are used. They are focused by acoustical lenses. The waves interact with inhomogeneities in the sample such as interfaces, cracks or voids depending on the properties of the involved materials, e.g. the density. A part of the waves is reflected back to the ultrasonic source and a part is transmitting through this inhomogeneity. Therefore, SAM can be operated in reflective and in transmission mode with two different detector systems.

For the acoustic characterisation of materials in a simplified model the acoustic impedance Z_x is used as a characteristic parameter that is defined by $Z_x = \rho_x \cdot v_x$ with ρ_x being the density of the material x and v_x being the sonic speed within this material. If sonic waves step from one material with Z_1 into another material with Z_2 then the reflexion R and the transmission T can be calculated by equation (9) and (10), respectively.

$$R = \frac{Z_2 - Z_1}{Z_2 + Z_1} \quad (9)$$

$$T = \frac{2 \cdot Z_2}{Z_2 + Z_1} \quad (10)$$

From this equation it can be derived that a reflection is larger the higher the difference of the acoustic impedance of the two materials is. For example if the waves pass from a gas (e.g. air with $Z_1 \approx 0 \text{ kg}/(\text{m}^2\text{s})$) into a solid material (e.g. silicon: $Z_2=20 \cdot 10^6 \text{ kg}/(\text{m}^2\text{s})$) then the reflexion $R \approx 1$ which means a total reflexion of the sonic waves occurs. The transmission in this case is $T \approx 0$, so no waves transmit the interface. In case

the difference of Z_1 and Z_2 is inverse meaning the sonic waves are passing from air to silicon referring to the above example, then also total reflection occurs, but in this case the reflectivity parameter is negative, $R \approx -1$. The detected signal polarity is inverse. The gas in this example can be a void or a delamination (= air gap) between two materials.

The signals collected during SAM are basically the amplitude and the time-of-flight for a signal. These signals are provided in different modes.

The A-mode shows only the signal amplitude as a function of time at one spot, the source and detector stay at a given spot.

The B-mode shows a vertical depth profile of the sample, source and detector are moved along one line over the sample.

Common within SAM results from electronic devices is the C-mode that shows the horizontal distribution of the signals over the x/y plane. In this mode a time-gate is defined by the operator related the area of interest and hence to the interface that needs to be investigated. Then the complete x/y plane is scanned and the signal amplitude and polarity at the various positions is linked to an individual colour and contrast. This procedure generates a colour map of the device in which interfaces with delamination are highlighted. In the given example in figure 25 delaminated areas are coloured yellow and red.

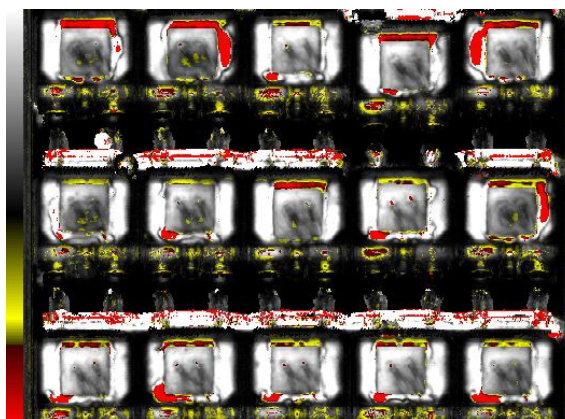


Figure 25: Example picture of a C-scan of a scanning acoustic microscopy analysis of 15 devices (TO263-3) showing the colour map of the received signals. In red and yellow strongly delaminated areas are visualized with an air gap between two materials. The grey contrasts show interfaces between two materials which are still intact.

Fourthly, also T-mode SAM is used reflecting picture of signals transmitting the sample. In this case the source and the detector of the sonic waves are opposite from the sample.

SAM is operated mostly by placing the sample in a water basin; the measurement head is also dipped into the water as the sonic waves travel through water without being reflected. For further information see Briggs and Kolosov [19] who give a deep insight in SAM methods.

2.11 Solder wetting balance for measuring wetting force-time-graphs

Solder wetting balance is a measurement method to obtain kinetic data of solder wetting processes to characterize either a solder alloy or a substrate material that is used for soldering. Usual test samples are terminals from semiconductor devices or wires. The test sample is attached to a holder in the equipment and is then at the start of the measurement automatically dipped 2,5 mm into a solder bath (e.g. 245°C; SnAgCu solder with colophonium flux in isopropanole) for a period of 20 seconds. During this period the force at the dipped sample is collected. Force-time graphs are obtained (see figure 26) that allow determination of several parameters:

F_L: Lifting force due to de-wetting of the solder in the first phase of the reaction time.

t_{WS}: Time of wetting start

t_{0x}: Time of crossing the zero-force-line

F_{max}: Maximum force

One major parameter for the velocity of wetting is t_{0x} that is the time the solder requires to start the reaction with the substrate material leading to a switch from the initial de-wetting (decrease of the force) to a wetting (increase of the force) reaching the initial force value at the start of the experiment again. This parameter often is used to characterize the wetting velocity of a solder on a specific substrate.

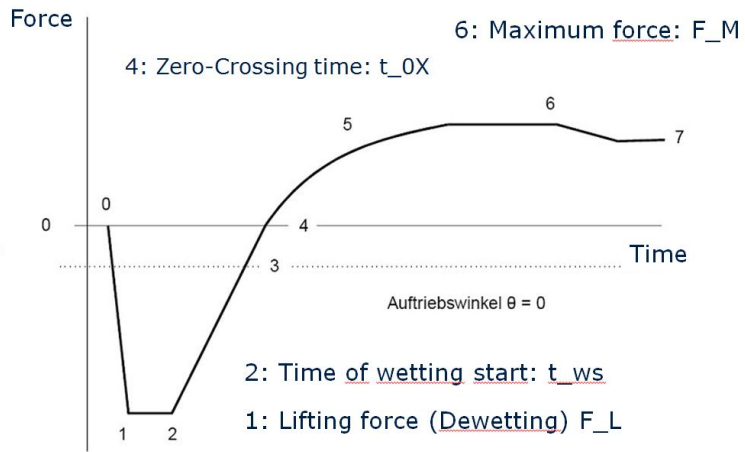


Figure 26: Example of a force-time graph obtained during wetting force balance measurement.

3 Adhesion promoter: Identification of A2 process as the target technology for adhesion in a MOSFET package.

During the last 20 years there were many investigations performed by various research groups mainly affiliated to semiconductor industry regarding adhesion of resins on copper since this metal is broadly used. Adhesion to Cu in particular means in reality adhesion to any of the two known oxides, Cu₂O and CuO. Influence of Cu oxidation on adhesion strength was investigated, for example, Cho [20] found an optimum oxide thickness of 20-30nm for highest adhesion and reported the crack path to be at the CuO/Cu₂O interface. Chung [21] claimed an optimum thickness of the overall Cu oxide of 30-40nm.

Macroscopic modification of the surfaces with for example dimples and holes can initially increase adhesion but may also lead to cracking of the molding compound due to stress peaks; furthermore, macroscopic modification is not preventing further oxidation of Cu [22]. Various specific treatments were tested from Fauty et al. to limit oxidation by choosing a particular Cu alloy, controlling oxidation within the manufacturing processes or using laser texturing [23] with some improvements on adhesion of resin to the specific Cu surface.

Various Cu coating and Cu etching processes are reported to improve the adhesion of resin to Cu. Black oxide coating increases adhesion through micro roughness and a stable Cu₂O /CuO layer deposited from an alkaline solution onto the Cu substrate [24]. Bondfilm^R from Atotech acts in a similar way, it is an anisotropic acid Cu etching process which is also improving adhesion through a porous etched Cu. In addition the bath prevents further oxidation of the Cu beyond a certain limit via Cu passivation coating with benzotriazole and imidazole derivatives [25], [26], [27]. A similar adhesion promoter for Cu was developed by the manufacturer Macdermit, USA, named Multibond^R [28], [29]. Benzotriazole and derivatives were also used as stand-alone adhesion promoters for Cu and also for Al [30]. Lee and Park [31] used black and brown CuO coating and observed different failure paths by cracking of the CuO/ Cu₂O layer depending on oxidation time.

In all those work the stack of Cu_2O / CuO on the Cu substrate was reported to be the weak link, the thickness of both Cu oxides is growing continuously and at a critical thickness the stack cracks. Therefore in parallel a different approach in electronic industry was checked to prevent the oxidation of Cu during the manufacturing processes, especially during the hot encapsulation process, which is usually done at a temperature of 180-200°C in the atmosphere. Besides the fact that a complete prevention of oxidation of copper can not be achieved in manufacturing due to lack of inert atmosphere the degradation of this interface during device lifetime was of great importance. The risk of further oxidation of the Cu during the lifetime of the device and delamination later in the application is present for all those Cu surface modifications which do not significantly act as a barrier against oxygen or water diffusion and therefore do not prevent Cu oxidation.

As the resins of molding compounds have significant water and oxygen permeability [7] further oxidation of the copper finally leads to the critical thicknesses and to the fatigue of the Cu / Cu_2O / CuO stack.

To overcome this latent weakness of Cu / resin interfaces the next step was to cover copper with various kind of organic substances and inorganic coatings like metals and alloys including nickel/phosphorus alloy, silver or nickel-palladium-gold metallisations [32]. These layers are able to act as a barrier for O_2 and H_2O .

In 1991, a US company named Olin, disclosed a patent that was the next step of advancement in this field. The authors claimed that a galvanically deposited Zn/Cr - alloy prevents Cu from oxidation [33], [34], [35]. The chemistry for this Zn/Cr coating was called “A2” by Olin. Looking at the materials used for a power-semiconductor-device, copper is mainly used as the leadframe material, hence industry was striving to use this Zn/Cr coating within the leadframe manufacturing process flow first instead of its application on a semiconductor.

In 1999 also Siemens Semiconductors, later known as Infineon, decided to purchase a license for the A2 chemistry and to further develop this method in addition to a couple of other adhesion promoter technologies mentioned above. Unfortunately there was a major drawback for the A2 chemistry at this point, it was only developed and used for

covering copper. For the approach to cover all device surfaces with an adhesion promoter the following criteria first have to be fulfilled:

Criterion a: Adhesion of the layer to every device material is required

The new material has to be electrochemically compatible with all the device surfaces including aluminium, copper, silver, nickel-phosphorus alloy, Pb-Sn-Ag solder, and polyimide. Strong adhesion to the metallic device surfaces can be achieved for example by a crystalline interface. This requires a metallurgical combination between adhesion promoter and device which either forms stable and reliable intermetallic compounds or which at least has a significant solubility of both partners to form a mixed crystalline system. It will be shown later that the Zn/Cr layer electrochemically deposited out of the A2 electrolyte shows a high adhesion to all used metals including Cu, NiP, Ag, Al, and Pb-Sn-Ag solders.

But the topology and chemical composition of the adhesion promoter layer has also to fit to the chemical composition of the molding compound. To fit to most resin systems in industry a standardization of the adhesion promoter function is favoured. The resin systems in industry vary strongly in their formulation acting on a molecular base regarding coupling to respective metals or metal oxides with bi-functional adhesion promoting molecules. As for some metals different adhesion promoter molecules are required, a standardization based on a molecular adhesion within the resin of the molding compound is very complex in formulation of the molding compound.

Mechanical interlocking does not require any dedicated adhesion promoter molecules at all and offers a standardized surface which works also with molding compounds without any addition of adhesion promoter. Humidity which is present within a molding compound is not able to weaken those interfaces as the water molecules are mainly interacting with the molecular bonds at the interface [36] rather than with the mechanical interlocks.

Mechanical interlocking through microscopic roughness and porosity is reported by many developers. For example Lebbai et al. [37] found mechanical interlocking as the major adhesion mechanism of black copper treatment to form a Cu₂O layer on Cu substrates in order to increase adhesion to molding compounds. Looking through the

work done on black CuO also Lee and Park found the adhesion of an epoxy resin on acicular CuO was good and the primary adhesion improving factor for black oxide coated leadframes is the mechanical interlocking [31]. The mechanical strength of the porous CuO layer was the limitation in this work. Furthermore the anisotropic Cu etching technologies named Bondfilm [25], [26], [27] or Multibond [28], [29]. are reported to mainly act over the mechanical interlocking between Cu and polymer .

A limitation of mechanical interlocking is related to the molding compound properties. Looking into the manufacturing processes of molding compounds the resins used are already prepolymerized, so oligomeric structures with up to 12 single units are present already. This makes the control of viscosity even more difficult during molding process. Figure 27 shows the size of two nanoporous adhesion promoters with their typical pore size of 30-50nm and a comparison to the linear size of oligomeric orthocresolnovolac (OCN) resin. Further increase of the OCN molecular weight during molding injection can get a limitation for penetration of the existing pore size. Therefore the control of the pore size of the nanostructured layer is an important process factor.

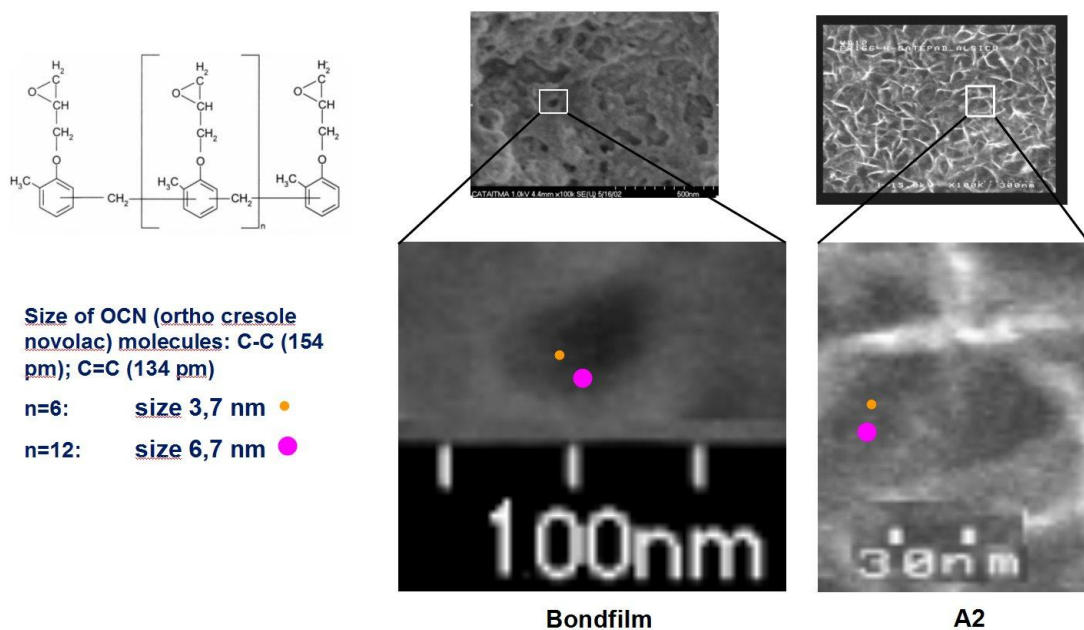


Figure 27: Example of an oligomer of OCN resin in standard molding compounds and the size of a linear oligomer compared to the pore size of A2 coating and of Bondfilm.

The mentioned A2 chemistry for deposition of a Zn/Cr alloy was chosen for further development to get a nanostructured surface as a standardized surface on all metallic device materials towards the molding compound as it was found that it can be deposited

in a nanoporous structure. In addition to this the layer is acting as a barrier for O₂ and H₂O in the device preventing further oxidation of the specific substrate metal. Controlling pore size during deposition means the molding compound has only to interact with one material and with one surface.

Polyimide coated chip surfaces are excluded here as the polyimide is activated with a specific plasma etching process on wafer level in order to improve adhesion to the molding compound.

Criterion b: Process of deposition for every device material has to be available

At the beginning of deposition of adhesion promoters, i.e. Zn/Cr alloy, the Cu of the leadframe was coated completely. But this procedure interferes with various manufacturing processes of the semiconductor device which are only possible on Cu, Ag or Ni. For example wirebonding with Al, Au or Cu is not possible on a Zn/Cr coating; chip soldering is not possible either as the formed Zn / Cr oxide is very resistive to the solder. Therefore, it is unavoidable to either leave these areas open on the leadframe by e.g. a selective plating process or to open these areas again after having plated the full surface of the leadframe. For both approaches there are complex industrial processes available from leadframe suppliers (e.g. Jade, Singapore; Possehl, Malacca). Unfortunately, the so called selective plating has a major drawback: Leaving out the adhesion promoter around the tiny wires, around the chip and on the sensitive chip surface may lead to delamination of the resin at those sensitive positions.

If the deposition of the adhesion promoter layer has to be performed onto all device surfaces it is unavoidable to execute the deposition directly before molding as only at this point all device surfaces are completely processed. Only then, complete adhesion in the device can be realized. The challenge is to have a deposition process available that is suitable for leadframe surfaces, the solder alloy, the wires and the chip in a contamination free cleanroom environment. For example, figure 28 shows how many different surfaces are plated with A2 in a TO263 package with a MOSFET chip.

Within the development work several adhesion promoters have been investigated regarding those criteria mentioned. Anisotropic Cu etching process Bondfilm from Atotech, Berlin, was investigated as mentioned above. Since this technology is only

possible on copper surfaces due to the Cu etching chemistry there is no adaptation possible to other metals. Therefore, this option was stopped early.

Another option was the burning of a gaseous mixture of butane and tetraethylsilane over a surface for vapor phase deposition of SiO₂ resulting in a nanoporous SiO₂ layer. The gas mixture was supplied by SurA Chemicals company, Bucha/Jena [38]. This technology was named "Nanoflame". In experiments this technology was investigated and it was found that the adhesion was suitable to meet the criteria given above. However, since at that time there was no manufacturing equipment available this option was not prioritized.

In a couple of experiments also on device level A2 showed up as one of the candidates with the best adhesion and the highest reproducibility. Towards the molding compound the A2 layer consists of a nanoporous spongy structure forming a mixture of polymer and strong inorganic fibres. The key issue is to get a deposition process that is able to produce similar structures on various metal surfaces which finally have contact to the molding compound. In figure 28 FESEM pictures show the morphology of galvanic deposited A2 layers on two different aluminium metallisations (Al-1Si and Al-1Si-0,5Cu), on two different aluminium wire alloys (Al-1Si-0,07Ni and Al-0,07Ni) and finally on Pb-2Sn-2.5 solder and on Cu.

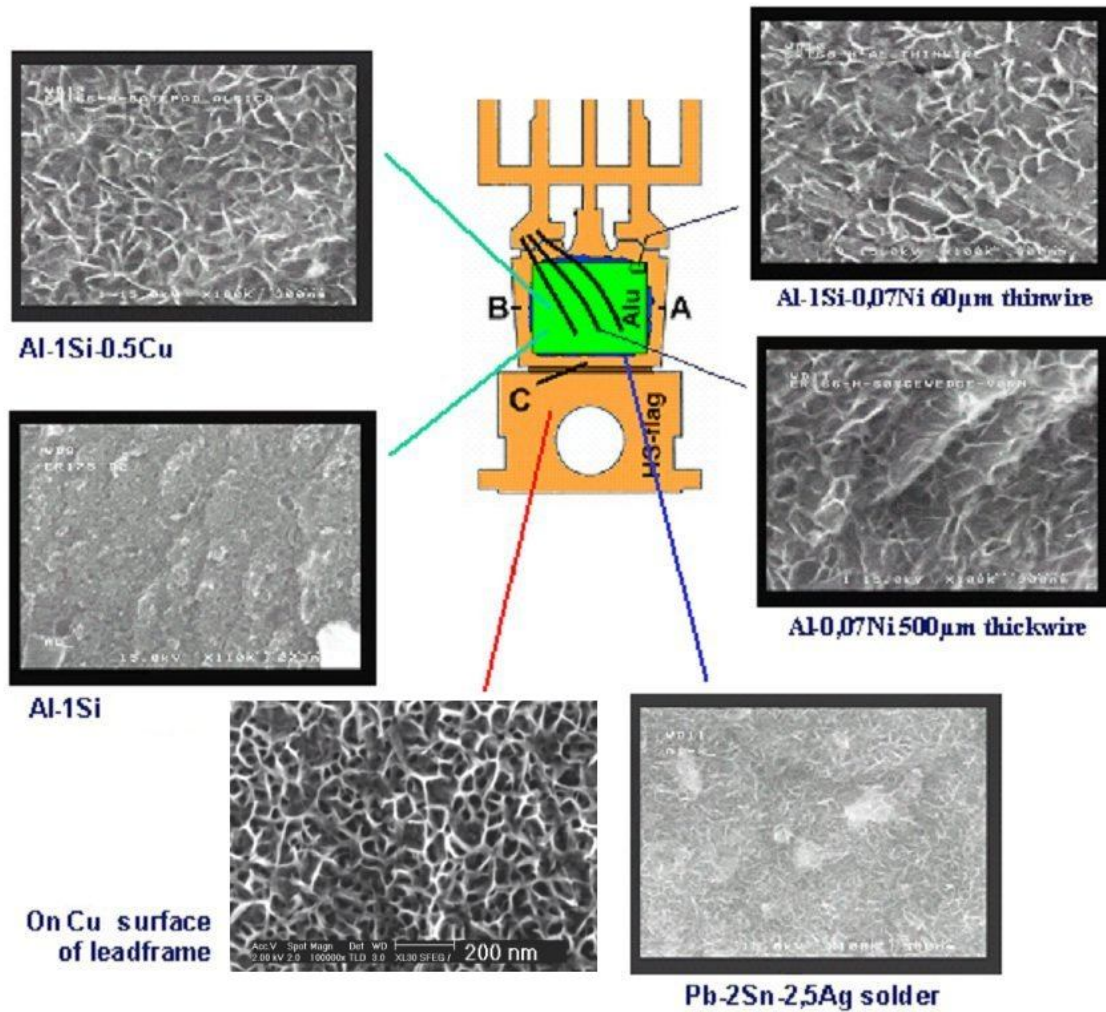


Figure 28: FESEM pictures for overview on electrochemically deposited nanoporous A2 structures on different substrate. Each substrate shows slightly different appearance A2-growth.

Using a process technology for deposition of nanoporous layer has the additional benefit of an easy monitoring of the process result as the morphology can be traced with microscope or FESEM. In figure 29 the basic process steps for A2 plating are described. Main process steps are the activation of the surface where metal surfaces are prepared over a variety of base metals (Al, Pb, Sn, Ni) and precious metals (Cu, Ag) and the growing of the A2-layer in a electrochemical reactor. The fundamental new approach is to do a nanoporous deposition of an adhesion promoter over all device surfaces in order to get adhesion at each position within the device through mechanical interlocking as a standardized adhesion mechanism. A detailed description of the various process steps within A2 process will be done in the next two sections.

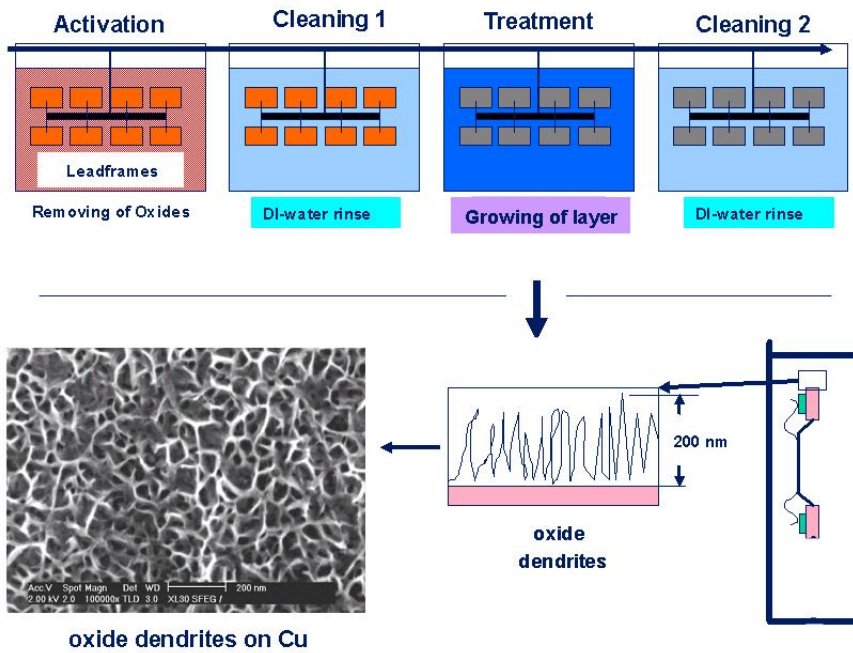


Figure 29: A2 process principal of nanoporous deposition of Zn/Cr alloy.

4 Theoretical background and models for the understanding of dendritic depositions

4.1 Activation of metal surfaces

4.1.1 Properties and states of the different surfaces prior to activation

Regarding the final deposition of A2 we have first to address the question how to prepare the individual surfaces. Furthermore, it is important to know in what condition the individual surfaces enter the activation section at the A2 plating process. Since the A2 plating process is embedded in the assembly process block at the very end of the manufacturing chain an analysis of the complete chain is necessary to describe those processes with the biggest influence to the surfaces which enter the A2 process and to define them properly.

The manufacturing flow consists of three main process blocks:

First there is the leadframe manufacturing process flow for the leadframe surfaces that are Cu and Ni/NiP. For some other devices this can also be Ag and NiPdAu derivatives depending on the specific manufacturing technology. In this work only Cu and Ni/NiP surfaces are considered. Secondly there is the wafer process flow preparing the semiconductor chip including the Al chip frontside metallisation and the chip backside metallisation. Thirdly both the leadframe and the chip are combined in the assembly process block at the chipsoldering process. In table 8 the complete process flow of leadframe, chip and package is shown to describe the different influences to the chip soldering and finally to the A2 process. Within the leadframe plating process block for example the plating of the nickel-phosphorus (NiP) layer is defining the chemical properties of the NiP for the leadframe. In the wafer process block the plasma etching of the AlSiCu wafer metallisation is generating the final aluminium surface of the chip frontside. Both surfaces are processed together in the chip soldering process in the assembly process block at high temperature which modifies them and in addition brings in the solder surface into the device.

Process block leadframe for TO263-3	Process block wafer for MOSFET
Manufacturing of Cu strips at Cu smeltery	Manufacturing of semiconductor active structures
	Sputtering metal Al-1Si-0.5Cu
	Lithography metal structure (photo resist coating, exposure, development)
	Wet chemical etching of Al-1Si-0.5Cu; CHF ₃ plasma silicon grain removal.
	Photo resist mask removal wet chemical and O ₂ -plasma
	Wet chemical cleaning.
	Tempering in forming gas N ₂ /H ₂ 10%, Θ=420°C, t=15min
Electrolytic cleaning of copper surface	Chemical vapor deposition (CVD) silicon nitride 40nm
Acid dip to remove copper oxides	Polyimide coating, exposure and development
Deionized water (DI) rinse	Plasma etching O ₂ -Flash to remove polyimide residuals
Nickel plating from Nickelsulfamate bath	Plasma etching silicon nitride with CHF ₃
DI rinse	Polyimide cyclization, N ₂ , Θ=380°C, t=60m
Nickel-phosphorus plating from NiSO ₄ and Boric acid bath	Plasma etching frontside AlSiCu pad activation: Option A: Ar/CF ₄ Option B: Ar/O ₂
Stamping of leadframe structure	Backside grinding and damage etching with HF
Degreasing with organic solvent	Backside implantation
Anti-tarnish organic acid	Sputtering of backside metallisation stack: Al (200nm) / Ti (200nm) / NiV (500nm) / Ag (200nm)
Rinsing with ultraclean DI water	Parameter measurement and inking of rejects
Drying	Sawing
Assembly process block	
Chip soldering in forming gas (N ₂ , 5%H ₂ , Θ=400°C, t≤5m)	
Al wirebonding	
A2 process	
Molding	
Lead forming and final plating	

Table 8: Overview on the process flow for leadframe, wafer and package.

The surfaces that finally enter the activation section of the A2 process therefore are depending on various factors which are discussed in the individual section for activating the various metal surfaces for A2 plating. Table 9 gives an overview on the surfaces and their condition after individual process steps within the assembly of a SFET2 MOSFET device in a TO263-3 package.

Assembly process steps	Process condition	Cu	Ni (1,3 μ m) NiP (120nm)	Pb-2Sn-2.5Ag	Al-1Si-0,5Cu	SiN 40nm + polyimide 5 μ m
Chip soldering	$\Theta=400^{\circ}\text{C}$; $t_{\text{max}} = 5\text{min}$; forming gas atmosphere with 5vol% H ₂ in N ₂ and traces of O ₂ (<100ppm).	Reduction of copper oxides results in a metallic surface and finally in a native thin Cu ₂ O/CuO. Benzotriazole coating of copper is desorbed [247]	Stable condition up to 5 minutes (WFH002). Recrystallisation of NiP.	No significant reduction of any PbO or SnO ₂ . Furthermore accumulation of SnO ₂ on the solder surface.	Option Ar/CF ₄ : No change of surface up to 5 minutes (WFH002). Option Ar/O ₂ : No change of surface	Stable condition, no change of surface up to 5 minutes
Al wirebonding	Room temperature	Stable condition, no change of surface	Stable condition, no change of surface	Stable condition, no change of surface	Stable condition, no change of surface	Stable condition
A2 plating	$\Theta=50-60^{\circ}\text{C}$; $t<60\text{s}$; electrochemical deposition of a zinc-chromium alloy.	Deposition of dendritic A2 layer	Deposition of dendritic A2 layer	Deposition of dendritic A2 layer	Deposition of dendritic A2 layer	No A2 deposition possible, influence of sodium and zinc on polyimide surface.
Molding	$\Theta=180-200^{\circ}\text{C}$ for a time of $t=180\text{s}$ under ambient atmosphere.	Common A2 surface for the molding compound				Polyimide surface towards molding compound
Trim and Form	Bending and cutting the device terminals	No influence to surfaces within the device anymore				
Deflashing	Removing molding compound residuals					
Final tin plating	Metallisation with tin for a solderable device					

Table 9 : Overview on assembly process steps for a SFET2 MOSFET device in a TO263-3 package. For each process step the influence to the specific device surface is described.

The major thermal budget for all device surfaces is applied during chipsoldering. For devices with an Al wirebonding technology this is also the last heat treatment and therefore this process will be described here in more detail as it is relevant for all device surfaces.

Figure 30 shows the process steps and conditions of chipsoldering. Chips are soldered onto a leadframe heatsink at $\Theta=400^{\circ}\text{C}$. This is done with a Pb-2Sn-2.5Ag solder wire in chip bonding equipment automatically. The leadframe is transported through a forming gas tunnel consisting of 5vol% H₂ in N₂ and traces of O₂ (< 50ppm) where it is heated up. Solder is dispensed onto the heat sink. Finally the chip is placed onto the molten solder through a bond window in the forming gas tunnel and the finished devices are transported further into the cooling zone to cool down to about 50-80 $^{\circ}\text{C}$ leaving the forming gas zone. The process usually takes only a couple of seconds depending on

specific process parameters and depending on the chipsize. The worst case however is a stop time of up to 5 minutes for cases of wafer change or solder wire change or other operator actions. All devices which exceed this limit are scrapped, therefore only this worst case needs to be considered for the specific surfaces.

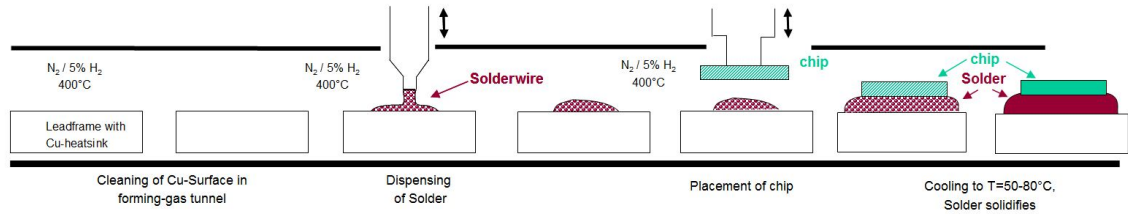
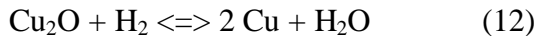
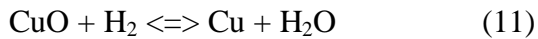
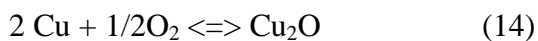


Figure 30: Process steps within chip soldering process where chips are soldered onto a leadframe heatsink.

At a temperature of 400°C under forming gas the reduction of metal oxides takes place, example given for CuO and Cu₂O according to equilibria (11) and (12).



However, concurring oxidation reactions (13) and (14) with the O₂ traces in the process chamber entail finally an equilibrium oxide thickness.



In addition, traces of water in the forming gas affect equilibria (11) and (12) and similar equilibria for other metal oxides. The reactions can be described by thermodynamic data based on free enthalpy of formation ΔG_f^0 yielding conditions of temperature, H₂-, O₂-, and H₂O-pressure for the removal of specific metal oxides. Some ΔG_f^0 -values for metals of the described device and observations related to reduction in chip soldering are given in table 10 .

Metal oxide	$\Delta G_f^0 / \text{kJ} \cdot \text{mol}^{-1}$ of oxide at 298K	$\Delta G_f^0 / \text{kJ} \cdot \text{mol}^{-1}$ of metal at 298K	Reduction in chip soldering (400°C; 5vol% H ₂ in N ₂)
Ag ₂ O	-11,2	-5,6	fast
CuO	-128,3	-128,3	fast
Cu ₂ O	-147,9	-74,0	fast
NiO	-211,5	-211,5	slow
PbO	-189,3	-189,3	slow
Pb ₃ O ₄	-601,6	-200,5	slow
PbO ₂	-215,4	-215,4	slow
SnO	-256,8	-256,8	slow
SnO ₂	-519,6	-519,6	slow
ZnO	-320,5	-320,5	slow
Al ₂ O ₃	-1582,3	-791,2	no reduction
Cr ₂ O ₃	-1058,0	-529,0	no reduction

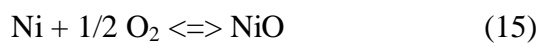
Table 10 : Comparison of ΔG_f^0 values for metal oxides extracted from D'Ans [2]. Those specific metals are present in a MOSFET device. Their metal oxides will be reduced with very different velocity during the chip soldering process.

As indicated from thermodynamic data, reduction of the oxides of Ag and Cu during the chip soldering process occurs easily. As ΔG_f^0 for water, that forms during reduction reaction (11) and (12), is quite high and the specific ΔG_f^0 -values for the metal oxides are quite low, the total free enthalpy of reaction ΔG_R^0 is higher for those two metals compared to the other metals. For Ag and Cu therefore the driving forces for reduction of the oxides are higher compared to the other oxides. However, thermodynamics states only whether a reaction is possible or not. Much more important for the process are the kinetics of these reactions. For example, Rodriguez et al. [39] found that CuO is reduced at 200°C already in a forming gas mixture consisting of 5vol% H₂ in He within 20 minutes, but with specific induction time about 5 minutes at p=600Pa. He mentioned also that defective CuO layers undergo a spontaneous reduction at this temperature. Kim et al. [40] reported a start temperature of 300°C for Cu₂O reduction and a start temperature of 280°C for the CuO reduction.

From Ni only NiO is known as oxidation product with O₂ with for example a rate constant of $k_p=8 \cdot 10^{-4} \cdot \exp(-172381/RT)$ [$\text{g}^2 \cdot \text{cm}^{-4} \cdot \text{s}^{-1}$] for the range of $\Theta=400-850^\circ\text{C}$ [41] along the reaction shown in equation (15). The reduction of NiO is happening at this chip solder process conditions through the reaction equilibrium given through equation (16). Comparing the reduction rate of CuO, Cu₂O and NiO shows, that the activation energies are in a similar range. For example Kim et al. [40] found

$E_{A,CuO}=60,7$ kJ/mol for CuO reduction (11) and $E_{A,Cu_2O}=114,6$ kJ/mol for the Cu₂O reduction (12). For the respective NiO reduction Utigard et al. [42] reported $E_{A,NiO}=90$ kJ/mol, but they noted also a very large range of activation energies starting from $E_{A,NiO}=43$ kJ/mol to 133kJ/mol reported in literature depending on experimental procedure and the NiO source. Rodriguez et al. [43] published results of NiO reduction from 250°C to 350°C and they found no induction time of the reduction reaction above 310°C for NiO powder. In contrast they noted that reduction of defect free NiO(100) surfaces is difficult and can have up to 10 minutes induction time at 350°C due to lack of O vacancies that have been made responsible for the fast dissoziation of H₂ on the NiO surface and finally for the reduction of the NiO.

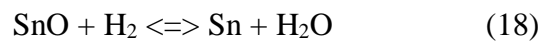
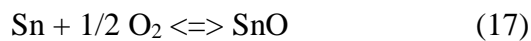
In conclusion the reduction of NiO with H₂ is not only dependent on the reaction parameters such as concentrations, pressure and temperature but also on the properties of the NiO crystal grown on the substrate. Especially induction times related to defect free NiO can lead to a domination of the oxidation reaction together with the oxygen traces in the forming gas. The concentration of these traces depends on the adjustment of the chip soldering process and can be as low as 10ppm in the best case but also can be bigger than 50ppm in the worst case.



The oxidation and reduction behaviour of the solder alloy Pb-2Sn-2.5Ag depends on the specific elements and on the stability of their oxides. In table 10 the ΔG_f^0 values of the specific oxides show that Sn forms the more stable oxides compared to Pb or Ag (Ag₂O: $\Delta G_f^0 = -11.2$ kJ/mol; PbO: $\Delta G_f^0 = -189.3$ kJ/mol; PbO₂: $\Delta G_f^0 = -215.4$ kJ/mol; SnO: $\Delta G_f^0 = -256.8$ kJ/mol; SnO₂: $\Delta G_f^0 = -519.6$ kJ/mol). At the positions of solder dispensing and chip placement (figure 30) a increase of the O₂ concentration in the forming gas can happen due to diffusion and convection of the ambient air through the openings of the forming gas tunnel in case of a non optimized forming gas flow through those openings. This can entail a growth of the respective oxide layers in the soldering equipment at those positions.

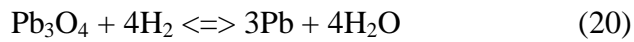
For Sn at temperatures between 200-270°C tetragonal SnO is reported and at higher temperatures from 280-390°C both SnO and SnO₂ is observed, but at reduced O₂ pressure (p<10 hPa) only SnO appears [41]. This is the case during the chip soldering process. Kubaschewski et al. [41] reported a parabolic rate constant of $k_p=1.7 \cdot 10^{-5} \cdot \exp(-83680/RT)$ [$\text{g}^2 \cdot \text{cm}^{-4} \cdot \text{s}^{-1}$] for the range of $\Theta=325-450^\circ\text{C}$ for this oxidation reaction (17). In contrast, at ambient O₂ pressure only SnO₂ is forming according these authors.

The reduction reaction of SnO through reaction (18) thermodynamically is possible in principle under the conditions of chip soldering at $\Theta=400^\circ\text{C}$ through forming gas with 5% vol H₂ in N₂, but the conversion rate is very slow. Humpston and Jacobson [44] reported a reduction rate for different Sn solders in the range of 1 nm/min at $\Theta=400^\circ\text{C}$ in H₂ with 10ppm O₂. This is possibly slower as the respective oxidation rate of Sn through traces of O₂ or H₂O leading to a growth of the Sn oxides as a concurring reaction to the reduction.



The second component of the solder is Pb. Pb as a pure metal is oxidizing with a parabolic law but with 4 specific rate constants, one for the temperature below the melting temperature of $\Theta_m = 327,4^\circ\text{C}$ and 3 different rates for the molten Pb. In the molten state there are complex interactions of the various oxides including red tetragonal PbO, yellow orthorhombic PbO, Pb₃O₄ and PbO₂. At $\Theta = 400^\circ\text{C}$ the stable formed oxide is reported to be Pb₃O₄ [41]. Within an alloy together with Sn the oxidation rate is dominated by the Sn, for example Pb alloy with 1wt% of Sn shows a reduction of the rate constant by factor 5 compared to pure liquid Pb as was presented by Kubaschewski et al. [41]. A linear approximation of this data leads to a rate constant reduction of one order of magnitude. Theoretically the Pb oxidation reaction (19) and reduction (20) occur competitively on a pure molten Pb. However, in the case of this solder alloy only SnO is present on the solder surface during the chip soldering process due to the higher thermodynamic stability of SnO in comparison to Pb₃O₄ as shown in table 10.





The third element within the solder is Ag that is not forming stable oxides at the conditions of chip soldering process. Ag_2O is decomposing under ambient pressure at $\Theta=300^\circ\text{C}$ into its elements, to form Ag_2O at higher temperatures a specific higher O_2 pressure is required [45].

In summary Sn is the species of the solder alloy Pb-2wt%Sn-2.5wt%Ag which will be preferably oxidized with presence of traces of O_2 or H_2O in the forming gas tunnel of the chip soldering equipment. This is for example seen in experiments er174 and er175 (chapter 5.2 "Activation process ") where the Sn oxide layer is prominent on the Pb-2wt%Sn-2.5wt%Ag solder surface in spite of the relatively low concentration of Sn in the alloy. Looking on the complete set of metals that are present within the discussed MOSFET device at chip soldering process (Cu, Ni, Pb, Sn, and Ag) finally only Sn is showing a significant oxidation rate because of the low reduction rate of SnO at those conditions.

The properties of the aluminium chip metallisation, its activation and behaviour during chipsoldering will be described in section "4.1.5 Activation of aluminium chip surfaces" because this metal has to be treated differently for a proper activation for A2 deposition.

A brief description of the thermodynamics of metal oxidation during soldering is given by Humpston and Jacobson [44] who also give information on the reduction rates and the kinetics of oxidation and reduction. A very broad overview on oxidation of metals and alloys can be read from Kubaschewski and Hopkins [41] who reviewed many results. A fundamental theoretical treatise of reduction thermodynamics and possible mechanisms is provided by Kung [46] and Fromm [47] giving also information about kinetics of metal-gas interactions at low temperature. A dedicated theoretical treatment of metal oxidation and reduction will not be given in this work as the main focus is the electrochemical deposition of the Zn/Cr alloy of A2-process.

4.1.2 Activation of Cu surfaces

As discussed above chip soldering as the last thermal process which has significant oxygen traces in its process atmosphere does not further oxidize the Cu surface as both

CuO and Cu₂O are thermodynamically not stable under this process conditions, being $\Theta=400^{\circ}\text{C}$ in forming gas of N₂ with 5vol% H₂. So CuO and Cu₂O only can form in the period after chipsoldering process through aluminium wirebonding process until the A2-process. This usually takes 2-3 days under ambient conditions in production in a cleanroom at room temperature.

On room temperature conditions, Boggio et al. [48] measured the growth of a Cu₂O and CuO layer on a Cu(111) surface at different O₂ pressures with ellipsometry. Iijima et al. [49] took high purity Cu films prepared by ion beam deposition and measured the growth of CuO and Cu₂O with XPS [49]. The data from these two groups shows a very low growth rate of Cu₂O/CuO at room temperature which can be seen in figure 31 as a comparison of these two results.

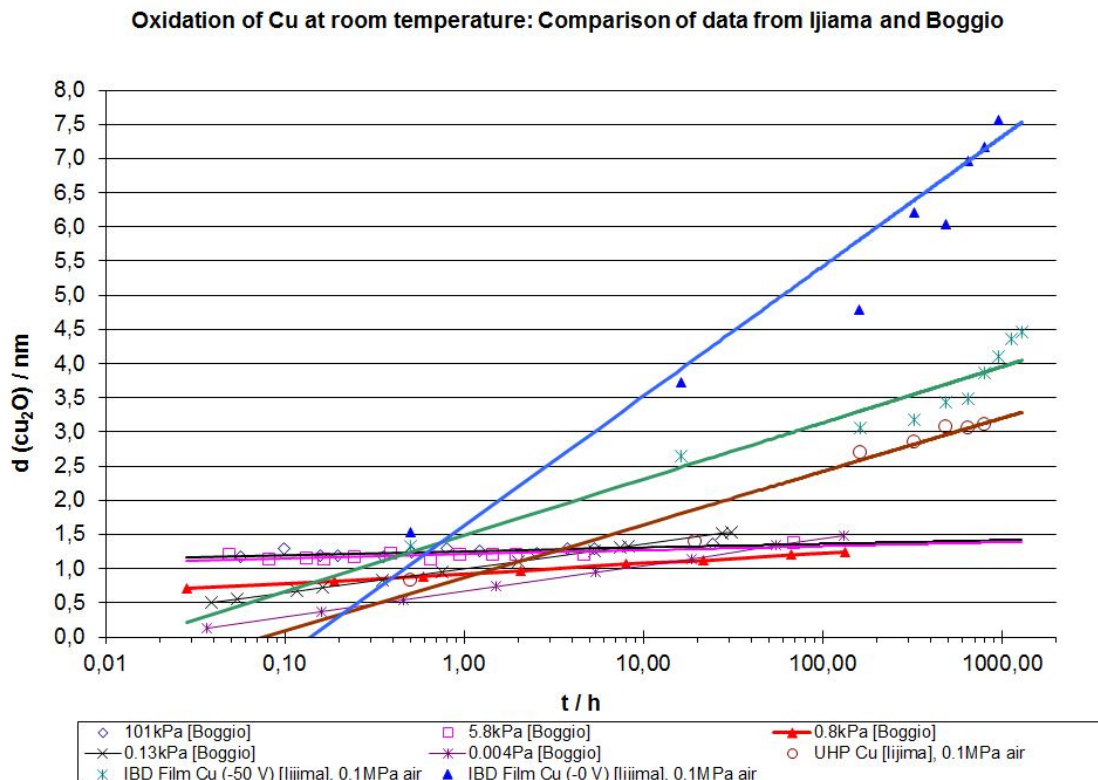


Figure 31: Room temperature oxidation of Cu. Data from Boggio et al. [48] at different oxygen pressures compared to data from Iijima et al. [49] at 0.1MPa oxygen pressure.

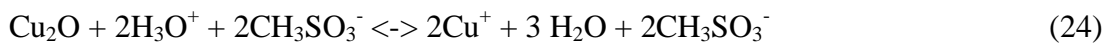
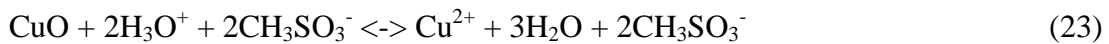
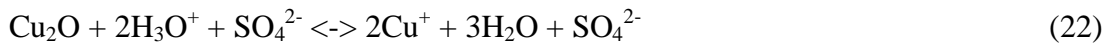
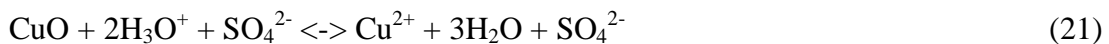
Since both data sets are correlating quite well it can be concluded, that the resulting thickness of CuO and Cu₂O on Cu is lower than 10nm after storing the Cu surfaces at

room temperature for 2-3 days in production environment. This value is also confirmed by Humpston and Jacobson [44].

Besides the mentioned TO263 device there are other devices with process flows having a higher temperature budget without a forming gas atmosphere. For example, devices with a glue chip bonding encounter a glue curing process at temperature of up to 220°C for up to 2 hours. In addition Cu- or Au-wirebonding processes are running at a similar temperature. For Cu running into such processes a much thicker CuO and Cu₂O layer forms and this can lead to limitations of the activation process at A2 process. Devices running within such a process flow were not in focus in this work. Oxidation of Cu at elevated temperatures will be discussed within chapter 6 regarding the passivation of Cu with organic molecules.

Activation of the metallic surfaces means the removal of metal oxides which were formed during the preceding processes of the device. For the A2-process activation in the early beginning was done with sulfuric acid. Usage of methanesulfonic acid (MSA) as a substitute for sulfuric acid was coming up later. The activation of Cu was done in 10-12wt% H₂SO₄ at 25°C for 10s time in the case of a TO263 device during the A2-process.

During activating of the Cu surface, the dissolution of the CuO / Cu₂O layer due to the acidic treatment by either H₂SO₄ or MSA is happening. The reactions are shown in equation (21) and (22) for H₂SO₄ and (23) and (24) for MSA, respectively.



Assuming that the transport of H₃O⁺ to the oxide surface and the reaction with the oxide is very fast due to the small size, fast transport and the high reactivity of the H₃O⁺ ions, the dissolution is limited by the transport of products back to the solution. One major kinetic parameter for this process is the saturation solubility of the formed salt in the

activating solution. A comparison of results on kinetic studies and dissolution rates was done for example by Casey [50], who was comparing the dissolution rates of CuO at pH=1 and pH=2 reported from various authors for the acids HNO₃, HCl and HClO₄. For the case of pH=1 he proposed a dissolution rate of 10^{-6.3} to 10^{-8.3} mol cm⁻² s⁻¹ for CuO at temperatures ranging from 20°C to 30°C. Calculation of the respective CuO thickness results in a dissolution rate of 0,6 to 63 nm/s. Specifically for H₂SO₄ Majima et al. [51] measured a dissolution rate of 10^{-6.7} mol cm⁻² s⁻¹ which results in 25.2 nm/s. Considering the process time for the activation of 10s a maximum CuO layer of 250nm can be dissolved.

Regarding the dissolution kinetics there are two models reported, a diffusion controlled mechanism as well as a reaction controlled mechanism. Casey [50] also highlighted discrepancies from different authors. For example Danilov et al. [52] found, that the dissolution rate is affected by the diffusion rate of the products back to the bulk solution. In contrast Majima et al. [51] concluded in their work a surface kinetical control. The authors reported that they found no influence of the fluid dynamics on the dissolution rate; however, they did only consider agitation for their rotating disc experiments of $f \geq 300 \text{ min}^{-1}$ which is a stronger agitation at the interface sample - solution compared to the conditions within the activation cell of the A2 equipment. Considering the disc geometry with a diameter of 20mm and a thickness of 6mm, which Majima et al. have been using, the relative movement between surface and liquid is $v = 18.85 \text{ m/min}$ for $f=300 \text{ min}^{-1}$ at the disc edge. In the activation cell of the A2 equipment the devices are moved through the acid with a speed of only $v = 3.6 \text{ m} \cdot \text{min}^{-1}$. Therefore for the current case in the activation cell a diffusion controlled mechanism is assumed as stated above. This result finally means that transport of the products from the device surface of the device into the bulk solution plays a major role for the dissolution rate.

Looking at table 11 the solubility of copper methanesulfonate salt (2 mol/L) is slightly higher when compared to CuSO₄ (1,35 mol/L). Therefore the use of methanesulfonic acid for activation is slightly more efficient. It will be discussed later that the solubility limit of methanesulfonic acid salts is of much higher importance for other metals which are present in the device.

Cation	Aqueous saturation solubility at 22°C [mol/l as metal]		
	Methane-sulfonate	Sulfate	Chloride
NH ₄ ⁺	6,83	8,17	5,06
Li ⁺	7,06	4,9	9,37
Na ⁺	5,65	2,78	5,57
K ⁺	4,48	1,25	3,86
Mg ²⁺	1,4	2,63	5,02
Ca ²⁺	2,92	0,025	5,51
Sr ²⁺	2,55	0,71*10 ⁻³ [54]	3,04
Ba ²⁺	1,59	0,11*10 ⁻⁴ [54]	1,71
Mn ²⁺	2,9	3,52	4,12
Co ²⁺	2,53	2,16	3,87
Ni ²⁺	2,13	2,44	4,38
Cu ²⁺	2	1,35	4,87
Ag ⁺	3,72	0,056	0,11*10 ⁻⁴ [54]
Zn ²⁺	2,16	3,32	13
Cd ²⁺	3,2	3,1	5,71
Sn ²⁺	3,73	1,42	4,91
Hg ²⁺	1,81	0,16*10 ⁻² [54]	0,24
Pb ²⁺	2,6	0,15*10 ⁻³ [54]	0,034

Table 11 : Aqueous solubility of various metal salts, including methanesulfonates, sulfates and chlorides. Data reproduced from Gernon [53] and from Lide [54]

In summary, the activation of the Cu surface for A2 plating is happening via dissolution of CuO in either H₂SO₄ or MSA. With a dissolution rate of 25.2 nm/s within the activation period of 10s a layer of 250nm can be dissolved. MSA theoretically is favoured because of the higher solubility of the MSA salts of Cu compared to the sulfate.

4.1.3 Activation of Ni and NiP surfaces

For the discussed device in a TO263 package, use of a fully Ni/NiP plated leadframe was the target material due to benefits in the manufacturing processes. On the leadframe therefore the major surfaces are consisting of the final NiP layer with a thickness of 150nm of NiP alloy on a 1.5µm Ni layer, both deposited electrochemically before the cutting of the leadframe structure in a stamping process. Only the cutting edges are consisting of a Cu surface.

There are two different galvanic Ni/NiP processes used in industry, the NiSO₄ bath also known as Watts-bath and the newer Ni(SO₃NH₂)₂ nickelsulfamate bath. An overview of electrolytes that can be used for NiP alloy plating is given by Winkler summarizing

different processes and bath compositions for galvanic [55] and for electroless NiP deposition [56]. For the NiSO₄ Watts bath Hu and Bai [57] performed a process study summarizing, that the main parameters determining the P-content within the deposited NiP layer are temperature, current density and pH-value of the electrolyte. These parameters need to be considered carefully during NiP plating in order to control the P-content as a major factor for the metallurgy, mechanical strength and corrosion resistance.

The leadframe material considered in this work was plated in a bath from supplier (P) with NiSO₄ electrolyte for NiP deposition. Table 12 shows the used electrolyte for the deposition of the Ni and NiP layer. In figure 32 analytical results of the Ni and NiP as an example for the discussed product show a very fine crystalline Ni layer and a nanocrystalline to amorphous NiP layer.

		Ni / NiP plating supplier (P)
Ni plating	Ni-sulphamate:	80-100g/l
	NiCl ₂	10-20g/l
	Boric acid	35-55g/l
	Ni PC3 additive	15-25ml/l
	pH	3.5-4.5
	Θ	60°C
NiP plating	NiSO ₄	270-330g/l
	NiCl ₂	30-70g/l
	Boric acid	35-55g/l
	Ni gleam EP additive	30-50ml/l
	pH	0.8-1.6
		Watts Ni plating [58]
Ni plating	NiSO ₄	310 g/l
	NiCl ₂	50 g/l
	Boric acid	40 g/l

Table 12: Ni plating and NiP plating electrolytes used for the deposition of the Ni / NiP layers. The NiP electrolyte is based on a standard Watts bath with Ni gleam EP additive, a trade name of the company Rohm + Haas, consisting of a mixture of H₃PO₃ and H₃PO₄ as the P-source and undisclosed organic additives. The additive PC3 for the Ni plating is also a trade name from Rohm + Haas consisting of undisclosed organic additives that are responsible for the crystallinity of the deposited Ni.

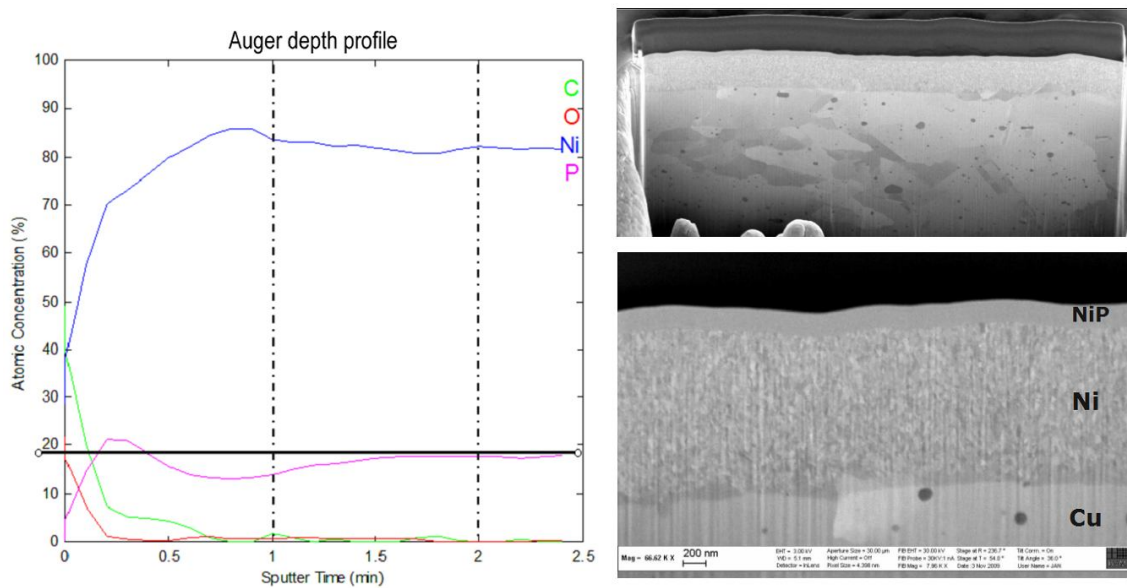


Figure 32: Auger and FIB cut of the NiP layer on a DSO-36-34 leadframe plated with the NiSO_4 plating process from supplier P. The same process is used for the TO263 (Sample from er218). The FIB cut picture on the right bottom shows a magnification of the Ni and the NiP layer from the FIB cut picture on the right top.¹

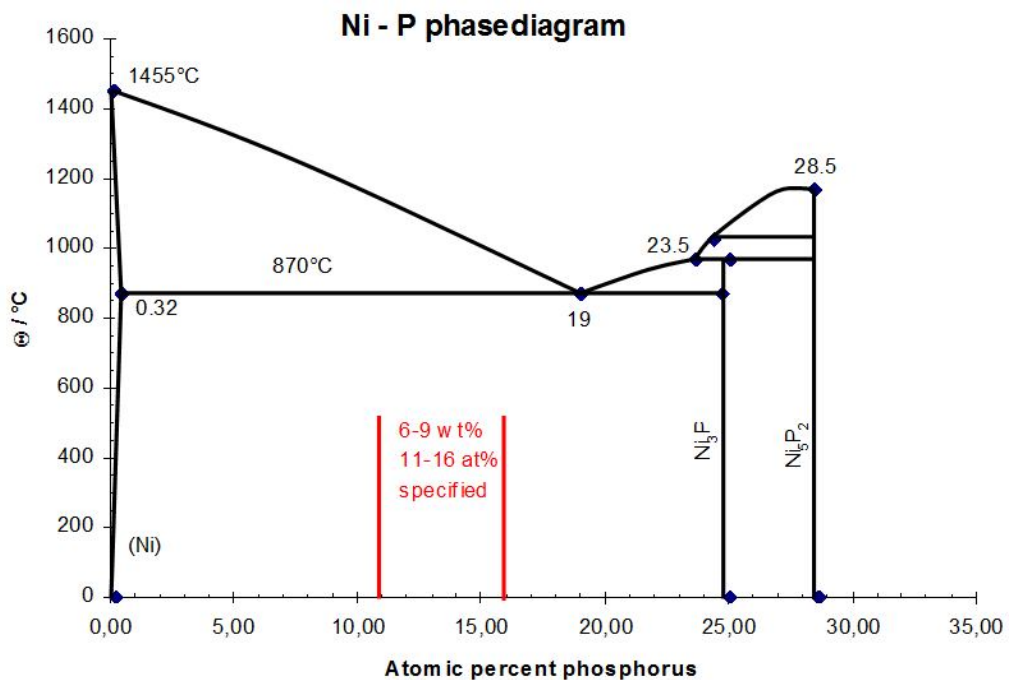


Figure 33: Phase diagram of the system Ni and P reproduced from data of ASM [59]. Indicated concentration area from 6-9 weight % is the specified P concentration for the NiP alloy plated from a NiSO_4 electrolyte from supplier P.

¹ : Investigation done by Steffen Jordan and the team.

The discussion of the thermal history of the NiP layer during the hot chip soldering process is similar to the preceding discussion with Cu. The NiP layer is an alloy with a P content of 8 weight % (14 at %) which is according to the phase diagram in figure 33 not an equilibrium phase. The concentration range of P in the NiP alloy is in a range of 6 to 9 wt % (11 to 15 at %) according to the specification of the discussed product in the TO263 package. In the phase diagram at a P concentration of 25 atom % a stable Ni₃P phase is reported. The NiP alloy is deposited in a meta-stable amorphous phase that can crystallize at higher temperatures after some minutes. This means that with heat treatment for example during the chip soldering process the NiP layer can change its morphology and crystallinity depending on the NiP deposition conditions and the resulting P-content and structure. An important factor is the concentration of P in the NiP layer. Huang et al. [60] reported the deposition of NiP from a NiSO₄ Watts bath and crystallisation of different NiP layers with weight percentage of P in the range of $0 \leq \text{wt}\% \leq 14$ at $\Theta = 400^\circ\text{C}$ during 1h annealing. They found crystalline NiP only at concentrations up to 4 wt% P within the NiP layer. Above this concentration of 4 wt%, for example at 8wt% and higher they measured an amorphous XRD pattern which led to the respective Ni₃P and Ni(111) pattern after annealing in contrast to the Ni(200) pattern of a pure Ni layer without any P inclusion. During the crystallisation while the annealing is done, a Ni crystal with dissolved P is forming (Ni/P solid solution). In addition Huang et al. [60] found that Ni₃P phase precipitates at the grain boundaries of the Ni/P solid solution crystals in grains which can have 20-50nm size. They report also that during this conversion the hardness of the NiP layer increases by a factor of 2. Compared to the underlying pure Ni layer the hardness is increased then already by a factor of 4.

Together with this precipitation of Ni₃P and the crystallisation of the amorphous NiP layer the tensile stress in the layer is increasing. This happens due to a volume shrink during the conversion which can also lead to cracks in the NiP layer. A similar amorphous phase of NiP was found experimentally for example in figure 32. Crystallization was seen already after the standard chip soldering process with $\Theta = 400^\circ\text{C}$ during 3 minutes. As the specification range for the P content in the NiP layer of the investigated product is 6-9wt%, it is in the range of the amorphous deposition.

NiP deposited from the nickelsulfamate electrolyte has a lower internal stress compared to NiP deposited from NiSO₄ but was not in focus in this work. For example, details of this plating bath are reported by Lin et al [61] who found similar correlations between P-content, microstructure and hardness similar to results obtained by Huang et al. [60] for the Watts NiP bath.

The surface of the NiP alloy can consist of NiO from leadframe manufacturing but similar to the case of CuO the NiO is slowly reduced during the chip soldering process through the forming gas. Oxidation of a Ni-19P alloy was investigated by Siconolfi et al. who found that the oxidation kinetics in the range of ambient temperatures up to 300°C is essentially the same as for pure nickel [62]. In his work the authors reported a steady state thickness of 0.6nm at 100°C and 1.5nm at 200°C after a oxidation time of up to 200h whereas at $\Theta=300^{\circ}\text{C}$ they observed a parabolic oxidation rate like it is shown in figure 34.

In practice the NiO thickness that enters the activation at A2-process has a thickness of less than 15nm after storing the surfaces at room temperature for 2-3 days in the production environment as reported by Humpston and Jacobson [44].

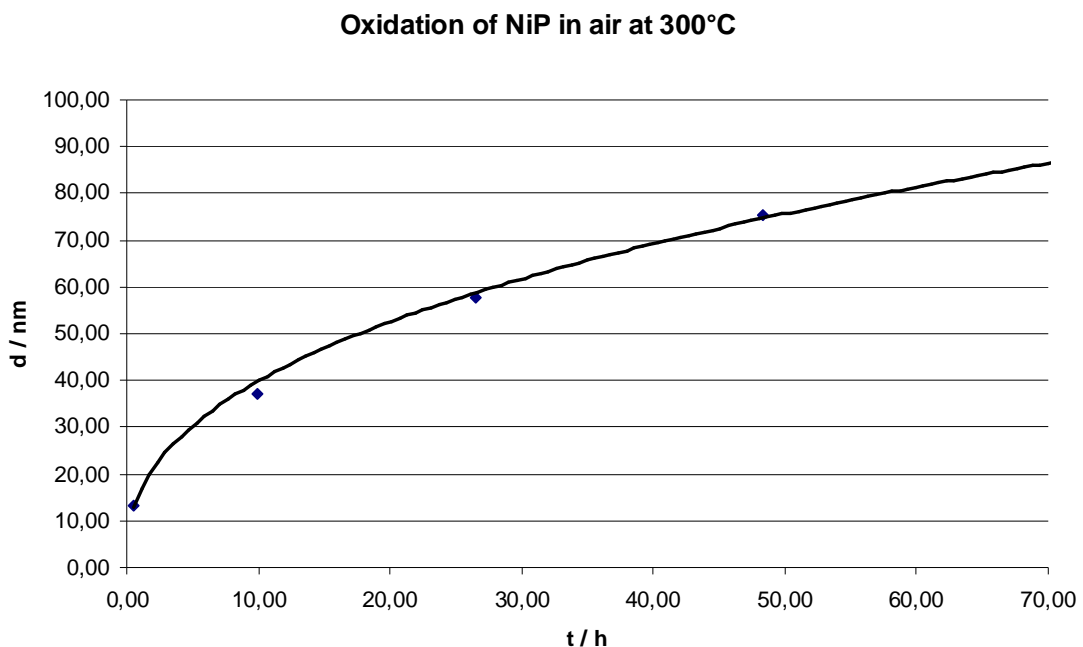


Figure 34: Parabolic oxidation rate of Ni-19P in air at $\Theta=300^{\circ}\text{C}$ measured by Siconolfi et al. [62].

During activation of the oxidized NiP surface in the A2 process the NiO undergoes similar reactions as the copper oxides following equation (25) and (26).

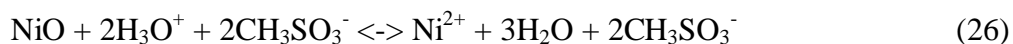
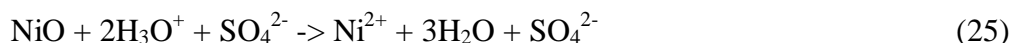
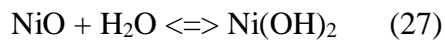


Table 11 shows that the solubility of NiSO₄ and Ni(SO₃CH₃)₂ are 2.44 mol/L and 2.13 mol/L respectively, they are in the same range as the respective copper salts.

However, the reported dissolution rates in acids are much lower for NiO. Casey [50] for example highlighted a dissolution rate of $10^{-13.7} \text{ mol cm}^{-2} \text{ s}^{-1}$ for the dissolution of NiO at $\Theta = 20\text{-}30^\circ\text{C}$ in HNO₃, HCl and HClO₄ comparing various authors. NiO therefore dissolves by a far slower rate when compared to CuO, where the dissolution range is $10^{6.3}$ to $10^{8.3} \text{ mol cm}^{-2} \text{ s}^{-1}$ as stated in chapter 4.1.2. For NiO taking the value of Casey [50] as an example the calculation of the layer dissolution rate results in $2 \cdot 10^{-6} \text{ nm/s}$ which is much too small for an acid activation of several nanometers of NiO during 10s activation time. Even an increase of the dissolution rate by other factors can not lead to a dissolution rate which may be comparable with CuO. For example, Colin et al. [63] found an increase of the dissolution rate by factor 200 with presence of strong oxidizing ions and by more than factor 200 for specific thermally pretreated NiO samples. A brief theoretical treatment of the oxide dissolution kinetics for NiO is presented by Diggle [64] who also described the very low dissolution rate of NiO. The author reports a maximum rate of 10^{-10} to $10^{-9} \text{ mol cm}^{-2} \text{ s}^{-1}$ at $\Theta=95^\circ\text{C}$ in 1 molar HCl.

In consequence to this data, the activation of the NiP via an acidic dissolution according to equations (25) and (26) must be of minor importance. The dominating activation in this case happens within the alkaline A2 electrolyte in the A2 plating cell. Considering the chemistry of Ni in aqueous solutions with the help of thermodynamic calculations of the Pourbaix diagrams published by Beverskog et al [65] shows, that all oxide and hydroxide phases of Ni are unstable at conditions present in the A2 cell. The conditions during A2 deposition are $\text{pH} > 12$ and a high cathodic overpotential with excessive H₂ formation. This means the potential lies in a range where water is unstable and is reduced electrochemically. The reaction of NiO in aqueous environment first undergoes a hydrolysis reaction as shown in equation (27) and which according to Diggle [64] is

happening fast. This reaction is starting already in the activation cell and moving continuing in the A2 deposition cell.



The reduction of the formed Ni(OH)_2 at the conditions within the A2 deposition cell being $\text{pH} > 12$ at a high cathodic overpotential can be derived from the respective Pourbaix diagram from Beverskog et al [65] following equation (28).



Referring to figure 35 in the region of high cathodic overpotential of $U < -0,6\text{V}$ and at $\text{pH} > 12$ the phase $\beta\text{-Ni(OH)}_2$ in aqueous milieu is thermodynamically instable and will be converted to pure Ni. In addition, at even higher cathodic overpotential of $U < -0.8\text{V}$ the formation of a nickel-hydrogen species is thermodynamically possible. However, the work of Wolf et al [66] showed that nickel hydride is not stable at $\Theta > 200\text{K}$. The consequences for the A2 deposition and the prerequisites at this process point will be treated later in chapter "4.2

Theory of the electrochemical deposition of a porous layer".

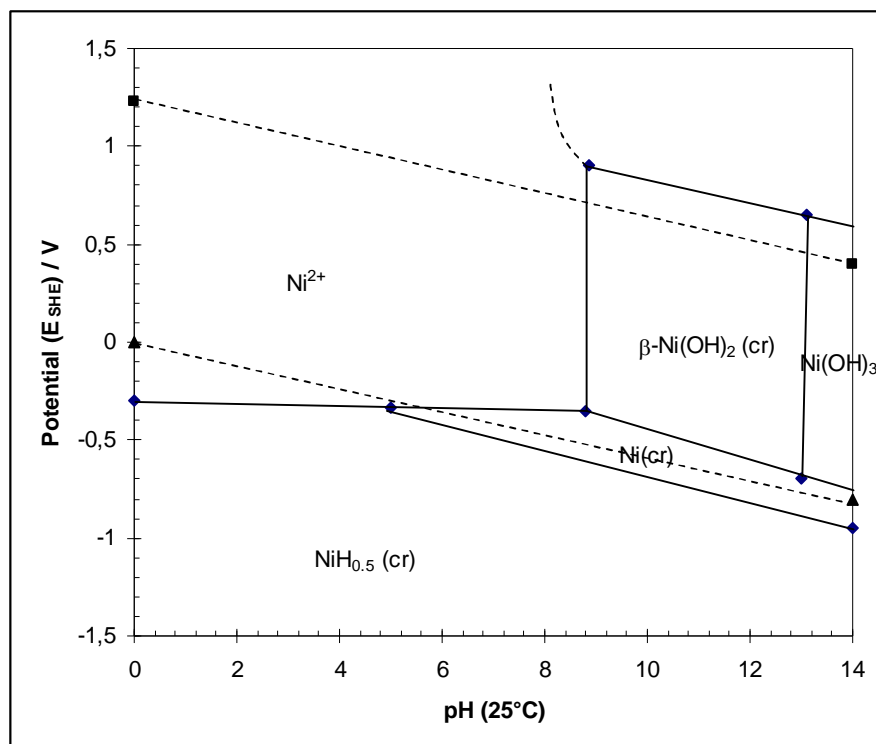


Figure 35 : Pourbaix diagram of Ni reproduced from calculated data from Beverskog et al [65] for $\Theta=25^\circ C$ and $[Ni(aq)]_{tot} = 10^{-6}$ mol/l.

The effectiveness and suitability of cathodic activation of Ni in alkaline solution is reported for example by Relitz [67] who used a cyanide based activation solution at room temperature for a time of 30 s to prepare electroplated bright Ni for further bright Cr plating. Cathodic activation of Ni was also described by Mandich et al. [68]. It is possible in acidic solution by a treatment time of 15 s at a potential -4 to -6V (vs. SHE) in 5% vol H_2SO_4 . Mandich mentioned in an additional work [69] also that Ni surfaces are easily getting passive to further deposition, for example for chromium deposition. In addition cathodic activation is reported by Mandich to be effective in acidic and alkaline milieus. A brief description about cathodic activation was done also by Durney [70] who also stated that passivation of Ni can be prevented by applying a direct cathodic potential after Ni plating.

To sum up, the activation of Ni is difficult due to the low dissolution rate of NiO in acidic solutions. Therefore Ni activation is performed simultaneously to the deposition of the A2 layer by cathodic activation at $pH \geq 12$. It should be stressed that nickel

oxidation from previous processes, for example during the chip soldering process with not optimized forming gas will have a big influence on activation of Ni and the A2 deposition on this surface.

4.1.4 Activation of Pb-2Sn-2.5Ag solder surfaces

In chapter "4.1.1 Properties and states of the different surfaces prior to activation" it was discussed that Sn is prominent on the solder surface due to the higher ΔG_f^0 value of SnO when compared to PbO and Ag₂O. In addition the reduction rate of SnO with forming gas (5% vol H₂ in N₂) during the chip soldering process is slower as compared to the oxidation happening competitively with O₂ traces in this gas. In the worst case the oxidation is dominating and a parabolic rate constant can be assumed with a value of for example $k_p=1.7 \cdot 10^{-5} \cdot \exp(-83682/RT)$ g² cm⁻⁴ s⁻¹ ($E_A=83,7$ kJ/mol) for the temperature range of 325-450°C as suggested by Gruhl et al. [71], also cited and discussed from Kubaschewski et al. [41]. In a kinetic study of Sn oxidation Nagasaka et al. [72] confirmed this rate constant with a value of $k_p=2.73 \cdot 10^{-6} \cdot \exp(-78242/RT)$ g² cm⁻⁴ s⁻¹ ($E_A=78,2$ kJ/mol) and the calculation of the SnO thickness over time for 400°C for the growth rates observed from both authors is in good agreement as shown in figure 36.

Oxidation kinetics of Tin: $\text{Sn} + 1/2 \text{O}_2 \Rightarrow \text{SnO}$

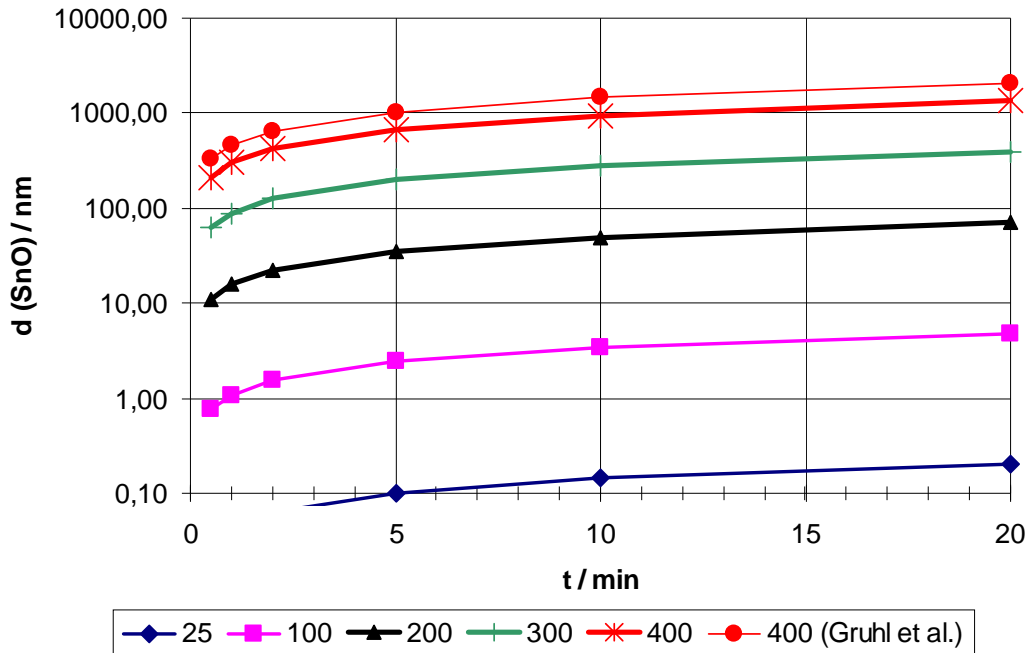
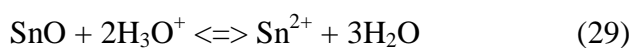


Figure 36: Oxidation kinetics of Sn calculated with the rate constants derived from Nagasaka et al [72] and with a rate constant for 400°C reported from Gruhl et al.[71].

The low concentration of O_2 in the process gas leads dominantly to SnO instead of SnO_2 formation in spite of the fact that SnO is a metastable phase under these conditions. Under ambient conditions with normal O_2 partial pressure of 21mbar the oxidation of Pb-Sn alloys also leads to the accumulation of tin oxide but in this case only SnO_2 can be found and this happens already with Sn-Pb alloys at Sn concentrations of 1%wt. The SnO will only react further via disproportionation to SnO_2 and Sn at higher temperature of $\Theta > 500^\circ\text{C}$, described in Gmelin [73] and by Kubaschewski [41].

For the activation of Sn in aqueous solutions the formed SnO is dissolved. SnO is soluble in both strong acids and strong bases. The acid reaction is represented by equation (29), the alkaline reaction is given by equation (30).



For acidic solutions the solubility of SnO is reported to be very low ($c = 4.75 \cdot 10^{-2}$ mol/L; $\Theta = 25^\circ\text{C}$; pH=1.8) and a similarly low solubility at higher pH values ($c =$

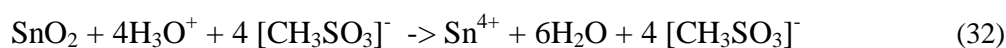
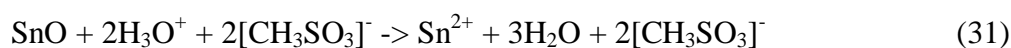
$4.2 \cdot 10^{-2}$ mol/L; $\Theta = 25^\circ\text{C}$; 0.3 n NaOH) [73]. The respective solubility of SnO_2 is much lower ($c = 4 \cdot 10^{-7}$ mol/L between pH=2 to pH=11.4 and $c = 3.4 \cdot 10^{-3}$ mol/L in 0.2 N NaOH; both at 25°C) according to Gmelin [73].

On the other hand more recent data regarding the solubilities of several Pb and Sn salts indicates high solubilities shown in the following comparison in table 13. The high solubilities of the MSA salts are one reason for the industrial favourisation of MSA as an effective activation acid for Sn and especially for Pb.

	CH_3SO_3^- [mol/l]	SO_4^{2-} [mol/l]	Cl^- [mol/l]	F^- [mol/l]	Source
Pb^{2+}	2.6		0.034		Gernon [53]
		$0.15 \cdot 10^{-4}$	0.039	$2.7 \cdot 10^{-3}$	Lide [54]
				$2.7 \cdot 10^{-3}$	Carter [78]
Sn^{2+}	3.73	1.42	4.91		Gernon [53]
		0.88	9.39		Lide [54]
		1.54			Römp [74]

Table 13: Comparison of data of solubilities for Sn^{2+} and Pb^{2+} salts with various anions.

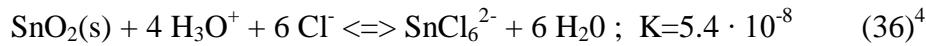
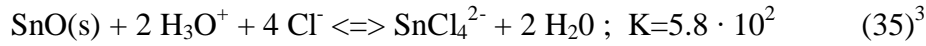
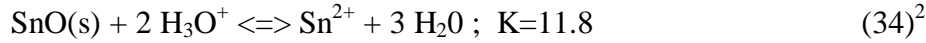
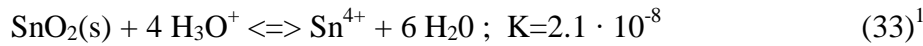
For the current activation process $\text{CH}_3\text{SO}_3\text{H}$ (MSA) is used, the dissolution follows equations (31) and (32).



The higher solubility of the methanesulfonic acid salts compared to the values of the sulfuric acid salts favors the dissolution of the SnO and SnO_2 . In figure 37 and in table 13 the data is showing a solubility of 3.73 mol/L for the $\text{Sn}(\text{CH}_3\text{SO}_3)_2$ salt in water that is by more than factor 2 higher compared to the solubility of the respective SnSO_4 salt.

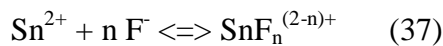
House et al. [75] report the difference in solubility comparing SnO and SnO_2 with the former being much more soluble indicated by equilibrium (33) and (34) with the respective K values calculated by these authors. They also highlight the dramatic increase of the solubility of SnO with addition of halogen ions like Cl^- ions shown in equilibrium (35). For the addition of Cl^- ions to SnO_2 this is not observed as shown in

equilibrium (36) with a similar value for K like for the equilibrium (33) without Cl⁻ addition.



This indicates already that also the addition of F⁻ ions to the MSA solution may increase dissolution rate of the SnO. It should be mentioned here that besides the activation with pure MSA the final option of activation chemistry for the A2 process was using 0.1wt% HF added to the MSA due to the difficulties in activation of the chip aluminium metallisation which will be discussed later in chapter "4.1.5.3 Activation of Al₂O₃ with aqueous HF / MSA chemistry".

For the Sn surface the expected effect is an increase of the dissolution rate because of the high stability of the formed species, including SnF⁺, SnF₂, and SnF₃⁻ that are described by various authors. For example Forbes et al [76] reported the preparation of SnF₂ through reaction of SnO with HF. Furthermore Stirrup et al. [77] gave a brief overview on the behaviour of Sn in aqueous systems and report high stability constants K for the the three species SnF⁺, SnF₂ and SnF₃⁻ (K_{SnF+}=1.1*10⁴ L/mol; K_{SnF2}=5.9*10⁶ L²/mol²; K_{SnF3-}=2.8*10⁹ L³/mol³) for reaction equilibria (37). In addition these authors also reported the stability constants of this three species in an aqueous system containing HF as shown in equilibria (38) (K_{SnF+}=32 mol/L; K_{SnF2}=35 mol/L; K_{SnF3-}=58 mol/L). In conclusion there is a positive effect expected for the activation efficiency of SnO by adding 0.1% wt HF to the MSA in the activation bath.

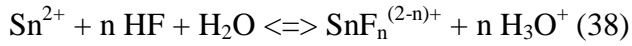


¹ : K was reported without a dimension from the autors. The following dimension is proposed: [mol² · L⁻²]

² : K was reported without a dimension from the autors. The following dimension is proposed: [mol · L⁻¹]

³ : K was reported without a dimension from the autors. The following dimension is proposed: [L⁻⁴ · mol⁴]

⁴ : K was reported without a dimension from the autors. The following dimension is proposed: [L⁻⁴ · mol⁴]



Furthermore in the alkaline plating solution after the activation bath the dissolution of remaining SnO will proceed because of the high cathodic overpotential and the high pH (pH > 12). In accordance with the potential-pH diagrams presented by House et al [75] the SnO will be converted to $[\text{Sn}(\text{OH})_3]^-$ and $[\text{Sn}(\text{OH})_6]^{2-}$ and therefore dissolve.

Even so that predominantly SnO is covering the surface of the solder there can be also some influence on Pb as the major part of the Pb-2Sn-2.5Ag solder. In MSA based solutions Pb is dissolved slowly due to presence of O₂ in the solution. In contrast H₂SO₄ is not dissolving Pb due to the formation of an insoluble PbSO₄ coating as described by Hollemann [45]. In figure 37 and in table 37 the solubility of the respective Pb- and Sn salts formed during activation with either H₂SO₄ or CH₃SO₃H (MSA) is shown. The difference in solubility of the PbSO₄ compared to Pb(CH₃SO₃)₂ in water is 4 orders of magnitude. For the Pb the very low solubility of the sulfate salt brings even the risk that the formed PbSO₄ is blocking the surface and leading to a galvanic barrier for the following deposition of A2. The addition of HF to the MSA based aqueous solution is assumed to increase the dissolution rate of the Pb due to a faster dissolution of PbO through hydrolysis by HF following a similar reaction scheme as shown in equation (34). Data from Carter [78] shows a solubility of PbF₂ of $2.7 \cdot 10^{-3}$ mol/L. In addition this author reports a similar solubility of CuF₂ ($7.4 \cdot 10^{-3}$ mol/L) and a very high solubility of NiF₂ (0.42 mol/L). Therefore, for those three metals Pb, Cu and Ni no negative influence of the addition of HF is seen.

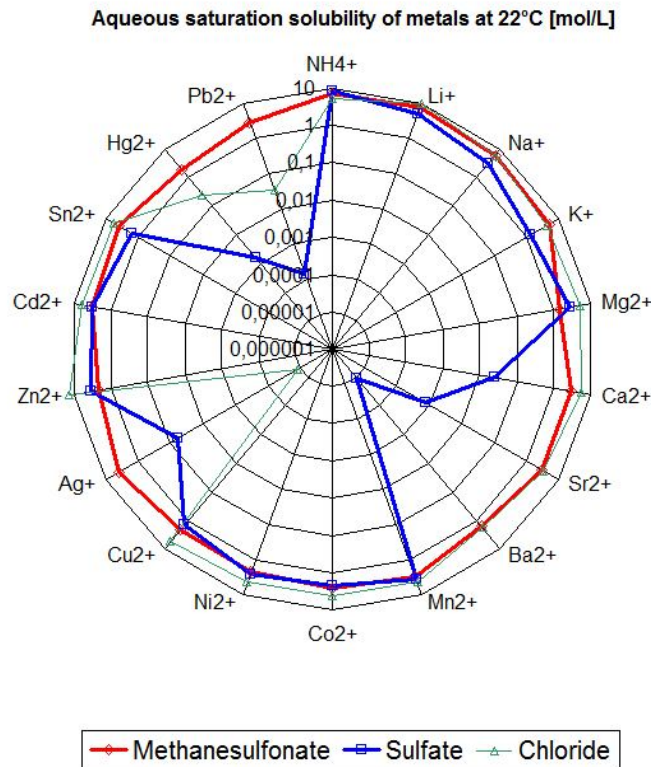


Figure 37: Aqueous solubility of different metal as methane sulfonates, sulfates and chlorides. For most of the metals described the solubility as a methane sulfonate is much better compared to sulphates. Data reproduced from Gernon et al. [53].

Summary

To sum up this chapter on activation of the Pb-2Sn-2.5Ag solder surface, the major component to dissolve is the SnO that dissolves much better when compared to the SnO₂. In spite of the fact that oxidation at normal atmosphere leads to SnO₂, the oxidation in the forming gas during chip soldering process at low O₂ pressure leads only to SnO due to presence of traces of O₂ only. Hydrolysis of the SnO happens in both milieus, acidic with MSA, alkaline with NaOH during A2 deposition. The addition of 0.1wt% HF to the aqueous MSA solution required for the activation of the aluminium chip metallisation is leading to a much stronger hydrolysis reaction of the SnO due to the formation of stable SnF⁺, SnF₂ and SnF₃⁻ species. Pb is dissolved by MSA solutions and therefore there is no barrier formation as it would be the case by using H₂SO₄ forming insoluble PbSO₄. The solubility difference for Pb salts from H₂SO₄ and MSA is more than 4 orders of magnitude. Regarding the addition of HF to MSA solutions there

is also no negative influence seen for the Cu and Ni due to a distinct solubility of the respective fluorides, the reaction products with HF.

4.1.5 Activation of aluminium chip surfaces

4.1.5.1 Reactions of the aluminium metallisation: Oxidation and corrosion

The aluminium chip metallisation is an important terminal to the device package. Especially power semiconductor chips have an area of metallisation covering nearly the complete chip area due to the vertical current flow in those MOSFET devices. This means the chip metallisation has a high contact area to the molding compound. Stress from the molding compound is affecting the chip frontside structures especially in case of a weak adhesion at this position. Weak adhesion leads to delamination and finally to a relative movement between molding compound and the chip frontside, hence finally to damage at the chip front side leading to a fail of the device. Proper adhesion is required at the chip frontside. Therefore it is stressed here that the deposition of the A2 layer is crucial for a successful and reliable metallisation.

Oxidation of aluminium

Electrochemical deposition on an Al surface requires a specific preparation because of the properties of Al with its high reactivity towards for example oxygen. As a result its oxide Al_2O_3 is highly stable. On bare Al, that can be generated via scratching of the Al surface, in a couple of seconds a stable amorphous Al_2O_3 coating is forming at room temperature in ambient atmosphere. Fromm [47] reports the formation of two monolayers stable Al_2O_3 thickness after a time of 20s at $\Theta=65^\circ\text{C}$. Jelinek [13] states that a stable thickness of 2-3 nm of Al_2O_3 layer is reached after 1 day. Other authors as those presented by Kubaschewski [41] confirm that range with 2-4 nm. The oxidation mechanism for pure Al in air is described similarly for example from Scamans et al [79], Field et al [80], and Olefjord et al. [81]. At a temperature of $\Theta < 425^\circ\text{C}$ an amorphous Al_2O_3 film growth occurs that provides a strong barrier between the metal substrate and the atmosphere due to lack of grain boundaries. Since the formed amorphous phase is undergoing a volume expansion compared to the bare Al, the Al_2O_3

film is under compressive stress ($V_{m,Al_2O_3} / V_{m,Al} = 1.26$)¹. This is one reason for the strong self annealing properties of Al because even with some deformation of the bulk Al the protecting oxide layer is not cracking. In the range between 400°C and 450°C crystallisation of γ -Al₂O₃ is starting below the amorphous layer. At those higher temperatures a duplex film is present consisting of a crystalline oxide at the metal and an amorphous top layer. Due to the higher diffusivity of oxygen and aluminium in the crystalline phase at the grain boundaries the oxidation rate increases at that point. In the lower temperature range $\Theta < 400^\circ\text{C}$ an inverse logarithmic oxidation is reported from for example Olefjord et al. [81] and Kubaschewski [41]. In the area around $\Theta \approx 400^\circ\text{C}$ the rate law is moving to a parabolic law and above 450°C a parabolic mechanism is proposed as a mixture between linear and parabolic growth behaviour.

For the case of a SFET2 MOSFET instead of bare Al an Al-1Si-0.5Cu alloy is taken for the chip frontside metallisation for different reasons. The Si is required to minimize the diffusion of the Si bulk material of the semiconductor into the metallisation that is known as Si spiking reported by Bailey [82]. With addition of Cu electromigration of the Al during the device lifetime can be reduced by orders of magnitude as presented by Walker et al. [83]. For the Al-1Si-0.5Cu alloy oxidation behaviour is slightly different to what is described for bare Al above. Addition of Si leads to a reduction of the growth rate, found for example from Nylund et al. [84] who measured 3.2 nm after annealing with 350°C in O₂ at 1bar for 5h for a bare Al sample and only 2.9 nm for Al-0.05Si at the same conditions. The authors also highlight the accumulation of Si between the formed Al₂O₃ and the Al.

For the used Al-1Si-0.5Cu alloy the downstream processes within wafer manufacturing have to be considered. For example, as shown in table 8 a plasma etching process on the silicon nitride passivation layer leads to a change of the respective Al oxide surface caused by F radicals leading to a specific F content of the Al₂O₃. Those impacts of plasma processes to the Al oxide will be discussed later in section 4.1.5.2.

¹ : Calculated with data from Dan's et al [2] who report for Al values of $\rho_{Al}=2.698 \text{ g/cm}^3$, $M_{Al}=26.9 \text{ g/mol}$ and giving for aluminiumoxide α -Al₂O₃ values of $\rho_{Al_2O_3}=4.050 \text{ g/cm}^3$, $M_{Al_2O_3}=101.9 \text{ g/mole}$. With $V_{m,i} = M_i / \rho_i$ values calculated are $V_{m,Al} = 10.0 \text{ cm}^3/\text{mole}$ and $V_{m,Al_2O_3} = 12.6 \text{ cm}^3/\text{mole}$.

Application of a thermal stress as introduced by the polyimide cyclisation ($\Theta = 380^\circ\text{C}$, $t=1\text{h}$, N_2 atmosphere) and the chipsoldering process ($\Theta = 400^\circ\text{C}$, $t=60\text{s}$, 5% vol H_2 in N_2 atmosphere) is marginally increasing thickness, but changes of the water content in the Al oxide due to the change of environment between humid air and dry process air are further increasing the Al oxide thickness. Olefjord et al. [81] showed that for Al_2O_3 stored in an air of 80% relative humidity for 1 week a strong increase in thickness from 1.5nm to 2.5nm results which is explained with the formation of $\text{Al}(\text{OH})_3$ according to equation (39) by the authors.



During $\text{Al}(\text{OH})_3$ film formation the thickness of the protective Al_2O_3 layer is reduced entailing further oxidation since the hydrolysed species offers no barrier against O_2 and Al diffusion in contrast to the protective Al_2O_3 layer.

Changing humidity and temperature within the standard downstream processes in wafer manufacturing and package assembly therefore lead to an Al-1Si-0.5Cu surface which is much more inert as compared to a bare Al surface with a native Al_2O_3 .

Corrosion and behaviour under aqueous conditions

Despite of the high reactivity of Al due to its low standard potential of $E_0 = -1.662 \text{ V}$ in aqueous solutions [2] it is very stable in pure water due to the high stability of the Al_2O_3 layer. Due to this extreme property activation of Al for electroplating is more difficult when compared to the more noble metals such as Cu or Ni because a rather strong reactivity is required to crack the native oxide. When the oxide is removed by a harsh chemical treatment the same chemicals induce a severe corrosion of the Al until it is covered with the respective A2 layer. Therefore, here corrosion of Al and its alloys is studied first to understand the difficulties regarding the activation of Al.

There are several corrosion mechanisms known and reported for Al and its alloys by for example Hufnagel [85], Jelinek [13], and Wernick et al. [86]. A continuous corrosion affecting the Al surface homogenously is mainly found on bare Al. Grain boundary corrosion also known as intercrystalline corrosion attacks the Al preferably at its grain boundaries and is seen mainly for Al alloys. Especially Cu containing Al alloys are

prone to this type of corrosion due to formation of AlCu₂ intermetallic phases at grain boundaries leading to local potential differences [13]. Attack of Al by bimetallic contact known as bimetallic corrosion happens for all Al alloys and bare Al having contact to metals that are nobler such as Cu and Ni [13]. Especially for geometries where the noble partner has a big surface area the corrosion of Al can be severe.

In contrast to the dry oxidation rate the corrosion rate of Al increases with addition of other elements that are able to form an alloy. The advantage of improved mechanical properties in Al alloys in most cases is accompanied with the disadvantage of a decreasing corrosion resistance as stated by Hufnagel [85] and Jelinek [13]. Therefore, in applications requiring a highly corrosion resistant Al surface, such as in food industry or chemical industries highly pure Al with >99.5 wt% or even >99.98% content has to be used [85].

Corrosion of Al is strongly dependent on the chemical environment including the pH of the solution and presence of specific ions in solution. According to Hufnagel [85] for example the corrosion of Al in the range of pH 4.5 to 8.5 is negligible. Above pH 8.5 and below pH 4.5 the solubility of the oxide increases depending on the respective ions in solution, for example Cl⁻ ions or F⁻ ions increase the solubility drastically. Revie et al [87] report a pH range of pH 4.5 to 7 stating corrosion rates of 0.025 g/cm²d at a pH of 4.5 and a corrosion of 0.05 g/cm²d at a pH of 7 for H₂SO₄ and NaOH respectively with a minimum at pH 6. These authors give directly data on the dissolution rate of pure aluminium not taking into account the influences that may come from the specific Al oxide films.

To understand the influence of the various Al oxide films the mechanism of Al corrosion has to be discussed. Considering a thermally grown Al₂O₃, in aqueous milieu at the outer interface between the Al₂O₃ and the solution Al(OH)₃ is forming according to equation (40). This species then is further reacting either with acids or with bases according to equation (41), (42) and (44) respectively. When the complete Al₂O₃ layer is converted the final dissolution of Al starts via the oxidation reactions given by equation (43) and (45).

Reported by Vedder et al. [88], the corrosion of Al over this mechanism starts with the dissolution of the protective oxide layer at a dissolution rate of approximately 0.6

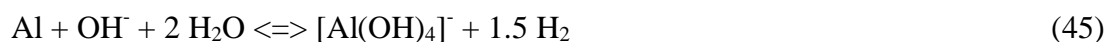
nm/min (KClO₄, 50°C). Diggle et al [89] found dissolution rates of 0.3*10⁻³ nm/s to 0.8*10⁻³ nm/s for H₂SO₄ and HCl based aqueous solutions at 25°C. Both Vedder and Diggle state that the rate determining step is the formation of the Al(OH)₃ according to equation (40) which is only slightly dependent on pH value in the range pH 1 to 10 based on their experimental results.



Acid aqueous milieu:



Alkaline aqueous milieu:



The dependency on pH value is due to the reactions of the aluminium hydroxide to form an Al³⁺ salt in acid milieu as shown in equation (41) and (42) or to form a tetrahydroxoaluminate complex according to equation (44). Those three reactions are also reported as dissolution of the Al(OH)₃ by Dyer et al [90] and are strongly pH dependent. According to Dyer the solubility difference is 7 orders of magnitude comparing the solubility of Al(OH)₃ at pH 3 being 0.1 wt% Al versus the solubility at pH of 6 being 10⁻⁸ wt% Al . At the alkaline side the solubility increase of Al(OH)₃ is still 6 orders of magnitude in the range pH 6 to 13 up to for example 0.1wt% of Al at pH 13.

Furthermore, anions such as Cl⁻ or F⁻ increase the dissolution rate via the formation of AlOCl or AlOF as shown in equations (46 a and b), reported also by Vedder [88] and Diggle [89].





Considering values of Al_2O_3 dissolution rates published by Vedder [88] and Diggle [89], the activation of the Al surfaces of the device during the A2 deposition process is very limited. The acidic activation consisting of an aqueous MSA at 25°C for 15s will only be able to dissolve only less than 0.05 nm of Al_2O_3 . Even during the A2 deposition in the A2 electrolyte at 60°C for 20s at a $\text{pH} > 10$ the dissolved thickness will be less than 1 nm. Therefore either a modification of the Al surface is required or a more reactive chemistry has to be used which will be discussed in sections 4.1.5.2 and 4.1.5.3 later.

Corrosion of Al-1Si-0.5Cu and Al in the device

Specifically, for Cu containing Al alloys such as Al-1Si-0.5Cu alloy grain boundary corrosion is known that can happen at Si or Al_2Cu grains [85] forming during sputtering of the metallisation. Those grains are precipitating because the Si and Cu concentration in the alloy exceeds the solubility limit that is 0.01wt% for Si and 0.1wt% for Cu at 20°C.

In addition, contact corrosion is known for Al having contact to more noble metals such as Cu or Ni. This is to be considered for example for Cu wirebonding technology on Al metallisations and for Al wirebonding technology on the NiP surface of the leadframe. Contact corrosion can lead to a significant loss of Al of the metallisation and of the bondwire, in figure 38 an example is shown for the corrosion of an Al wire at a NiP surface. On the right side a cross section of an Al wire contact on a NiP plated leadframe is shown with a corroded channel at the interface between NiP and Al. On the left side the contact corrosion mechanism is sketched.

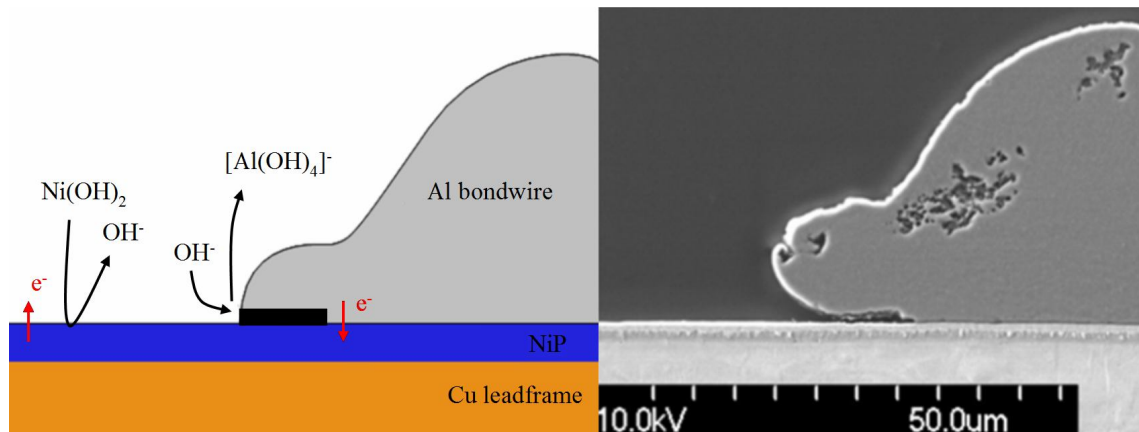


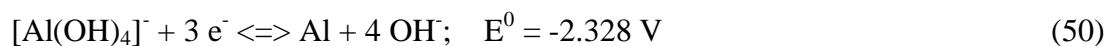
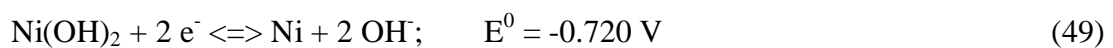
Figure 38: Mechanism of Al etching during contact corrosion at a Al / NiP contact between the NiP coated leadframe and the Al bondwire. The sample on the left side was taken after a total exposure of 60 s to A2 chemistry at 50°C.

During this contact corrosion the large surface area of the NiP is acting as a counter electrode for the small Al wire leading to an increase of the dissolution rate of the Al especially at the interface between the two metals. At the cathode Ni^{2+} is reduced according to equations (47) and (49), at the anode Al is dissolved shown in equations (48) and (50) for acidic and alkaline milieus, respectively.

Acidic milieu:



Alkaline milieu:



This adds to a corrosion potential of approximately -1.41 V for the acid milieu and -1.61 V for alkaline solutions which leads to higher dissolution rates at contact points as shown in figure 38. That is a major reason that the activation of the Al prior or at A2 deposition with harsh chemicals providing higher reactivity towards Al_2O_3 is limited by the entailing corrosion of the Al wires and of the Al metallisation.

4.1.5.2 Activation of Al₂O₃ with an Ar/CF₄ plasma process

It was indicated already that Al₂O₃ is very stable towards attack from the acidic chemistry used in the MSA activation section of the A2 process. Furthermore also the exposure to the alkaline A2 electrolyte brings no satisfying dissolution rates. A possibility to activate the Al-1Si-0.5Cu metallisation of the chip is to modify the Al₂O₃ layer to be more reactive to aqueous solutions of MSA or NaOH.

During manufacturing of the chip metallisations several lithographic steps are done including plasma etching processes with various process gases. An option is the use of an Ar / CF₄ gas, because it is known that with Ar any organic contaminations can be removed. In addition, reported by Ramos et al. [91] and Cunge et al. [92], plasma processes using CF₄ in the process gas are generating fluorinated Al-F-O compounds. In these works the focus was the Al chamber wall of plasma etching equipment forming AlF₃ which can lead to blistering and process instability in this case. Both authors found species such as AlF₃ and AlOF within the Al₂O₃ in significant high concentrations. Both species are known to be stable and especially AlF₃ has a significant solubility in aqueous milieu. At a temperature of 25°C solubility of AlF₃ in water is 0.5 wt% and reaches 0.8 wt% at 50°C as reported by Lide [54]. Dan's et al [2] published a solubility of AlF₃ of even 0.4 wt% at 20°C in water. With the formation of AlF₃ in the Al₂O₃ at the plasma process the ability to passivate Al by its stable oxide gets lost. Al surfaces treated in this way are known to be more prone to corrosion compared to Al with a pure Al₂O₃ protection layer, published for example by Alberici et al. [93]. The authors claimed the formation of various species in the Al oxide such as AlF₃·xH₂O (aluminium fluoride hydrate), Al(OF)_x, and AlF(OH)₂ which can act as precursor for the easy formation of Al(OH)₃ in aqueous milieu following equation (51).



The obtained Al(OH)₃ readily dissolves in either acidic or alkaline aqueous solution as discussed above following equation (41), (42), and (44), respectively. This fluorine induced corrosion was also reported by Ernst et al. [94] using a CF₄ / O₂ gas mixture for the plasma process. Thomas et al. [95] used CHF₃ and CF₄ / H₂ mixtures observing Al oxyfluorides and Al carbides.

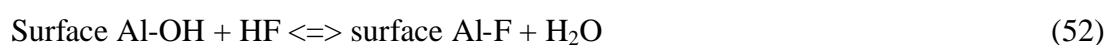
In contrast to the reactivity of AlF_3 and AlOF in aqueous solutions both species are thermally stable in gaseous environment. Yamai et al [96] published a temperature of 1400°C for the hydrolysis of AlF_3 in Ar with a partial pressure of water of about 0,1 bar. This means that an Al surface conditioned in this way is stable also within the downstream processes such as during the chip soldering process at 400°C in forming gas atmosphere as discussed in section 4.1.1. It will be shown in the experimental section that the conditioning of the Al-1Si-0.5Cu chip metallisation with a plasma consisting of a Ar / CF_4 gas mixture is effectively increasing the reactivity of the Al oxide layer to achieve an activation in the alkaline electrolyte of the A2 process with exposure times of less than 20 s in the standard A2 electrolyte at 50°C at a $\text{pH} \geq 13$.

4.1.5.3 Activation of Al_2O_3 with aqueous HF / MSA chemistry

A second method of activating the Al surface for proceeding with A2 deposition is the use of aqueous HF directly inside the A2 equipment, preferably in a mixture with MSA. Due to disadvantages of the plasma conditioning with Ar / CF_4 which will be discussed in the experimental section 5.2.3 and 5.2.4 the use of HF as an activation chemical was also checked.

The use of HF in aqueous solutions is reported by several authors and also in use in industry. For example Jelinek [13] suggests solutions of HNO_3 (30 wt %) and HF (10 wt %) to activate Al prior to tin or zinc deposition, Wernick [86] proposes a mixture of NH_4F (105 g/L), HF (56 g/L), HNO_3 (15 g/L) and PbNO_3 (0.03 g/L) as an acid etch cleaner of Al surfaces. One example for such an industrial solution is the "Aluminiumbeize AL-B" from the company Schloetter [97].

As already discussed, anions like F^- or Cl^- are known to have a very strong influence to the dissolution rate of Al_2O_3 , Grauer [98] explains this effect with the formation of surface complexes in aqueous solution at the oxide - solution interface. In a first step in aqueous solution the oxide surface is covered by hydroxyl groups. Those hydroxyl groups are being exchanged with fluoride F^- ions following equation (52).



Furthermore Grauer [98] suggests the formation of fluoride complexes (surface- AlF_2) at the surface and finally leading to formation and dissolution of AlF_3 . This model was confirmed by Zutic et al. [99] with studies on the dissolution kinetics of hydrous alumina in the pH range 3 to 6 reporting a transport control reaction of the Al_2O_3 dissolution at HF concentrations from $5 \cdot 10^{-6}$ to 10^{-3} mol/L and at pH values of lower than 4. At pH 6 Zutic et al. found the dissolution rate being independent from mass transport. These authors explained this unique increase of dissolution rate with the ability of F^- ions to substitute O^{2-} ions in the Al_2O_3 due to nearly identical ion radii of $r_{\text{F}^-} = 140$ pm and $r_{\text{O}^{2-}} = 136$ pm, respectively. The equation for the complete reaction scheme can be summarized as follows (equation (53)).



The diffusion coefficient of F^- in aqueous solution at pH 3 for the transport controlled dissolution of Al_2O_3 given by the authors is $D_{\text{F}^-} = 1.4 \cdot 10^{-5} \text{ cm}^2\text{s}^{-1}$. The activation in the A2 process is done with a mixture of 12.5 wt% MSA and 0.1 wt% HF at 25°C. An estimation of the dissolution rate can be done with Fick's first law of diffusion as shown in equation (54)

$$J = -D \text{grad } c \quad (54)$$

where D is the diffusion coefficient with the dimension of cm^2/s and $\text{grad } c$ is the gradient of the concentration of the diffusing species in the x-, y- and z-direction. J is the diffusion flow with the dimension of $\text{mol} \cdot \text{cm}^{-2} \cdot \text{s}^{-1}$. Considering only a one-dimensional diffusion this simplifies to equation (55).

$$J = -D \frac{\partial c}{\partial x} \quad (55)$$

Assuming a linear diffusion with a linear concentration profile c_i of the F^- ions as shown in figure 39 this further simplifies to equation (56) with $c_{i,\text{bulk}}$ being the F^- ion concentration in the solution and δ being the diffusion layer. The concentration of the F^- ions at $x=0$ is assumed to be zero due to the finding, that the transport of the F^- ions to the surface is the rate limiting step after Zutic et al. [99].

$$J_i = -D_i \frac{C_{i,bulk}}{\delta} \quad (56)$$

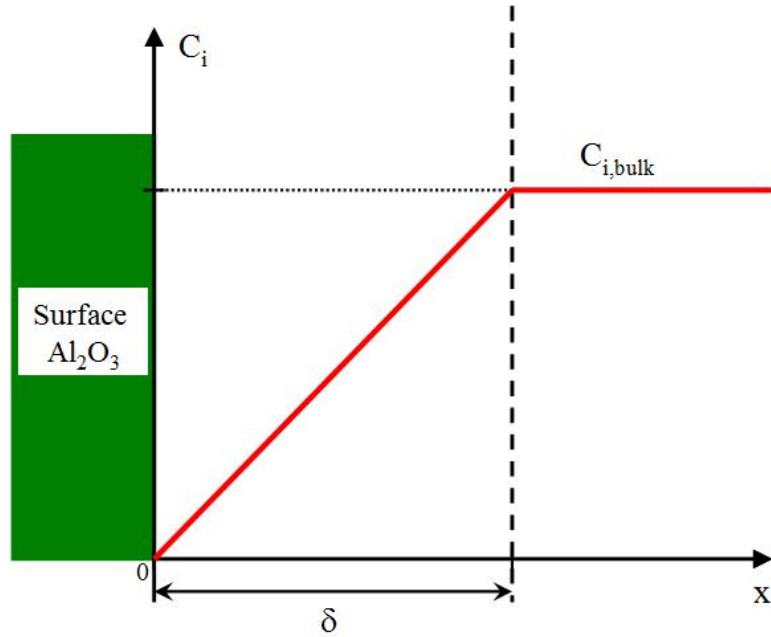


Figure 39: Concentration profile of F^- ions within the diffusion layer during dissolution of Al_2O_3 through HF.

According to reaction in equation (53) for the dissolution of 1 mol of Al_2O_3 leading to 2 mol of AlF_3 an amount of 6 moles of F^- have to diffuse to the surface. To obtain the dissolution rate of the Al_2O_3 ($r_{Al_2O_3}$ / (nm/s)) first the relation between the diffusion flows of F^- , and AlF_3 is given in equation (57), where $J_{Al_2O_3}$ being the diffusion flow of the dissolved Al_2O_3 .

$$J_{Al_2O_3} = \frac{1}{2} \cdot J_{AlF_3} = -\frac{1}{6} \cdot J_F \quad (57)$$

The dissolution rate of the Al_2O_3 is expressed via equation (58) with d being the thickness, V the volume, A the area, n the amount and V_m the molar volume of the dissolved Al_2O_3 layer.

$$r_{Al_2O_3} = \frac{d_{Al_2O_3}}{t} = \frac{V_{Al_2O_3}}{A_{Al_2O_3} \cdot t} = \frac{n_{Al_2O_3} \cdot V_{m,Al_2O_3}}{A_{Al_2O_3} \cdot t} \quad (58)$$

Equation (58) is simplified with $J_{Al_2O_3} = \frac{n_{Al_2O_3} \cdot V_{m,Al_2O_3}}{A_{Al_2O_3}}$ (59).

This leads to $r_{Al_2O_3} = J_{Al_2O_3} \cdot V_{m,Al_2O_3}$ (60).

In addition substituting equation (57) into (60) yields (61).

$$r_{Al_2O_3} = -\frac{1}{6} J_F \cdot V_{m,Al_2O_3} \quad (61)$$

Finally by equation (56) with i being the F⁻ ions the final equation (62) is obtained.

$$r_{Al_2O_3} = \frac{1}{6} \cdot D_F \cdot \frac{c_{F,bulk}}{\delta} \cdot V_{m,Al_2O_3} \quad (62)$$

The following values are taken to estimate the dissolution rate with this equation:

$$D_F = 1.4 \cdot 10^{-5} \text{ cm}^2/\text{s} \text{ (Zutic et al. [99])}$$

$$c_{F,bulk} = 0.05 \text{ mol/L (specified concentration of HF in MSA)}$$

$$V_{m,Al_2O_3} = 25.2 \text{ cm}^3/\text{mol}$$

$$\delta = 10 \mu\text{m} = 10^{-3} \text{ cm (estimation according to Wedler [100])}$$

A dissolution rate of $r_{Al_2O_3} = 29.4 \text{ nm/s}$ is calculated. Discussion of the used values shows, that the diffusion coefficient proposed by Zutic et al. [99] is rather large compared to the value reported by Dan's et al [2] being $D_F = 0.64 \cdot 10^{-5} \text{ cm}^2/\text{s}$ ¹. In addition the value for δ for the diffusion layer in the activation bath of the A2 process is most probably larger because there is no direct flow of the solution towards the substrate. As an upper limit therefore a value of $\delta = 5 \cdot 10^{-2} \text{ cm} = 500 \mu\text{m}$ can be assumed as reported by Hamann and Vielstich [101] for calm solutions.

¹ : The authors report a diffusion coefficient of $0.45 \cdot 10^{-5} \text{ cm}^2/\text{s}$ for infinite diluted aqueous KF solution and $2.3 \cdot 10^{-5} \text{ cm}^2/\text{s}$ for a concentration of 0,5 mol/L. The linear approximation yields a diffusion coefficient of $0.64 \cdot 10^{-5} \text{ cm}^2/\text{s}$ for a solution of 0,05 mol/L KF.

In the worst case both factors add up to a dissolution rate of only $r_{Al_2O_3} = 0.26$ nm/s. For the activation time of 15s this means an Al_2O_3 thickness of 3.9 nm is removed.

To sum up as a minimum dissolved Al_2O_3 thickness 3.9 nm and as a maximum a thickness of 441 nm are obtained. The lower value of the dissolved layer is in the range of the Al_2O_3 thickness measured for a not conditioned Al metallisation surface being 4.6nm (see section 5.2.3). Therefore for the conditioning of the Al metallisation an Ar/ O_2 plasma was used to reduce the thickness of the Al_2O_3 layer and in addition to generate a fluorine free and stable Al metallisation. This will be not further discussed here but shortly touched again in the experimental section in section 5.2.5.

Summary for aluminium activation

The Al metallisation Al-1Si-0.5Cu of power semiconductor is a very important terminal to the package and adhesion at this terminal is highly important for the reliability of the device. Proper activation of the Al surface for A2 deposition therefore is essential. In atmosphere Al forms a very stable Al_2O_3 passivation layer with a thickness up to 2 nm and in the thermal down stream processes a thickness up to 5 nm. This thickness cannot be removed easily via an acidic treatment with MSA.

Al has an outstanding corrosion resistance without any dissolution of the amorphous Al_2O_3 between pH 4.5 to 7 [85] and with a maximum dissolution rate of 0.06 nm/min in the ranges of pH 1-4.5 and pH 7-10, respectively [88]. In contrast, as soon as the Al_2O_3 protective layer is removed a strong corrosion of the Al results due to a low standard potential of $E_0 = -1.662$ V in aqueous solution. Local corrosion caused by contacts to other more precious metals has to be considered, such as the contact corrosion of an Al / Ni contact.

A possibility of decreasing the stability of the Al_2O_3 layer is the incorporation of fluorine via a plasma process on the wafers consisting of an Ar/ CF_4 gas mixture. During this process the Al_2O_3 layer is forming AlF_3 which has a solubility of up to 0.5 wt% in water and is easily hydrolysed to form $Al(OH)_3$, the species that finally dissolves in acid or alkaline aqueous solutions. The solubility of the $Al(OH)_3$ is strongly dependent on pH value and can reach 0.1 wt% Al at pH 3 and even more underneath this pH value. In spite of the reactivity of such AlF_3 containing Al oxide layers in aqueous solutions the

stability in gaseous environment is high yielding a stable surface at all thermal downstream process in production. The dissolution of the fluorinated Al oxide layers is finally done inside the A2 deposition cell through the alkaline electrolyte with a pH value of $\text{pH} > 13$.

A second possibility is the activation of the Al through dissolution of the Al_2O_3 with a mixture of HF and MSA in aqueous solution directly during the A2 process in the acidic activation part. Fluoride ions form complexes with the Al_2O_3 surface and finally also form AlF_3 which can be dissolved in the acidic solution. For this dissolution the rate determining step is reported to be the F diffusion to the surface [99]. Calculation based on a linear diffusion model and based on literature data yields a dissolution rate of at least 0.26 nm/s which is two orders of magnitude higher compared to the dissolution of an Al_2O_3 layer in acidic solution without the addition of HF.

4.2 Theory of the electrochemical deposition of a porous layer

In this chapter basic theories for the deposition of a porous and sponge like layer with a typical electrolyte used for A2 deposition are discussed based on theoretical considerations and based on literature findings. First, theories for electrochemical processes are discussed, and then chemical aspects including equilibria of the A2 electrolyte are elaborated. Finally, some difficulties of deposition kinetics and alloy deposition are discussed for the A2 electrolyte comparing it to similar electrolytes. In addition, the mechanisms for the formation of the sponge like A2 layer are considered starting from a theoretical perspective.

4.2.1 Basics for electrochemical deposition

In this section basic laws considering electrochemical equilibria and kinetic mechanisms at electrode surfaces are summarized. For further reading showing the derivation of the discussed and used equations the following authors may be consulted: Bard and Faulkner [105], Hamann and Vielstich [101, 104], Paunovic and Schlesinger [102], and Fisher [103].

4.2.1.1 Electrode potential and overpotential

An electrochemical cell consists of a cathode, an anode and a compartment for the electrolyte between the electrodes. Sometimes, the electrolyte compartment is divided into two different compartments by a diaphragm to separate two different electrolytes for two different electrochemical processes at the cathode and the anode, respectively, as shown for a Daniell element in figure 40. Figure 41 shows the equivalent circuit of this cell.

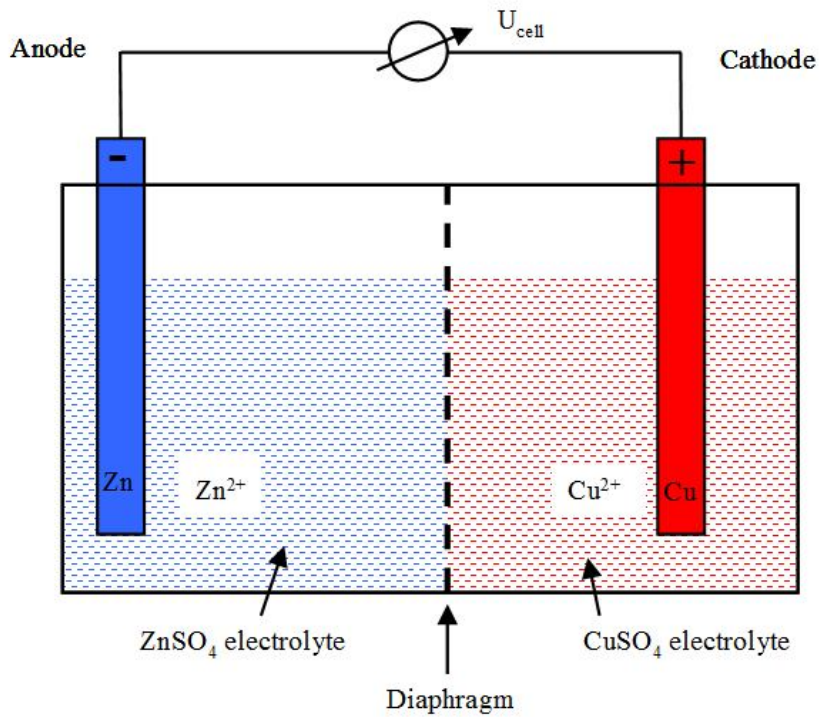


Figure 40: Principle of a Daniell element as an example for an electrochemical cell.

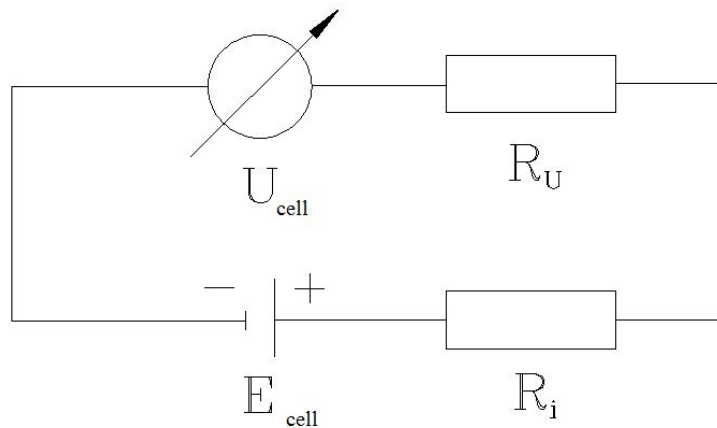


Figure 41: Equivalent circuit of the Daniell cell shown in figure 40.

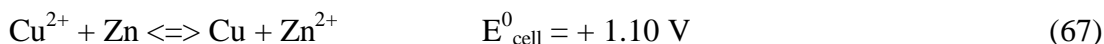
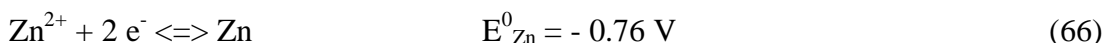
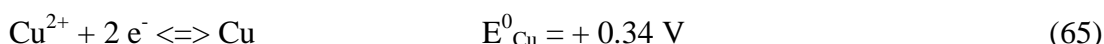
The anode of this cell is Zn-metal in contact with aqueous ZnSO_4 solution, the cathode is a Cu electrode in contact with an aqueous CuSO_4 solution. When the electrodes are connected to a voltage meter the voltage of the cell U_{cell} can be measured. E_{cell} is the equilibrium voltage, the so called electromotive force of the cell, that can be approximately measured with a voltage meter with a very high inner resistance R_U so

that the current I is nearly zero. R_i is the inner resistance of the cell. Therefore from equation (63) the approximation (64) is obtained.

$$U_{\text{cell}} = E_{\text{cell}} - IR_u - IR_i \quad (63)$$

$$U_{\text{cell}} \approx E_{\text{cell}} \quad (64)$$

The two equilibria (65) at the anode and (66) at the cathode without current flow combine also to the overall reaction (67) that takes place, when the electrodes are connected.



In equilibrium under standard conditions the cell voltage U_{cell} is the difference between the two half cell potentials E_{Cu}^0 and E_{Zn}^0 giving E_{cell}^0 . The half cell potentials are the standard potentials of the respective reduction and oxidation equilibria see equation (65) and (66). In table 14 some E^0 values that are used in this work are listed for standard conditions i.e. $T=298.15\text{K}$, $p=1013.25 \text{ mbar}$ and for an activity of the dissolved metal of $a=1$.

The values of the standard potentials are given relatively to the normal hydrogen electrode (NHE, SHE)¹ as a reference electrode. The standard potential of this reference electrode is fixed to zero volts per definition. All equilibria with a positive value of E^0 are oxidizing; all with a negative E_0 are described as reducing materials.

¹ : A NHE, also SHE consists of a platinum electrode in aqueous HCl. It is used as a standardized reference electrode at an activity of protons $a(\text{H}^+)=1$. During the measurement H_2 is bubbled onto this electrode at $T=298.15\text{K}$ and $p=1013 \text{ mbar}$.

Electrochemical equilibrium	Standard potential E^0 (V)
$\text{Ag}^+ + \text{e}^- \rightleftharpoons \text{Ag}$	0.800
$\text{Cu}^{2+} + 2 \text{e}^- \rightleftharpoons \text{Cu}$	0.342
$2 \text{H}^+ + 2 \text{e}^- \rightleftharpoons \text{H}_2$	0.000
$\text{MoO}_3 + 6 \text{H}^+ + 6 \text{e}^- \rightleftharpoons \text{Mo} + 3 \text{H}_2\text{O}$	0.075
$\text{CrO}_4^{2-} + 4 \text{H}_2\text{O} + 3 \text{e}^- \rightleftharpoons \text{Cr}(\text{OH})_3 + 5 \text{OH}^-$	-0.130
$\text{V}(\text{OH})_4^+ + 4 \text{H}^+ + 5 \text{e}^- \rightleftharpoons \text{V} + 4 \text{H}_2\text{O}$	-0.254
$\text{Zn}^{2+} + 2 \text{e}^- \rightleftharpoons \text{Zn}$	-0.762
$\text{Zn}(\text{OH})_4^{2-} + 2 \text{e}^- \rightleftharpoons \text{Zn} + 4 \text{OH}^-$	-1.199
$\text{Zn}(\text{OH})_2 + 2 \text{e}^- \rightleftharpoons \text{Zn} + 2 \text{OH}^-$	-1.249
$\text{Cr}(\text{OH})_3 + 3 \text{e}^- \rightleftharpoons \text{Cr} + 3 \text{OH}^-$	-1.480

Table 14: Standard potential of various electrochemical equilibria that are used in this work, taken from Lide [54]

The dependence of the equilibrium potential of a given redox system, such as for Zn/Zn^{2+} on the concentration of the metal ions in the electrolyte and on the temperature is described by the Nernst equation which is derived thermodynamically from the chemical potential μ and the free enthalpy of reaction ΔG_R . A detailed derivation was given for example by Hamann and Vielstich [104] or by Paunovic and Schlesinger [102]. For the given example of a Daniell element shown in equation (68) the following equation (69) is obtained. With the activities of the metals being $a = 1$ per definition finally equation (70) is obtained. R represents the universal gas constant, T the temperature, z the number of transferred electrons, F is the Faraday constant, a is the activity of the respective species and ν is the stoichiometric factor which is 1 in the given example for each species.

$$E_{\text{cell}} = E^0_{\text{cell}} + \frac{RT}{zF} \ln \prod_i a_i^{\nu_i} = E^0_{\text{cell}} + \frac{RT}{zF} \ln \frac{a_{\text{Cu}^{2+}} \cdot a_{\text{Zn}}}{a_{\text{Cu}} \cdot a_{\text{Zn}^{2+}}} \quad (69)$$

$$E_{\text{cell}} = E^0_{\text{cell}} + \frac{RT}{zF} \ln \frac{a_{\text{Cu}^{2+}}}{a_{\text{Zn}^{2+}}} \quad (70)$$

The activity of a species B is given by equation (71) where $\gamma_{c,B}$ is the activity coefficient of B at a given molar concentration c_B and c_B^0 is the standard concentration.

$$a_{c,B} = \gamma_{c,B} \cdot \frac{c_B}{c_B^0} \quad (71)$$

Following this example for the calculation of the half-cell potential E_{Zn} for zinc shown in equation (66) equation (72) can be used which will be further discussed in chapters 4.2.1.4 and 4.2.6 on deposition of alloys.

$$E_{Zn} = E^0_{Zn} + \frac{RT}{zF} \ln a_{Zn^{2+}} \quad (72)$$

To leave the equilibrium conditions of the given example towards the direction of deposition of Zn an overpotential η to the equilibrium potential E_{Zn} has to be applied given by equation (73) leading to the applied deposition potential U_{dep} of a potentiostat shown in figure 42. This three electrode setup consists of the Zn-electrode (cathode) as the working electrode, the Cu electrode (anode) as the counter electrode and the reference electrode, determining the required potential U_{dep} for the deposition. Of course, the potential U_{pot} delivered by the potentiostat (the voltage difference between the working and the counter electrode) is much larger than the potential U_{dep} .

$$U_{dep} = E_{Zn} + \eta \quad (73a)$$

$$\eta = U_{dep} - E_{Zn} \quad (73b)$$

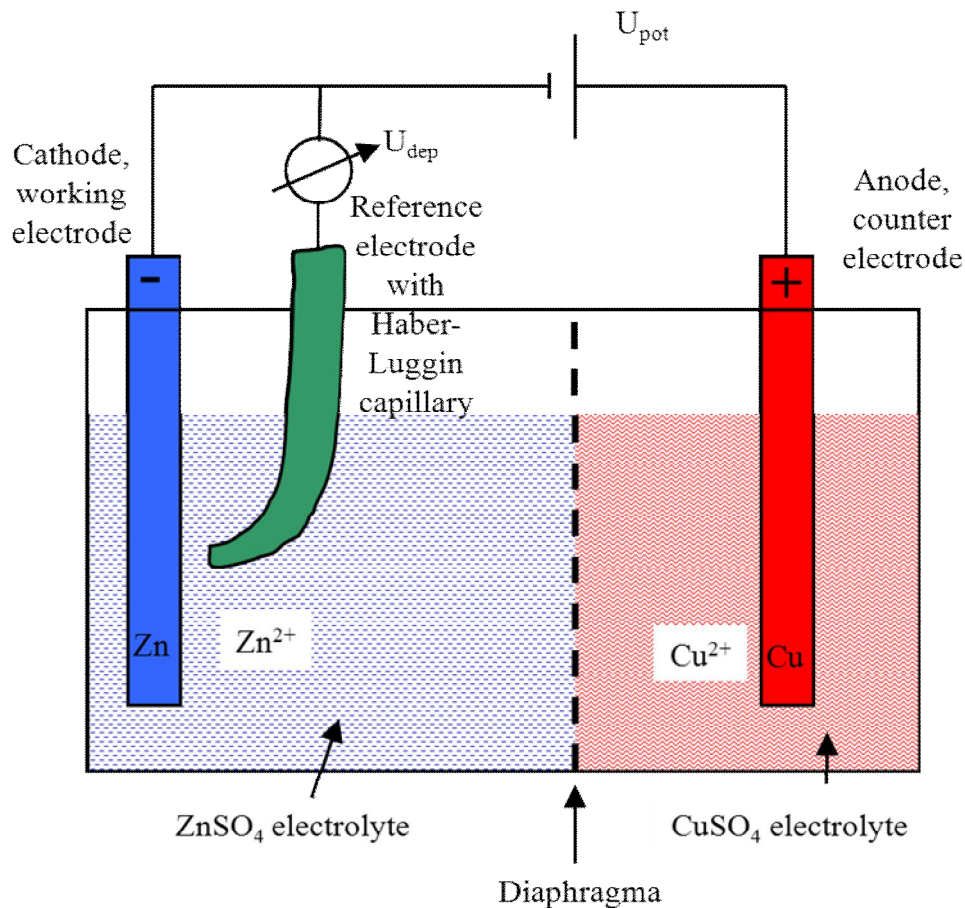


Figure 42: Three electrode setup of a Zn/Cu element with a reference electrode, a working electrode and a counter electrode.

The applied voltage for depositing of zinc U_{dep} is symbolized by a high Ohmic potentiometer via a reference electrode that is placed nearby the Zn electrode with a Haber-Luggin capillary to minimize Ohmic losses through the electrolyte conductivity. U_{pot} symbolizes the potential delivered by the potentiostat in order to obtain the selected potential U_{dep} vs. the potential of the reference electrode. For potentials of highly reversible reference electrodes see the cited standard books for electrochemistry.

In most cases of depositions there are various overpotentials η_x that sum up to a total overpotential η required to drive the equilibrium into one direction. Overpotentials are often also called polarization. Revie and Uhlig [87] noted three causes of polarization, other authors like Hamann and Vielstich [101] and Paunovic and Schlesinger [102] describe additional causes, in summary the following five cases are described:

1. The Ohmic potential drop is due to the limited electrolyte conductivity and to surface layers with Ohmic resistance leading to Ohmic losses between the working and the reference electrode.
2. The concentration polarization (diffusion overpotential) results from a drop of the metal ion concentration at the electrode surface during deposition of the metal. This polarization is related to diffusion and mass transport and will be discussed in section 4.2.1.3.
3. Reaction polarization happens from slow electrode reactions and from a kinetically induced inhibition of the surface by upstream equilibria, i.e. adsorption, complex decomposition or desorption reactions.
4. Crystallization overpotential is caused by deposition of a selected metal on another metal because both crystal lattices of both metals are not fitting, therefore crystallization of the deposited metal is inhibited; it is zero for electrodeposition of metals at the same metal.
5. Charge transfer polarization describes the electron transfer inhibition at the interface of the ion medium and the electron medium.

Especially for the overpotentials of point 3-5 the electrode material plays an important role. This can be seen when comparing the hydrogen overpotentials η_{H_2} required to develop hydrogen at various electrode materials as summarized in table 15. In addition the exchange current density j_0 is given there as defined by the Butler-Vollmer equation, see chapter 4.2.1.2.

Metal	Solution	j_0 [mA/cm ²]	η_{H_2} at 1 mA/cm ² [V]
Pt	1 N HCl	1	0.00
Pd	0.6 N HCl	0.2	0.02
Ag	0.1 N HCl	$5 \cdot 10^{-4}$	0.30
Ni	0.1 N HCl	$8 \cdot 10^{-4}$	0.31
Cu	0.1 N HCl	$2 \cdot 10^{-4}$	0.44
Al	2 N H ₂ SO ₄	10^{-7}	0.70
Sn	1N HCl	10^{-5}	0.75
Zn	1 N H ₂ SO ₄	$1.6 \cdot 10^{-8}$	0.94
Hg	0.1 N HCl	$7 \cdot 10^{-10}$	1.10
Pb	0.01-8N HCl	$2 \cdot 10^{-10}$	1.16

Table 15: Hydrogen overpotential η_{H_2} and exchange current density of various metal electrodes for hydrogen evolution after Revie and Uhlig [87].

Various electrode materials are limited concerning the deposition of metals when their standard potential is above the deposition potential of hydrogen. Instead, hydrogen evolution may replace metal deposition or at least the current yield is decreased. For example, the deposition of zinc on a zinc electrode in aqueous solution is only possible adequately due to the high overpotential of hydrogen at zinc surfaces reaching a value of $\eta_{H_2} = 0.94V$. This means only at $U < -0.94 V$ hydrogen would evolve which is below the standard potential for the zinc deposition being only $E^0_{Zn/Zn^{2+}} = -0.762V$. For the A2 process on a device with various surfaces such as NiP, Cu, Al, and Pb-2Sn-2.5Sn solder alloy this means that the evolution of hydrogen is changing for every of these surfaces, hence the current efficiency (CE, see chapter 4.2.1.5) is very inhomogeneous along the device surface. Referring to table 15 therefore the CE seems to be lowest at Ni and at Ag, especially for the early stage of the A2 deposition. At a later stage when the first Zn has deposited over the whole device interface the CE will increase.

4.2.1.2 Kinetic mechanism of deposition with reaction control

A further question to be discussed is how fast theoretically the reactions on an electrode surface will happen without considering any mass transport limitation. The relation between the applied overpotential η and the resulting current density j , the Butler-Volmer equation, is based on the Eyring's transition state theory for chemical reactions. It implies both the Nernst equation (vanishing current) and the famous Tafel Gerade relating $\log(j)$ to η .

A general equilibrium at an electrode surface can be described by equation (74) with ox being the oxidized species, i.e. Zn^{2+} and red being the reduced species, i.e. Zn:



Derivation of the relation between applied overpotential η and the resulting current density j for both cathodic and anodic direction of the equilibrium lead to the current density-overpotential equation (75) as described by Bard and Faulkner [105]¹. The first exponential term of the function represents the cathodic reduction whereas the second exponential term represents the anodic oxidation within the redox system. For the case without mass transport limitation the surface concentration of red or ox is approximately equal to the bulk concentration of the respective species ($c_{red}^s = c_{red}$ and $c_{ox}^s = c_{ox}$). Then a specific form of the j - η equation can be obtained, see equation (76).

$$j = j_0 \left\{ \frac{c_{ox}^s}{c_{ox}} \exp\left[\frac{-\alpha z F}{RT} \eta\right] - \frac{c_{red}^s}{c_{red}} \exp\left[\frac{(1-\alpha) z F}{RT} \eta\right] \right\} \quad (75)$$

$$j = j_0 \left\{ \exp\left[\frac{-\alpha z F}{RT} \eta\right] - \exp\left[\frac{(1-\alpha) z F}{RT} \eta\right] \right\} \quad (76)$$

In equations (75) and (76) the following parameters and constants are used:

F: Faraday constant (96485.3 As/mol),

z: Number of transferred electrons

α : Transfer coefficient

R: Universal gas constant (8.3145 J/(mol·K))

T: Temperature [K]

c_{red}^s and c_{ox}^s : Concentration of the reduced and the oxidized species at the electrode surface, respectively [mol/L]

c_{red} and c_{ox} : Concentration of the reduced and the oxidized species in the bulk electrolyte, respectively [mol/L]

¹ : The derivation is reported in various books, e.g. Bard and Faulkner [105], Hamann and Vielstich [101] and Paunovic and Schlesinger [102] and will not be reproduced here.

j_0 : Exchange current density [A/m²]. This value is given by equation (77) with k^0 being the standard rate [mol/(m²*s)] constant after Fischer [103].

$$j_0 = F \cdot k^0 \cdot c_{red}^\alpha \cdot c_{ox}^{(1-\alpha)} \quad (77)$$

The "Butler-Volmer" equation (75) is valid only for reaction controlled processes excluding mass transport limitations. For the discussion of the polarization behaviour shown in a polarization curve in figure 43 specific approximations can be made.

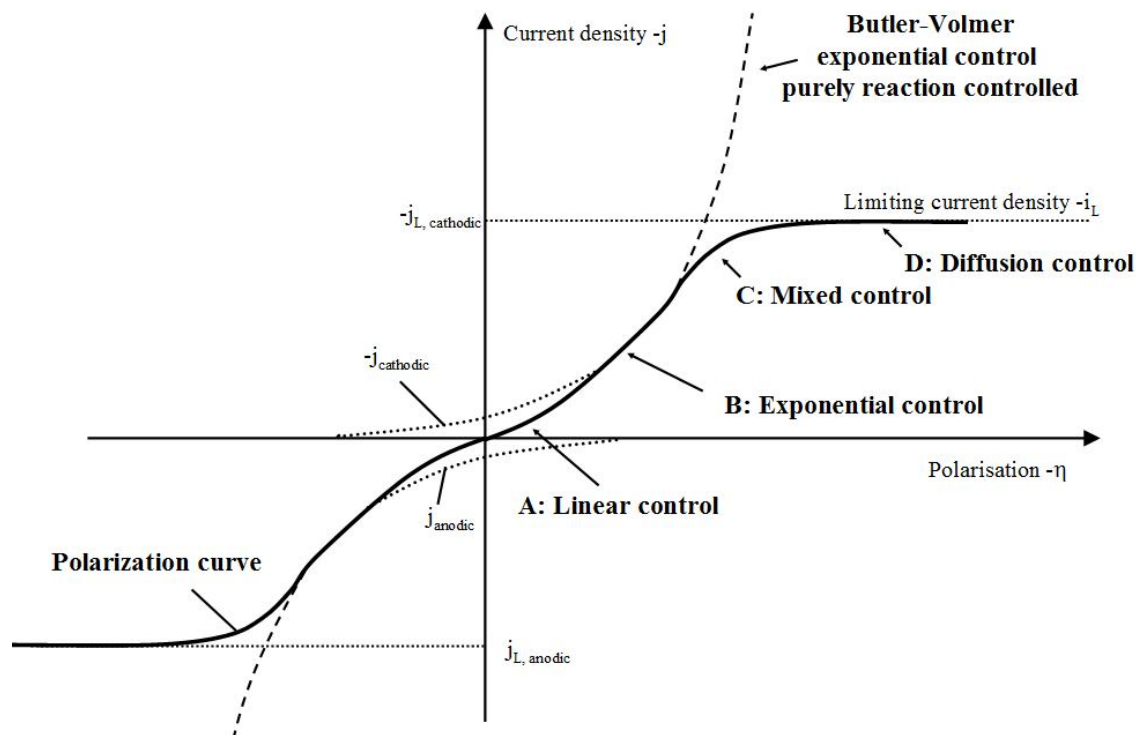


Figure 43: Current - overpotential relationship with 4 kinetical regions of electrode reactions: A-linear control, B-exponential control, C-mixed control, D-diffusion control (reproduced after Paunovic and Schlesinger [102] with signs of current and polarization following recent IUPAC conventions).

Low overpotential: For the first region A of the polarization curve a very low overpotential of $\eta < 10\text{mV}$ is assumed. At this low overpotential diffusion and mass transport is assumed to play no role. Both the cathodic and the anodic reactions are considered. Boundary conditions are $c_{ox}^s = c_{ox}$ and $c_{red}^s = c_{red}$ which means that the concentrations of the oxidized and the reduced species show no difference comparing the surface of the electrode to that of the electrolyte bulk. With the low overpotential $\eta < 10\text{ mV}$ the exponent in equation (75) is getting significantly below a value of 1. Both

exponential functions can be written as power series and only the first order terms as shown in equation (78) are taken. Using the approximation equation (78) for equation (75) results in a linear relation between the current density j and the overpotential η shown in equation (79).

$$e^x = 1 + x + \frac{x^2}{2!} + \frac{x^3}{3!} \approx 1 + x; \text{ (for } x < 1) \quad (78)$$

$$j = j_0 \cdot \frac{zF}{RT} \cdot \eta \quad (79)$$

This equation can be interpreted in terms of Ohms law ($i = \frac{1}{R}U$; $i = j \cdot A$) yielding

$$j = \frac{1}{A \cdot R_{ct}} \eta \text{ meaning that the charge transfer resistance } R_{ct} \text{ is completely determined}$$

by the exchange current density j_0 . As stated by Bockris et al. [106], if j_0 is large at about 10^{-3} A/cm² the electrode process is nearly reversible (nearly no reaction polarization). If j_0 is very small at about 10^{-10} A/cm² the contrary is true. The exchange current density j_0 is a very important parameter for a deposition process. This will be further discussed in chapter 5.3.

Large overpotential: A second approximation can be made for large overpotentials described by region B for negative overpotentials in figure 43 representing the exponential relation between η and j . It is assumed that the overpotential is high enough so that the counter reaction, i.e. the anodic reaction can be neglected and therefore only one direction of the equilibrium reaction can be taken into account. In addition it is necessary that the overpotential is still far away from the region C and D and does not reach any mass transport limitation. The "Butler-Volmer" equation (75) then can be written in a simplified form, for the cathodic direction equation (80) is derived.

$$j = j_0 \cdot \exp\left[-\frac{\alpha z F}{RT} \eta\right] \quad (80)$$

Applying the logarithm derives equation (81) and with conversion from the natural to the decadic logarithm equation (82) introduced by Tafel 1905 [107] is obtained for the cathodic direction.

$$\ln j = \ln j_o - \frac{\alpha z F}{RT} \cdot \eta \quad (81)$$

$$\log j = \log j_o - \frac{\alpha z F}{2.303 \cdot RT} \cdot \eta \quad (82)$$

Arranging experimental data of a polarization curve in the Tafel plot $\log j = f(\eta)$ enables the determination of the kinetic parameters of electrode reactions. The point of intersection of the Tafel line with $\eta=0$ represents the value of the logarithm of exchange current density $\log (i_0)$ and from the slope of the line the value of the transfer coefficient α can be obtained.

4.2.1.3 Kinetic mechanism with mass transport control

Deposition under mass transport controlled conditions means that the surface reactions, e.g. adsorption, charge transfer and electro crystallization are very fast and the transport of the reaction species to the electrode surface or of the products from the electrode surface to the bulk electrolyte becomes the dominating factor and is rate limiting. In the polarization curve shown in figure 43 this mechanism is represented by regions C and D. The mixed control mechanism in region C is a combination of polarization via reaction control and diffusion control. In region D only mass transport limits the current for a given overvoltage at an electrode, i.e. transport through diffusion that is represented by the diffusion laws of Fick¹. For describing the mass transport control of an electrochemical deposition using the first law of Fick, the "Nernst diffusion layer" model can be applied [101, 102] shown in figure 44 representing the steady state condition at the electrode surface.

¹ : Mass transport is represented by diffusion, ion migration and convection which is described by the Nernst-Planck-equation. In this work for simplification only diffusion will be considered. For further reading of the complete description of the mass transport mechanism see Bard and Faulkner [105] or Hamann and Vielstich [101].

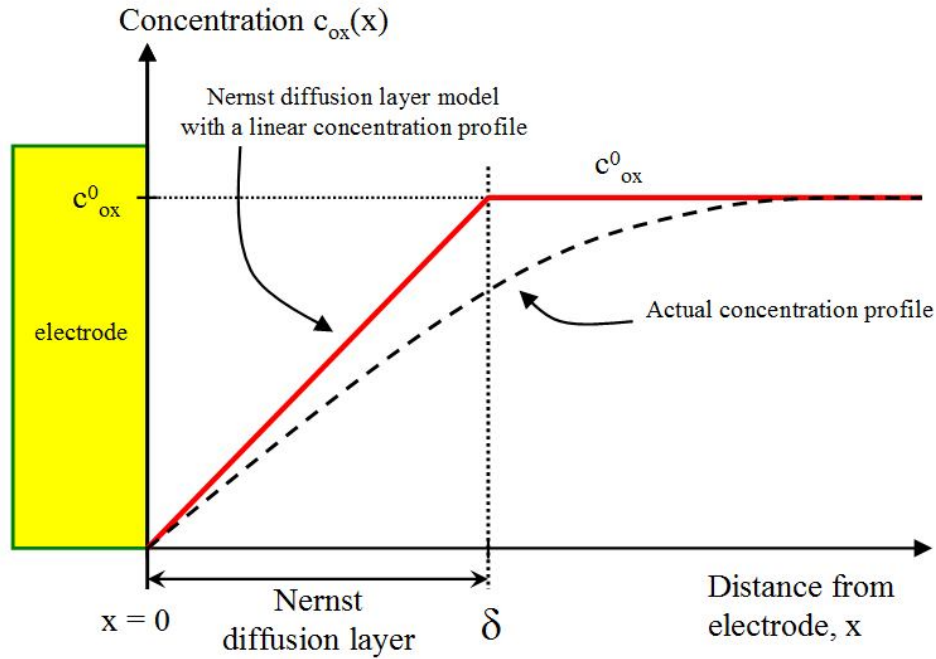


Figure 44: Nernst diffusion layer δ with a linear concentration profile and with the indication of the real concentration profile on an electrode surface under steady state condition [101, 102].

In this model the transport of e.g. the oxidized species ox is described with a simplified version of the 1D version of the first law of Fick shown in equation (83) for diffusion towards the cathode. The simplification assumes a linear concentration profile. In reality this profile is more complex as indicated in figure 44.

$$J = -D \frac{\partial c}{\partial x} \approx -D \cdot \frac{\Delta c}{\Delta x} = -D \cdot \frac{c_{ox}^0 - c_{ox}^s}{\delta} \quad (83)$$

D: Diffusion coefficient of ox; δ : Thickness of the Nernst diffusion layer

c_{ox}^0 : Bulk concentration of ox; c_{ox}^s : Surface concentration of ox

With the equation for the material flow $J = \frac{\Delta n}{\Delta t} \cdot \frac{1}{A}$ and the equation for the current

density $j = \frac{i}{A} = zF \frac{\Delta n}{\Delta t} \cdot \frac{1}{A}$ equation (83) turns to equation (84) showing the relation

between current density j and the diffusion rate of the involved ions.

$$j = -zFD \frac{c_{ox}^0 - c_{ox}^s}{\delta} \quad (84)$$

When the overvoltage η is sufficiently large all oxidized species that reach the electrode are reduced instantaneously so that surface concentration becomes zero ($c_{ox}^s = 0$), e.g. Zn^{2+} is discharged to Zn metal leading to equation (85) for the limiting current density j_L .

$$j_L = -zFD \frac{c_{ox}^0}{\delta} \quad (85)$$

For the case of a galvanostatic deposition of the species ox any current density exceeding this limiting current density j_L will not result in a further increase of the deposition and reduction speed of ox, but in an increase of the electrode polarization until the overpotential of the next possible reaction is reached. For example the decomposition of the solvent such as the reduction of H_2O in an aqueous electrolyte leads to hydrogen formation at the cathode and oxygen formation at the anode.

The complete j - η equation including also the mass transport controlled part is obtained by substituting the j - η equation (75) with the terms (86) and (87) as shown by Bard and Faulkner [105]. This leads to the j - η equation for the complete range of η shown in equation (88) with $j_{L,c}$ being the cathodic and $j_{L,a}$ the anodic limiting current density.

$$\frac{c_{ox}^s}{c_{ox}} = 1 - \frac{j}{j_{L,c}} \quad (86)$$

$$\frac{c_{red}^s}{c_{red}} = 1 - \frac{j}{j_{L,a}} \quad (87)$$

$$j = j_0 \left\{ \left(1 - \frac{j}{j_{L,c}} \right) \exp \left[-\frac{\alpha z F}{RT} \eta \right] - \left(1 - \frac{j}{j_{L,a}} \right) \exp \left[\frac{(1-\alpha) z F}{RT} \eta \right] \right\} \quad (88)$$

Because many metal deposition processes, such as Zn deposition and the A2 deposition, are under galvanostatic ($j=\text{const.}$) control, this mechanism will be further discussed in terms of time until a steady state condition and the limiting current density is reached in a deposition process. This discussion will be needed for the experimental interpretations

and the discussion of the models in section 4.2.8, because one model assumes, that dendritic deposition of a metal only starts when the limiting current density j_L is reached.

For calculating the change of the surface concentration c_{ox}^s over time after the start of a galvanostatic deposition ($t = 0$) the first law of Fick cannot be used because it assumes steady state conditions which is not the case at that time. The 1D version of the second law of Fick is applied here as given in equation (89). It describes the change of the concentration c (e.g. c_{ox}) over time t and over the distance x from the electrode surface.

$$\frac{\partial c}{\partial t} = D \frac{\partial^2 c}{\partial x^2} \quad (89)$$

To solve this equation two appropriate boundary conditions and one initial condition is needed. According to Hamann and Vielstich [101] for the case of a galvanostatic deposition¹ the following conditions are appropriate:

The initial condition: At the start of the deposition everywhere at the electrode surface the concentration $c_{ox}(x)$ is identical to the concentration in the bulk electrolyte ($t = 0$; $x \geq 0$; $c_{ox}(x) = c_{ox}^0$).

First boundary condition: After switching on the current the concentration near to the electrode is changing with time but the concentration in the bulk electrolyte remains constant ($t > 0$; $x \rightarrow \infty$; $c_{ox} = c_{ox}^0$).

Second boundary condition: The slope of the concentration profile at the surface of the electrode remains a constant and is related to the constant selected current.

$$\left(\frac{\partial c}{\partial x} \right)_{x=0} = \frac{i}{nFD}$$

With this initial and boundary conditions the solution of equation (89) for the surface of the electrode ($x = 0$) leads to equation (90) [101].

¹ : The derivation of the equation of $c=f(x, t)$ from the second law of Fick for galvanostatic electrolysis is also given by Bard and Faulkner [105].

$$c_{ox}^s(t) = c_{ox}^0 - \frac{2i}{nF\sqrt{\pi D}} \cdot \sqrt{t} \quad (90)$$

From this equation the time can be calculated until the surface concentration has dropped to zero and a steady state condition with the limiting current i_L has been reached ($c_{ox}^s(t) = 0$) shown in equation (91) known as Sand's equation [101, 105]. This time, which is called the transition time τ , is related to the square of the amount of electrons involved in the individual reaction ($\tau \sim (c_{ox}^0 \cdot z \cdot F)^2$) and inversely to the square of the current applied during the deposition ($\tau \sim 1/i^2$) in a calm electrolyte without agitation during the experiment.

$$\tau = (c_{ox}^0 \cdot z \cdot F)^2 \cdot \frac{1}{i^2} \cdot \frac{\pi \cdot D}{4} \quad (91)$$

The consequences of this relation for the A2 deposition will be further discussed in section 4.2.8 related to the models of dendritic and sponge deposition. A calculation of the limiting current density i_L and of the transition time τ will be done dependent on the concentrations of the involved species and will be compared to the experimental data.

4.2.1.4 Deposition of alloys

For electroplating of alloys a co-deposition of two or more different metals is required. Co-deposition of different metals occurs depending on the electrochemical properties of the respective metals such as their standard potential E^0 , their concentrations and their chemical behaviour in solution, e.g. in aqueous solution. In figure 45 the polarization curves of three different metals A, B and C are shown. The metal ions have a minimum deposition potential of φ_A , φ_B and φ_C , respectively including the specific standard potential, the concentration and any polarization required for start of deposition of the individual metal referring to equation (92) reported by Paunovic and Schlesinger [102] and by Vagramyan [108]. For simplification all potentials and currents are written with positive algebraic sign, in contrast to IUPAC definition assigning negative currents and negative potentials to cathodic reactions.

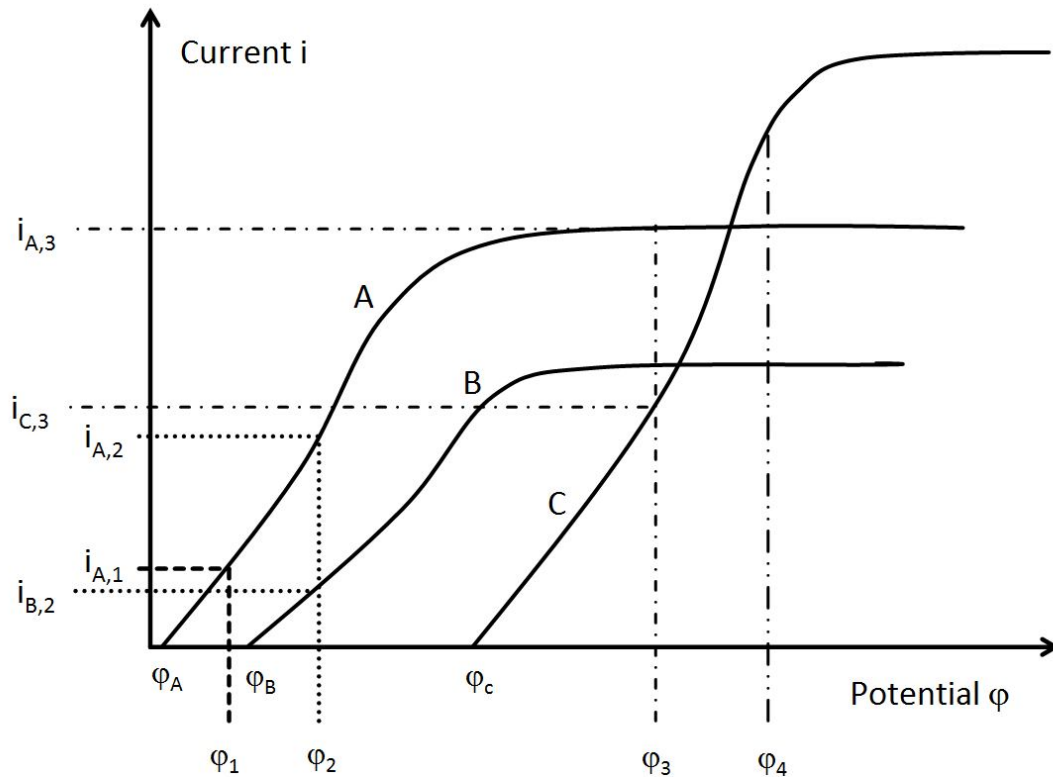


Figure 45: Polarization curves of three different metals A, B and C with three different deposition potentials φ_A , φ_B and φ_C . For descriptive reason the cathodic processes are shown as positive potential and current density.

$$\varphi = E^0 + \frac{RT}{zF} \cdot \ln a - \eta \quad (92)$$

If now a potential of φ_1 is applied only the metal A is deposited with a deposition current $i_{A,1}$. Both metals B and C are not deposited due to their much lower deposition potential. Decreasing the potential to φ_2 entails now also the deposition of metal B. Co-deposition of both metals A and B happens with a total current of $i_2 = i_{A,2} + i_{B,2}$ consisting of the current of deposition of metal A ($i_{A,2}$) and the current of the deposition of metal B ($i_{B,2}$). The composition of the deposited alloy will be roughly proportional to the ratio of both currents (e.g. $x_B \sim i_{A,2} / i_{B,2}$). If the deposition potentials of both metals are far away from each other then it will be very difficult to deposit significant amounts of the metal with the lower deposition potential, e.g. for metal B at a potential of φ_2 . A control of the alloy composition is not possible at a given potential, e.g. the deposition of an alloy consisting of a high amount of metal B.

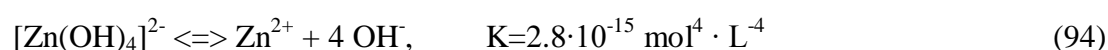
However, there are two possibilities to achieve a specific control of the co-deposition. The first possibility is to narrow the deposition potentials of both metals by adjusting the concentrations of the metal salts. According to the Nernst equation the potential required for the start of the deposition of a metal can be described by equation (92) where E^0 is the standard potential, a is the activity of the metal ions in solution and η is any polarization required for the deposition, to circumvent resistances such as the charge transfer or the reaction polarization.

To narrow the start of deposition of two metals A and B their deposition starting potentials have to be narrowed or even brought to equal. With the prerequisite $\varphi_A = \varphi_B$ equation (93) is obtained [108].

$$E_A^0 + \frac{RT}{z_A F} \cdot \ln a_A - \eta_A = E_B^0 + \frac{RT}{z_B F} \cdot \ln a_B - \eta_B \quad (93)$$

Because E^0 and η are fixed values for both metals A and B due to their electrochemical properties, this approximation can only be achieved with the terms containing the activities a_A and a_B . However, to achieve a significant change of the individual value of a deposition potential φ a large variation of the activity or the concentration is required. For example for Zn^{2+} with $z = 2$ a change of the concentration by a factor of 100 only results in a change of the potential by 58 mV. Such a large change of the concentration is not possible for some metal salts due to the limitation of their maximum solubility in the respective solvent, here generallyly water.

Furthermore lowering the concentration of the other partner by several orders of magnitude is also not practical because the low concentrations will finally lead to a very low rate of the co-deposition of this partner. To obtain large drops in activities of the deposited species it is more efficient to use complexing agents such as cyanide or hydroxide [102, 108]. The formed metal complexes can have very high stability. Therefore they release only a very low amount of free metal ions. However, as they are located at the electrode they can act as a stock for the free metal ions to deliver those to the electrode at a very low activity. One example is given in equation (94) for the zincate equilibrium according to Jelinek [115].



The second possibility of co-deposition of metals with a large difference of the deposition potential is to perform the deposition at a much higher potential indicated in figure 45 as φ_3 for the example of co-deposition of metal A and C. Now metal A is deposited at a constant rate at its limited current density. The rate of metal A is not changing with a variation of the potential, but the rate of metal C changes with this variation. Hence the alloy composition of the alloy $x\text{A}-y\text{C}$ can be controlled with the applied potential. As an example Vagramyan [108] describes the co-deposition of Zn and Cd with equilibrium deposition potentials of -0.76 V and -0.40 V , respectively. According to the author the deposition of ZnCd alloy is done at a potential where the Cd deposition is at its limiting current density and the amount of Zn in the alloy is regulated via slight potential changes in the range, where the Zn deposition is still in the reaction controlled area.

Besides those two simplified models of alloy deposition Vagramyan [108] additionally describes the case of alloy deposition with a coupling between the two metal ions in solution. Also changes of the electrode surfaces during the co-deposition are described. It is necessary to keep in mind that there are more complex processes involved in the alloy deposition as those described in the two models above.

There are for example systems such as Zn-Co alloy which undergo an anomalous deposition meaning that Zn deposition is preferred even though Co is more precious. The mechanisms of this anomaly are not proven yet, but there are indications that formation of $\text{Zn}(\text{OH})_2$ at the surface inhibits the deposition of Co as reported by Paunovic and Schlesinger [102].

This anomaly is also reported for the co-deposition of Zn and Cr from Vagramyan [108] and Schlesinger [114]. There is no co-deposition of Zn in hexavalent Cr electrolytes in spite of the fact that Zn is deposited at much more precious potentials when compared to Cr. Vagramyan [108] in this case describes the formation of a film of chromates and reduction products thereof on the cathode surface to be the reason for this anomaly. In addition also foreign anions such as SO_4^{2-} , SiF_6^{2-} , Cl^- , Br^- , and BF_4^- are suggested to be responsible for this phenomenon according to this author.

4.2.1.5 Current efficiency and concurring reactions

During an electrochemical deposition the mass of the deposited material, e.g. a metal, is proportional to the amount of electrons used for this deposition and therefore proportional to the applied current and the deposition time. Equation (95) describes this relation that is known as the law of Faraday.

$$m = \frac{M}{zF} \cdot i \cdot t \quad (95)$$

m: Mass of deposited metal [mol]

M: Molar weight of the metal [g/mol]

z: Charge of the metal ion

i: Current [A]

t: time [s]

F: Faraday constant; F=96485.3 As/mol

With this law also the thickness of a deposit can be calculated using equation (96) knowing the respective area A of the electrode and the density σ of the deposited metal.

$$d = \frac{1}{\sigma A} \cdot \frac{M}{zF} \cdot i \cdot t \quad (96)$$

Beside the primary deposition reaction electrochemical deposition in most cases involves additional electrochemical reactions such as the co-deposition of other metals present in the electrolyte. In many cases the reduction of the solvent occurs as a side reaction to the primary deposition, e.g. the reduction of water in aqueous solutions leading to the formation of H₂ at the cathode shown in equation (97).



The potential at which this reduction starts depends on the electrode material as described in chapter 4.2.1.1 and is related to the hydrogen overpotential of the specific electrode material. The amount of electrons over a specific time, hence the current used for the primary deposition is lower in this case than the total current. The ratio between the current for the primary deposition and the total current is called current efficiency (98):

$$CE = \frac{i_{\text{primary}}}{i_{\text{total}}} \quad (98)$$

Especially for deposition processes at low metal concentrations and high current density, such as the A2 process the values of CE are rather low. A calculation of CE for the A2 deposition process can be done with equation (99) combining equation (98) and (96) considering only the deposition of pure Zn.

$$CE = \frac{x\rho AzF}{itM} \quad (99)$$

Parameters and typical values in equation (99):

- x: Thickness of the A2 layer (100 nm) ρ : Density of Zn (7.14 g/cm³)
A: Area of substrate (228.4 cm²; TO263-3) i: Current (13.7 A; from j = 60 mA/cm²)
t: Deposition time (20 s) z: Number of electrons (Zn²⁺: z=2)
F: Faraday constant (96485.3 As/mol) M: Molar mass (65.4 g/mol)

With those typical values a CE of 17.5% is obtained. Considering the A2 layer structure that will be shown in chapter 5.3.2 consisting of a 10 nm compact seed layer and of a approximately 90 nm dendritic layer on top of this seed layer the value of CE is most probably by factor 10 lower in the range of 1 to 2 %.

4.2.2 Electrolyte chemistry for A2 deposition and comparison to other electrolytes

The typical composition of the A2 electrolyte is consisting of 12 g/L (300 mmol/L) NaOH, 0.07 g/L (2.5 mmol/L) Si⁴⁺ from Na₂SiO₃, 0.6 g/L (11.5 mmol/L) Cr⁶⁺ from Na₂Cr₂O₇ x 2H₂O and 0.9 g/L (13.8 mmol/L) Zn²⁺ from Na₂Zn(OH)₄ in aqueous solution. Details on the electrolyte preparation are available in chapter 5.3.3.1 table 29. In this alkaline milieu several equilibria of the different species are involved. At this point an approximate comparison can be done already. In the following chapter this comparison will be refined.

Comparing this electrolyte with standard electrolytes used for usual metal plating in industry the concentrations of zinc and chromium are about factor 10 and factor 100 lower in the A2 electrolyte, respectively. Table 16 shows an overview comparing the

metal contents of the A2 electrolyte with standard electrolytes for Zn and Cr deposition and with chromate conversion coating (CCC) solutions used for the passivation of Zn coatings.

Electrolyte solutions	Zinc electrolytes [115]	Cr(VI) electrolytes [114]	Chromate conversion coating solutions [115]	A2 electrolyte
c_{Zn} [mmol/L]	50-300			13.8
c_{NaOH} [mmol/L]	2125-5500			300
$c_{\text{Zn}} / c_{\text{NaOH}}$	1/15			1/22
c_{Cr} [mmol/L]		1000-4000	5-300	11.5
c_{Si} [mmol/L]				2.5
pH	>13	< 2	< 2	>13

Table 16: Comparison of metal concentrations of various electrolytes with the concentrations used for the A2 electrolyte.

For example an alkaline zinc bath for zinc deposition can consist of a Zn concentration of 50 to 300 mmol/L Zn. Plating baths for chromium usually consist of Cr concentrations of 1000 to 4000 mmol/L. Only the Cr concentrations used within the CCCs are in a similar range when compared to the A2 electrolyte, however those solutions are used at rather acidic milieu at $\text{pH} < 2$. From this simple comparison it can be seen that a dedicated discussion is required to theoretically understand the equilibria within the A2 electrolyte because many of the electrolytes used for Zn and Cr deposition deviate strongly from the A2 electrolyte at the first view.

In order to understand the possible deposition mechanisms from A2 electrolyte and the properties of the A2 layer, the chemistry and deposition of the single metals Zn and Cr will be discussed in chapters 4.2.3 and 4.2.4., followed by the ZnCr alloy plating and the chemistry of the very important silicate that is also present in the A2 electrolyte.

4.2.3 The deposition of zinc

Electroplated Zn is widely used in industry and work has been done by many authors since more than 150 years. One reason for the effort on Zn electroplating is the passivation of Zn which makes it suitable as a corrosion protection for other metals, especially of steel [115]. As described by Jelinek [115] the relatively un-noble Zn ($E_0 = -0.763\text{V}$; Zn^{2+}/Zn equilibrium) can only be deposited from aqueous Zn^{2+} solutions due

to the high hydrogen overpotential in aqueous milieu, i.e. 0.72V in acid solutions and 0.70V in alkaline solutions.

It was realized early that Zn deposits easily as a spongy, dendritic morphology in acidic and alkaline electrolytes if the deposition conditions are not well chosen. However, for the Zn electroplating for corrosion protection smooth layers are required. Many efforts have been spent on mainly six electrolyte systems shown in table 17 as reported by Jelinek [115].

pH range	Description	Electrolyte
3.5-4.5	strongly acidic	ZnSO ₄ or ZnCl ₂ based
4.5-5.5	weakly acidic	ZnSO ₄ with NH ₄ ⁺
4.5-5.5	weakly acidic	ZnSO ₄ without NH ₄ ⁺
6.5-7.0	neutral	Zn ²⁺ with NH ₄ Cl
≥12	alkaline	Zn(OH) ₄ ²⁻ with cyanide
≥12	alkaline	Zn(OH) ₄ ²⁻ without cyanide

Table 17: Overview on available Zn electrolyte systems after Jelinek [115].

For aqueous acidic electrolytes the deposition mechanism is the reduction of Zn²⁺ to Zn, the dominant work in literature is available for this pH, but for comparison to the alkaline A2 electrolyte this pH area will not be touched here but will be discussed separately in chapter 5.4.2.2 on investigations on new acidic chromium-VI free electrolytes.

For aqueous alkaline electrolytes various even more complex mechanisms have been reported by several authors, including Epelboin [109], Despic [110] and Cachet [111]. In the further discussion the focus will be on the alkaline electrolytes without cyanide. The mechanism with the most consensus is described in the work of Bockris et al. [112] and was also confirmed by Hendrikx et al [113]. It is also resumed by Schlesinger and Paunovic [114] and Jelinek [115] shown in equations (100), (101), (102), and (103):



Reaction (101) represents the rate determining step slowing down the delivery of Zn(OH)_2^- entailing a dense deposition of Zn. In competition to the Zn deposition H_2 formation occurs because the deposition potential of Zn is more negative as the potential of the starting H_2O reduction [114]. It is also worth mentioning that during the deposition the formation of OH^- leads to a local increase of the pH value at the vicinity of the cathode which is similar during Cr deposition and ZnCr alloy deposition reported in chapters 4.2.4 and 4.2.6, respectively.

Alkaline Zn electrolytes in industry achieve up to 85% of current efficiency (CE) [116] but reducing the concentration of Zn by 30% from 120 to 80 mmol/L decreases the CE to less than 60% [114]. This may explain the low CE of the A2 electrolyte with a concentration of only 13.8 mmol/L being 1 to 2 %.

Besides the low CE a second difficulty for this type of Zn electrolytes is the formation of colloidal, dendritic and sponge Zn at the electrode. Additives are required such as polyvinylalcohol or casein which inhibit the further growth of crystal nuclei entailing the growth of further nucleation of Zn. This results in a smooth layer growth instead of a powdery deposit [115].

Schlesinger [114] indicates the high exchange current density of those electrolytes with values in the range of 20-310 mA/cm². With those high values the surface reaction (101) may not be rate limiting but the limitation may come from the diffusion of the Zn(OH)_4^{2-} ions to the electrode surface. A diffusion controlled deposition mechanism for the deposition of Zn from alkaline electrolytes is described by several authors and on various substrates.

For example Naybour [117] investigated the morphologies of Zn deposits from 5N KOH saturated with ZnO on Zn single crystals at 4 different crystal planes. Naybour used three different current densities 100, 20 and 4 mA/cm² and defined three corresponding morphologies: Dendritic, layer type and mossy, respectively. On the four investigated crystal planes the author found a lower number of nuclei formation on the basal plane compared to the other three crystal planes, but with further growth of the dendrites the substrate did show no influence. Naybour [117] described a 2-step diffusion controlled mechanism for the growth of dendrites:

1. Initial nucleation and deposition influenced by high current density and crystal orientation at low growth rate.
2. Increase of the diffusion controlled deposition growth rate through the penetration of growing dendrites into the Nernst diffusion layer. As the zincate concentration increases in the Nernst diffusion layer also the growth rate of the dendrites increases.

In another work Naybour [118] confirms this model and related the morphology to the applied current density and the bulk electrolyte velocity represented by the Reynolds number (Re)¹ [119]. He defined three morphologies: Flat layer like, bulbous and dendritic. For the shift from flat to bulbous morphology Naybour obtained a linear relation ($i \sim Re^{1.0}$) and for the shift from bulbous to dendritic he obtained other exponents $i \sim Re^{1.1}$ for $Re > 2000$ and $i \sim Re^{0.7}$ for $Re < 2000$. An increasing electrolyte movement reduces the thickness of the Nernst diffusion layer entailing an increase of the concentration gradient of the active (deposable) species. This results in an increase of the limiting current density according to equation (85) that is required to get into diffusion controlled deposition.

A similar mechanism was described by Diggle et al. [120] for the deposition of Zn on Zn electrodes in alkaline milieu. The authors refined and formulated the mechanism of initial dendrite growth as a pyramidal growth from dislocations at the Zn substrate under diffusion control. However, the second step of growing dendrites into and beyond the Nernst diffusion layer was described as activation controlled deposition by Diggle et al. [120]. They reported a critical overpotential in the range of $-75 < \eta_{crit.} < -85$ mV for the initiation of the dendritic growth of Zn. In the concentration range $10 \leq c \leq 200$ mmol/L and in the temperature range $25 \leq \Theta \leq 50$ °C Zn dendrites of a length of up to 600µm were grown over a time of 10 to 60 min. A relation between the applied overvoltage η and the initiation time for dendrite growth was derived that was experimentally and theoretically in quite good agreement. However, for this work neither the length of the dendrites nor the initiation times for dendritic growth of more

¹ : Reynolds number $Re = v \cdot l \cdot \nu^{-1}$: v is velocity of the fluid, ν is its kinematical viscosity, l is the characteristic length of the sample in the fluid, such as the length of a plate with a parallel flow of the fluid to the plate.

than 5 min allows the comparison to the A2 process with resulting dendrite length of less than 100 nm and deposition times reaching less than 10 s.

Also on other substrates the formation of Zn dendrites was found to be under diffusion controlled growth, i.e. Justinjanowic and Despic [121] showed this for a Fe substrate and Popov and Krstajic [122] for Cu. The latter authors stated a critical overpotential $\eta_{crit.}$ of 100 mV for the dendritic Zn deposition on Cu with a $K_2Zn(OH)_4$ concentration of 100 mmol/L. Below $\eta_{crit.}$ a spongy deposit was obtained. From their experiments on Cu the authors also derived a relation between the ratio i_0/i_L and the morphology of the deposit, i_0 is the exchange current density and i_L the limited current density. With $i_0/i_L \ll 1$ a flat Zn through activation controlled deposition and with $i_0/i_L \gg 1$ a dendritic Zn through diffusion controlled deposition is obtained according to the authors.

A more recent study of dendritic Zn deposition was presented by Wang et al. [123] giving also a brief overview on the results of other authors. Wang defined five different categories of morphologies: 1. Heavy spongy; 2. Dendritic; 3. Boulder like (compact); 4. Layer like (compact); 5. Mossy. In this sequence the authors related the morphologies to a decreasing current density. The current density limit for the shift from a compact to a dendritic morphology was investigated as a function of $[Zn(OH)_4]^{2-}$ and KOH concentration, temperature and stirring. In summary the following was stated:

1. The current density for dendritic growth of Zn decreases with decreasing $[Zn(OH)_4]^{2-}$ and increasing KOH concentration.
2. A higher temperature and stronger stirring requires a much higher current density for dendrite initiation.

Based on their results the authors concluded that dendritic Zn growth is purely under diffusion control.

However, in all discussed publications structures are shown with a dendrite thickness of $>1\mu m$ and with length of several μm which differs significantly from the structure known from the A2 layer. Diffusion control plays probably a role during the A2 deposition similar to what is known from pure zincate electrolytes, but it cannot be fully explained with this mechanism. At least three further factors need to be discussed that

are the influence of the strong H₂ development, the inhibition of the surface through other electrolyte components such as the chromate and the role of the silicate in the bulk electrolyte.

4.2.4 The chemistry of chromates and the deposition of chromium

For the discussion of the influence of chromium on the A2 deposition the basic chemistry and deposition conditions for chromium is important. Metallic Cr is self passivating due to the formation of the very stable oxide Cr₂O₃ with $\Delta G_f^0 = -1058$ kJ/mol that is responsible for the high corrosion resistance of Cr. This is similar to the passivation of metallic Al where $\Delta G_f^0 = -1582$ kJ/mol [2] is the corresponding value for Al₂O₃ formation. Chromium forms various oxidation states from -II to +VI, the most important one in aqueous solutions are Cr(II), Cr(III) and Cr(VI) [45, 114]. The trivalent chromium ion is the most stable in aqueous solutions due to formation of various stable complexes such as [Cr(H₂O)₆]³⁺ or [Cr(NH₃)₆]³⁺. Hexavalent chromium is mainly known from chromate and dichromate which are strongly oxidizing agents. In aqueous solution the structure of hexavalent chromium is depending on its concentration and the solution pH value. In dilute solutions the equilibrium shown in equation (104) can be moved into both directions by adjusting the pH value. Moving the equilibrium to the left by adding base brings up a yellow CrO₄²⁻ solution at pH values above 7. By adding acid the dichromate Cr₂O₇²⁻ as an orange solution is obtained between pH 2 to 6.



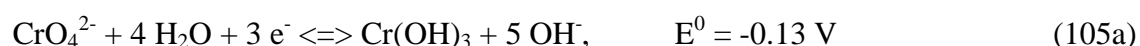
With further lowering the pH value and increasing the concentration further condensation occurs forming trichromate Cr₃O₁₀²⁻, tetrachromate Cr₄O₁₃²⁻ and polymeric chromates, the colour of the solutions turns to deep red [45].

Within the A2 electrolyte with its alkaline pH mainly CrO₄²⁻ exists which will be considered in the discussion of chromium deposition. Most of the chromium deposition in the last 80 years in industry has been done out of strongly acidic electrolytes using CrO₃ as the chromium source. The purposes were corrosion protection of steel, surface hardening and decorative plating [124]. Acid chromium electrolytes based on CrO₃

additionally require at least one catalyst to work properly such as sulphate SO_4^{2-} or silicofluorides SiF_6^{2-} . Typical electrolytes can contain between 1 to 4 mol/L of CrO_3 (100-400g/L) with 1 wt% catalyst at a pH value of $\text{pH} \ll 1$ [114]. Typical deposition conditions require high current density between 50 to 250 mA/cm² and a temperature in the range of 20 to 55°C. Due to the low CE of 10 to 25% strong H_2 development occurs during the deposition.

There is one exception of a chromium electrolyte that is working in the weakly acidic pH region, the tetrachromate electrolyte also known as "Bernhauser" electrolyte. This electrolyte comprises an aqueous solution of 300g/L CrO_3 with 60g/L NaOH, 0.75g/L H_2SO_4 and 0.8g/L ethanol [124, 125, 126] and can be operated at lower temperatures in the range of 16 to 22°C, therefore also known as "cold electrolyte". Due to its lower reactivity it is mainly used for the deposition of Cr on Zn and Al. Furthermore it can be operated at much higher current density of 200 to 800mA/cm² reaching a higher CE of 30 to 37% [124].

Comparing the discussed Cr electrolyte to the A2 electrolyte then no similarity of either the concentration of the dissolved Cr salt not the pH value can be seen. Due to the low concentration of the CrO_4^{2-} of 11.5 mmol/L and the high pH value of $\text{pH} > 13$ according to the equilibrium (104) only the species CrO_4^{2-} is present in the A2 electrolyte. Because of this the co-deposition of Cr with Zn forming the A2 layer is probably happening over equations (105a) and (105b) after Lide [54] for an alkaline aqueous solution, not considering any intermediate steps of the deposition mechanism.



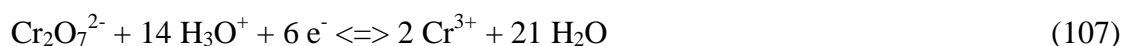
Due to the high pH value and the additional formation of OH^- ions during the deposition of Cr (equations (105a) and (105b)) and of Zn (equations (100) f.f.) at the vicinity of the cathode a further increase of the pH value will happen, therefore the $\text{Cr}(\text{OH})_3$ will stay dissolved as $[\text{Cr}(\text{OH})_6]^{3-}$ [45]. Because the deposition takes place at a very high overpotential with strong H_2 evolution the deposition of the Cr may also happen directly from the CrO_4^{2-} without the formation of the intermediate $[\text{Cr}(\text{OH})_6]^{3-}$ as it is assumed for the typical acidic Cr electrolytes [124, 114, 127]. For the Cr deposition from typical

acidic electrolytes one model is the formation of a cathodic film of porous trichromate that is protected by the catalyst, e.g. SO_4^{2-} . Within this cathodic film the reduction to metallic Cr happens, but it is not fully understood today which reactions are involved [124, 114]. Lausmann and Unruh [128] published that a direct mechanism of reduction of $\text{Cr}_2\text{O}_7^{2-}$ to Cr has a low probability from kinetics point of view because 27 different particles are involved into this reaction. They state that it is much more probable that the reduction happens over several steps forming various Cr(III) and Cr(II) species.

It is worth noting that due to the strong H_2 development it is known that chromium hydrides CrH and CrH_2 are formed primarily during the typical acidic chromium deposition processes. These hydrides decompose into H_2 and Cr metal leading to volume shrinkage of over 15% vol [114]. The formation of hydrogen also entails hydrogen embrittlement of steel. Currently, it is not clear whether formation of Cr hydrides also may play a role during A2 deposition in the alkaline electrolyte.

4.2.5 Chromate conversion coatings (CCCs) on zinc

Besides the electrochemical deposition of Cr there are several chemical deposition processes used in industry called chromate conversion coatings (CCCs). Also for Zn with CCC an excellent corrosion protection can be achieved. Specifically for Zn protection there are various processes leading to transparent, blue, olive or black CCCs with increasing corrosion protection, as reported by Jelinek [115]. CCCs are formed by a redox reaction between Zn metal and $\text{Cr}_2\text{O}_7^{2-}$ in the first step as shown in equation (106) and (107) for the example of an acidic solution.



In addition, Jelinek [115] proposes also the precipitation of ZnCrO_4 to form the final CCC as due to the high proton consumption the pH at the surface rises and at this pH the CrO_4^{2-} ions dominate (equation (104)). CCCs are mainly deposited from acidic solutions, but the process is also known at an alkaline $\text{pH} \geq 13$, where the Zn dissolution can take place and is not leading to precipitation of $\text{Zn}(\text{OH})_2$ [115]. Other authors such as Martyak [129] and Zhang et al. [130] further investigated the chemical composition

of CCCs and found Cr(VI) species in a matrix of Cr, Cr(OH)₃ and Cr₂O₃ with a typical thickness of 400 nm deposited from an acidic solution¹. It is notably that no Zn was observed in the CCC deposited with a Cr(VI) containing solution. Zn was only found inside the CCC deposited with an acidic Cr(III) solution² embedded also in a Cr, Cr(OH)₃ and Cr₂O₃ matrix with a thickness of 90nm.

Comparing the A2 electrolyte composition with a pH of 13 and a concentration of 11.5 mmol/L of CrO₄²⁻ with the solutions used for CCCs with concentrations between 5-300mmol/L [115] only a slight similarity can be seen. In addition it is stressed that mostly solutions at an acidic pH of < 2 are used and very rare experience exists with alkaline solutions.

4.2.6 The deposition of Zinc - chromium alloy

The electrochemical deposition of Zn-Cr alloys has been getting into focus especially for steel and automotive industry due to the high corrosion resistance of Zn-Cr alloy coatings compared to Zn coatings. Various patents have been published on such alloys with Cr concentrations of 5-40 %wt stating excellent corrosion resistance [131, 132, 133, 134]. Guzmann et al. [135] have described quantitatively that the corrosion resistance of Zn-15Cr on steel is four times higher compared to bare Zn and its hardness is even five times higher. At a concentration of 10%wt of Cr the corrosion resistance of ZnCr alloys increases strongly [136]. However below a concentration of 5 wt% there is only a slight increase of the corrosion resistance compared to bare Zn [137, 134].

In addition to the higher corrosion resistance and the much higher mechanical strength ZnCr alloys with Cr contents \geq 1%wt are permeable to H₂ that is entrapped in the substrate or in the alloy layer itself. During downstream processes or during electrochemical deposition it is able to diffuse out preventing blisters or craters those are known from bare Zn layers [138].

¹ : The solution consisted of 200 g/L Na₂Cr₂O₇ and 10 g/L H₂SO₄ with pH=1.2. Deposition time was 60 s at 25°C.

² : CCC solution consisted of commercial Permapass ImmunoxTM 3k solution (pH=1.8) with Cr³⁺, SO₄²⁻ and F⁻ ions.

Despite the growing interest on ZnCr alloys the metallurgical knowledge is rare. The equilibrium phase diagram of the binary system is still incomplete. Figure 46 shows the phase diagram of the side of the high Zn concentrations.

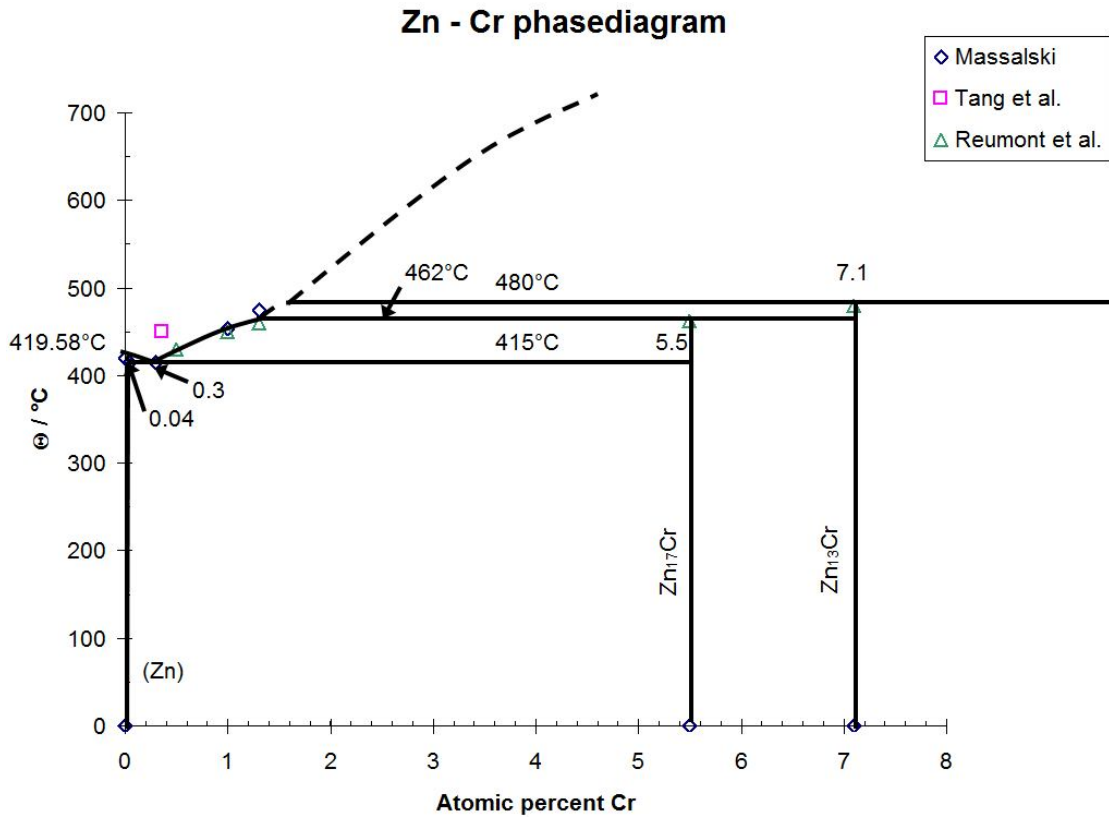


Figure 46: Zn Cr binary phase diagram reproduced from Massalski [139] with additional data points of Tang et al. [140] and Reumont et al. [141].

Cr has a very low solubility of 0.04%at in solid Zn at 415°C. In liquid Zn it dissolves with about 1%at at 450°C [142, 139], however there are results indicating a much lower solubility of 0.36%at Cr at this temperature [140]. Two intermetallic phases Zn₁₇Cr and Zn₁₃Cr are known to exist in equilibrium. On the side of the high Cr concentrations there are only few experimental data available, e.g. Tang et al. [140] gave estimations of a solubility of 25%at Cr in solid Zn at 0°C and more than 65%at at a temperature of 450°C.

More importantly, there are some non-equilibrium phases forming under specific conditions such as during vapour phase deposition [143, 135] or during electrochemical deposition [144, 145, 146, 136, 147, 132]. In figure 47 a scheme of some non-equilibrium phases is shown as reported in the work of Scott et al. [143] on vapour

phase deposited ZnCr alloy and Boiadjieva et al. [145] on electrochemically deposited ZnCr alloy on a Fe substrate.

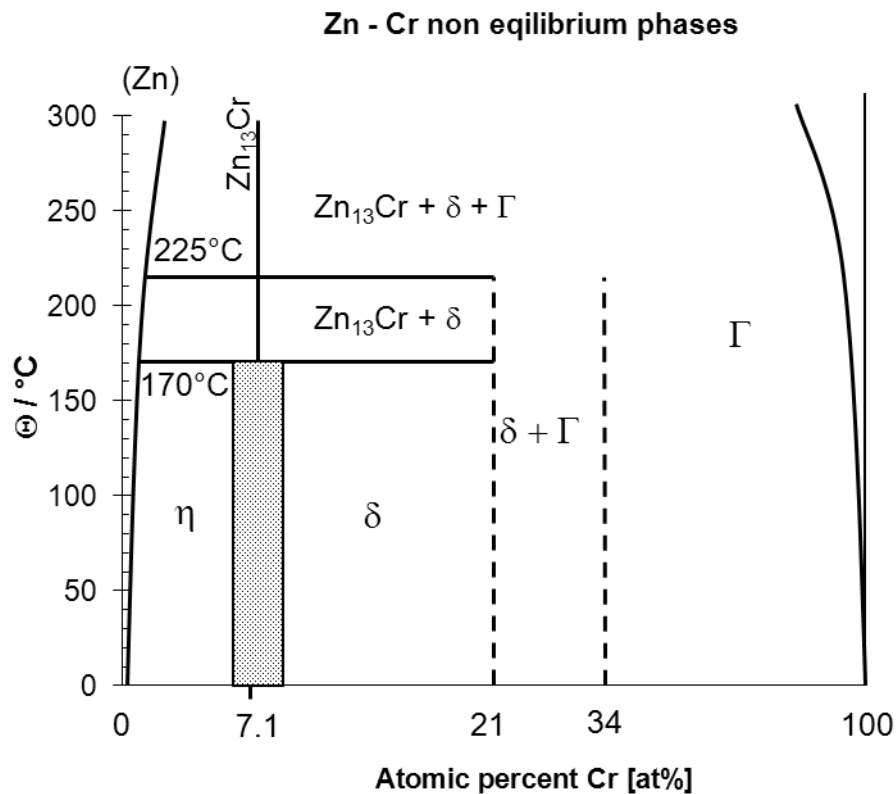


Figure 47: Schematic of non-equilibrium phases in the binary system Zn-Cr. The concentration axis is not true to scale and shows only specific points.

From this schematic it can be seen that for lower temperatures below 170°C and lower Cr concentrations a η - and a δ -phase exist. Beside the η -phase which is considered to be a phase of the equilibrium phase diagram, the δ -phase is a non-equilibrium phase and a supersaturated solid solution of Cr in a Zn matrix. The calculated range for the δ -phase according to Boiadjieva et al. [145] is $9 < x_{Cr} < 21$ %at, experimentally obtained data shows a lower limit of 6.2%at. For higher concentrations a Γ -phase was identified as a disordered Cu_5Zn_8 γ -brass type phase. In the intermediate region both δ -phase and Γ -phase coexist as a mixture. Heating the specific phases up further above 170°C leads to phase transitions. The δ -phase is converted into (Zn) and $Zn_{13}Cr$ below the concentration of 7.1 %at represented by the intermetallic phase $Zn_{13}Cr$. Above this concentration the δ -phase transforms partly to $Zn_{13}Cr$ and partly remains. For higher temperatures (225°C for Scott et al. [143] and 260°C for Boiadjieva et al. [145]) the

authors found in their x-ray diffraction studies that the δ -phase transformation also generates Γ -phase. Both authors found similar structural results despite the fact that Scott et al. [143] deposited via vapour phase deposition and Boiadjieva et al. [145] performed an electrochemical deposition from acidic aqueous electrolyte.¹

The electrolytes used for plating of ZnCr alloys are mainly based on acidic aqueous Zn^{2+} and Cr^{3+} solutions. There is almost no alloy plating done with hexavalent chromium [114]. According to Vagramyan [148] the reason for this is the anomaly of deposition meaning that dichromate is reduced exclusively in the presence of cations of other metals such as Cu^{2+} , Zn^{2+} , Ni^{2+} , and Co^{2+} despite of the fact that the reduction potentials of those metals are more positive. The mechanism was already discussed in section 4.2.1.4.

Acid ZnCr alloy electrolytes on the basis of Cr^{3+} are only working with the addition of polyethylene glycol with a molecular weight of $M \geq 1540$ g/mol, otherwise a Cr content of maximum 1%wt Cr is achieved [146, 147, 149]. Furthermore the Cr content in the alloy decreases with increasing pH to approximately zero at a pH = 5 [137]. Further increase of the pH results in the precipitation of $Cr(OH)_3$, at a pH of 10 the maximum solubility of Cr^{3+} ions is only 10^{-3} mmol/L and at pH = 13 still only 0.1 mmol/L [90]. Electrolytes for ZnCr alloy plating based on Zn^{2+} and Cr^{3+} have to be operated in acidic aqueous milieu to prevent any precipitation and keep the bulk electrolyte stable. However, due to the low CE of $\leq 50\%$ of those electrolytes the strong H_2 development increases the pH value at the vicinity of the cathode [137]. This means that the real deposition pH at the electrode surface is in the alkaline milieu.

In summary a similarity between the chemistry of the A2 electrolyte and the electrolytes used for ZnCr alloy plating can hardly be identified. The alkaline A2 electrolyte contains chromate ions and should show anomalous co-deposition behaviour of Cr and Zn preferring Cr deposition [148]. A further discussion is required whether possibly

1 : The electrolyte in this work was consisting of 40 g/L Zn^{2+} and 15 g/L Cr^{3+} (both added as SO_4^{2-}) with 1 g/L polyethylene glycol at a pH of 2, a temperature of 40°C and in a current density range of 120 to 180 mA/cm².

catalysis or inhibition of the surface via silicate or hydrogen plays a role for the deposition of a sponge and dendritic Zn-Cr layer representing the A2 layer.

4.2.7 Chemistry and function of silicate: Co-deposition of SiO₂

The major metals present in the A2 electrolyte are Zn and Cr, but also silicate is present playing an important role even in a small portion of 70ppm. The silicon is added to the electrolyte as a sodium metasilicate solution. As described by Hollemann and Wiberg [45] those solutions consist of oligomeric [SiO₄]_n forming silicic acid domains with a diameter of 2 nm or bigger. The terminals of those spheres are consisting of Si-OH groups in strongly acidic solutions. Starting at a pH value of 2 and especially in alkaline solution those groups are deprotonated leading to a negative charge at the surface of those spheres. The electrostatic repulsion stabilizes those polysilicic acid molecules and prevents further agglomeration and further growth of the spheres. These so called colloids can be stored without any precipitation for several years [45]. Particle size of SiO₂ colloids produced from natural quartz with a size of 150nm is stable within a pH range from 2 to 10 [150; 151] without flocculation.

In the alkaline A2 electrolyte Zn²⁺ ions are adsorbed preferentially to the deprotonated OH-groups, at lower pH value through deprotonating of the terminal OH groups. The amount of adsorption increases with pH value. At a silica gel with a surface¹ of A_{BET} = 1110 m²/g at a pH value of 8.3 the amount of adsorbed Zn²⁺ is 1.58 mmol/g; reducing the pH to 6.2 leads to a reduction by factor 5 with only 0.335 mmol/g as reported by Kozawa [152]². For the concentration of silicate in the A2 electrolyte of 70 mg/L silicon (13.8 mmol/L) this means that 0.11 mmol/L Zn²⁺ is adsorbed which is theoretically 1% of the complete zinc ions in solution assuming the same adsorption rate of the silicate compared to the silica gel used from Kozawa [152]. The adsorption of Zn²⁺ results in a positive charging of the SiO₂ colloid particles [153, 154, 155] and this would enable an

¹ : The surface of a powder can be described by A_{BET} with BET meaning Brunnauer-Emmett-Teller, who have described the BET adsorption kinetics involving multi-layer adsorption of molecules on surfaces. The BET measurement specifically is done with nitrogen adsorption, refer to standard literature of physical chemistry.

² : Also Cu²⁺ ions are adsorbed at silica gel in an amount of 0.33 mmol/g which is similar to the amount of the Zn²⁺ adsorption at a pH of 6.2; this indicates that for this mechanism of deposition Cu²⁺ ion contamination in the A2 electrolyte may intoxicate the SiO₂ catalyst through a concurring adsorption.

electrophoretic mechanism of deposition in an electric field. Further discussion of a possible dendritic and porous deposition via an electrophoretic mechanism will proceed in chapter 4.2.8 within the comparison of existing models for dendritic growth.

4.2.8 Mechanisms of deposition kinetics for porous and dendritic electrodeposits

Based on the discussion of the theory of electrochemical kinetics and the review of deposition technologies of Zn and Cr and its' alloys four models for the electrodeposition of porous, dendritic or fan-shape metallisations are described in this chapter. The models will be compared to the theoretical deposition conditions of the A2 process, such as the limiting current density and the transition time for the limited current density. Finally in chapter 5.3.8 a resume will be given. It will be shown which of these models fits to the experimental data from the A2 process and the deposition of this type of surface morphology.

Four models that can be found in literature are discussed:

A: Dendritic growth via mass transport controlled deposition

B: Dendritic growth via surface inhibition followed by mass transport controlled deposition

C: Dendritic growth via surface topology and mass transport controlled deposition

D: Dendritic growth by electrophoretic deposition via silicate carrier due to steric hindrance of the colloid carrier.

For the discussion and calculation on specific electrochemical parameters the reaction equilibria and the respective standard potentials E^0 shown in equations (108), (105a) and (105b) after Lide [54] are taken with the respective values for the electron transfer for complete reduction of the metal ions, $z_{Zn^{2+}}=2$ and $z_{Cr^{6+}}=6$.



4.2.8.1 Dendritic growth via mass transport controlled deposition

A simplified view of the deposition of a metal can be separated into two main parts being first the transport of the metal ion to the substrate's surface and secondly the reduction (electron transfer) reaction at the surface. The first model discussed for dendritic deposition is the classical deposition of a species under non equilibrium mass transport limited conditions which was discussed in chapter 4.2.1.3. What does this mean for dendritic growth?

In figure 48 a simplified sketch of a deposition is shown via three subsequent phases including three regions, the substrate on the left side, the Nernst diffusion layer in the middle and the bulk electrolyte on the right side. The concentration of the metal ions in solution is given on the y-axis and the x-axis represents the distance to the substrate surface. The Nernst diffusion layer in the middle represents the electrolyte layer on the substrate that is not affected from convection of agitation as it is the case within the electrolyte bulk, indicated by the stirrer. The thickness of the Nernst diffusion layer δ depends on the intensity of stirring, δ decreases with increasing stirring intensity.

At time $t = 0$ with $i = 0$ indicated by phase 1, equilibrium conditions exist within the electrolyte; the concentration of the metal-ions in solution are identical at each position in the electrolyte.

In phase 2 at $t = t_1$ the current is switched on, $i = i_1$; deposition starts indicated through the black deposited layer. At the same time the concentration of the metal ions within the Nernst diffusion layer decreases as metal ions are reduced at the interface to the substrate with a reaction rate v_1 . Assuming the current i_1 is reaching the limited current i_L or the limited current density j_L then the reaction rate is increasing to v_L and the concentration of the metal ions at the surface reaches a value of zero. The reaction rate v_L in this case is fast enough to reduce any metal ions immediately, that just reach the surface. Any further increase of j will not lead to a higher deposition speed. The deposition is transport limited. Due to the fast surface reaction metal ions reaching the surface will not have any time for surface diffusion and will be immediately deposited at the next reachable substrate position which is indicated in phase 3.

Experimentally it was shown by many authors that the growth of dendritic structures is related to transport parameters such as concentration, diffusion coefficients¹, and electrolyte agitation and to surface reaction parameters such as current density and temperature [117, 118, 120, 197, 192, 156, 157, 158]. The dendrite growth direction follows the diffusion path [123] and the size of the dendritic structures can grow up to the millimetre scale [195]².

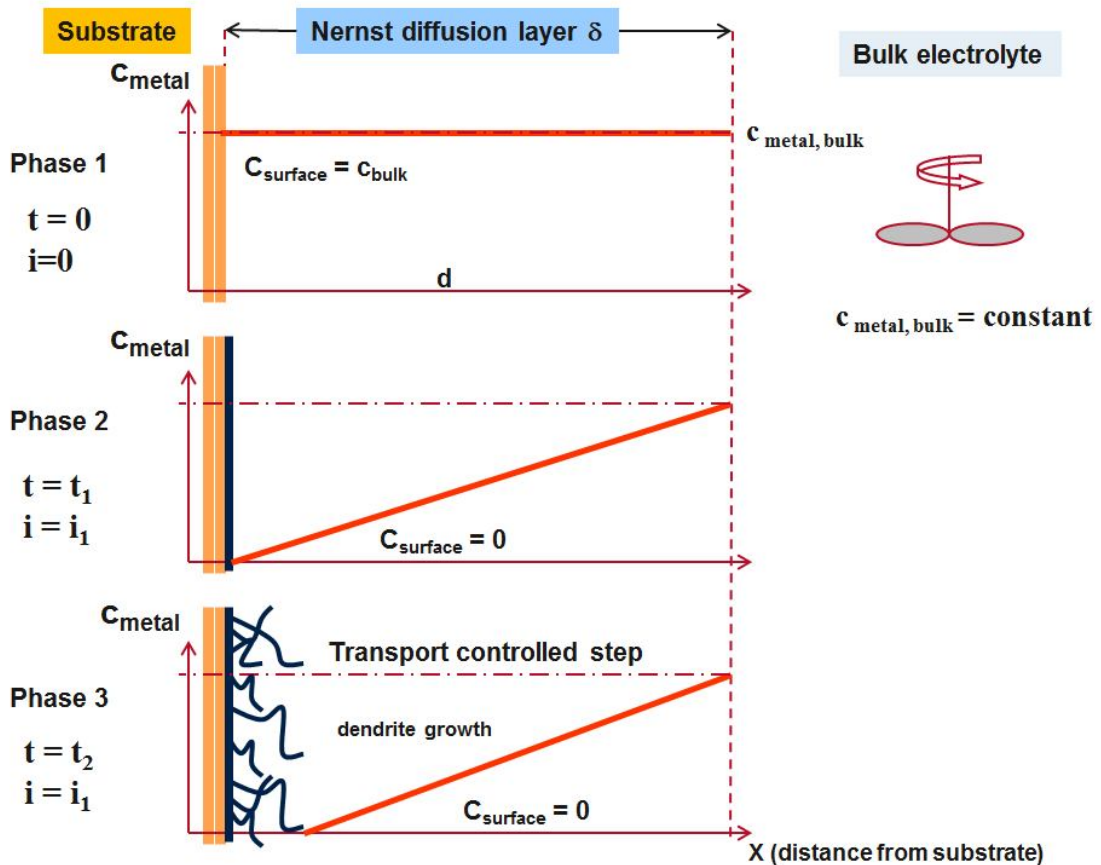


Figure 48: Sketch of transport limited deposition mechanism leading to dendritic deposition of a metal.

An important factor is neglected in this description. The initiation of dendritic growth would be statistically distributed and this is not seen experimentally. Therefore an

¹ : Diffusion coefficients are depending on other parameters such as viscosity, temperature, concentration in a simplified model. Additional contributions by migration and convection according to Planks equation can also be part of mass transport.

² : Argoul et al. showed in interferometric studies on the growth of Zn dendrites from ZnSO₄ that a sudden growth of some dendrites is inhibiting the growth of neighboring dendrites. Dimensions of dendrites grown under those conditions where up to a length of 2mm (1mol/L ZnSO₄; j = 150 mA/cm²).

important factor in phase 2 is the nucleation of the metal at specific sites and the further growth at these sites in a diffusion controlled deposition afterwards [122, 159, 160]. This is described in figure 49 for phase 2 and 3 with nuclei formed as starting points for dendritic growth followed by hemispherical growth over those nuclei until a homogenously distributed Nernst diffusion layer has formed over all growing nuclei and dendrites [161, 162, 163].

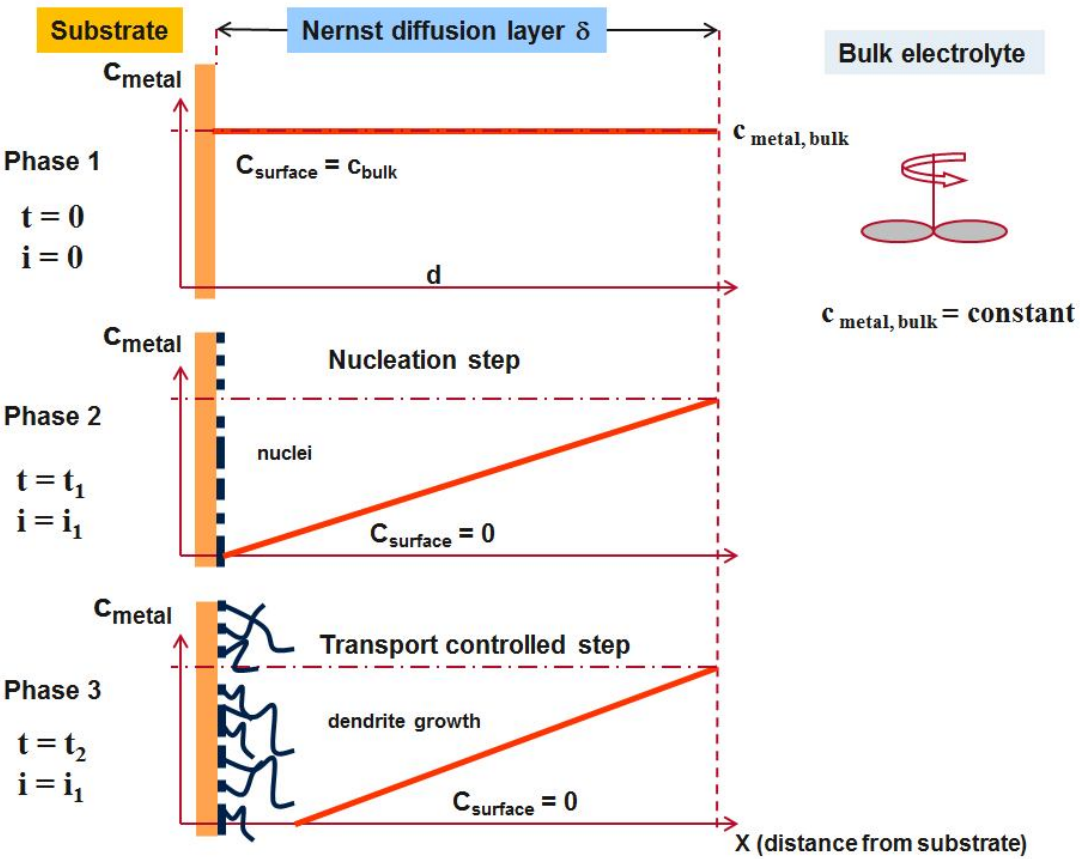


Figure 49: Sketch of transport limited deposition mechanism including nucleation step leading to dendritic deposition of a metal.

Characteristic parameters for this model are the time until the limited current density is reached which indicates the theoretical minimum initiation time of the dendrite growth (transition time τ) and its value indicating the theoretical minimum current density j_L for transport limited dendrite growth (see chapter 4.2.1.3).

To compare the experimental data from the A2 process to the theoretical values an estimation of those two parameters was done based on calculation with specific

simplifications. First the value of the limiting current density j_L was calculated as a function of the Nernst diffusion layer thickness δ according to equation (109) that was derived from equation (85) considering two ionic species Zn^{2+} and Cr^{6+} being co-deposited as an alloy. The co-deposition of Zn^{2+} and Cr^{6+} was assumed to be in a ratio of 1:1 leading to an alloy composition of Zn-50Cr. A further prerequisite of the calculation was that for both species identical diffusion coefficients have been assumed in aqueous solutions after Lide [54] due to similar ionic size of $[Zn(OH)_4]^{2-}$ and CrO_4^{2-} .

$$j_L = -zFD \frac{c_{ox}^0}{\delta} \quad (85)$$

$$j_L = -\frac{F \cdot D}{\delta} (z_{Zn^{2+}} \cdot c_{Zn^{2+}}^0 + z_{Cr^{6+}} \cdot c_{Cr^{6+}}^0) \quad (109)$$

F: Faraday constant (96485.3 As/mol)

D: Diffusion coefficient, $D_{Zn(2+)} = D_{Cr(6+)} = 10^{-5} \text{ cm}^2/\text{s}$

z: Number of transferred electrons; $z_{Zn^{2+}} = 2$; $z_{Cr^{6+}} = 6$

For the calculation five different concentrations in the electrolyte have been taken as shown in table 18 taken from the process window evaluation in chapter 5.3.4 with a range of 0.6 to 5 times the specified target concentrations of either the chromate or the zincate. The calculated chart is shown in figure 50.

	c_{spec} for $c_{Zn^{2+}}$ and $c_{Cr^{6+}}$	$c_{Zn^{2+}}=0.6 \cdot c_{\text{spec}}$	$c_{Cr^{6+}}=0.6 \cdot c_{\text{spec}}$	$c_{Zn^{2+}}=5 \cdot c_{\text{spec}}$	$c_{Cr^{6+}}=5 \cdot c_{\text{spec}}$
$c(Zn^{2+})$ [mmol/L]	13,8	8,28	13,8	69	13,8
$c(Cr^{6+})$ [mmol/L]	11	11	6,6	11	55

Table 18: The concentrations of Zn^{2+} and Cr^{6+} used for the calculation of the limited current density j_L and the transition time τ were taken from the process window evaluated in chapter with a range of 0.6 to 5 times the specified target concentration.

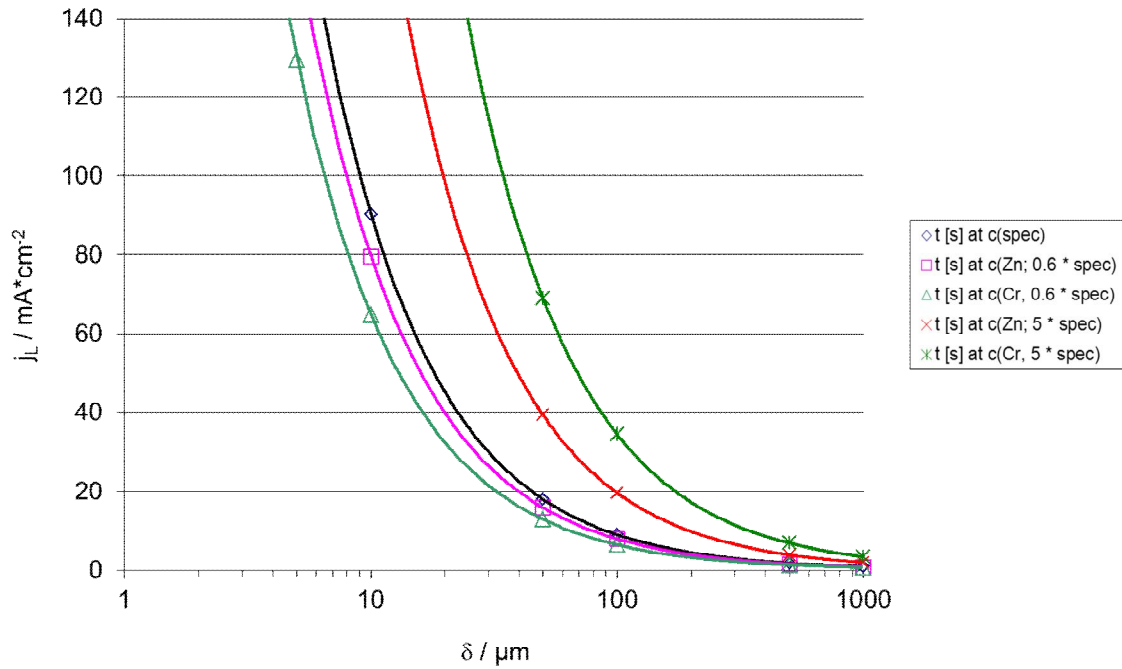


Figure 50: Calculation of the limiting current density for the A2 electrolyte. The 5 graphs represent five different concentrations from the process window with a range of 0.6 to 5 times the specified target concentration.

The interpretation is limited to values of δ in the range of 1 to 500 μm corresponding to strongly agitated to calm aqueous solution, respectively [101, 100]. Under the defined prerequisites this estimation shows, that within this range of δ the calculated value of the limiting current density j_L is not always below the process target current density of 60 mA/cm². For higher concentrations and for stronger agitation, the limiting current density is not reached with the applied process current density. This estimation indicates that the A2 deposition is mostly not under transport control, at values of $\delta < 10\mu\text{m}$ the deposition turns out to be reaction controlled for the observed concentration window.

A further estimation was done based on the transition time until the limited current density j_L is reached. Based on Sand's equation (91) that is valid for the prerequisite of an unstirred solution and the prerequisites made above, equation (110) is obtained and used for calculating the chart of the applied current density j over the transition time τ in figure 51 for the concentrations shown in table 18.

$$\tau = (c_{Ox}^0 \cdot z_{Ox} \cdot F)^2 \cdot \frac{\pi \cdot D}{4} \cdot \frac{1}{j^2} \quad (91)$$

$$\tau = \left((c_{Zn^{2+}}^0 \cdot z_{Zn^{2+}})^2 + (c_{Cr^{6+}}^0 \cdot z_{Cr^{6+}})^2 \right) \cdot \frac{\pi \cdot D \cdot F^2}{4} \cdot \frac{1}{j^2} \quad (110)$$

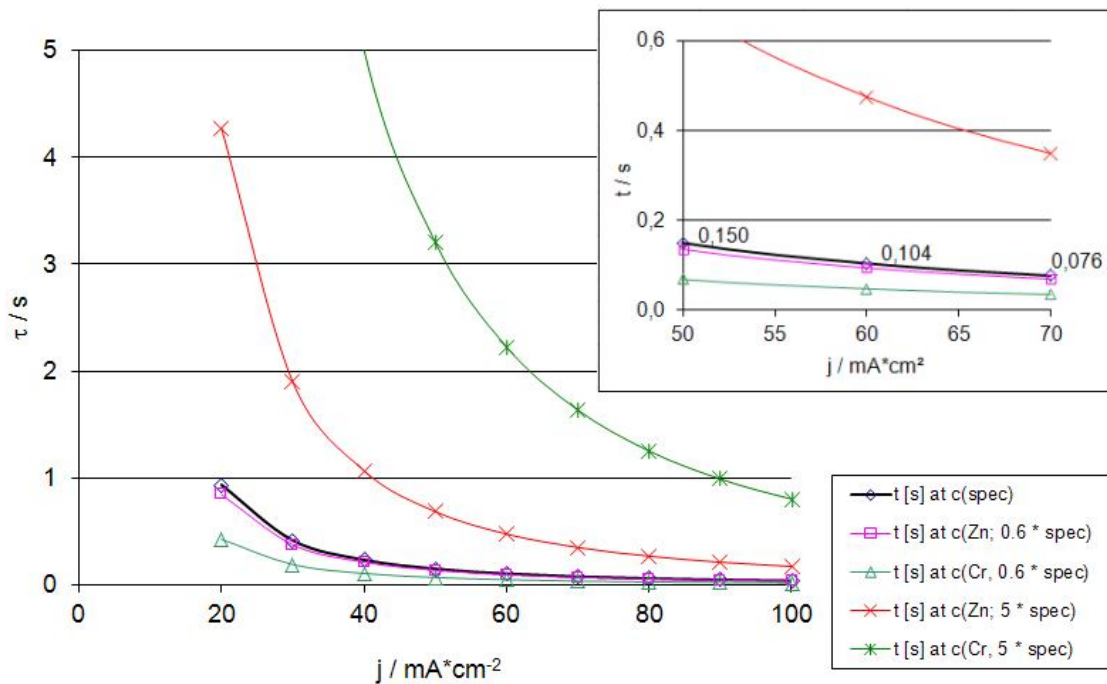


Figure 51: Calculated values for the transition time required to reach the surface concentration $c_{Ox}^s = 0$ as a function of the applied current density. The 5 graphs represent five different concentrations from the process window with a range of 0.6 to 5 times the specified target concentration. The plot in the upper right corner shows the magnification of the graphs around the target current density for the deposition process in the range from 50 to 70 mA/cm²

Considering a target process current density of 60 mA/cm² this estimation shows, that for high concentrations a time of two seconds is required to theoretically reach a mass transport controlled deposition through reaching the limited current density. For the lower concentrations including the target concentrations used in the process $c(spec)$ only a time of less than 200 ms is required. As discussed above due to the usage of the Sand equation the result is limited to an unstirred electrolyte that has a value for δ of about 500 μ m [101].

In summary, the theoretical limited current density is much higher than the applied process current density for a typical Nernst diffusion layer δ in the range of 1 to 10 μ m. A mass transport limited dendritic growth mechanism is not possible in this region. In addition, the growth of dendritic Zn-Cr alloy from the A2 solution on aluminium substrates has been found to be possible even without application of a current (see

chapter 2.6 where deposition experiments on aluminium electroless are described). This finding supports the hypothesis that the deposition mechanism must not be a transport limited mechanism but a different one as discussed below.

4.2.8.2 Dendritic growth via surface inhibition followed by mass transport controlled deposition

Another possible reason for the deposition of porous and dendritic structures is also related to the previous model of a mass transport limited deposition. The important difference is the inhibition of the surface or of parts of the surface prior to the start of the deposition. Inhibition means a blocking of the surface via inorganic phases such as metal hydrides [164] or oxides, organic molecules (see chapter 6) or by a mechanical blockage of the surface by materials such as hydrogen gas bubbles [165].

For example for stronger inhibition such as the adsorption of polyethyleneglycole (PEG) additives dendritic growth of Zn was observed even at lower current densities from Trejo et al. [166]. They found a sudden switch from coarse crystalline deposition to dendritic growth by adding $5 \cdot 10^{-3}$ mol/L PEG to a ZnCl_2 electrolyte. With increasing molecular weight of the PEG of 400, 8000 and 20 000 g/mol finer dendritic shapes were observed similar to the nanostructure of A2.

For the A2 electrolyte an inhibiting factor can be the presence of chromate that may form a Cr_2O_3 layer at parts of the substrate. Secondly, formation of hydrogen occurs that may act as an inhibitor.

4.2.8.3 Dendritic growth via surface topology and mass transport controlled deposition

A model that is not necessarily coupled to the requirement of a mass transport controlled deposition but is a possible explanation for dendritic growth is the favoured deposition of metal ions at very rough surface topologies. During the deposition on a rough surface two factors lead to an increased current density on the peaks of the surface: First the lower diffusion distance an ion has to cover within the Nernst diffusion layer. Secondly, the higher voltage gradient between the anode and the rough cathode at a peak increases the electrochemical driving force at this position. The roughness that is present on a Cu surface of a leadframe is about 1-2 μm , for the NiP

surfaces used in the experiment a roughness of one order of magnitude less was measured being in the range of 100-200nm. Considering the distance of the cathode to the anodes i. e. 5 cm means the difference of the voltage gradient between peak and valley over the rough substrate is marginal.

Regarding the lower diffusion length the similarity between the roughness of the surface and the diffusion layer thickness is much bigger. Considering a diffusion layer thickness of 10 μ m for a laminar flow at a surface [100] a roughness of a Cu surface of 1-2 μ m reduces the diffusion length for about 10-20%. According to Neogi [167] surface roughness is a basic requirement explaining the growth of dendrites especially in systems that are reaction controlled and not transport limited. He mentioned also that modern electrolytes for Cu plating are designed to prevent rough and dendritic growth on rough surfaces through addition of additives such as urea that adsorb at the peaks of the surface acting there as inhibitors enabling a smoothening of the roughness during the deposition. As those inhibitors preferably adsorb on the peaks, this mechanism of shorter diffusion length is also working with concurring reactions such as adsorption processes during deposition.

4.2.8.4 Dendritic growth by electrophoretic deposition with silicate carrier.

The dendritic growth of zinc via a colloidal silicate carrier is also not coupled to mass transport but to a steric mechanism. Like shown in chapter 4.2.7 SiO₂ colloid particles can carry a significant amount of Zn²⁺ ions leading to cathodic polarisation and to an access of an electrophoretic mechanism.

For a Zn²⁺/Cr³⁺ electrolyte at a pH of 2 Takahashi et al. [154] reported that the addition of SiO₂ colloid catalyses the co-deposition of Cr and Zn in a similar way as polyethylene glycol. The anomalous deposition characteristic of this system vanishes. The authors also observed an incorporation of the SiO₂ particles into the Zn-Cr layer and proposed a model of electrophoretic deposition of Zn from [Zn-SiO₂]ⁿ⁺ colloid particles. In the deposition they noticed an oxygen content of 8-10 at% due to this incorporation. This inclusion of SiO₂ particles is also seen within the deposited layers of Zn deposited from ZnSO₄ solutions. Kondo et al [168] showed that those colloid

particles line up in the early stage of the Zn deposition, preferred sites are at kinks but also statistically located at crystal planes.

In addition, deposition of Zn via an electrophoretic mechanism can form dendritic and spongy Zn layers. Cabot et al. [153] observed Zn needles with a diameter of 10 to 100nm and a length of 100 to 1000nm using an electrolyte of 50 mmol/L ZnSO₄ with 1 wt% sodium silicate and 30 %wt polyethyleneglycole adsorbed to SiO₂; they applied a deposition time of 5 minutes in an electric field of 1.5 V/cm on a steel substrate with a zinc and chromium conversion coating (CCC) layer.¹

Tuaweri et al. [155] confirmed the dendritic and needle like deposition of Zn using a very similar electrolyte of 870 mmol/L ZnSO₄ with 15.5 % wt SiO₂ of 2 μm particle size and 0.1 % vol of N,N-dimethyldodecylamine (NND) at a pH of 2. The authors applied a current density of 300 mA/cm² at a temperature of 50°C and found a Zn dendrite morphology in FESEM studies that was nearly identical to the layer structure obtained with the A2 process described in section 2.1. Experiments with SiO₂ of 20 nm particle size gave crystalline, but non-dendritic morphology in this work. However, the work of Tuaweri et al. [155] was directed to electrophoretic deposition of Zn-SiO₂ composites and the result on dendritic deposition of Zn was obtained incidental and not further investigated from this team.

Similar dendritic and fan-shaped Zn-SiO₂ composites were also prepared by Hiramatsu et al [169] with an acidic aqueous ZnSO₄ electrolyte and various additives, such as dodecyltrimethylammoniumchloride (DTAC) and poly(oxyethylenelaurylamine) (POELA). It is remarkable that concentrations of those additives played a major role for the fan-shaped deposition of Zn in their work. For example a concentration of 5-10 mmol/L POELA resulted in a fan-shaped deposition of Zn whereas a concentration of 17 mmol/L failed the fan-shape morphology. In contrast, using DTAC only a concentration of 0.5-1 mmol/L was required to obtain a fan-shaped Zn layer. The addition of SiO₂ particles in this case was done mainly for the purpose of getting a high

¹ : In this case the SiO₂ colloid was prepared through precipitation of sodium silicate in an acidic milieu leading to colloid particles of about 20nm diameter with a surface of A_{BET} = 145m²/g.

corrosion resistance. The co-deposition of SiO₂ particles had no influence on the morphology of the plated Zn-SiO₂ layer according to these authors.

Apart from the morphology also an increase of polymer adhesion to those fan-shape layers was observed by Hiramatsu et al. [169] indicating an additional similarity to the A2 layer investigated in this work.

To sum up the mechanism of a SiO₂ colloid catalysed electrophoretic deposition, three arguments from experimental studies suggest that this mechanism is appropriate for explaining the deposition of the A2 layer as well:

1. The SiO₂ colloids lead to a co-deposition of Zn and Cr. The known anomalous deposition behaviour for Zn and Cr is moved to a normal deposition behaviour preferring the deposition of Zn as the more noble species compared to Cr [154] at low pH values of the solution.
2. The SiO₂ colloids catalyse the dendritic deposition of Zn observed in aqueous acidic electrolytes. The SiO₂ colloid particles are positively charged due to Zn²⁺ adsorption and possibly act as carriers for zinc [154].
3. SiO₂ particles are included into the deposited Zn-Cr layer. This also would explain the Si content seen in depth profiles of Auger spectroscopic data.

It will be further discussed whether this mechanism is also possible in an alkaline electrolyte containing zincate and chromate which will be discussed in chapter 5.3 and following on the experimental data gained with the A2 deposition.

5 Deposition of A2 layer: Experimental results of the development of an industrial process

5.1 Overview on the A2 process and technology

To start with the discussion of the experimental results at first a short overview on the three existing A2 process options is given. Two different plasma wafer conditioning steps for the activation of the aluminium metallisations, an Ar plasma with CF₄ reactive gas and an Ar plasma with O₂ reactive gas were used. Besides this, two different wet chemical activation options within the A2 process were used as shown in table 19. First, pure methanesulfonic acid (MSA) and secondly a mixture of hydrofluoric acid (HF) and MSA (HF/MSA) were used. Furthermore, three variants were present within the A2 deposition step in terms of two different bath temperatures and three different plating times. These variants at different process steps were combined with three existing variants of the A2 process flow, see table 19. Because all three variants were used throughout the experiments of this work the naming of the version will be "Ar/CF₄ + long A2", "Ar/O₂ + short A2", and "Ar/O₂ + pulse A2".

	Wafer conditioning	A2 process				
Version	Al-1Si-0.5Cu	Activation chemistry	A2 electrolyte	Temperature	Plating time	Current and mode
Ar/CF ₄ + long A2	Ar/CF ₄ plasma	12% wt MSA	12 g/L NaOH 0.9 g/L Zn ²⁺ 0.6 g/L Cr ⁶⁺ 70 ppm Si ⁴⁺	60°C	20s	45mA/cm ² DC
Ar/O ₂ + short A2	Ar/O ₂ plasma	12% wt MSA + 0.1% wt HF	16 g/L NaOH 1.2 g/L Zn ²⁺ 0.6 g/L Cr ⁶⁺ 70 ppm Si ⁴⁺	50°C	10s	45mA/cm ² DC
Ar/O ₂ + pulse A2	Ar/O ₂ plasma	12% wt MSA + 0.1% wt HF	16 g/L NaOH 1.2 g/L Zn (from ZnO) 0.6 g/L Cr-VI (from Na ₂ Cr ₂ O ₇) 70 ppm SiO ₄	50°C	5s	200mA/cm ² pulse function

Table 19: Overview on the three process variants of A2 technology.

For those experiments that were run on a productive equipment a belt plating machine from Mecos company was used that is able to run various leadframe geometries. The loading of the leadframes within this equipment is done automatically from a magazine

handler onto a stainless steel transport belt. Then they are transported through the different compartments and cells. Figure 52 shows the geometry of the equipment with photos from the front and the back. In addition the A2 cell is shown in the middle with the cell gates and the transport belt moving the leadframe through the yellow electrolyte.

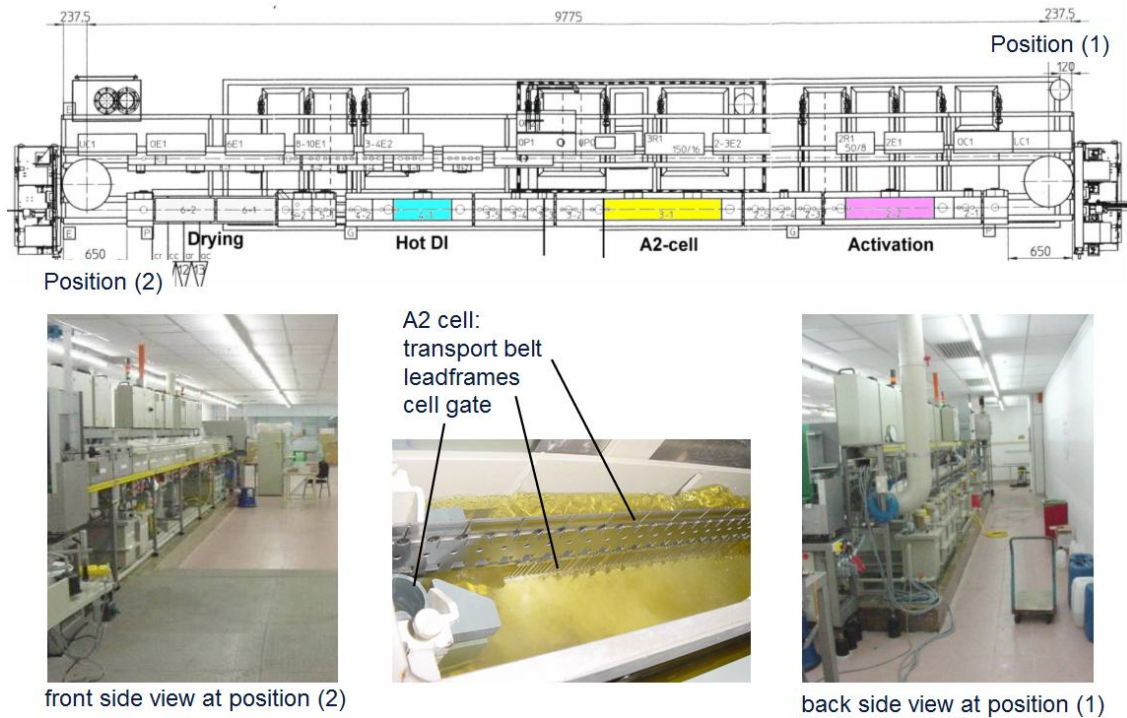


Figure 52: Drawing and photo of A2 deposition equipment (top, bottom left and bottom right) and the deposition cell (bottom middle).

The substrate used throughout this work mainly was a TO263-3 leadframe with a standard MOSFET soldered onto the leadframe heat sink and connected to the leads with a Al thick wire ($350\mu\text{m}$ diameter) for the source chip pad and with a Al thin wire ($75\mu\text{m}$ diameter) for the gate pad. The soldered chip backside represents the drain contact of the MOSFET. In figure 53 an example leadframe with a magnified device is shown. The area of the TO263-3 leadframe was calculated to be $A = 228.4\text{ cm}^2$ from the drawing.

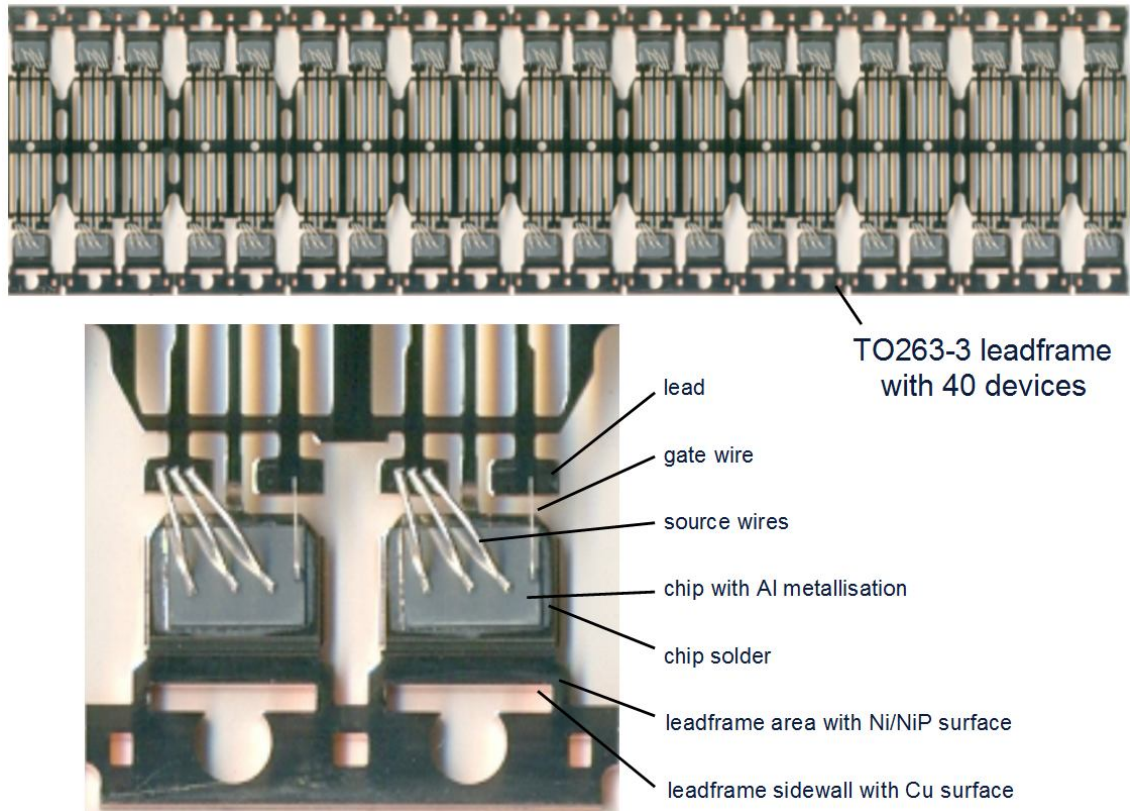


Figure 53: TO263 leadframe ($A = 228.4 \text{ cm}^2$) with MOSFET chips (top) and two magnified devices (bottom)

In addition in some parts of the experimental work a TO220 leadframe was used having a single row of devices as shown in figure 54. This product consists of a similar geometry of the single devices with a MOSFET chip and contact wires of thick and thin Al wires. The area of the TO220 leadframe was calculated to be $A = 120.7 \text{ cm}^2$ from the drawing.



Figure 54: TO220 leadframe with single row of devices and with NiP surface, blanket without chips ($A = 120.7 \text{ cm}^2$).

5.2 Activation process

5.2.1 Investigation of activation with H₂SO₄ and MSA (er81 and er98)

Activation of Cu, Sn and Pb in acid solutions was tried out in two experiments by processing devices with either MSA or H₂SO₄ activation, following with A2 deposition, molding and final manufacturing processes. The assessment of the various groups was done with SAM before and after specific stress tests and in addition with Auger depth profiles to analyse possibly present sulphur from either the MSA salts or the sulphates which specifically for Pb ions have a very low solubility in the activation bath. The results as shown in table 20 and table 21 were consistent for both experiments using two different molding compounds being MP195H from Nitto for er81 and XKE 7459 from Toshiba for er98.

Experiment group	ER81-A	ER81-B	ER81-C	ER81-D
Solder	Alloy-J	Pb-solder	Alloy-J	Pb-solder
Activation	Activation with H ₂ SO ₄ (c=180 g/l, Θ=40°C, t=10s)		Activation with MSA (c=150 g/l, Θ=40°C, t=10s)	
A2 parameters	Galvanic A2-coating: Laboratory equipment with 20 L electrolyte and standard V4A anodes. Parameters: t=15 sec, I=30 mA/cm ² ; Θ=57°C.			
Auger results	Traces of sulfur found under the A2 layer	Traces of sulfur found under the A2 layer	No sulfur signal detected	No sulfur signal detected
Further processing	Molding with MP195H, 120 min post mold curing, SnPb deposition, cutting and pin forming of the TO263-3-1 package.			
SAM results	No delamination	No delamination	No delamination	No delamination
Soldering stress	Preconditioning by fast soaking (48h autoclave at 121°C, p _{H2O} =2 bar); 3 times infrared soldering with 260°C peak temperature profile.			
SAM results	80% delamination	60 % delamination	No delamination	20 % delamination

Table 20: Experiment matrix and results of er81

All groups which have been activated with H₂SO₄ in experiment er81 show significant delamination after specific temperature stress, there was no delamination at initial state

showing, that the manufacturing of the devices was done correctly. There was only a 20% delamination observed in group er81-D with MSA activation, therefore the experiment was done a second time to reproduce the result and to confirm the positive trend for the MSA activation. In addition the comparison of the solder surfaces and layers on the solder dot in the Auger depth profiles in er81 after the deposition of the A2 layer shows traces of sulphur for those groups which were activated with H₂SO₄. In contrast this S signal is missing in the groups activated with MSA which can be seen in table 22

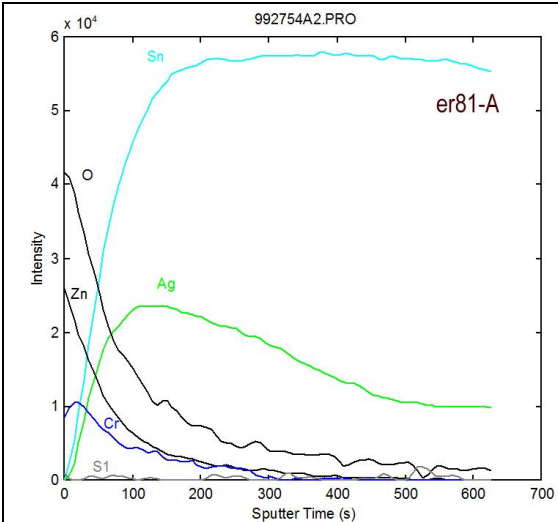


Figure 22a: Auger depth profile of group er81-A, Alloy-J with H₂SO₄ activation, sample taken after activation and after complete A2 process.

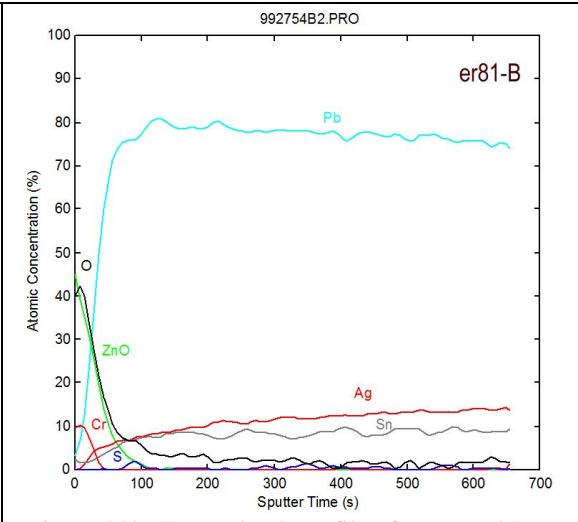


Figure 22b: Auger depth profile of group er81-B, Pb-solder with H₂SO₄-activation, sample taken after activation and after complete A2 process.

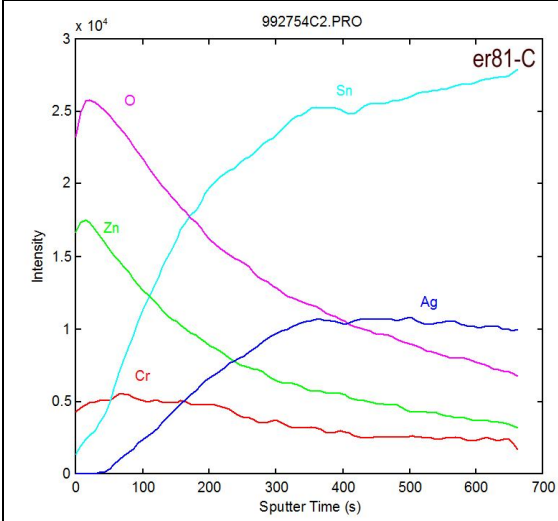


Figure 22c: Auger depth profile of group er81-C, Alloy-J with MSA activation, sample taken after activation and after complete A2 process.

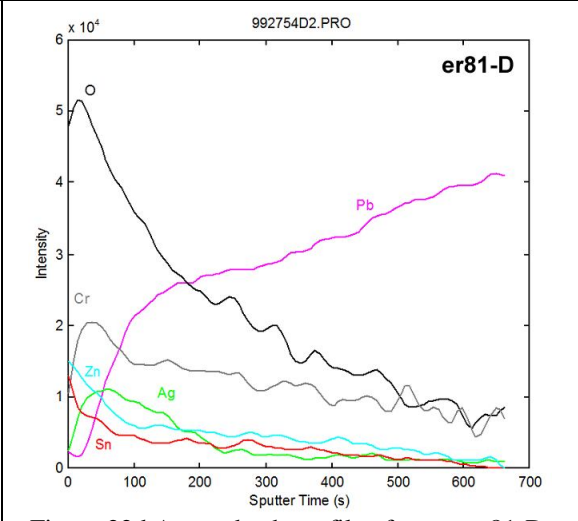


Figure 22d: Auger depth profile of group er81-D, Pb-solder with MSA-activation, sample taken after activation and after complete A2 process.

Figure 22a-d: Comparison of solder surfaces and layers on the solder dots within the various groups in er81 with Auger depth profiles after A2 deposition.

Within the experiment er98 for those groups which have been activated with MSA after specific stress tests no delamination was detected with SAM. This experiment was done with a different Toshiba molding compound and A2 deposition was done on a productive plating machine which is considered much more reproducible compared to A2 plating on laboratory equipment as in the case of experiment er81.

	ER98-A1	ER98-A2	ER98-B1	ER98-B2
	Alloy-J		Pb-solder	
Activation	H₂SO₄	MSA	H₂SO₄	MSA
Conditions	H ₂ SO ₄ (c=180 g/l, Θ=25°C, t=10s); MSA (c=150 g/l, Θ=40°C, t=10s)			
A2 deposition	Galvanic A2-coating: LPL strip-to-strip plating equipment (I=30 mA/cm ² ; Θ=57°C, v=2,5m/min t=15 s)			
Molding	Toshiba XKE 7459 (120 min post mold curing)			
SAM initial	No delamination initial	No delamination initial	No delamination initial	No delamination initial
Soldering stress	Preconditioning by fast soaking (48h autoclave at 121°C, p _{H2O} =2 bar); 3 times infrared soldering with 260°C peak temperature profile.			
SAM after preconditioning	no delamination	no delamination	30% delamination	no delamination
Temperature cycle stress	100 temperature cycling (-55 to 150°C)			
SAM after TC100	no delamination	no delamination	30% delamination	no delamination
Temperature cycle stress	500 temperature cycling (-55 to 150°C) for lifetime reliability			
SAM after TC600	no delamination	no delamination	30% delamination	no delamination

Table 21: Experiment matrix and results of er98

In conclusion, both experiments show that MSA offers a better activation of the solder surface. The Auger results indicate the formation of sulphates for the case of activation with H₂SO₄ which is unfavourable for the deposition of A2 and for the adhesion between molding compound and the device. Therefore it was decided to use MSA instead of H₂SO₄ for activation of the device surfaces.

5.2.2 Investigation of the influence of oxidation during chip soldering on deposition of A2 (er175)

It was discussed in the theoretical part “4.1 Activation of metal surfaces” that downstream processes have an influence to the device surfaces being loaded into the A2 deposition process. Especially the chip soldering process can lead to a specific oxidation of the solder surface at unfavourable chip soldering process conditions. For example an oxidation of the Ni surface of the device can occur. In experiment er175 this influence was studied for different chip soldering conditions for the Cu, the NiP and for the solder surface comparing best case soldering process to unfavourable process conditions with only half of the forming gas flow rate. The latter conditions led to an oxidation of the Cu in spite of the presence of the forming gas with 5%H₂ in N₂ during chip soldering. Also two different chip soldering processes were tried out, one with spanker¹ and one with only a single solder dot. Table 23 shows the experimental matrix and the results of the FESEM analysis regarding the morphology of the deposited A2 layer which was analysed on various positions of the device shown in figure 55. The assessment of the A2 morphology was done according to the defined categories A to D in the morphology catalogue described in the analytical section “2.1 Field emission scanning electron microscope (FESEM): Surface morphology” representing the quality level of the obtained A2 layer with A=best and D=worst.

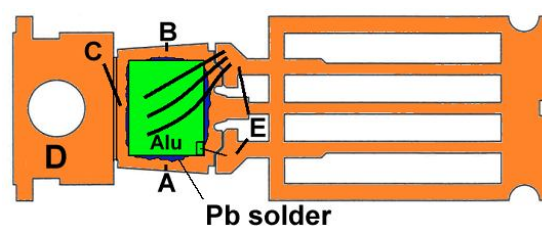


Figure 55: Positions of FESEM analysis for morphology analysis of the A2 layer

In addition the SAM results of the devices after stress test are included in table 23 which was done to get the real adhesion in the product within the respective

¹ : A spanker is a steel tool that is used to shape the solder during chip soldering prior to the chip placement.

experimental groups. The percentage of delamination after stress test on the devices was derived from the specific SAM pictures.

Trial	Device: BUZ111S with different diebond equipment, 4 leadframes each group		FESEM analysis on devices: For position A, B, C: Dendrite check on 3 locations For position D, E, Pb-solder, Al chip: Dendrite check on only 1 location.							SAM results on devices after precon MSL1/260°C and TC100	
Er175	Lead frame surface	Chip soldering	A	B	C	D	E	Pb sold.	Al chip	Percentage of delamination	
A1	Cu-K80	E2007 single, good N2/H2	3A	3A	2A 1B	A	A	A	B	10%	
A2	NiP		3A	3A	3A	A	A	B	A	5%	
B1	Cu-K80	E2007 single, bad N2/H2	3A	3A	1A 2C	A	A	A	A	<5%	
B2	NiP		3A	3A	3A	A	A	B	D	<5%	
C1	Cu-K80	E2007 spanker, good N2/H2	1A 2C	3A	3C	C	A	B	D	10%	
C2	NiP		2A 1B	2A 1B	3A	A	A	B	A	0%	
D1	Cu-K80	E2007 spanker, bad N2/H2	3A	2A 1B	3C	A	A	B	D	10%	
D2	NiP		3A	3A	3C	A	A	B	D	0%	
E1	Cu-K80	Pure Cu leadframe	3A	1A 2B	3A	A	A	n.a.	n.a.	n.a.	

Table 23: Er175 experimental matrix, FESEM and SAM results.

For all groups Auger depth profiles were performed after the chip soldering on the Cu, NiP and Pb-2Sn-2.5Ag solder surface to get information about the extent of oxidation and the surface condition with the activation with MSA at a concentration of $w = 12,5\%wt$ and at $\Theta = 25^\circ C$ for a time of $t = 10s$. A2 plating was done on a productive plating machine with standard parameters of $i = 60mA \cdot cm^{-2}$, $\Theta = 58^\circ C$ and $t=20s$.

The A2 morphology check with SEM showed no significant difference between groups with low oxidation (A and C) and groups which have been strongly oxidized (B and D). All groups show sufficient positive morphology of the A2 layer. The uniformity of grown dendrites is higher in the NiP groups. This may be due to the lower surface-roughness of NiP in comparison to the Cu and the Pb-2Sn-2.5Ag solder surface. There were some positions showing a C-grade morphology for the Cu, NiP and the solder surface, but no correlation can be obtained with any oxidation within the different groups as they were found also on groups without any oxidation. Those single less positive morphologies are considered to be the normal variation of the A2 layer on the

surface. The Al chip metallisation was also analysed in this experiment showing groups with very bad morphology grade D or even a missing A2-layer. This weakness regarding the activation is further discussed in the next experiment and is of no importance in this experiment as the focus was Cu, NiP and the solder surface here.

In the SAM analysis after the stress tests all groups show good adhesion which correlates with the positive results of the FESEM morphology check after A2 deposition. Especially within the groups with NiP the devices of groups C2 and D2 show very good results without any delamination in the SAM monitoring after stress tests.

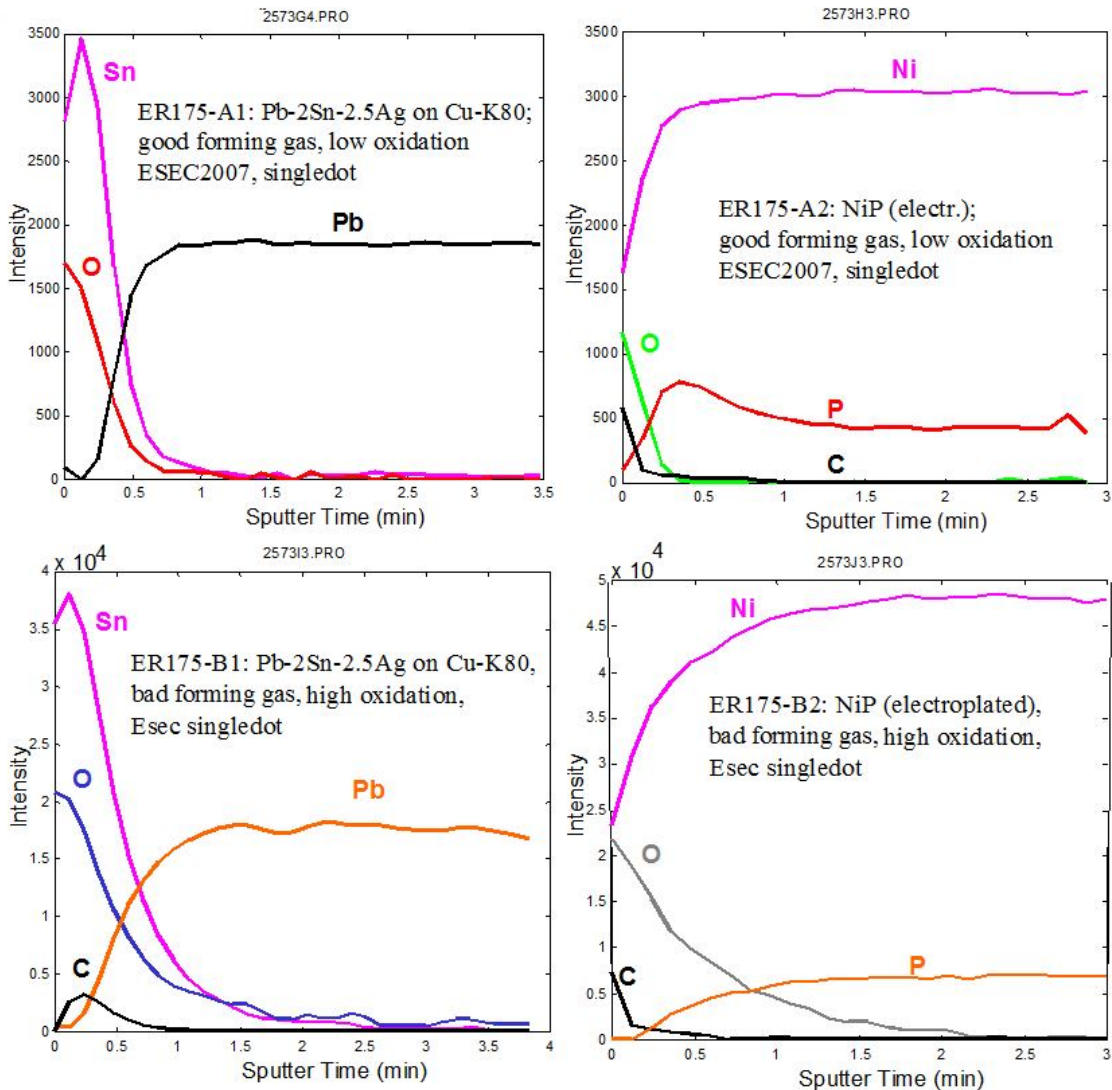


Figure 56: Auger depth profile of groups A1 and A2 with low oxidation and groups B1 and B2 with high oxidation rate during chip soldering.

In figure 56 four examples are given from the Auger depth profile results. Comparison of group A1 (low oxidation) with group B1 (strong oxidation), both analyses done on the Pb-2Sn-2.5Ag solder surface, show no big difference of the surfaces. There is a very small increase of the Sn oxide thickness visible for the strongly oxidized group B1. For both groups the Sn oxide is accumulating on the solder surface due to the higher stability of SnO which was discussed in chapter "4.1.1" already. A much larger difference can be seen on the NiP surfaces comparing group A2 (low oxidation) with group B2 (strong oxidation). The Auger depth profile shows a much thicker NiO layer for the group B2 of about a factor of 4 looking at the half value of the sputter time of the O signal. This shows that Ni is further oxidizing in presence of O₂ in spite of the presence of forming gas. The reduction of NiO with H₂ is too slow and the oxidation reaction dominates.

In summary this experiment shows that the used activation with MSA of a concentration of $w = 12,5\%wt$ at $\Theta = 25^\circ C$ for a time of $t = 10s$ combined with the A2 plating at $i = 60 \text{ mA cm}^{-2}$, $\Theta = 58^\circ C$ and $t=20s$ in the respective electrolyte provides a sufficient activation of the Cu, NiP and Pb-2Sn-2.5Ag solder surface even for the worst case of a strongly oxidized device after chip soldering.

5.2.3 Argon / CF₄ plasma process for activation of the Al chip metallization (er265)

One of the major challenges for the A2 technologies was the preparation and activation of the Al chip metallisations for deposition of the porous A2 layer. Because of its high chemical stability Al₂O₃ is not etched away within the acidic activation section in MSA and due to the short plating time in the alkaline A2 electrolyte the Al is activated only insufficiently through the NaOH there. This entails to a very inconsistent plating result on the chip metallisation which is a high risk for the device reliability. On the other hand corrosion of the thin Al wires of for example 50µm thickness and the chip metallisation with low thickness of for example 5µm for Al-1Si-0.5Cu is limiting the chemical attack that can be applied at the A2 process.

One way of solving this problem was found through a specific conditioning of the Al surface by a wafer plasma process to make the Al surface oxide less stable against alkaline attack in the A2 electrolyte. To find the appropriate wafer process several

studies were done starting with experiment er265 that is consisting of various plasma etching processes with various process gases as shown in table 24 stated under the process "Conditioning of Al metallisation".¹

For experimental groups r-ref(#8) and r1 no additional conditioning was performed as those groups were the reference groups with the standard processes but from two different production lines 1 and line 2. In groups r2 and r3 a anisotropic reactive ion Ar/CF₄ plasma etching (SuperE-Overetch) was used with 600W RF power, 450cm³/min Ar, 50cm³/min CF₄ gas at two different times of 20s and 40s. Group r4 was consisting of an isotropic and indirect plasma etching process. This means that no plasma is directly present at the Al-1Si-0.5Cu surface but only the radicals generated in a plasma side chamber are guided to the wafer (CDE-overetch).

Furthermore in groups r5 and r7 additionally to the SuperE-overetch an O₂-plasma was applied which is normally used for the removal of lithography resist residuals. For group r5 finally a wet chemical polymer removal with a mixture of 2-(2-aminoethoxy) ethanol and hydroxylamine for a time of 20 min at 25°C was done (EKC) to additionally remove any residuals of lithography resins. Group 6 was representing another reference group without any conditioning step but leaving out the annealing of the front side metallisation as a standard process to see whether the prevention of this temperature budget influences the reactivity of the Al surface positively, see also table 8 in chapter "4.1.1 Properties and states of the different surfaces prior to activation". Finally in group r9 a wet chemical treatment was done using a dip in 1 wt% HF at 25°C because of a positive indication of the usage of HF conditioning in a pre-experiment.

The assessment of the different groups in this first study was done with an A2 dip test described in chapter 2.6 treating the specific samples with the A2 electrolyte by dipping the specimen for a certain time which leads to a chemical deposition of the A2 layer with a similar morphology as compared to the electrochemical deposition. This offered a very fast possibility to generate samples with A2 coating in the laboratory for further analysis with FESEM and to get information about the morphology of the obtained A2

¹ : The development of the surface conditioning process was done with the help of Dr. Zechmann Arno and his team at Infineon Villach in Austria that took care of the necessary wafer processes options and wafer manufacturing.

layer. This finally indicates the reactivity of the respective Al surface, which is generated through the individual plasma conditioning, towards alkaline attack. Very inert Al surfaces in this test do not show any deposition, hence no visible A2 structure. In contrast, Al surfaces whose reactivity towards alkaline attack is similar as for example a native Al₂O₃ show a typical sponge A2 layer after the test.

In addition for each group a XPS depth profile for fluorine, oxygen, carbon and aluminium was measured for the fresh surfaces prior to the A2 dip. The XPS results are summarized in table 24. To compare the various groups in terms of their F content within the surface the intensity of F in the XPS after one cleaning sputter cycle was taken. The second XPS value is the signal ratio I_F / I_O , the third value represent the signal ratio I_F / I_{Al} and finally the sputter time to reach the half value of I_F derived from the XPS depth profiles is given.

er265 group	Wafer frontside processes			XPS results after the conditioning process			
	Metallisation application	Conditioning of Al metallisation	FESEM results after A2 dip	Intensity of F at surface [10 ⁴ counts]	Signal ratio F/O at surface	Signal ratio F/Al at surface	Sputter time for F half value [min]
r-ref (#8) ¹	standard, line 1	no	no A2 dendrites detected	1.5	0.16	0.75	0.8
r1	standard, line 2	no	no A2 dendrites detected	n.a.	n.a.	n.a.	n.a.
r2	standard, line 2	SuperE overetch t=20s	Homogenous A2 dendrites detected	13	3.71	5.56; (peak: 6.5)	1.2
r3	standard, line 2	SuperE overetch t=40s	Homogenous A2 dendrites detected	n.a.	n.a.	n.a.	n.a.
r4	standard, line 2	CDE overetch	no A2 dendrites detected	2.5	0.31	1.38	0.6
r5	standard, line 2	SuperE overetch t=20s + O2 plasma + EKC	Single A2 dendrites detected.	3	0.38	1.38; (peak: 1.45)	0.8
r6	standard, line 2, but no aneal of frontside	no	no A2 dendrites detected	n.a.	n.a.	n.a.	n.a.
r7	standard, line 2	SuperE overetch t=20s + O2	Homogenous A2 dendrites detected	9	1.2	3.61; (peak1: 3.75; peak2:	2

¹ : All wafers for this experiment have been taken out of production line 2 except for experiment r-ref(#8) taken out from line 1 on a different manufacturing site regarding the processes for producing the front side metallisation consisting of Al-1Si-0.5Cu.

		plasma				4.09)	
r9	standard, line 2 + HF dip	no	No A2 dendrites detected	n.a.			

Table 24: Experimental matrix of er265 with a variation of plasma etching processes on wafer to prepare the Al surface for further A2 deposition.

The following results were obtained: From the 9 groups investigated 3 yield excellent results with smooth dendrite growth during A2 dip. Those are the process variations with SuperE-overetch (group r2, 20sec; group r3, 40sec) and the group r7 with an additional O₂-plasma showing the best FESEM results with spongy deposition of the A2 layer, referring to figure 57a and figure 58a respectively.

In the XPS depth profiles the ratio of F and O signal was the highest for those groups ($I_F / I_O = 3.71$ for group r2; $I_F / I_O = 1.2$ for group r7) excluding group r3 that was not analyzed. These high values are also observed for the ratio of F and Al giving values of $I_F / I_{Al} = 5.56$ for group r2 and $I_F / I_{Al} = 3.61$ for group r7. Formation of a mixture of AlF₃ and AlOF within those groups can explain those high values, the formation of those species in CF₄ plasma etching processes on Al surfaces is well known and for example reported by Ramos et al. [91] and by Cunge et al. [92]. Figure 57b and 58b shows the respective XPS depth profiles with the very high peaks of the F signal. In the latter XPS depth profile of group r7 the F containing layer seems to be additionally covered by a layer with a higher amount of oxygen that may be due to the additional O₂ plasma after the Ar/CF₄ conditioning step. It can be concluded that this does not have a negative influence on the obtained A2 morphology in this experiment.

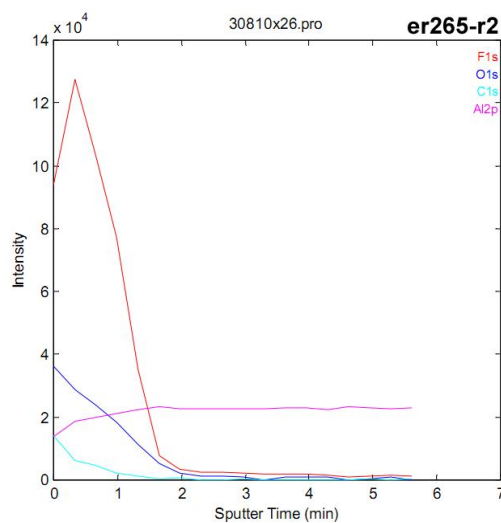
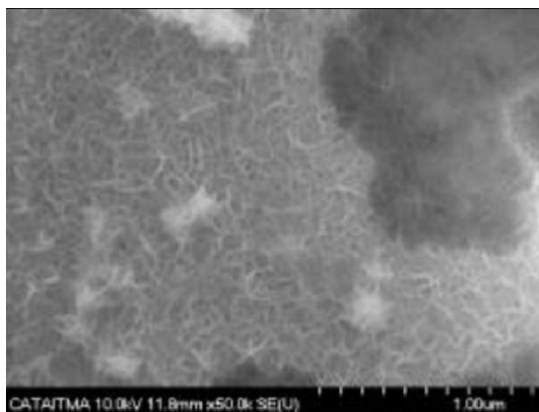


Figure 57 a and b: FESEM image after A2 dip and XPS depth profile before A2 dip of group r2 (Ar/CF₄ plasma conditioning, t=20s)

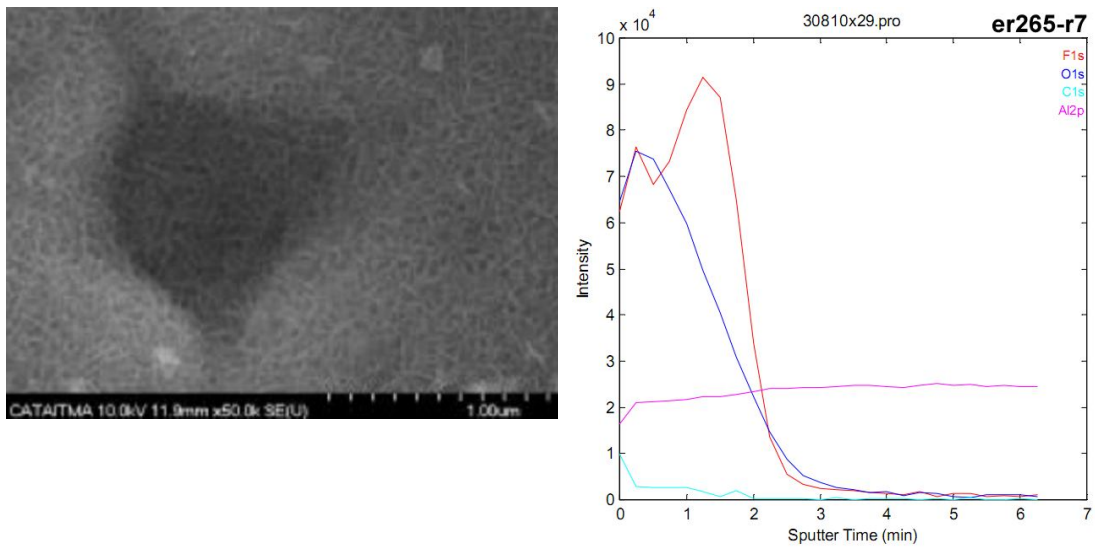


Figure 58 a and b: FESEM image after A2 dip and XPS depth profile before A2 dip of group er265-r7 (Ar/CF₄ plasma conditioning, t=20s, + O₂ plasma);

Group r5 with an additional EKC process compared to group r7 showed only the deposition of single small dendrites referring to figure 59a. Also a much lower value of the F -content ($I_F / I_O = 0.38$ for group r5) is measured which can be seen in figure 59b. As the only difference to the above discussed group 7 was the usage of the EKC cleaning process one assumption for this negative result was a contamination happened during the EKC process.

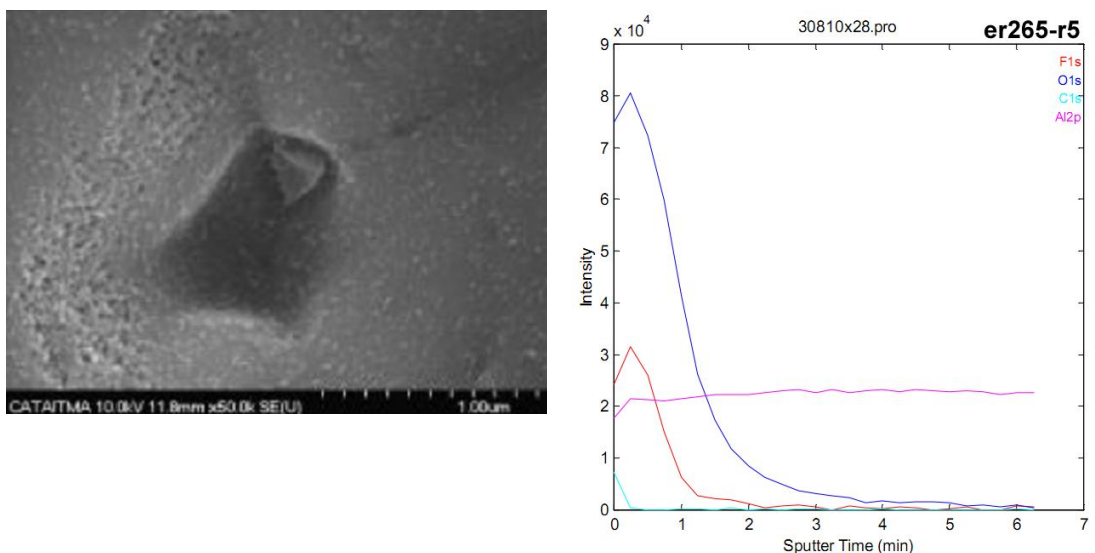


Figure 59a and b: FESEM image after A2 dip and XPS depth profile before A2 dip of group r5 (Ar/CF₄ plasma conditioning, t=20s, + O₂ plasma + EKC).

All other 5 groups showed negative results without any sign of deposition of an A2 layer after A2 dip in FESEM. For groups r-ref(#8) and r4 the FESEM results are shown as an example in figures 60a and 61a, respectively. The F contents for all analyzed groups are significantly lower compared to the groups with positive A2 growth discussed above ($I_F / I_O = 0.16$ for group r-ref-#8; $I_F / I_O = 0.31$ for group r4). The ratio of intensities of F and Al is too small to suggest any formation of AlF_3 as it can be seen in the XPS depth profiles in figures 60b and 61b. Especially for the latter result from group r4 it is to mention that the usage of an indirect F-containing plasma (CDE-overetch) did not lead to a significantly high incorporation of F into the Al surface and therefore did not lead to a activated Al surface. For the remaining 3 groups there was no XPS analysis done.

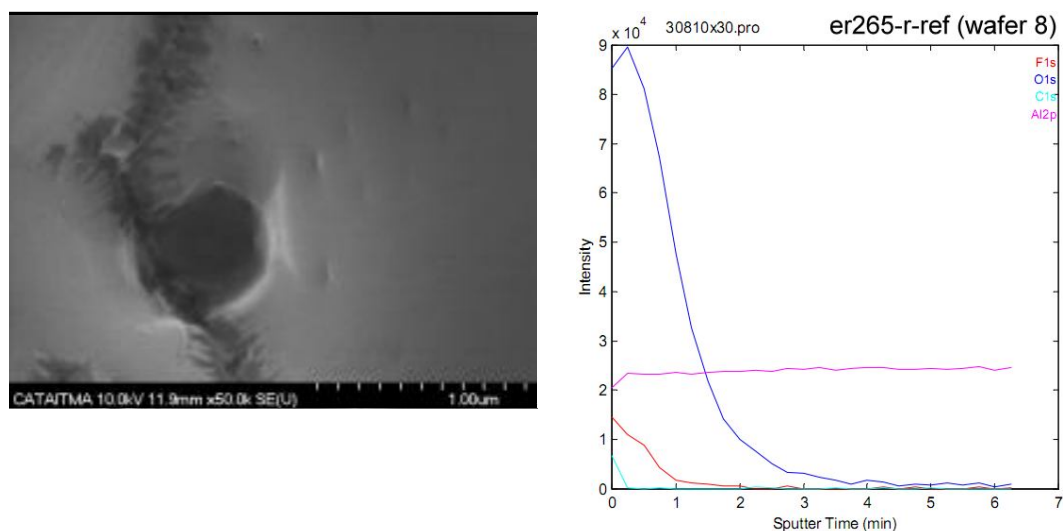


Figure 60a and b: FESEM image after A2 dip and XPS depth profile before A2 dip of group r-ref (reference without conditioning).

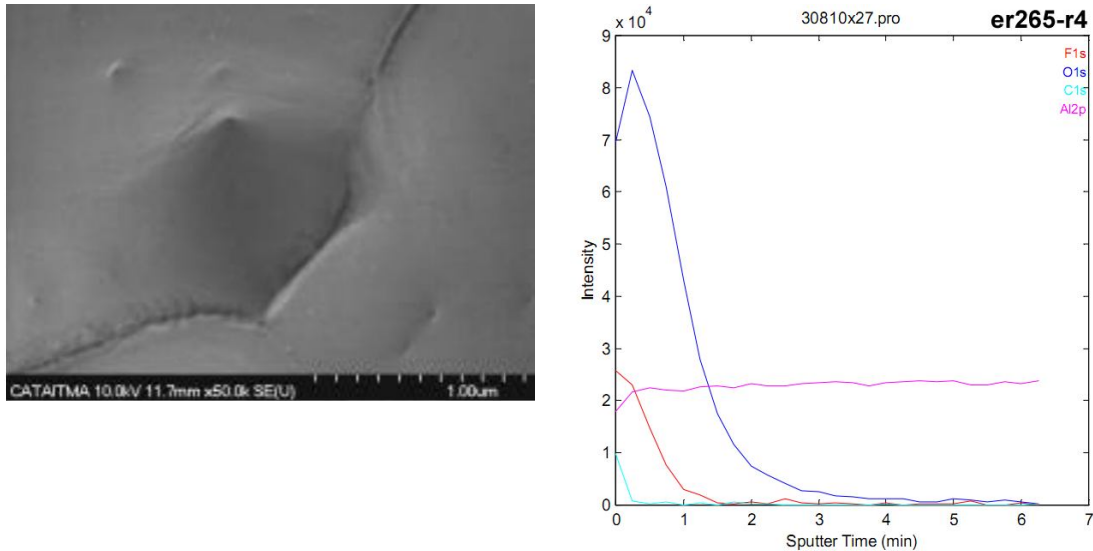


Figure 61a and b: FESEM image after A2 dip and XPS depth profile before A2 dip of group r4 (CDE-overetch conditioning).

These results basically show that with higher F content of the surface the reactivity of the Al-1Si-0.5Cu is increasing regarding attack from alkaline aqueous solutions. Two major questions remained unanswered at this point:

I: What nature has the inert surface prior to the Ar/CF₄ plasma condition leading to this high resistance to alkaline aqueous solutions?

II: How does the activated Al surface look like in terms of the chemical structure and derived from this how does it behave at the downstream processes? The formation of AlF₃ and AlO_F at the Al surface during the plasma treatment was indicated via XPS already.

To get an answer for the question I the XPS analysis of those groups with a negative result were refined. One suspect was the presence of highly stable fluorinated carbon, i.e. poly tetra fluorine ethylene (Teflon, PTFE) or lower fluorinated species [C₂F_xH_{4-x}]_n (2 < x < 4). That polymers are known to form especially for strongly anisotropic CF₄ plasma etching processes like they are used for dry etching processes during lithographic structuring of the wafer frontside, this is described for example by Hoppe [170].

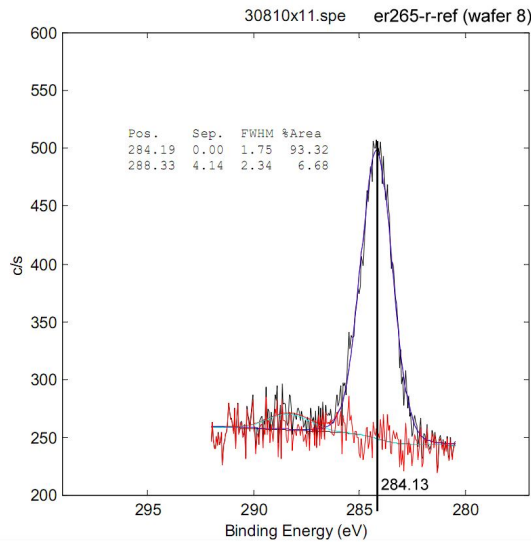


Figure 62: XPS spectrum of the C1s line at 284.13 eV typical for a C-C or a C-H bond. Example taken from group er265-r-ref.

Therefore from all analysed samples a high resolution scan of the C1s signal was done with XPS, figure 62 shows one example spectrum with the C1s peak at 284.13 eV. That binding energy is typical for a carbon atom within for example a aliphatic polymer ($-\text{CH}_2\text{CH}_2-$)_n ($E_B=285.00$ eV) or within aromatic hydrocarbons such as tetracene ($E_B=284.3$ eV) that can be found in the databank of National Institute of Standards and Technology NIST [171]. The C1s line of fluorinated polymers can be found in the energy range between $E_B = 286\text{eV}$ ($\text{C}-\text{CF}_x$) to 293eV ($\text{C}-\text{F}_3$) as shown by Cunge et al. [92] in an XPS spectrum of a Teflon^R sample, other sources indicate similar values, for example for $(-\text{CF}_2\text{CF}_2-)_n$ a binding energy of $E_B=292.60$ eV also given by NIST [171]. In none of the samples C1s signals of fluorinated carbon could be found. Therefore it was concluded that there was no deposition of polymeric $\text{C}-\text{F}_x$ during the different plasma etching processes in the downstream processes which might have built up an inert barrier on the Al-1Si-0.5Cu. The higher probability is seen in the formation of a thicker and more inert Al_2O_3 layer along the downstream processes forming a strong barrier towards the A2 deposition. This hypothesis is also supported by the fact that the A2 deposition is working positively on a fresh Al-1Si-0.5Cu sample with a native Al_2O_3 layer.¹

1 : This was seen in the experiment er265. In scratches applied to the metallisations before the A2-Dip for those groups with a negative A2 deposition result, the dendritic deposition could be observed within those scratches. This shows that the barrier in those groups can be removed mechanically and that the native Al_2O_3 forming inside of a scratch is much easier to activate during the A2 dip.

To get further answers to the second question, how the activated Al surface looks like in terms of the chemical structure and how it behaves at the downstream processes, further analysis with TEM and TOFSIMS were done¹. To study the thickness, crystallinity and chemical composition of the layer formed during the Ar / CF₄ plasma activation two samples were subjected to TEM and STEM with EDX. Sample er265-r-ref with negative A2 dip result and low F content in the surface layer and er265-r2 with positive A2 dip result and specifically high F content in the surface layer were chosen.

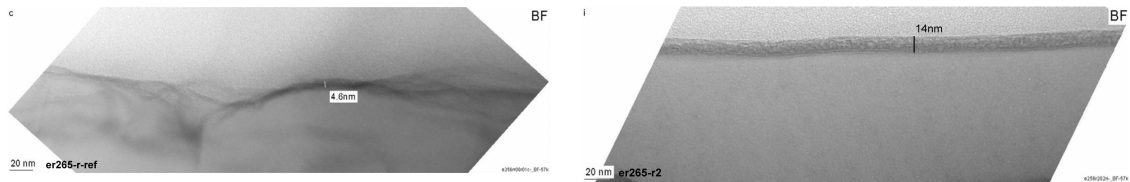


Table 63a and b: TEM image of sample er265-r-ref (left, no Al conditioning) and sample er265-r2 (right, 20s Ar/CF₄ Al conditioning with SuperE-overetch) showing significant differences of the Al oxide (4.6nm) and Al oxyfluoride (14nm).

In figure 63 a and b the TEM images of those two groups are shown. Group r-ref with a negative A2 deposition result shows a layer similar to Al₂O₃ with a thickness of 4.6nm, in the TEM section the layer appears amorphous shown in figure 63a. The thickness of that Al₂O₃ layer is at least by factor 2 thicker compared to a native Al₂O₃ layer having about 2nm thickness [47]. In contrast group r2 with a positive deposition result shows a much thicker layer of 14nm. In addition this layer appears to be very fine crystalline to amorphous with crystal sizes ≤ 5 nm referring to figure 63b.

¹ : TEM analysis was performed with the help of Dr. Andreas Rucki from Siemens CT- TOFSIMS analysis was provided from Dr. Treichler from the same department.

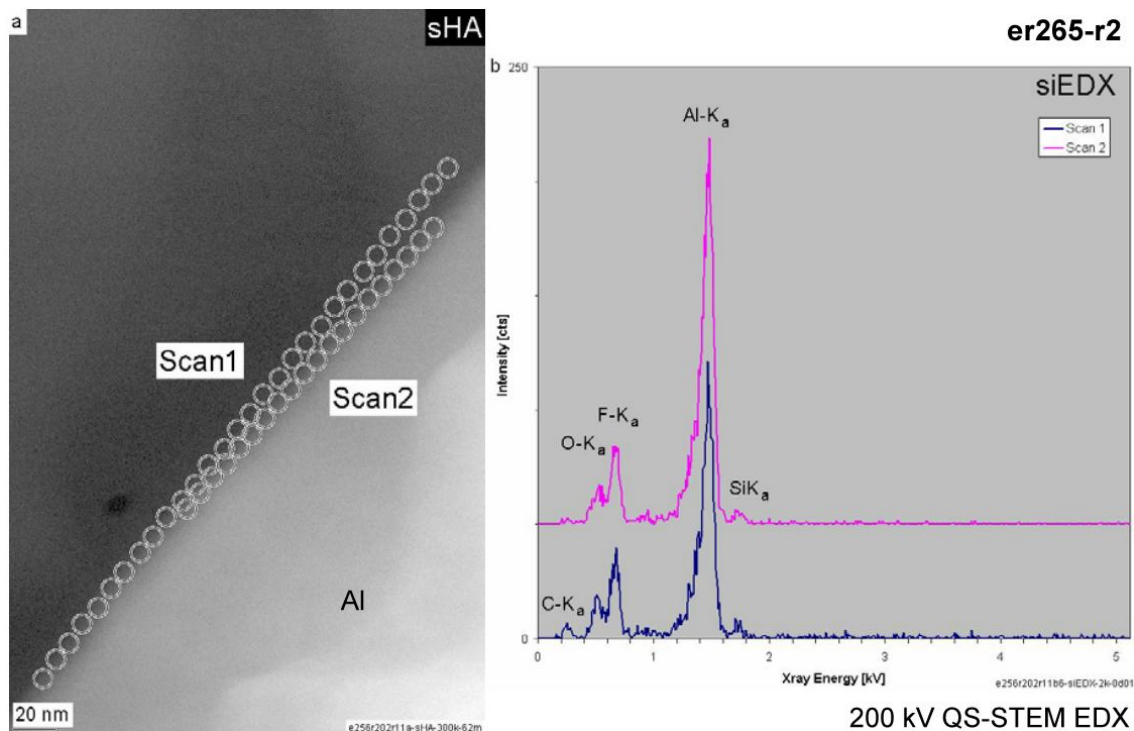


Figure 64a and b: 200kV STEM EDX, two line scans side by side. The spectra of the individual scan are added together to form one spectrum for scan 1 and one spectrum for scan 2.

Two parallel STEM EDX line scans of the 14nm thick layer in group r2 resulted in similar spectra with an Al K_{α} -line, a F K_{α} -line and a O K_{α} -line confirming also the presence of F in the layer. In figure 64 a the TEM section with the respective line scans can be seen, figure 64 b shows the two corresponding EDX spectra. However, due to the rapid change of the very thin sample during electron bombardment in the TEM chamber a quantitative interpretation was not possible.

Additionally to the XPS analysis TOF SIMS analysis were performed for samples of 6 groups of experiment er265 to get information about possibly trace elements that cannot be detected adequately via XPS. Surface mass spectra and consequently depth profiles were performed on those samples after the specific wafer processes.

In the surface mass spectra for the negative ions all samples show signals for AlO_x and AlO_xF_y clusters but for those groups with a positive A2 deposition result those signals are much more pronounced.

An example is given in figure 65 a and b showing the negative ion mass from 0 to 800u of two groups that are group er265-r-ref without Al conditioning with a negative A2

deposition and group r2 with an Ar / CF₄ conditioning with positive A2 deposition. The proposal of species for the respective masses was done by the TOFSIMS equipment databank.

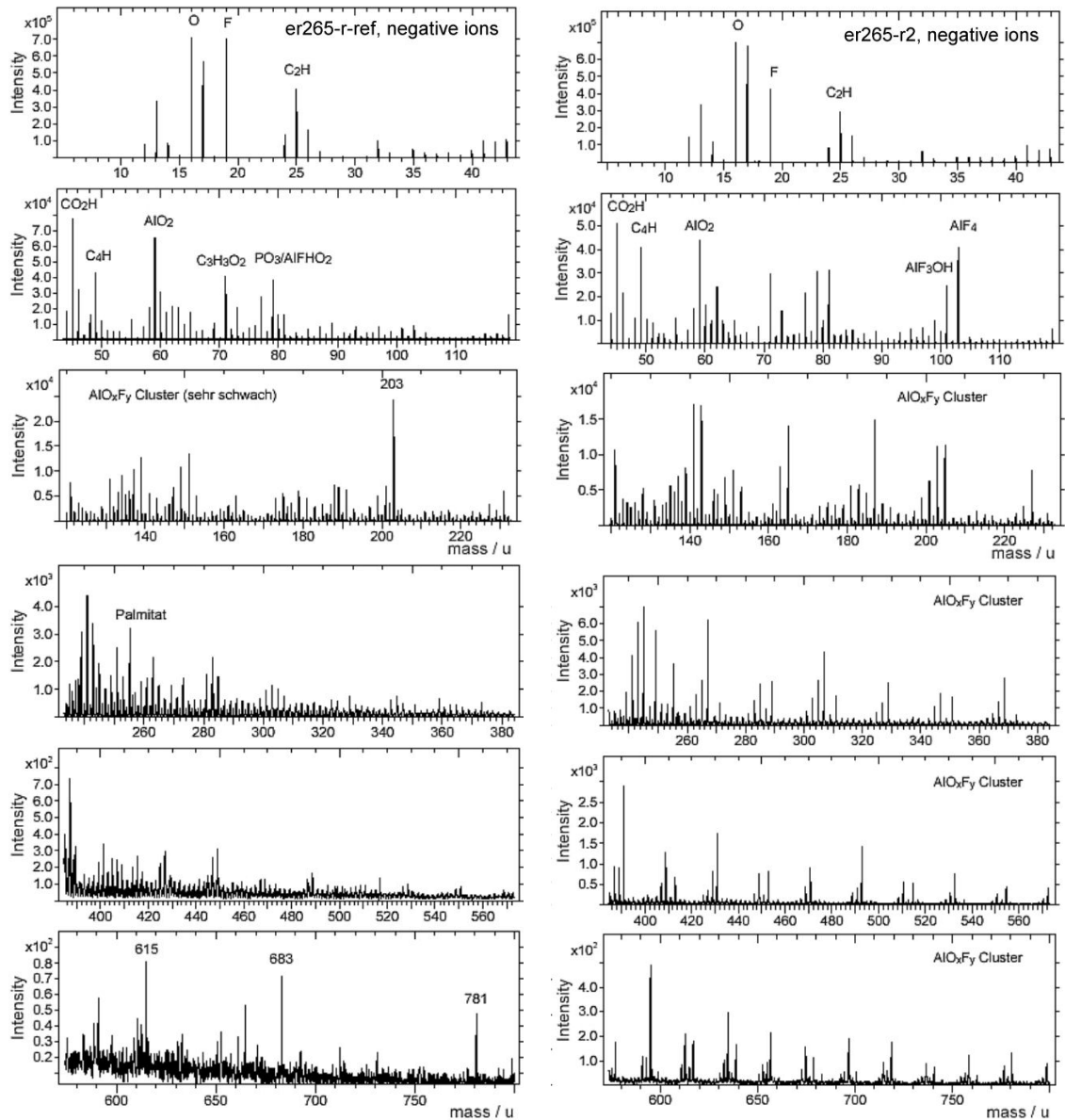


Figure 65 a and b: TOF SIMS mass spectra of negative secondary ions of surfaces within group er265-r-ref (no plasma conditioning) on the left side and group er265-r2 (20s Ar/CF₄ plasma conditioning) on the right side.¹

¹ : Group numbering differs slightly between experimental matrix (r-ref and r2) and TOFSIMS analysis files (#8(-) and #2(-)) respectively.

In figure 65 b the sample r2 shows regular patterns that were identified as AlO_xF_y clusters between a mass of 140u and 800u. These signals are very soft or are even absent for the spectrum of sample r-ref shown in figure 65 a. This gives an indication of AlOF presence in the layer especially within those experimental groups which have a well-conditioned surface for A2 deposition as it is the case for group r2.

In addition, for the given example in group r2 around a mass of 100u in figure 65 b clusters of $[\text{AlF}_3\text{OH}]^-$ and $[\text{AlF}_4]^-$ appear as indicators for the presence of AlF_3 on the surface. Those masses are not detected in the spectrum of the reference group r-ref shown in figure 65 a.

Furthermore there is a slightly bigger amount of hydro carbons detected on the reference group r-ref from 220u to 280u (e.g.: palmitate; $[\text{C}_{16}\text{H}_{31}\text{O}_2]^-$; 255u) that is softer for sample r2. This indicates an cleaning effect of the Ar/ CF_4 plasma conditioning process for the sample r2.

Additional signals of for example $[\text{O}]^{2-}$, F^- , and $[\text{AlO}_2]^-$ had similar intensities for both example groups, besides that there were also masses of negative ions which could not sufficiently be identified from the databank of the TOFSIMS equipment (e.g. 615u, 683u, 781u).

For those two examples r-ref and r2 also the positive mass spectra were recorded shown in figure 66 a and b respectively.

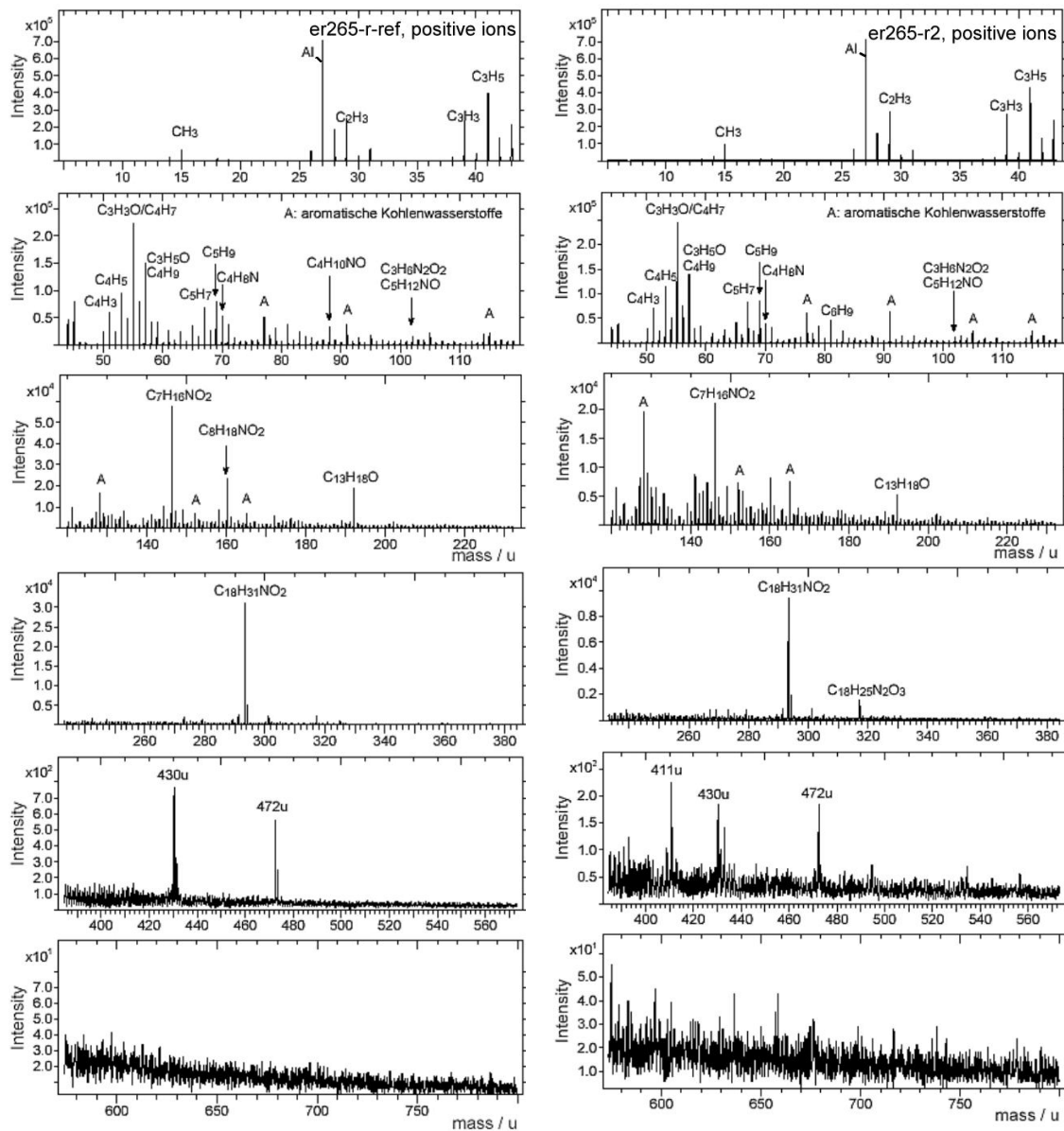


Figure 66 a and b: TOF SIMS mass spectra of positive secondary ions of surfaces within group er265-r-ref (no plasma conditioning) on the left and group er265-r2 (20s Ar/CF4 plasma conditioning) on the right side.¹

Comparing the surface mass spectra of the positive ions then on both samples r-ref and r2 several aromatic hydro carbon fractals were detected together with nitrogen and oxygen containing hydro carbons between a mass of 0u and 220u as shown in figure 66

¹ : Group numbering differs slightly between experimental matrix (r-ref and r2) and TOFSIMS analysis files (#8(+) and #2(+)) respectively.

a and b, respectively. The latter sample showed stronger signals in this mass area, but for both samples these species were regarded as contamination due to sample handling and therefore not further interpreted.

Several additional signals for higher masses > 220u were detected on both samples such as for example $[C_{18}H_{31}NO_2]^+$ or unidentified species with a mass of 430u and 472u. Especially the N containing fractals may be due to residuals from preceding processes from lithography as those molecules are present in resins and may be further carried along the processes. Also for this mass range from 220u to 800u a sample contamination was considered to overlay the analytical results of the surface analysis. One species with a mass of 411u was found to be present only on sample r2 as shown in figure 66 b, but there was no identification possible with the available databank of the TOFSIMS.

In addition to the surface spectra also depth profiles brought out significant results. For example the F distribution in the different groups which is shown in figure 67 as an overlap of all 6 analyzed samples showed differences of both the F intensity maximum and the depth of the F-distribution in the top layer.

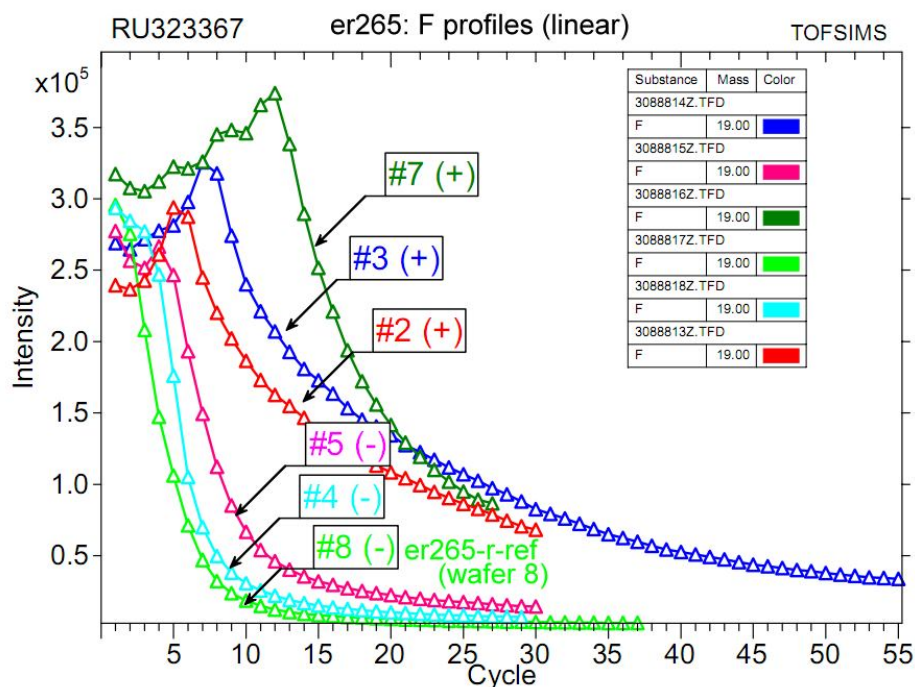


Figure 67: Overlap of TOF SIMS depth profiles of fluorine for all analyzed groups of er265.

The results obtained here are correlating with the findings from XPS studies. For the three groups r2, r3 and r7 with positive A2 deposition behaviour a higher F content within the surface layer appears. Also the maxima of the F content are confirmed for group r2 and r7. The maxima for group r3 and r7 are much deeper inside the layer which can be due to the longer plasma etching time (40s) for group r3. For group r7 the additional O₂ plasma conditioning after the Ar/CF₄ plasma etching seems to push the F peak further into the metallisation through oxidation of the surface.

Besides the F also other species were measured during the recording of the depth profiles, in figure 68 a and b the patterns of group r-ref (no plasma conditioning) and group r2 (20s Ar/CF₄ plasma conditioning) are shown for the negative masses.

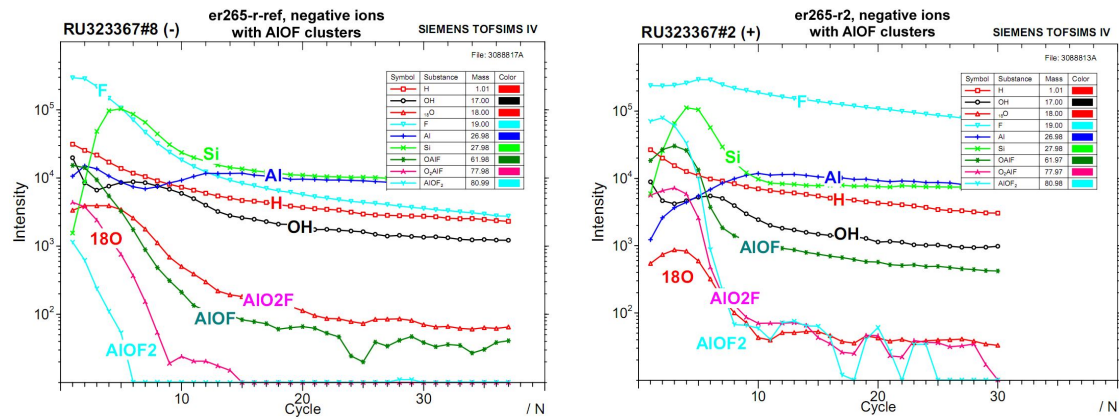


Figure 68a and b: TOF SIMS depth profiles of negative ions from group er265-r-ref (no plasma conditioning) on the left and group er265-r2 (20s Ar/CF₄ plasma conditioning) on the right side.

Depth profiles on other species for negative ion mass spectra can be summarized as follows: On both samples an enrichment of Si is seen. As the metallisation is consisting of a Al-1Si-0.5Cu alloy also SiO₂ or mixed oxides may be present at the surface especially because the formation of SiO₂ may be favoured due to the very high free enthalpy of formation of $\Delta G_f^0 = -856.4\text{kJ/mol}$ which is larger when compared to the value for Al₂O₃ formation with $\Delta G_f^0 = -791.2\text{kJ/mol}$ of metal, both values given by Dan's et al. [2]. The species [AIOF], [AIO₂F], and [AIOF₂] show much higher intensities in sample group r2 (20s Ar/CF₄ plasma conditioning) when compared to reference group r-ref (no plasma conditioning), also the thickness of the layer with presence of those species is much higher in group r2. In figure 69 the total counts within the first 10

sputter cycles during TOF SIMS depth profile recording are summarized in a chart for those three species.

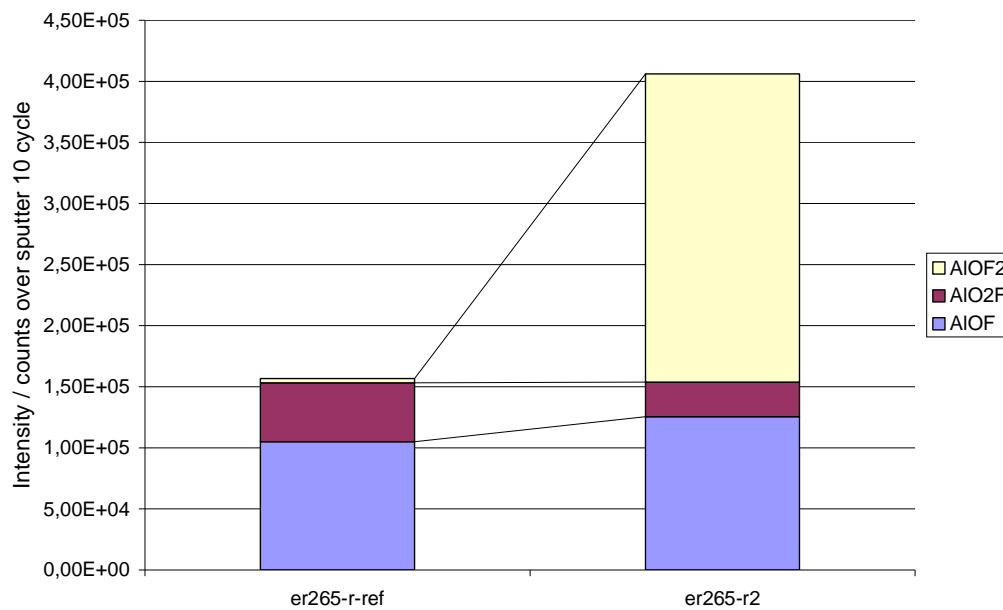


Figure 69: Comparison of the intensities from TOFSIMS depth profile signals of the species [AlOF₂], [AlO₂F], and [AlOF] integrated for the first 10 sputter cycles.

The chart shows that the intensity of [AlO₂F] is slightly reduced. For [AlOF] a slight increase is observed, furthermore for the species with the highest F content [AlOF₂] an increase of factor 71 is observed. The latter result indicates the presence of AlF₃ in the layer of the groups with high F content, i.e. group r2. This result is in accordance with the XPS analysis reported and discussed above.

On the side of the additional species for the positive ion depth profiles there are less differences detected between sample r-ref and r2 as shown in figure 70 a and b, respectively.

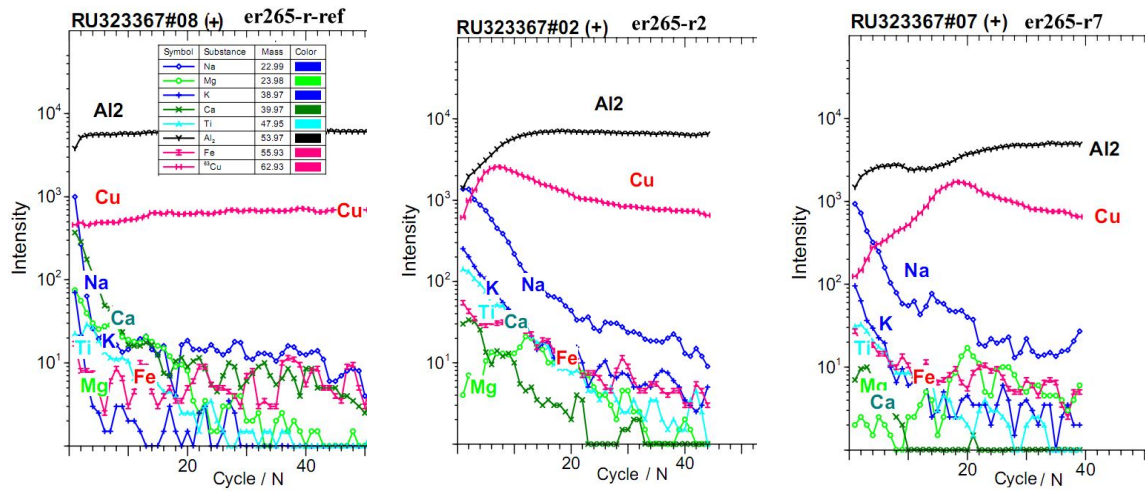


Figure 70 a to c: TOF SIMS depth profiles of positive ions from group er265-r-ref (no plasma conditioning) on the left (a), group er265-r2 (20s Ar/CF₄ plasma conditioning) in the middle (b) and group er265-r7 (20s Ar/CF₄ plasma conditioning and O₂-plasma) on the left (c).

The major difference is the shape of the Cu signal that has a peak for the Ar/CF₄ plasma conditioned sample r2 shown in figure 70 b. This accumulation of the Cu at that point cannot be explained sufficiently, a hypothetical explanation may be based on accumulation of Cu due to the formation of the AlF₃ / AlOF layer pushing the Cu more towards the bulk material of the Al-1Si-0.5Cu metallisation. As this Cu peak was observed in all 3 groups with a plasma conditioning sufficient for A2 deposition this hypothesis gets more probable. For group r7 with the additional O₂ plasma process this peak is much more pronounced and reaches down to a depth of 20 sputter cycles as in the case of group r2 with the peak being located at a depth of 10 sputter cycles.

The interpretation is that the Cu is pushed by both the formation of the AlF₃ / AlOF and by the formation of the oxide containing top layer in this experimental group r7 as shown in figure 70 c.

Traces of various other metals within this analysis were not further considered because they are obtained at the detection limit of the used method with large signal noise of the individual species. Only the signal of Na should be mentioned here that was more pronounced for sample r2 and r7 which may be an indication that the formed AlF₃ / AlOF has more tendency to incorporate Na from ambient exposure of the samples compared to the Al₂O₃ layer found in the reference sample r-ref.

Summary:

To sum up, by experiment er265 nine groups with various plasma processes were investigated to achieve and study a conditioning of the Al-1Si-0.5Cu metallisation on wafers for proceeding with A2 deposition. The success of A2 deposition was analysed with FESEM after A2 dip to trace the formation of the sponge like and dendritic A2 layer on the Al-1Si-0.5Cu metallisation. Plasma conditioning with an Ar/CF₄ process gas turned out to have the best effect for surface activation. Analysis of the formed layer by XPS showed a clear correlation between the F content and the reactivity of the surface for A2 deposition. TEM analysis showed a relatively thick and crystalline layer of 14 nm in contrast to the unconditioned surface with an amorphous layer of about 4nm that is still by factor 2 higher compared to a native Al₂O₃ layer having only 2 nm thickness. TOFSIMS analysis confirmed the findings of XPS studies with a clear correlation that high F content leads to a high reactivity of the Al-1Si-0.5Cu surface for A2 deposition and vice versa.

Furthermore, after TOFSIMS studies it can be stated that the active layer is composed by a mixture of AlF₃ and AlOF. Si and Cu alloy partners undergo an accumulation directly under the surface most probably due to the plasma conditioning process which did not have an influence on the A2 deposition capability. Finally, several organic species were found at the surfaces from preceding manufacturing processes and from sample preparation.

5.2.4 Integration of Ar / CF₄ plasma process for activation of the Al chip metallization in the process flow (er269, er270)

Referring to the results obtained by experiment er265 in the previous section a suitable Al surface conditioning step is an Ar/CF₄ plasma conditioning process on the wafer. The next step was to refine the respective process parameters and to consider the major constraints within the process flow between the plasma conditioning process on the wafers and the A2 deposition on the soldered and wire bonded device. It can be seen in table 8 in chapter 4.1.1 that between those two processes there are multiple other stages and several specific processes that must be considered. As two examples the etching

effect of the plasma on the BPSG (boron phosphorus silicon glass) layer and the influence of the chip soldering process will be discussed here.

To obtain suitable parameter settings for the plasma etching a similar experiment like er265 was conducted again on wafer with A2 dip and FESEM analysis called VE322803. In addition to the fine tuning of the plasma etching parameters an additional focus was set on the integration of the process into the product manufacturing flow. This requires also checking the influence of the Ar/CF₄ plasma process to other surfaces on the wafer apart from Al-1Si-0.5Cu. The F-based plasma etching occurs also on BPSG, which is used as an isolation layer between individual metal lines on the chip, due to its chemical nature as a doped SiO₂. F radicals react with this material forming volatile Si species such as SiF₄. This second experiment confirmed the Ar/CF₄ plasma etching process on equipment from Lam Company as an effective conditioning process to obtain a reactive Al-1Si-0.5Cu metallisation for A2 deposition with an etching time of only 15s. The etching rate of BPSG was found to be 137 nm as shown in figure 71 after this process.

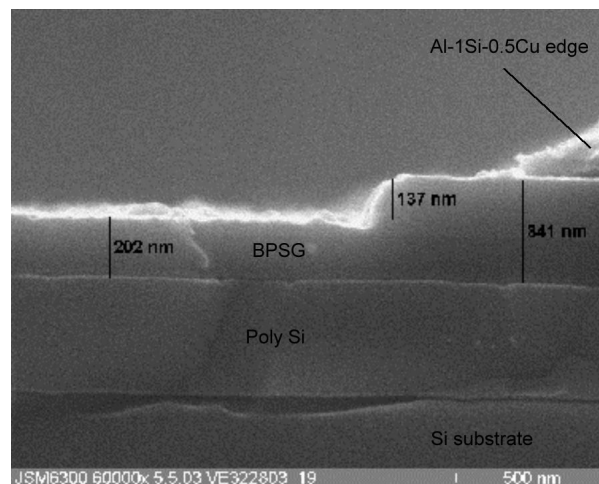


Fig 71: FESEM of cross section of experiment VE322803. Etching rate of BPSG within the 15s Ar/CF₄ conditioning process is 137nm per 15s.

The initial thickness of the BPSG was 340nm, the remaining thickness of 200nm BPSG was considered to be a low risk for the electrical isolation behaviour of the MOSFET. Nevertheless in the following experiment the Ar/CF₄ etching time was further reduced to t=10s.

In this experiment er269 the assessment of the various surfaces generated from the different plasma conditioning process conditions was done with the complete downstream processes and the real A2 deposition process with the productive manufacturing equipment. A SFET2 MOSFET (Basic type: L1855R; chipsize: 30.15mm²; Lot: VE330903) was used in a TO263-3 package with standard wafer processes and package processes including chip soldering like described in table 8 in chapter 4.1.1.¹

Plasma conditioning was done in two steps for each group, the first step being a etching with 600W for 10s with ignited plasma, and the second step being a purging without any plasma. In groups er269-1 to 4 and 9 plasma conditioning was done with a mixture of Ar and CF₄ in the plasma chamber with a variation of the CF₄ concentration controlled via the mass flow controller of the gas supply. In this plasma Ar, F and CF_x radicals are forming at the same time, attacking the surface of the wafer frontside. After the first step in those groups the purging was done with N₂.

For experiments er269-5 to 8 a different approach was tried to show, whether the formation of a AlF₃ / AlOF layer is happening also with the activated Al surface by purging with a mixture of O₂ and CF₄ after the first plasma etching step with Ar. Here during the first step only Ar radicals are present in the plasma removing organic layers and damaging the Al₂O₃-layer. The hypothesis was founded on the hypothesis that during subsequent purging with a mixture of O₂ and CF₄ the highly reactive Al surface may react with the gas forming AlF₃ / AlOF.

To measure the F content on the obtained Al-1Si-0.5Cu metallisation before the A2 deposition samples were taken out to record a Auger depth profile from each group. After A2 deposition the surfaces were analysed with FESEM and rated according to the morphology catalogue from chapter 2.1 with quality is decreasing from A (best) to D (worst). Both results were compared to derive the Ar/CF₄ plasma etching process parameters for obtaining the optimum behaviour during A2 deposition that is correlated with the F content within the Al top layer in the various groups. In addition, the

¹ : The experimental work and integration of the surface conditioning process into wafer manufacturing was done together with Dr. Zechmann Arno and his team at Infineon Villach in Austria.

discolouration of the metallisation was recorded after the long A2 process, that was run with $t=20$ s, $i = 60 \text{ mA}\cdot\text{cm}^{-2}$, $\Theta = 58 \text{ }^\circ\text{C}$, and standard A2 electrolyte as defined in table 29 in chapter 5.3.3. The activation within the A2 process was also done standard with $t = 10$ s activation time in aqueous MSA solution at $\Theta = 25 \text{ }^\circ\text{C}$. The matrix and overview on the obtained results is shown in table 25.

Group	1	2	3	4	5	6	7	8	9
Wafer #	1	3	8	9	11	16	18	19	23
Plasma	Step 1. Ar / CF ₄ : 10s; 600W; 450cm ³ /min Ar; CF ₄ flow [cm ³ /min]				Step 1. Ar plasma: 10s; 600W; 450cm ³ /min Ar;				standard (10s; 600W; 450cm ³ / min)
	Step 2. Purge with N ₂ .				Step 2. Purge with V (O ₂ /CF ₄) without plasma.				
Step 1: CF ₄ flow [cm ³ /min]	40	30	20	10	-	-	-	-	50
Step 2: O ₂ flow ratio of flows [cm ³ /min]	-	-	-	-	4	8	15	40	-
Step 2: CF ₄ flow [cm ³ /min]	-	-	-	-	40	40	40	40	-
Step 2: V(O ₂ /CF ₄)	-	-	-	-	1:10	1:5	1:3	1:1	-
Ratio I _F / I _O in Auger depth profile	0.73	0.57	1.10	0.85	0.17	0.17	0.17	0.13	0.83
FESEM category of A2 layer at top row	A	B	A	A	D	D	D	D	A
FESEM category of A2 layer at bottom row	A	A	A	A	D	D	D	D	A
Discolouration of Al-1Si-0.5Cu after A2 deposition	high	high	medium	low	no	no	no	no	high

Table 25: Experimental matrix of er269 with a variation of the CF₄ gas flow during anisotropic direct plasma etching (group 1 to 4 and 9) and purging with various CF₄ flow rates (group 5-8) on a Rainbow equipment from LAM company. FESEM A2 quality is decreasing from A (best) to D (worst).

The results of FESEM obtained in groups er269-1 to 4 and 9 are similar positive with only category A and one category B morphology. The ratio I_F / I_O in the Auger depth profiles were in the range of 0.57 to 1.10 throughout those groups. Still at a value of I_F / I_O = 0.57 the deposition of the A2 layer was possible on the Al metallisation of the chip, but at the top row of the leadframe within the A2 process morphology category B was seen already as shown in table 25 in group 2. In figures 72a to f FESEM and Auger depth profiles of three example groups are shown.

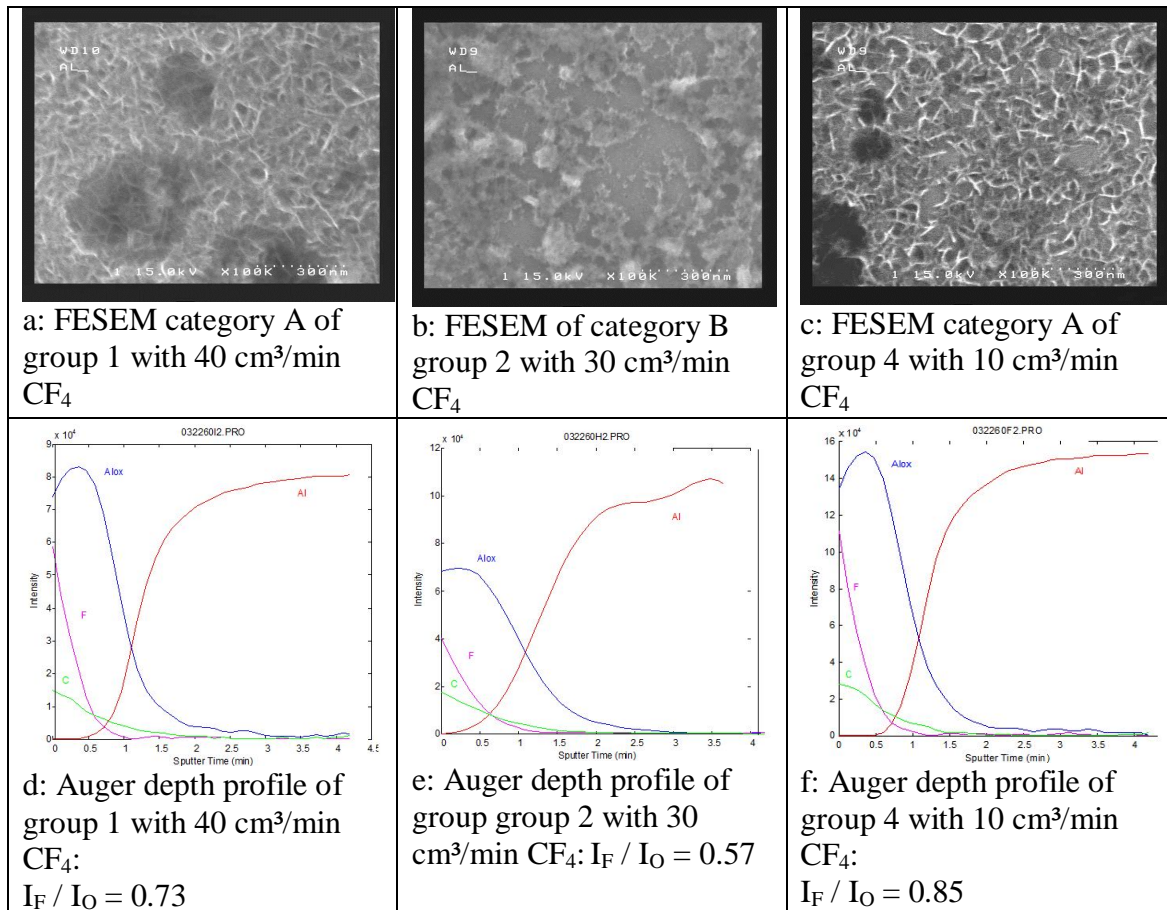


Figure 72 a to f: Example of FESEM and Auger results obtained from groups er269-1, -2, and -4. The FESEM pictures were taken from the top row of the leadframe after A2 deposition which is the worst case condition; Auger samples were taken before A2 deposition.

In figure 72 b and e the FESEM and Auger depth profile is shown for that experimental group representing the critical limit of F content indicated by a value of $I_F / I_O = 0.57$ in the Auger depth profile and indicated by the category B morphology of the A2 layer shown in the FESEM. The example groups 1 and 4 in figure 72 a and c respectively showed a much better morphology of category A. The corresponding Auger depth profiles shown in figure 72 d and f brought out much higher F content with values of $I_F / I_O = 0.73$ and $I_F / I_O = 0.85$, respectively. This indicates, that a value of $I_F / I_O = 0.57$ is near to a limit of the reactivity and its value should not be lower.

For the remaining groups er269-5 to 8 the FESEM results showed no deposition of any A2 layer, therefore the rating given was category D. Examples are shown in figure 73 a to d for groups 5 and 8.

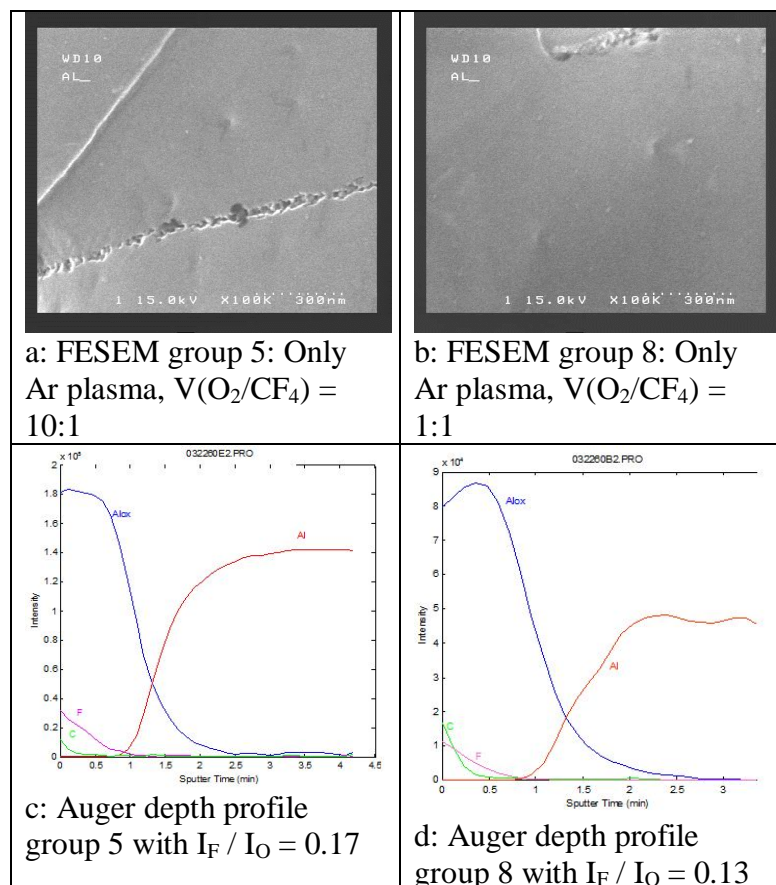


Figure 73a to d: Example of FESEM and Auger results obtained from groups er269-5 and 8. The FESEM pictures were taken from the bottom row of the leadframe after A2 deposition which is the best case condition; Auger samples were taken before A2 deposition.

Both groups 5 and 8 showed a low F content with $I_F / I_O = 0.17$ and $I_F / I_O = 0.13$ respectively as shown from the Auger depth profiles in figure 73 c and d. In correlation to this for both samples in FESEM no A2 deposition was observed, figure 73 a and b only show the bare Al-1Si-0.5Cu surface. Obviously in the 2-step conditioning process the Al-1Si-0.5Cu surface was not properly activated from the Ar plasma in step 1 and the purging with O_2 and CF_4 in step 2 did not lead to a F content of the surface that is high enough to form AlF_3 or $AlOF$. The low ratio of I_F / I_O in the range of 0.13 and 0.17 indicated mainly the presence of Al_2O_3 and lack of AlF_3 or $AlOF$.

The observed discolouration of the Al-1Si-0.5Cu surface with optical microscopy showed also a significant difference between the various groups. Three examples are shown in figure 74.

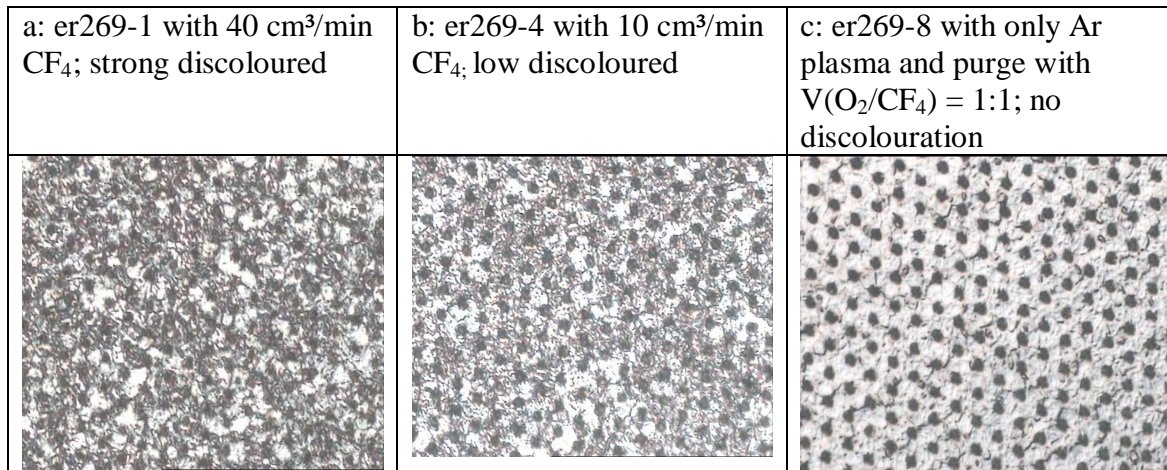


Figure 74 a to c: Microscopy images with a magnification of 500x showing three examples of the discolouration of the Al-1Si-0.5Cu metallisation with rating "strong", "low", and "no discolouration" from left to right.

Unfortunately those groups with positive results at A2 deposition show discolouration which is a sign for grain boundary etching of the Al-1Si-0.5Cu as it can be seen in figure 75 b. For example group 1 as shown in figure 74 a shows strong discolouration even with a good A2 deposition quality. In contrast to this group 8 showed no discolouration pointed out in figure 74 c but also did not reveal any A2 deposition. As a compromise group er269-4 was chosen with 10 cm³/min CF₄ flow showing only low discolouration and still a A2 morphology that was rated with quality A in the FESEM.

This results show one weakness of this specific activation concept for the aluminium metallisation with an Ar / CF₄ plasma conditioning. It is not possible to reach a optimum level of fluorine at the surface because the high reactivity of the metallisation with the A2 electrolyte entails a stronger grain boundary etching and also the risk of ion penetration through the metallisation. In the case of Al-1Si-0.5Cu for a SFET2 MOSFET with a thickness of 5µm this is acceptable for the specified device lifetime, but this can get critical for other semiconductor technologies with thinner metallisation. In the next chapter 5.2.5 the further development of this activation concept will be discussed to overcome this problem.

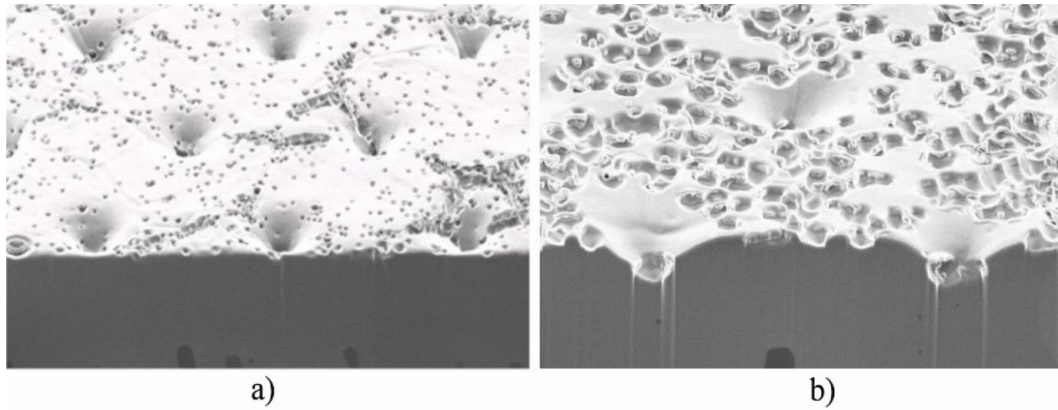


Figure 75: Image of FIB cuts into the Al-1Si-0.5Cu metallisation after A2 deposition. a) shows the surface of a normal discolouration whereas b) shows the surface of a strong discoloured sample (picture taken from experiment JL008 from Lodermeier [172]).

Due to the fact that the F content within the Al-1Si-0.5Cu top layer is a critical parameter for the activity of the aluminium for A2 deposition, also the influence of the chip soldering process was checked. Especially during longer soldering stop times under those conditions being $\Theta=400^{\circ}\text{C}$ in forming gas consisting of 5% H_2 in N_2 changes of the AlF_3 / AlOF_3 surface may happen.

In experiment er270 various chip soldering line stops were checked with the same device used in experiment er269 above. The Al-1Si-0.5Cu was Ar/ CF_4 plasma conditioned according to group er269-4. The results obtained from FESEM can be seen in table 26.

Stop time chip soldering	0 min (control group)	5 min	10 min	15 min
FESEM of Al-1Si-0.5Cu	A	A	C	C
FESEM of NiP surface	A	A	C	C

Table 26: Results from experiment er270, FESEM after A2 deposition was done on 4 positions for each group on Al-1Si-0.5Cu and on the NiP surface. The quality rating was done with A (best) to D (worst).

Starting with 10 min stop time at the chip soldering process a degradation of the A2 deposition quality can be observed for both the Al-1Si-0.5Cu substrate and the NiP substrate. This result shows a second weakness of this activation concept with a Ar/ CF_4

plasma process, the obtained AlF_3 / AIOF surface seems to be unstable during its exposure at higher temperature leading to a bad process result at the A2 deposition.

To avoid wafer batches with a surface of the Al metallisation that is unsuitable for A2 deposition a dedicated process control with A2 dip, FESEM and ellipsometry was installed during the first time of production within the wafer manufacturing. Especially the former method led to high yield loss because the A2 dip is a destructive test. This was another weakness of this activation concept which required further investigations that are shown in the next section.

Summary:

The integration of an Ar/CF_4 plasma conditioning process on wafer was done considering all downstream processes until A2 deposition. The F content of the surface layer of the Al-1Si-0.5Cu metallisation after the conditioning was found to be a major control parameter. A refinement of the Ar/CF_4 plasma process parameters was done leading to $P=600\text{W}$, $t=10\text{s}$, $450\text{ cm}^3/\text{min}$ Ar; $10\text{ cm}^3/\text{min}$ CF_4 on an equipment from Lam corporation. The limit of F content within the AlF_3 / AIOF top layer that still leads to a good A2 deposition quality was found to be $I_F / I_O = 0.57$ in the Auger depth profile. High temperature downstream processes have an influence on the activity of the aluminium surface, for example stop times at chip soldering process at $\Theta=400^\circ\text{C}$ in forming gas consisting of 5% H_2 in N_2 with more than 5 minutes decrease the quality of A2 deposition on the aluminium chip metallisation. On the other hand activation with this plasma process can also lead to surfaces with very high reactivity leading to the risk of grain boundary etching of the Al-1Si-0.5Cu metallisation during A2 process with the risk of ion penetration into the MOSFET device. Both extremes, the reactivity being too low and the reactivity being too high, are difficult to control in production along a long chain of various processes and require an extensive process control with A2 dip, FESEM and ellipsometry. In addition, by the very short ignition time of the plasma for the Al conditioning process of $t = 10\text{ s}$ a stabilization of the conditions within the plasma chamber becomes very difficult. In consequence, this fact triggered further modifications of the Ar/CF_4 plasma process together with the A2 process via the increase of the plasma etching time from 10s to 15s and by reduction of the A2 deposition time from 20s to 10s.

5.2.5 Aluminium activation in A2 process with HF chemistry and Ar / O₂ plasma conditioning of wafer

The limitations of the initial activation concept for the Al metallisation of the chip given in the last section have generated two new important questions.

I. How can the Ar/CF₄ plasma conditioning process be substituted by a surface conditioning that generates a more stable Al surface?

II. How can this Al surface then be activated inline during the A2 process?

The second question was investigated first because the motivation was to find a chemistry for the activation section at the A2 process that is capable to activate also the Al surface of the chip that is not plasma treated. In consequence this would mean that no additional plasma conditioning process would have to be run simplifying manufacturing of the wafers. Therefore in the first experiment in the laboratory chips with an unconditioned Al-1Si-0.5Cu surface were used and activation with either an aqueous NaF solution or with a HBF₄ solution was done as shown in the experimental matrix in table 27. The samples were analysed by Auger spectroscopy to measure the amount of F on the Al surface and in parallel a A2 dip was performed at two different temperatures for subsequent FESEM analysis to identify any kind of A2 deposition and its morphology. The rating was done again with quality A (best) to D (worst).

er318	A1	A2	A3	B1	B2	B3	ref1	ref2
Activation chemical	NaF 0,1 mol/l			25 %wt HBF ₄			no activation	
Activation time [s]	10	60	10	10	60	10	n.a.	n.a.
A2 dip (t=15s) at Θ [°C]	25	25	60	25	25	60	25	60
FESEM result [category]	D	D	D	C	B	B	D	D
Ratio I _F / I _{Al-oxide} from Auger	n.a.	0.05	n.a.	0.21	n.a.	n.a.	0.03	0.03

Table 27: Experiment matrix of er318 for investigation of activation of Al-1Si-0.5Cu with NaF or with HBF₄ solution.

The results of this experiment also confirm the correlation of the F content within the Al₂O₃ of the Al-1Si-0.5Cu and the activity for A2 deposition during A2 dip. The groups A1 to A3, that have been activated in a solution of 0.1 mol/l NaF, did not show any signs of deposition in the FESEM. The same as expected was found in the two reference groups ref1 and ref2 without any activation and for both A2 dip temperatures of 25 °C

and 60 °C. In figure 76a to d the Auger depth profile of the Al surface and the FESEM of the obtained A2 morphology after the A2 dip is shown.

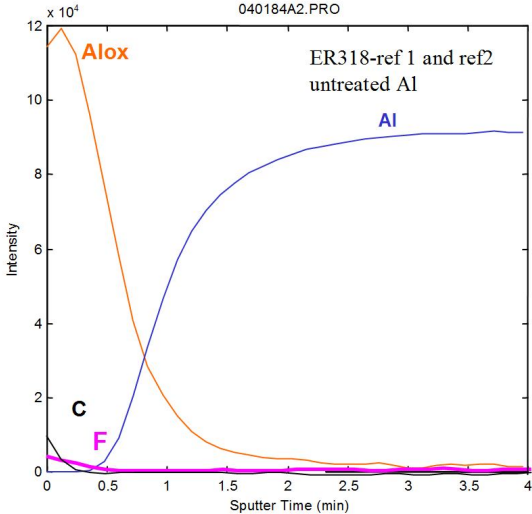


Figure 76 a: Auger depth profile of sample er318-ref2 (no activation)

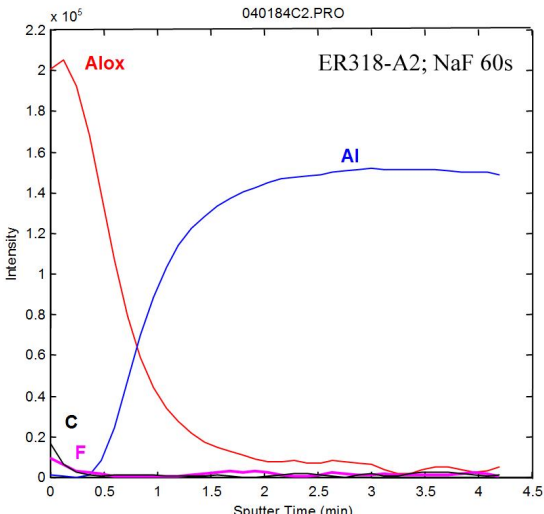


Figure 76 b: Auger depth profile of sample er318-A2 (activation with NaF solution)

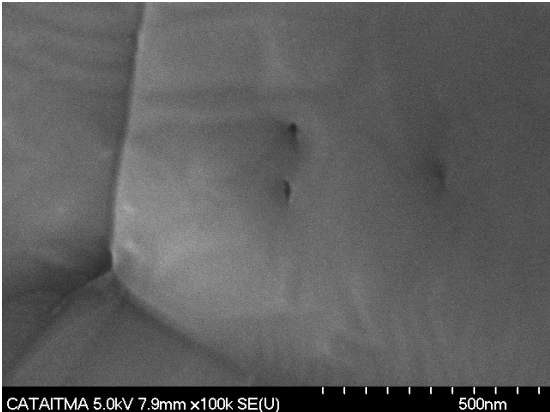


Figure 76 c: FESEM after A2 dip at $\Theta=60^\circ\text{C}$ of sample er318-ref2 (no activation)

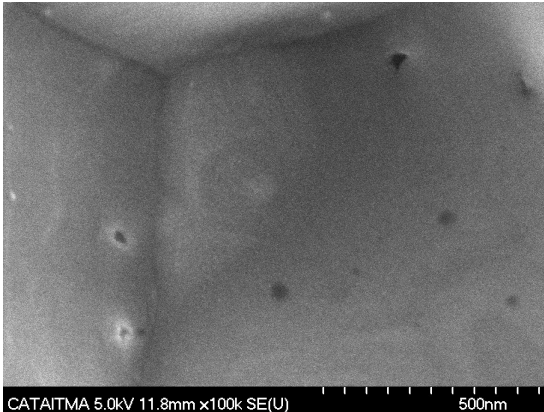


Figure 76 d: FESEM after A2 dip at $\Theta=25^\circ\text{C}$ of sample er318-A2 (activation with NaF solution)

Even using an A2 dip at higher temperature of 60°C leading to higher reactivity of the A2 electrolyte did not reveal any deposition of A2 or any etching of the surface for the not activated samples as shown in figure 76 c. Also the F content in that group is very low with $I_F / I_O = 0.03$. The Auger depth profiles of the NaF activated groups also showed no significant increase of the F content in the Al_2O_3 as well. As what can be derived from figure 76 b showing the result of group A2 the F content increases only to a value of $I_F / I_O = 0.05$ compared to the not activated groups with $I_F / I_O = 0.03$. However this difference is insignificant because this variation can be found from wafer

to wafer on reference groups. FESEM results for the groups ref2 and A2 as shown in figure 76 c and d only showed the bare Al-1Si-0.5Cu surface without any sign of A2 deposition.

In those groups with activation by HBF₄, however, for all three groups deposition of A2 sponge and dendrites were observed. In figure 77 b to c the FESEM of those groups are shown together with the Auger depth profile of group B1 and B3, for group B2 Auger was not performed.

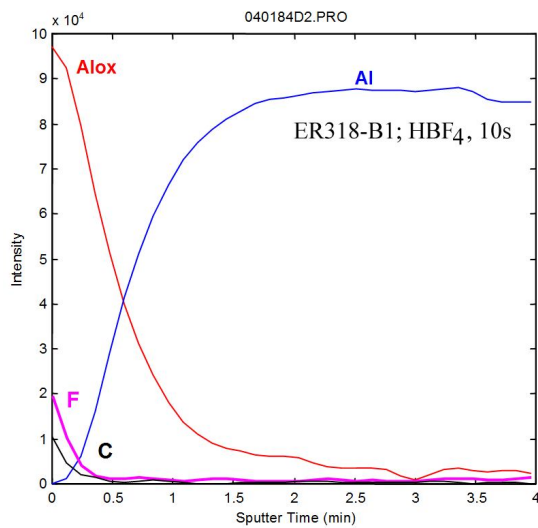


Figure 77 a: Auger of group er318-B1 and B3 with HBF₄ activation (10s).

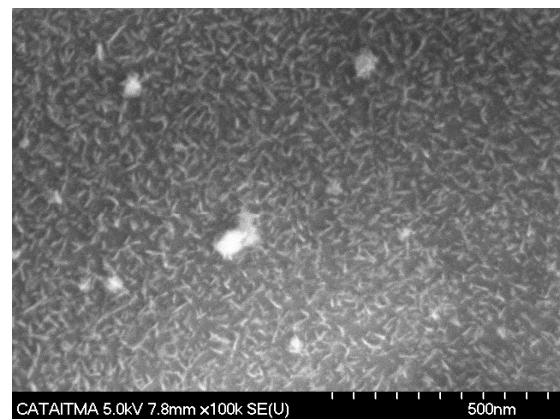


Figure 77 b: FESEM of group er318-B3 with HBF₄ activation (60s) and A2 dip at $\Theta=60^\circ\text{C}$.

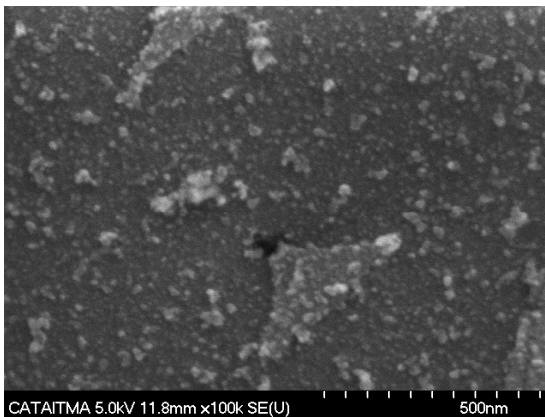


Figure 77 c: FESEM of group er318-B1 with HBF₄ activation (10s) and A2 dip at $\Theta=25^\circ\text{C}$.

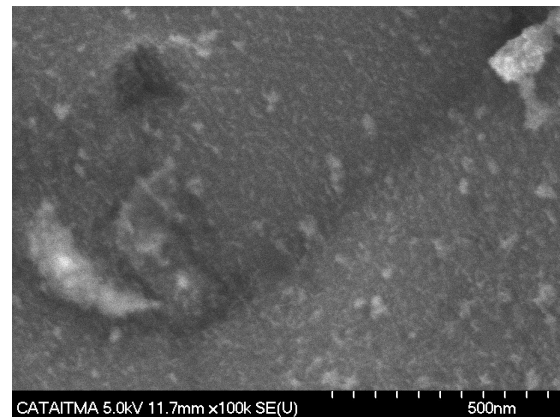


Figure 77 d: FESEM of group er318-B2 with HBF₄ activation (60s) and A2 dip at $\Theta=25^\circ\text{C}$.

First it can be seen in the Auger depth profile in figure 77 a that the conditioning with HBF₄ has been leading to a significant higher F content with a value of $I_F / I_O = 0.21$ compared to the groups with a NaF activation discussed above. The depth profiles

brought out a F content that is by factor 4 higher compared to the groups with NaF activation and that is by factor 7 higher compared to the reference groups that were not treated with any F⁻ based chemistry.

Regarding the A2 dip result for the group B1 shown in figure 77 c even for an activation time of 10 s in HBF₄ with an A2 dip at only 25°C starting dendrite growth can be observed. For this group B1 the deposit was only rated with category C as the deposit of A2 was found to be grainy and did not appear in a sponge and dendritic form. But even with the A2-dip performed at $\Theta=25^{\circ}\text{C}$ the reactivity of the Al-1Si-0,5Cu surface was high enough to reach the starting point of the chemical deposition of the A2 layer.

Furthermore increasing the activation time to 60 s in group B2 (figure 77 d) and increasing the A2 dip temperature to 60°C at an activation time of 10 s (figure 77 b) yielded already a A2 morphology of category B in the respective FESEM analysis.

To sum up, the experiment er318 showed that activation of the Al-1Si-0.5Cu surface is possible with acidic F⁻ chemistry even without any Ar/CF₄ plasma conditioning of the Al surface and with the standard Al surface that comes out of the aluminium metallisation lithography. At that time production was already done with the activation concept described in chapter 5.2.4 with Ar/CF₄ and to switch to new activation chemistry at the A2 process meant to perform a completely new qualification of the product. Therefore there was first no further work done on a new activation concept because the risks described for Ar/CF₄ Al conditioning were moderate for SFET2 MOSFET semiconductor generation.

With qualification of newer semiconductor generations and smart power devices the Ar/CF₄ concept was revised due to the finding of gateoxide damages through the influences of F that was associated with the high level of F inducted by the Ar/CF₄ plasma conditioning of the Al metallisation. In addition to this F related risk for the gateoxide of different semiconductor technologies there were other arguments to get away from surfaces with high F content on the aluminium. Fluorine contamination on Al metallisation together with humidity during transport or during dicing process can cause discolouration of the pads.

5.2.6 Further work and development of fluorine free alternative conditioning of Al-1Si-0.5Cu

For the new products the requirement was to have an activation concept for A2 plating that does not involve F incorporation into the chip Al metallisation and that also does not leave F on the chip after the A2 deposition. The findings from the experiment er318 reported above would have suggested further work with focus on F based chemistry at the A2 process. However there were some major challenges to install acidic F containing solutions in production because of safety requirements and environmental concerns. Safety requirements would require a design change of the A2 plating equipment to be able to use F based chemistry without any risk for the operating staff. To be compliant with environmental regulations especially of waste water but also for HF containing gases the installation of a wastewater treatment and an exhaust gas washing system would be unavoidable, and that is expensive and time consuming. Therefore a broader concept was worked out regarding all possibilities to activate the Al metallisation of chips for proceeding A2 deposition in order to avoid the usage of an aqueous F chemistry at the A2 process. It can be mentioned here already that it was finally the better way to take all those challenges stated above because the use of an aqueous F based chemistry offers the best process results for A2 deposition. Table 28 gives an overview of the different possibilities that have been studied during this research work.

No.	Activation concept	Description	Constrain or challenge
1	Hot water batch process before MSA solution.	Weakening the Al ₂ O ₃	Long process time t > 5min requires offline batch process.
2	A2 electrolyte spraying after MSA solution.	Increased exposure time to A2 electrolyte.	Stronger etching at critical areas, e.g. thin Al wires.
3	A2 electrolyte dip after MSA solution.	Increased exposure time to A2 electrolyte.	Stronger etching at critical areas, e.g. thin Al wires.
4	Plasma etching before MSA solution.	Removal of thick Al ₂ O ₃ layer	Integration of plasma etch equipment into the A2 equipment or offline batch process.
5	HNO ₃ solution instead of MSA	Weakening the Al ₂ O ₃	Modification of A2 equipment to use corrosive liquids.

6	HNO ₃ / H ₂ O ₂ solution mixture instead of MSA	Weakening the Al ₂ O ₃	Modification of A2 equipment to use corrosive liquids.
7	Citric acid solution	Complexation of Al	Long process time.
8	MSA / H ₂ O ₂ solution	Weakening the Al ₂ O ₃	Modification of A2 equipment to use corrosive liquids.
9	HBF ₄ / MSA solution	Formation of AlOF and AlF ₃	Modification of A2 equipment to use HF containing solutions. Special wastewater treatment.
10	HF / MSA	Formation of AlOF and AlF ₃	Modification of A2 equipment to use HF containing solutions. Special wastewater treatment.

Table 28: Overview on investigated possibilities to activate Al-1Si-0.5Cu surfaces for proceeding A2 deposition. In addition to the described versions also combinations of different activations were considered, for example version 5 combined with version 3.

The suitability of the various concepts of activation of Al metallisations was experimentally worked out in a team of chemists; results have been described in a PhD work of Lodermeier [172]. Therefore at this point further experimental results will not be described in detail but only the final results of this development work will be reported. The outcome of this experimental program was that the use of a mixture of 0.1wt% HF in 12.5%wt MSA performs best to activate the aluminium. As stated above a modification of the equipment and the installation of a waste water treatment system were required as a consequence.

In addition, to prevent any F contamination of the semiconductor device on wafer level a sealing step was implemented for the Al-1Si-0.5Cu by the use of an Ar/O₂ plasma process which will not be discussed in this work. With this sealing process a pure Al₂O₃ layer without any F can be generated on the Al-1Si-0.5Cu and therefore the metallisation is stabilized for all the downstream processes until finally the opening of the sealing at the A2 process with the HF / MSA chemistry as stated above.

In addition to this remarkable advantage the implementation of this plasma sealing brought a modification of the polyimide surface topology that is beneficial for the adhesion to the molding compounds. It is to mention here that several semiconductor technologies require the use of a polyimide coating as a passivation on the chip surface.

The adhesion of this polyimide coating cannot be improved with the A2 technology because there is no deposition possible on this surface. With the final concept as shown in figure 78 both the adhesion of the polymer surfaces of the chip and the metallic surfaces of the chip and the package towards the molding compound have been improved.

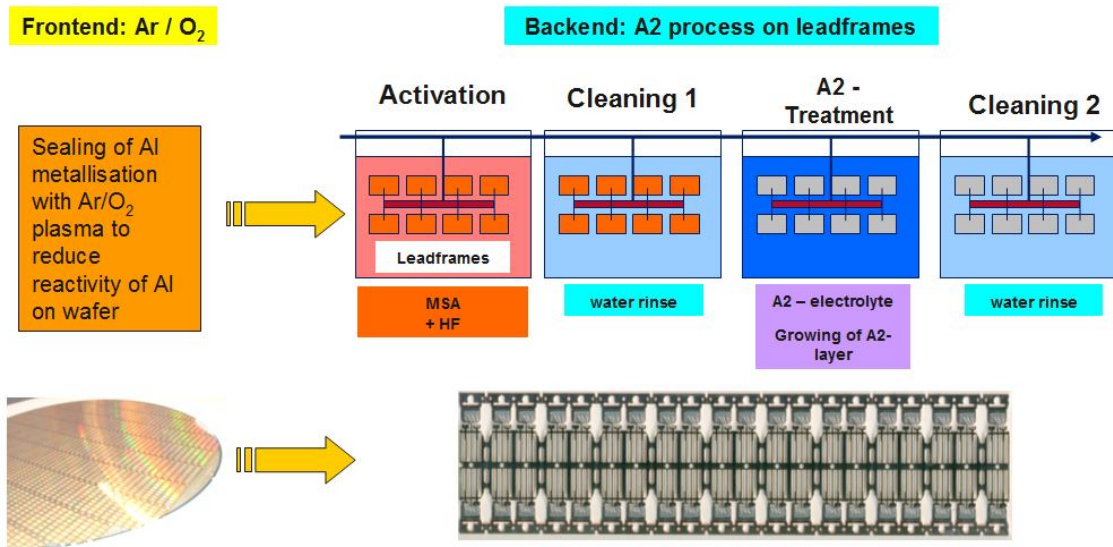


Figure 78: Description of the final concept of sealing the Al metallisation with a Ar / O₂ plasma and opening the stable Al₂O₃ within the A2 process through HF / MSA before A2 deposition.

5.2.7 Summary of activation procedures

Activation of all involved metal surfaces is a key factor for a useful A2 plating quality. Multiple metal substrates are involved during A2 deposition after the assembly of a power semiconductor package. The importance of a suitable activation for the deposition of A2 showed up in the fact that a remarkable amount of effort was spent in the development of an activation concept contributing with all involved metals in the device.

The primary activation with H₂SO₄ was changed to methanesulfonic acid (MSA) in an early stage of the project already due to higher dissolution rates of the obtained MSA salts of the involved metals. However, this concept showed some weaknesses concerning activation of the Al metallisations of the chip.

Especially Al metallisations turned out to be challenging to find appropriate activation conditions. This surface was activated by a combination of an Ar/CF₄ plasma etching process on wafer level leading to the formation of an AlOF / AlF₃ / Al₂O₃ layer on Al. Within the following wet chemical activation in MSA and with the alkaline A2-electrolyte this modified Al surface can easily be activated for A2 deposition. The disadvantage is fluorine incorporation at an early stage of the semiconductor manufacturing process leading to corrosion and risks of degradation of the gate oxide caused by fluoride ions.

Due to that finding, effort was spent to substitute the fluorine chemistry by other materials. The concept was changed finally to a combination of an Ar/O₂ plasma process on wafer level that evolves a stable and reproducible Al₂O₃ layer on the Al chip metallisation and a wet chemical activation of this surface with a mixture of HF and MSA during the A2-plating. The usage of HF in an electroplating plant triggered a huge effort on concerning safety equipment and waste water treatment processes. But finally this concept provides a sealing of the Al metallisation ensuring chemical stability during the downstream processes from the wafer frontside manufacturing until the A2 plating in the assembly area of the package. Here the Al surface is opened reproducibly for A2 deposition.

Following the future of power semiconductor technologies, Al metallisations are going to loose more and more importance moving towards Cu as a source and gate metallisation that makes activation for A2 deposition much easier. Further work on the treatment of Cu surfaces is reported in the addendum in chapter “6.3.2”.

5.3 Deposition of A2 with constant current

5.3.1 Overview on deposition parameters

The deposition process of the A2 layer was first developed as a DC deposition in the laboratory where the relevant parameters influencing the deposition result can be summarized as shown in figure 79 with one exception which is the transport belt speed $s(\text{belt})$. This parameter which is related to the transfer of the process to an industrial scale for mass production shows that with an continuous production process an increasing number of parameters has to be taken into account. For the given example of $s(\text{belt})$ there is also a link to the deposition time t and to the hydrodynamic conditions within the electrochemical cell. Parameters like current density i , cell voltage $U(\text{cell})$, temperature Θ , and the concentrations of all electrolyte species are unique and easier described compared to the volume flow within the cell and the transport speed of the product $s(\text{belt})$ through the electrolyte. The latter influences plating time and hydrodynamic properties, the former one is depending on the geometry of the plating cell. In this chapter the dependency of the A2 layer properties on the major parameters given in figure 79 will be discussed. To define which properties of the A2 layer are relevant for the deposition process we start with the description of the known A2 layer properties and the possible variations. Then the performed work will be given and discussed how the required properties of the A2 layer are formed correctly within the deposition.

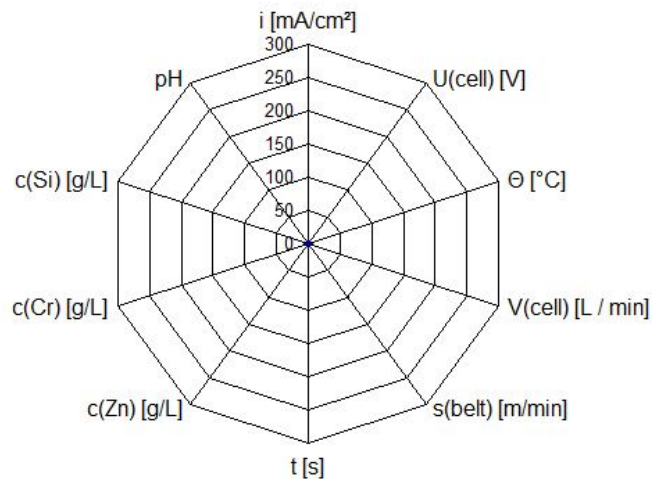


Figure 79: Overview on the major parameters influencing the deposition of an A2 layer.

5.3.2 A2 layer characterization and properties

The analysis of A2 layer morphology in this work was done mainly with FESEM and TEM. The chemical compositions of the different parts of the layer were investigated with EDX and Auger. Results were gained for all involved surfaces that basically generated similar results. Therefore here only two examples are given to demonstrate the basic properties of the A2 layer and also to indicate the distribution of these properties within a certain deposition parameter window.

The first example is the A2 morphology and composition on the chipmetallisation¹. Figure 80 shows a TEM image of an A2 layer deposited on a Al-1Si-0,5Cu chip metallisation with typical plating parameters of $i=60\text{mA/cm}^2$, $\Theta=60^\circ\text{C}$ and $t=20\text{s}$. The sample was prepared from a molded device. A dendritic and sponge like layer structure with a thickness of 50 to 200nm is observed.

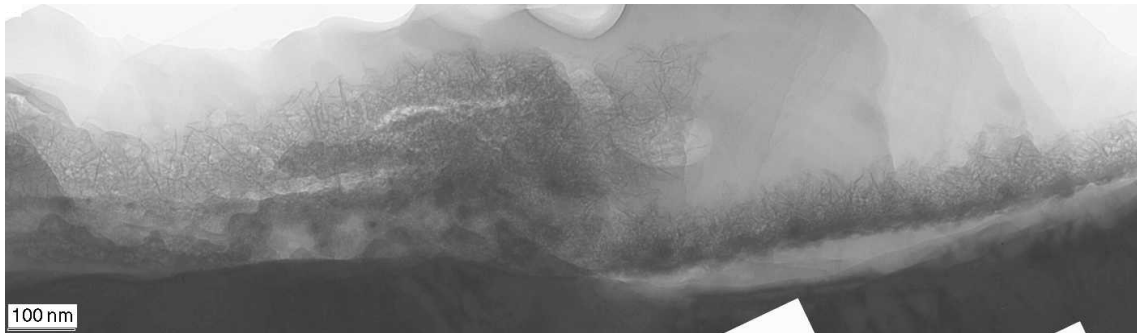


Figure 80 : TEM image of A2 layer on Al-1Si-0,5Cu deposited on chip metallisation (experiment er103-B)

Figure 81 shows the same sample and some spots where EDX was recorded. On the Al metallisation (spot d1) a compact ZnCr layer can be seen (spot c1) changing to a spong-shaped and dendritic layer structure (spot b1) at the interface to the molding compound (spot a1). A quantification of the EDX spectra of spot c1 and b1 gives values of $X_{\text{Zn}}/X_{\text{Cr}} = 1.45$ and 2.63 , respectively. This means that the outer dendritic layer has a much higher concentration of Zn compared to the more compact seed layer underneath. These results are in good agreement with the Auger results that are reported below.

¹ : The TEM analysis in this example was provided by Dr. Andreas Rucki from Siemens CT.

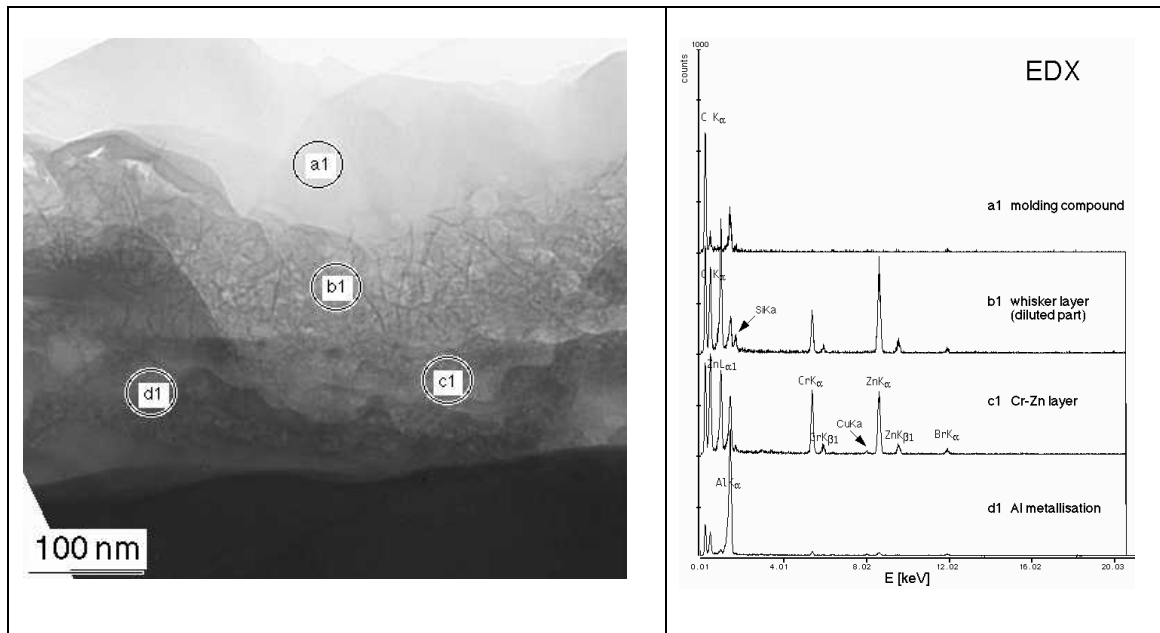


Figure 81 a and b: TEM section (left) and respective EDX spectra (right) at characteristic positions within a typical A2 layer deposited on Al-1Si-0,5Cu chip metallisation in a molded package (experiment er103-B)

The second example shows the characterisation of the A2 layer being deposited on Cu. A variation of plating conditions was done in this experiment. Three different current densities (30, 60 and 90 mA/cm²) were chosen at two different plating times (14,4 s and 20 s) and at two different temperatures (45 °C and 57°C). For each experiment an Auger surface spectrum and a depth profile was recorded for the major elements involved that are Zn, Cr, Cu and oxygen. It is worth noting here, that in the surface spectra also traces of Si were found which were not further investigated as the signal was not reproduced in every spectrum. It will be discussed later, that the source for Si may be the inclusion of Si colloids within an electrophoretic deposition mechanism, see chapter 4.2.8.4.

Figure 82 shows an example of this characterization study for a deposition experiment at $i=60\text{mA/cm}^2$, $\Theta=57^\circ\text{C}$ and $t=20\text{s}$ and the correlating FESEM image regarding the morphology of this A2 layer is demonstrated in figure 83

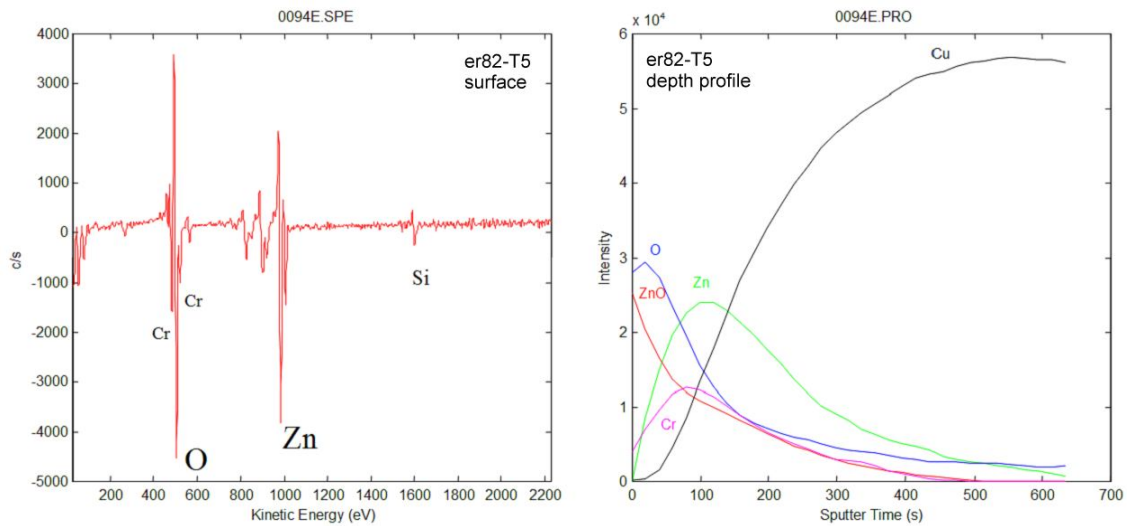


Figure 82 : Auger surface spectrum (left) and depth depth profile (right) of an A2-layer deposited on Cu (experiment er82-T5). Deposition was done in a productive plating equipment at $i=60 \text{ mA/cm}^2$, $\Theta=60^\circ\text{C}$ and 20s platingtime.

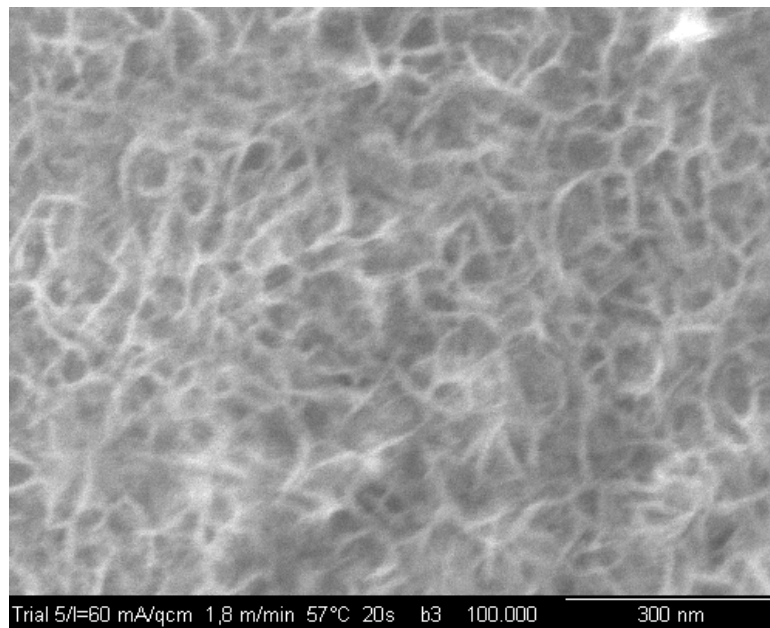


Figure 83: A2 layer morphology of experiment er82-T5 recorded in FESEM.

A comparison of the Auger results of the different experiments at various plating parameters is shown in figure 84. The ratio of the signals $[(\text{Zn} + \text{ZnO})/\text{Cr}]$ shows again, that the Zn concentration in the upper dendritic layer is approximately by factor 2 higher compared to the Zn concentration in the seed layer underneath. The ZnCr alloy concentration is varying between Zn-20Cr and Zn-35Cr. There is no correlation visible

between the different plating conditions and the alloy composition of the deposited layers. Also the thickness of the A2-layers from the different experiments shows only minor differences.

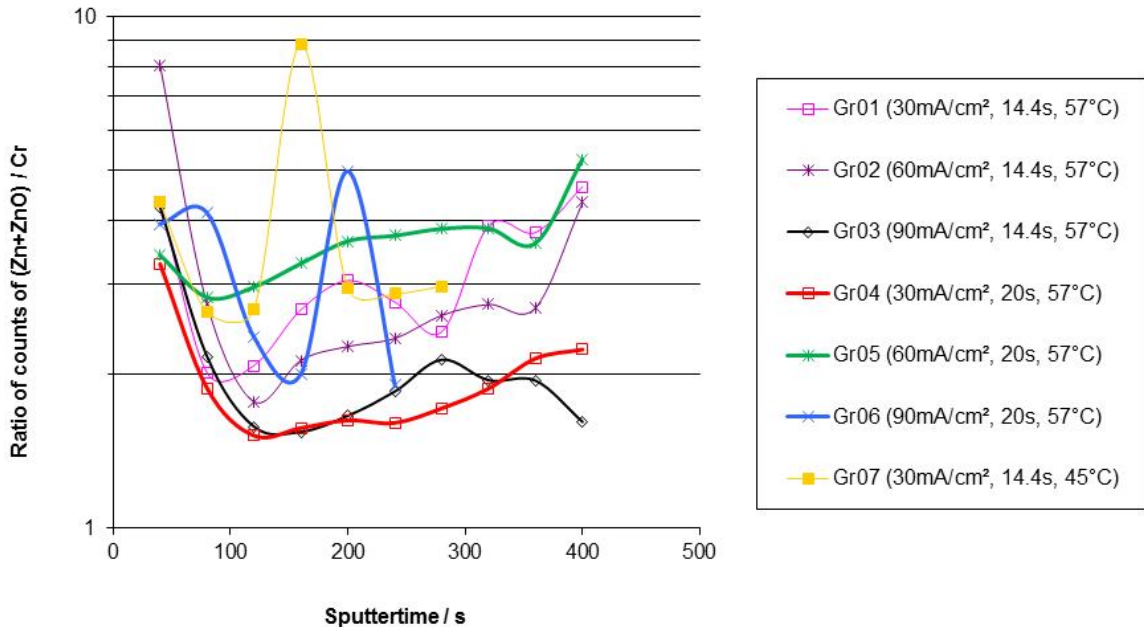


Figure 84 : Diagram showing the Auger signal ratio of (ZnO+Zn)/Cr over a variation of temperature, plating time and current density (experiment er82)

In conclusion, the A2 layer properties regarding alloy composition, layer thickness and morphology is not significantly changing in the investigated window of deposition parameters. This means the current efficiency of the deposition is very low. A classical layer growth with increasing layer thickness at increasing current density is not seen. Therefore a more complex deposition mechanism is assumed for this electrolyte that will be further discussed in chapter 4.2.8.

5.3.3 Electrolyte for A2 process and chemical interactions

5.3.3.1 Preparation of the electrolyte for A2 deposition

First the preparation of the electrolyte solution is described to answer the question in which way the various electrolyte components interact. Table 29 shows an overview how to prepare the 4 necessary concentrated aqueous solutions A to D for setting up the electrolyte for the A2 deposition. After the concentrated stock solutions have been

prepared the electrolyte is produced with the following obligatory steps, typically of a volume of about 150 litres matching the usual tank size within a plating equipment:

First 140 L of deionised (DI) water are filled into the electrolyte tank ($V_{\max}=150\text{l}$) at room temperature. Then the respective volumes of the concentrated stock solutions are added following the row of characters A to D, concentrations are given in table 29. First concentrate A (NaOH; 2.7 L) is added and then the solution in the tank is pumped for 10 minutes over the filter and the plating cell to enable a constant concentration in the whole system. Then solution B (sodium metasilicate; 0.420 L) is added and after 5 minutes of pumping the concentration should be homogenous. After this solution C (Sodium dichromate dihydrate; 0.360 L) can be filled in and finally, after 5 minutes more pumping the concentrate D (Sodium zincate; 0.900 L) is slowly filled in under continuous agitation. Finally, the tank volume is adjusted to 150l with DI-water. It is stressed that it is important to reach a high pH value at all parts of the equipment before the filling of the tank with sodium metasilicate Na_2SiO_3 and sodium zincate $\text{Na}_2\text{Zn}(\text{OH})_4$ otherwise ZnO precipitation will happen immediately and the electrolyte will degrade within less than one hour.

Preparation of the concentrated stock solutions with w_{conc}					A2 electrolyte specification		
	Chemicals	M [g/mol]	Procedure of preparing one litre of concentrated stock solution	w_{conc} [g/L]	V_{conc} for 150 L of electrolyte [L]	$w_{\text{electrolyte}}$ [g/L]	$C_{\text{electrolyte}}$ [mmol/L]
A	Sodium hydroxide, NaOH	39.997	500 g of NaOH are dissolved in 500 ml deionised (DI) water, cooled to 25°C and further diluted to 1 L with DI water with permanent cooling to 25°C.	500	2.7	9 NaOH (Total: 12 g/L NaOH)	300 NaOH
B	Sodium metasilicate solution, 27% SiO_2 (Na_2SiO_3) ¹	60.08	198 g (147 ml) of waterglass solution with 27% SiO_2 are diluted to 1 litre with DI-water	25 Si	0.420	0.070 Si	2.5 Si
C	Sodium dichromate dihydrate, $\text{Na}_2\text{Cr}_2\text{O}_7 \times 2\text{H}_2\text{O}$	297.95	715 g of sodium dichromate dihydrate are dissolved in DI water and brought to 1 L.	250 Cr^{6+}	0.360	0,6 Cr^{6+}	11.5 Cr^{6+}
D	zinc oxide ZnO and	81.39	187.5 g of ZnO are suspended in 500-600 ml of	150 Zn^{2+}	0.900	0,9 Zn	13.8 Zn

¹ : Example: MERCK No.: 105621, sodium metasilicate solution $\text{Na}_2\text{O}:\text{SiO}_2$, waterglass, extra pure; Assay: Na_2O 7.5-8.5% (acidimetric); SiO_2 25.5-28.5 % (acidimetric); Density: 1.35 g/cm³ (25°C)

	sodium hydroxide NaOH		water, 500 g of NaOH platelets are added slowly and carefully due to a strong temperature rise. ¹ The volume is brought to 1 litre with hot DI water and after cooling to 25°C adjusted again.	+ 500 g/l NaOH		+ 3 g/L NaOH	
--	-----------------------	--	---	----------------	--	--------------	--

Table 29: Preparation of the A2 concentrates and of the standard electrolyte for process variant "Ar/CF₄ + long A2". For all chemicals reagent grade quality was taken.

The interaction between the Na₂Zn(OH)₄ and the Na₂SiO₃ is important for the lifetime of the electrolyte and furthermore for the amount of particles formed in the electrolyte through precipitation of ZnO. Without the addition of Na₂SiO₃ the electrolyte is spoiled already during the first heating to process temperature of Θ=50-60°C within a couple of minutes. The mechanism of this precipitation will be discussed later together with the interactions of the different electrolyte species.

5.3.3.2 Characterization of the electrolyte

For the characterization of the electrolyte several studies have been made. One study performed by Schedlbauer [173] within a bachelor work is summarized here.

The electrolyte was investigated by cyclo voltametry to determine the equilibrium potential E_0 , the exchange current density i_0 , and the transfer coefficient α for the area of reaction controlled deposition. As a working electrode a Teflon coated stainless steel rod was used with a flat Cu tip having an area of $A=0.2083\text{cm}^2$. The electrode was well polished. All the measurements were done with the standard A2 electrolyte as described in the previous chapter at the standard process temperature of $\Theta = 60^\circ\text{C}$ and N₂ purging during the measurement to exclude side effects from O₂. The following values were obtained:

$$E_0(\text{vs. Ag/AgCl}) = -1.463 \pm 0.008 \text{ V}$$

$$i_0 = 1.221 \pm 0.08 \text{ mA/cm}^2$$

$$\alpha_{n=12} = 1,0289 \pm 0.0001$$

¹ : The temperature can rise to 100°C. The solution should become clear. If the solution is not clear further heating is required to dissolve the ZnO.

The high value for α exceeding a theoretical maximum value of 1 was explained by the difficult experimental conditions leading to an electrolyte breakdown during the experiments.

In addition, for the area of higher potentials and of diffusion controlled deposition the diffusion coefficient D_{ox} for the oxidizes species $Cr_2O_7^{2-}$ was investigated by applying a rotating disc electrode (RDE) with a polished Cu surface at the RDE. The following value was obtained:

$$D_{ox} = 9.44 \times 10^{-5} \text{ cm}^2/\text{s}$$

Furthermore in this study the current efficiency was determined with a gravimetric measurement of the deposited Cr out of a solution consisting of 0.6g/L Cr^{6+} at a current density of $i = 45\text{mA}/\text{cm}^2$ for a time of $t = 3380\text{s}$. A very low current efficiency of 2.04% was found.

5.3.4 Influence of the concentration of the various electrolyte species on the morphology of A2 deposit.

Besides the characterization of the electrolyte under laboratory conditions with the reported electrochemical methods, the behavior of the electrolyte during the A2 deposition process and the influence of the concentration of the different species on the process result were investigated. As the major property of the A2 layer is its functionality to act as a interlock to the molding compound the most important process result was it's morphology that was analyzed with FESEM in parallel to the analysis of the homogeneity of the deposited layer with the tape test, both described in chapter 2. The correlation between electrolyte composition and layer morphology was investigated with four different experiments. The various concentrations of the specific electrolyte species in those experiments are shown as a normalized value $c_i/c_{0,i}$ (i : Cr^{6+} , Zn^{2+} , Si^{4+}) relatively to the specified concentrations shown in table 29. The concentration range above $c_{0,i}$ has been investigated on laboratory scale, the range underneath $c_{0,i}$ was studied with the productive process and equipment.

Upper concentration range with $c_i/c_{0,i} > 1$ (i : $Zn(OH)_4^{2-}$, CrO_4^{2-} , SiO_3^{2-} , OH^-)

The motivation of this study was mainly to increase the zincate concentration as one important parameter for the dosing of the electrolyte species in the production equipment and to extend the process window for the electrolyte species for minimizing the effort for manual adjustment of the concentrations at that time. Experiment er214 was done in the laboratory using a laboratory cell consisting of a 2L beaker with a diameter of 160mm filled up with 1.5L electrolyte. Two parallel stainless steel (V4A) anodes were positioned with a distance of 10cm fully shielded from the sample at the cathode with a polypropylene sheet. Both shielding and anode area were fully covering the sample area consisting of a Cu stripe with 20mm width, 100mm length and 1.2mm thickness with a 4 μ m layer NiP by electroless plating. The electrolyte agitation was done by a magnetic stirrer (stirrer rod: l=80 mm, d=8 mm) at a frequency of 300 min⁻¹. Prior to the deposition each substrate was activated for 10 s at 25°C in 12 wt% aqueous MSA and the A2 deposition was done for 20s at a temperature of 60°C and at a current density of 60mA/cm². In table 30 the results for the respective concentrations are shown. The samples were analyzed by tape test and in addition some selected samples were analyzed via FESEM to confirm the morphology of the deposited A2 structure.

Gr. #	NaOH [c₀]	Si⁴⁺ [c₀]	Cr⁶⁺ [c₀]	Zn²⁺ [c₀]	U [V]	i [mA·cm⁻²]	Tapetest [%]
1	1	1	1	1	7	60	100
2	1,25	1	1	2	3,8	60	50
3	1,25	1	1	2	5	190	100
4	1,25	1	2	2	5	150	100
5	1,25	2	2	2	5	150	100
6	1,25	2	2	5	5	227	100
7	1,25	2	5	5	5	208	100

Table 30: Experimental matrix of er214 for concentrations above the standard concentration c_{0,i} for the various electrolyte species.

For the first two groups #1 and #2 the experiment was run galvanostatically at a constant current of 60mA/cm². Due to the strong drop of voltage and at the same time a strong drop of the tape test quality to 50% in group #2 the rest of the experiment from #3 to #7 was run potentiostatically at a voltage of 5V. The result for the tape test readout showed a positive quality for all groups except group 2 after the first increase of the concentrations of the NaOH and the Zn²⁺. In this group the voltage dropped significantly to a voltage of 3.8V at the a current density of 60mA/cm² compared to 7V in group 1. This low voltage probably hindered the wanted dendritic growth of the

metals. In group 3 the voltage was adjusted to see the influence to the deposition at the same concentrations and suddenly the tape test result was 100%. For experiment #4 to #7 deposition was done with a constant voltage of 5V and the concentrations c_i were increased up to a value of $5 \cdot c_{0,i}$ for the Cr^{6+} and Zn^{2+} and a value of $2 \cdot c_0$ Si^{4+} with a stable value of 100% in the tape test. The experimental row was reproduced with a different substrate (TO263 leadframe piece, refer to chapter 5.1) with a slightly bigger area with the same result.

It should be stressed here, that the samples showing a positive tape test also showed a positive morphology in the FESEM.

In conclusion, this experiment shows that it is possible with this electrolyte to generate a sponge layer with concentrations of $5 \cdot c_{0,i}$ for the electrolyte species Zn^{2+} and Cr^{6+} and with a concentration of $2 \cdot c_{0,i}$ for Si^{4+} on laboratory scale. The unexpected drawback was the finding, that the electrolyte stability starting from group #5 was very poor. A precipitation of ZnO was observed already after 30 minutes and therefore it was not considered to perform additional investigations.

In addition the installation of an automatic dosing system at the production equipment made it possible to control the concentrations much easier near or higher than the optimum concentrations $c_{0,i}$. Difficulties arose with the control of the concentrations lower than $c_{0,i}$ due to the limited accuracy of the dosing system. Therefore in the next experiments the concentrations window for $c \leq c_{0,i}$ was investigated.

Lower concentration range with $c_i/c_{0,i} < 1$ (i: $\text{Zn}(\text{OH})_4^{2-}$, CrO_4^{2-} , SiO_3^{2-} , OH^-)

The next three experiments were performed directly on the productive deposition equipment described in figure 52. As substrates for the first experiment er163 a TO220 substrate was used as shown in figure 54, for the second experiment er176 a TO263 leadframe with two rows of devices was used referring to figure 53. The investigations were done on bare leadframes without any solder or chips, but on both Cu and NiP surfaces.

Due to the knowledge from the previous study a current density of 60mA/cm^2 was chosen to ensure that the cell voltage during A2 deposition was kept above a voltage of

9V for each group of the experiment. Activation of the substrate was done with standard aqueous MSA at 25°C for 15s and A2 deposition was done at 60°C for 20s. All groups were analyzed with FESEM of the A2 layer on the Cu and the NiP surface and the rating was done with the morphology categories A to D defined in chapter 2.1. To quantify the obtained morphologic categories the characters A to D were renamed with numbers 3 to 0 respectively with number 3 equal category A being the best quality and with number 0 equal category D being the worst quality. Those groups that show a completely different A2 layer morphology which was not defined yet were also rated with a zero and the respective FESEM results were discussed individually. The various concentrations of the specific electrolyte species are again shown as a normalized value $c_i/c_{0,i}$ (i: $\text{Zn}(\text{OH})_4^{2-}$, CrO_4^{2-} , SiO_3^{2-} , OH^-) again.

In the first two experiments the influence of the concentrations of Cr^{6+} and Zn^{2+} was investigated within 13 experimental groups, some of the groups are shown in figure 85. The NaOH and the Si^{4+} concentrations were kept at their specified concentrations $c_{0,i}$.

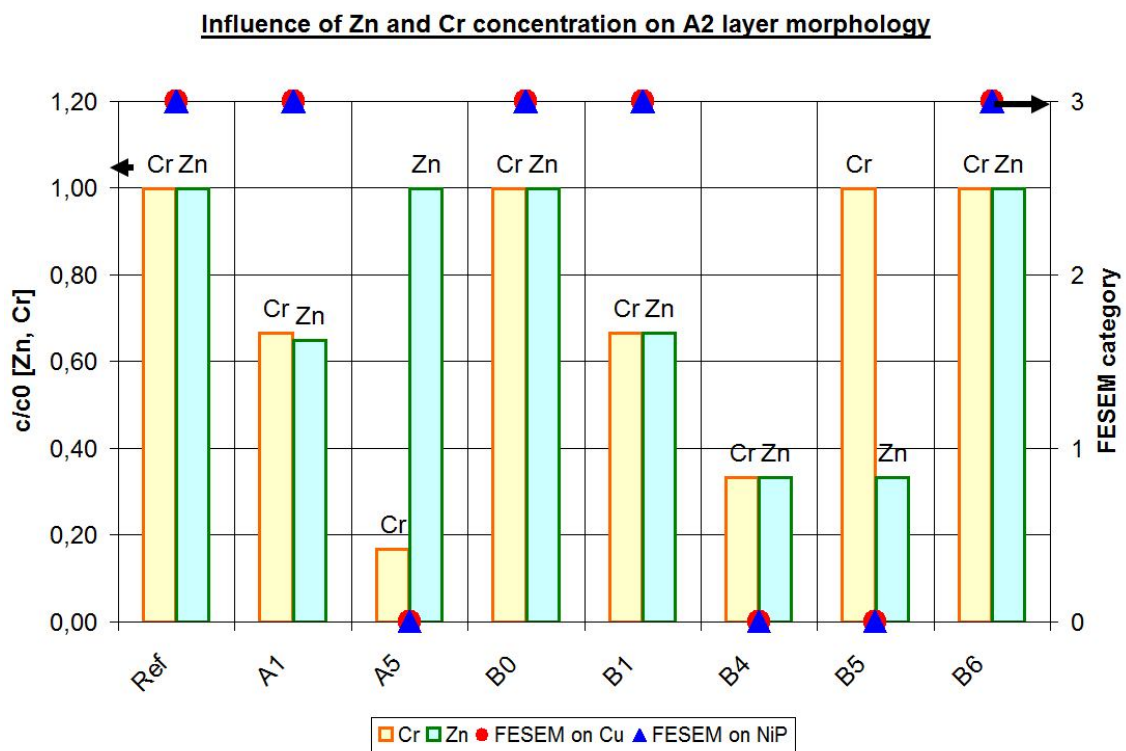


Figure 85: Diagram of the variation of the Cr^{6+} and the Zn^{2+} concentration during A2 deposition and the obtained quality of the A2 layer morphology rated with category 0 to 3. The data have been extracted from experiments er163 and er176.

The concentrations of Cr^{6+} and Zn^{2+} were decreased first symmetrically from $c_{0,i}$ to $2/3c_{0,i}$ without any influence to the FESEM result on both Cu and NiP leadframe in group Ref and A1 in figure 85. A reduction of the concentration of Cr^{6+} showed a change of the A2 layer morphology without observation of any sponge structure, but with a platelet layer structure. The platelets had the size of about 300nm diameter and 30nm thickness on the Cu substrate as shown in the FESEM image in figure 86 a. For the NiP surface also the structure was changing to a loose and hairy structure as shown in Figure 86 b. Both morphologies were rated as low quality via FESEM as they were unknown in terms of the adhesion to the molding compound.

Through addition of Cr^{6+} to the electrolyte in group B0 it was observed that the known A2 morphology builds up again, one example is given in figure 86 c. Consequently the electrolyte recovers after adjusting the concentration of this species to $c_{0,i}$.

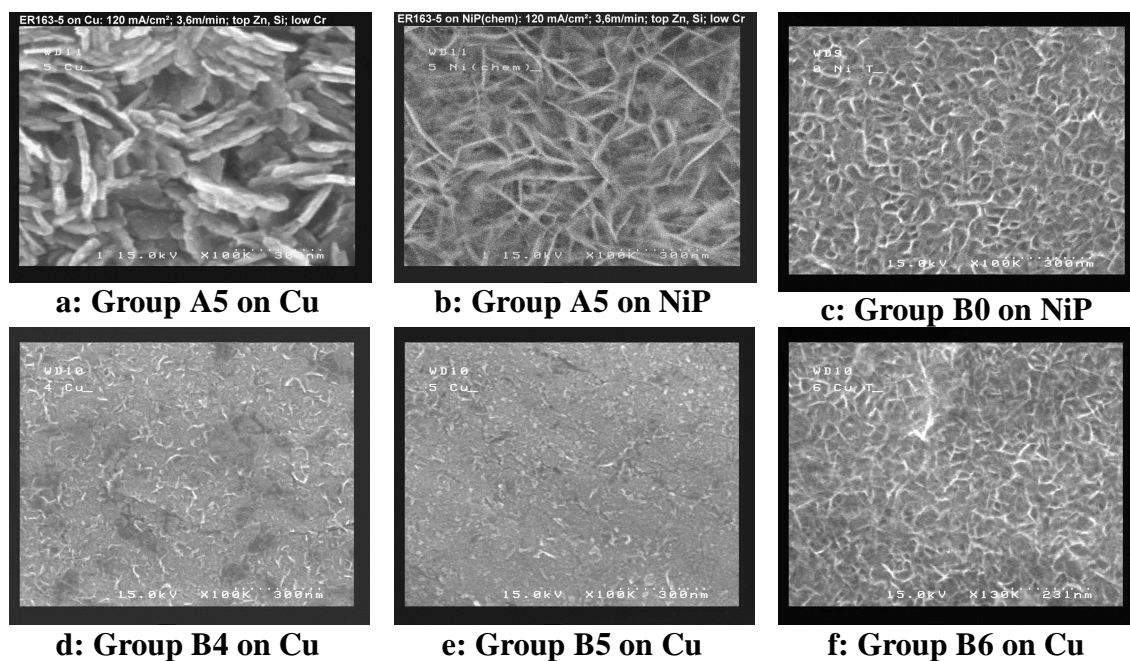


Figure 86 a to f: FESEM analysis of specific groups illustrated in figure 85. All FESEM pictures have been taken at a magnification of 100k x.

In groups B1 and B4 in figure 85 then the concentrations of Zn^{2+} and Cr^{6+} have been decreased in 2 steps down to a value of $1/3 \cdot c_{0,i}$. Group B1 with a concentration ratio of $2/3 \cdot c_{0,i}$ was able to reproduce the result of group A1. However, an additional decrease of those concentrations in group B4 resulted in a very low quality of the deposited A2 layer as seen in the FESEM images. Figure 86 d illustrates that there is no sponge

structure obtained at those deposition conditions. Adjusting the Cr^{6+} concentration back to the value of $c_{0,i}$ showed no improvement in group B5. Under those conditions with only the Zn^{2+} concentration reduced to $1/3 \cdot c_{0,i}$ no sponge structure is obtained as illustrated in figure 86 e. Finally, in group B6 it can be seen that adjusting also the Zn^{2+} concentration to $c_{0,i}$ brings back the condition of a sponge deposition of the A2 layer.

The last experiment in this chapter was done to investigate the influence of the Si^{4+} species to deposition. The conditions regarding plating and analysis of the obtained surfaces were identically to the previous experiment. The NaOH concentrations were kept at their specified concentrations $c_{0,i}$. The starting point was chosen with a Zn^{2+} concentration at $2/3 c_{0,i}$ because this was the specified lowest control limit for this parameter according to the results of group A1 and B1 discussed above that still showed a good quality. In figure 87 the specific concentration variations are illustrated.

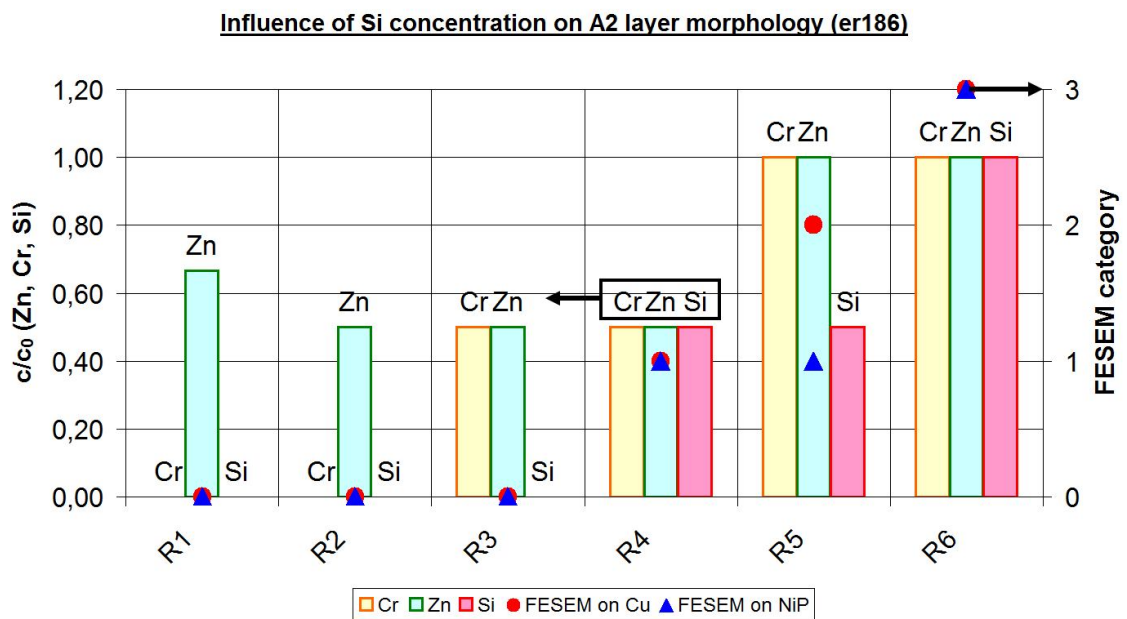


Figure 87: Diagram of the variation of the Cr^{6+} , Zn^{2+} and Si^{4+} concentration during A2 deposition and the obtained quality of the A2 layer morphology rated with category 0 to 3.

For groups R1, R2 and R3 there was no Si^{4+} present in the electrolyte and the deposited A2 layer showed only a grainy morphology with single platelets for both Cu and NiP substrates. For the NiP substrates figure 88 a to c shows the respective morphologies.

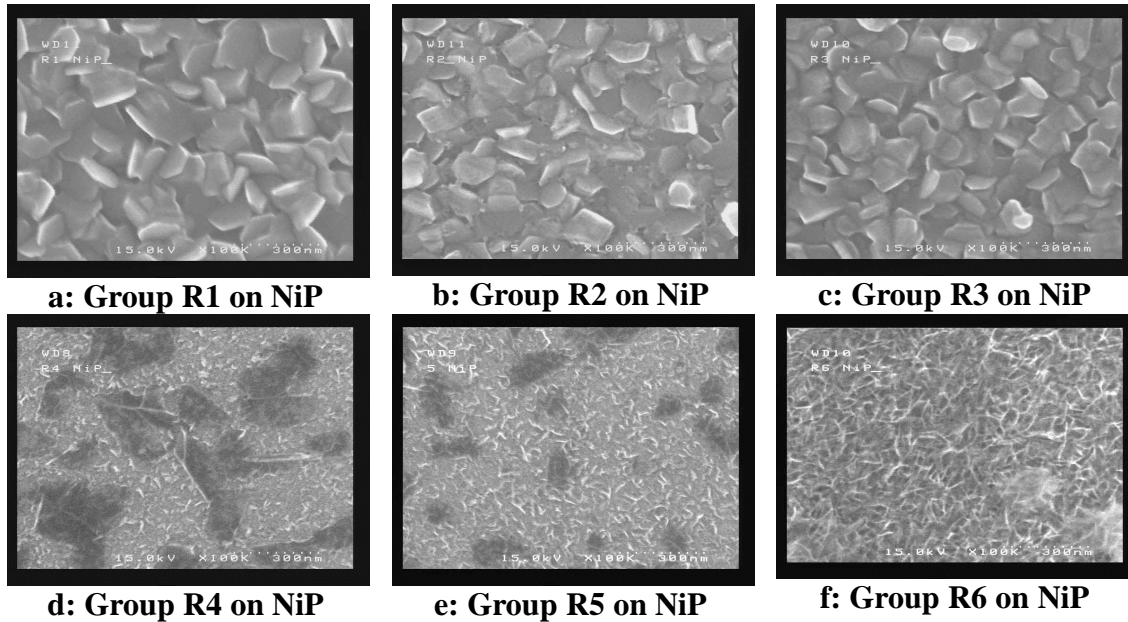


Figure 88 a to f: FESEM analysis of specific groups illustrated in figure 87. All FESEM pictures have been taken at a magnification of 100k x.

The rating was done with a bad quality category 0 due to the lack of any sponge structure. Adding silicate to the electrolyte with a concentration of $1/3 \cdot c_{0,i}$ in group R4 and R5 changed the morphology of the A2 layer to a very fine dendritic coating with a lot of black spots. For both groups the deposit obtained on NiP was rated with a quality of 1 due to the presence of single dendrites as shown in figure 88 d and e. The deposit on the Cu substrate showed a better morphologic quality in group R5 compared to the NiP substrate and therefore was rated 2.

Finally, adjusting the concentration of the silicate to the specified value of $c_{0,i}$ in group R6 the obtained A2 layer was showing the required sponge morphology in the FESEM again that was rated with quality factor 3 as shown in figure 88 f.

Summary

In conclusion, these experiments in the area of the lower concentrations of electrolyte species show that the reduction of the Cr^{6+} concentration is significantly changing the morphology of the deposited A2 layer. With an alkaline electrolyte only consisting of the Zn^{2+} species the obtained structure is showing platelets and no sponge structure and is therefore considered to be a risk for the adhesion of the molding compound. Furthermore, reducing the concentration of the Zn^{2+} species to $1/3 \cdot c_{0,i}$ is leading to a smooth deposit without any sponge or dendritic morphology. The lower limit for both

the Zn^{2+} and the Cr^{6+} species was found to be $2/3 \cdot c_{0,i}$ that is 0.6 g/L and 0.4 g/L respectively.

Finally, the Si^{4+} species plays an important role in building up the required A2 sponge layer. Without any silicate in the solution no dendritic or sponge growth is possible with this electrolyte, the lower limit found for this species was also $2/3 \cdot c_{0,i}$ that is 0.045 g/L. Due to the very low value of the specified concentration $c_{0,i}$ of the silicate that is 0.070 g/L in the electrolyte solution, a very precise and frequent analysis is required to maintain the lower limit. From all three situations with too low Cr^{6+} , Zn^{2+} or Si^{4+} concentrations a recovering of the electrolyte is possible by adding the missing species up to the specification concentrations of $c_{0,i}$. This shows that the electrolyte is not degrading with concentration variations of those three species.

For the upper concentration range of the electrolyte species with $c_0 / c_{0,i} > 1$ the results showed that it is possible to obtain a sponge deposit up to higher concentrations also. For Zn^{2+} , Cr^{6+} , and NaOH concentrations up to $5 \cdot c_{0,i}$ and for Si^{4+} concentrations up to $2 \cdot c_{0,i}$ are leading to a sponge and dendritic A2 layer morphology found on laboratory scale. But the drawback is fast electrolyte degradation through precipitation of ZnO within less than 1 hour.

In addition this higher concentrations lead to a much stronger corrosion rate of the respective Al metallisations and Al wires of the device during plating that will be discussed in chapter 5.3.8.

5.3.5 Influence of deposition current density

The DC current density is one of those parameters that is automatically controlled by the rectifier unit during the current controlled (galvanostatic) deposition. The question was how strong is the influence of the current density and the resulting cell voltage to the morphology of the obtained deposit. The same question arises for the potentiostatic deposition at a selected voltage and a resulting current density.

Experiment er161: Variation of the current density and influence to A2 morphology on a TO220 leadframe.

In the first experiment the deposition current was varied and its influence to the deposition morphology was determined with the FESEM at two positions on the heatsink, the center and the edge. In addition, the adhesion properties of the deposit were tested via the tape test (see section 2.5). Both analysis results were obtained on the Cu (K80, Cu-0.15Fe-0.02P) and on a chemically deposited NiP surface. The substrate used was a TO220 leadframe without a chip as the focus was the investigation of the deposition current for the Cu and NiP only. The plating was done on the productive plating equipment using a plating cell with a length of 120 cm and with anodes consisting of stainless steel (V4A) with polypropylene shields. In addition, a flow guide base plate as shown in the drawings in figure 91 cell type B was installed. At this time this was the defined cell geometry for this substrate. Table 31 shows the variation of the current density with the related cell voltages and the respective results of the FESEM and the tape test analysis. The rating of the FESEM analysis was done again with category A to D reflecting decreasing quality as defined in chapter 2.1. From the FESEM pictures that were taken at a magnification of 100k x approximate pore size minima and maxima were measured.

ER161		0	1	2	3	4	5	6	7	8
i [mA/cm ²]		5	10	30	60	90	120	150	180	210
U [V]		2,5	3,0	4,4	6,3	8,3	10,3	12,3	14,2	16,0
Tape test [%]	Cu	80	90	80	95	100	100	100	100	100
	NiP	<10	<10	60	100	100	100	100	100	100
FESEM	Cu	BB	BB	AA	AA	AA	AA	AA	AA	AA
	NiP	DD	D	CC	AA	BB	BB	AA	CB	CB
Pore size [nm]	Cu	30-60	30-60	30-100	30-150	30-150	30-150	30-150	30-150	30-150
	NiP	no dendr.	no dendr.	0-30	30-60	0-60	0-60	30-60	0-60	0-60

Table 31: Evaluation of current densities; The tape tests were performed with Scotch 600. The FESEM-check at 100k x was done on two positions for each group and for each surface, the edge and the centre of the heatsink.

The results show that deposition of dendrites is possible over a wide range of current density and voltage for the Cu surface. At current densities below 30 mA/cm² (4.4 V) the tape test shows a slight decrease for Cu which indicates a reduced homogeneity of porous deposit over the analyzed surface. Spot analysis with FESEM still showed suitable dendrite structure of the deposited layer with category B. The pore sizes obtained at $i \leq 30 \text{ mA/cm}^2$ are decreasing for the upper pore size from 100nm to 60nm, the lower pore sizes stay at approximately 30nm. With the upper values of the current densities and cell voltages in the range $i = 60 \text{ to } 210 \text{ mA/cm}^2$ and $U = 6.3 \text{ to } 16 \text{ V}$ no

change of morphology of the sponge layer was found and the layer was homogeneously distributed as indicated by the 100% tape test result for all those groups on Cu and on NiP substrate. Also the porosity of the structure was found constant on Cu in this range being 30-150nm. For the Cu surface therefore the upper limiting current density could not be determined due to the voltage limitation of the used rectifier that was limited to 16V. The lower current density limit for the Cu substrate seems to be underneath $i = 5\text{mA/cm}^2$ at $U = 2.5\text{V}$. However the quality rating is already reduced below $i = 30\text{mA/cm}^2$ with a morphology of category B in the FESEM analysis for the given experiment as shown in figures 89-5a and -30a.



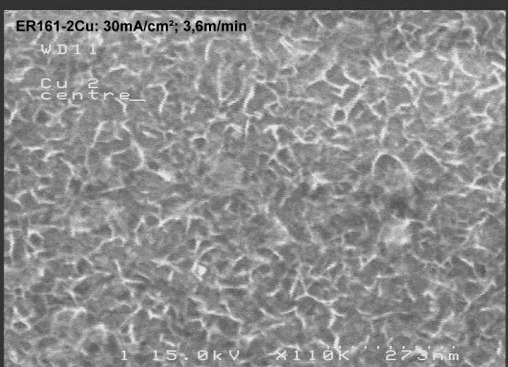
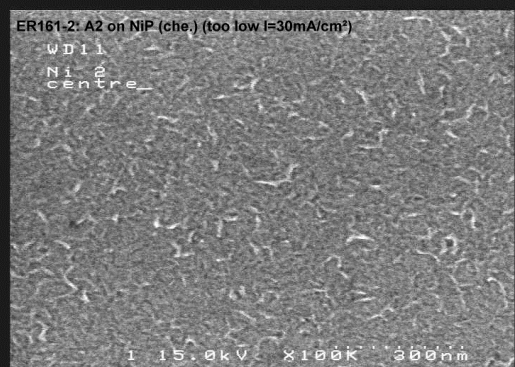
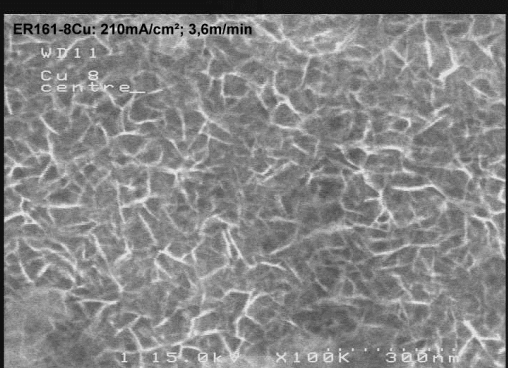
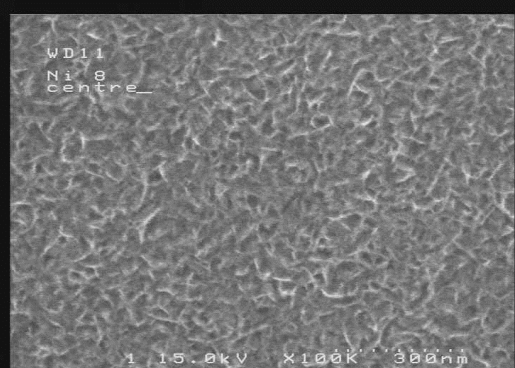
i	FESEM on Cu	FESEM on NiP
5 mA/cm ²		
30 mA/cm ²		
210 mA/cm ²		

Figure 89: Examples of FESEM results of the morphologies found in experiment er161 for the centre position on the heatsink. The pictures are named according to the used current density with characters a (left for Cu surface) and b (right for NiP surface).

Results obtained for the electroless NiP surfaces were different. At lower current densities $i < 60 \text{ mA/cm}^2$ the tape test result is significantly decreasing. At $i=5 \text{ mA/cm}^2$ and $i=10 \text{ mA/cm}^2$ there seemed to be nearly no deposition of the wanted dendritic A2 layer as only $<10\%$ of the tested area showed a positive tape test. This result was confirmed via FESEM where no A2 dendrites were found for those two current densities, one example given for the former current density in figure 89-5b . For $i=30 \text{ mA/cm}^2$ only a compact and less porous layer was obtained that was rated with category C as shown in figure 89-30b. In addition also the pore size in this group is indicating a much more compact layer compared to the layer obtained on Cu for the same current density.

Also for deposition current above 30 mA/cm^2 the pore size within the A2 layer on NiP is much smaller compared to the A2 layer on the Cu substrate which can be seen for example for $i = 210 \text{ mA/cm}^2$ comparing figures 89-210a and -210b. Groups 3 to 8 with show similar values of the pore size with 60 nm maxima and areas with a compact layer without any pores. For the two highest current densities of 180 mA/cm^2 and 210 mA/cm^2 the morphology found in the FESEM showed a decrease in the quality of the deposit with spots consisting of category C dendrites. For the NiP surface there seems to be a limit of the maximum deposition current density of about 180 mA/cm^2 at $U = 14.2 \text{ V}$. The lower current density limit for the NiP surface was found to be 30 mA/cm^2 with a clear lack of A2 sponge indicated by both the tape test and the FESEM analysis. Results for two examples are given in figures 89-5b and -30b.

To confirm the surface analytical results on product level devices plated with 90 mA/cm^2 , 120 mA/cm^2 and 150 mA/cm^2 were used for complete assembly of the product in order to perform stress tests together with one reference group without A2 plating. A MOSFET device (SFET1; BUZ111S; $3.2 \mu\text{m}$ of Al-1Si metallisation) was used within a TO220 package with standard chipsoldering and $2 \times 500 \mu\text{m}$ Al thick wire and $60 \mu\text{m}$ Al thin wire. A molding compound from Shin Etsu company was used (KMC 289-3ES-X1). All final down stream processes were done with standard manufacturing. Before and after a stress of preconditioning MSL1 with $3 \times 260^\circ\text{C}$ solder heating (PC)

the devices were analyzed with SAT for detecting delamination. Furthermore additional stress of 100 temperature cycles from -65°C to 150°C (TC100) was applied. In table 32 the images of the SAT (see section "2.10 Scanning acoustic microscopy") scans are shown for all 4 experimental groups at initial condition and after respective stress tests.

Gr.	ref	4	5	6
i	no A2	90 mA/cm ²	120 mA/cm ²	150 mA/cm ²
SAT initial				
SAT PC				
SAT TC100				

Table 32: SAT images of groups er161-reference, -4, -5, and -6 with focus on the device frontside at initial condition and after a stress of preconditioning MSL1 with $3 \times 260^{\circ}\text{C}$ soldering (SAT PC) and after a stress of 100 temperature cycles from -65°C to 150°C (SAT TC100).

No delamination of the devices was seen for devices at initial condition before stress tests. For the reference group without A2 layer a strong delamination around the chip on the heatsink is seen after the first stress. In contrast for all three groups with A2 deposition at various current densities there is no delamination visible after this stress. This shows that the A2 morphologies obtained at the respective current densities of $90\text{mA}/\text{cm}^2$, $120\text{mA}/\text{cm}^2$, and $150\text{mA}/\text{cm}^2$ in the given experimental setup with the standard electrolyte are suitable to reach a higher level of adhesion in the device compared to the untreated reference group. The SAT analysis after the additional stress of TC100 shows slight delamination also for the groups who have been treated with A2. In those groups a systematic delamination of the left side of the device heatsink was

observed ("left side" delamination). A possible root cause was assumed to be the insufficient hydrodynamic control within the plating cell which will be discussed in chapter "5.3.6 Hydrodynamic influence: Electrolyte flow and transport belt speed".

Experiment er174: Variation of the current density and influence to A2 morphology on a TO263 leadframe.

The second experiment (er174) was done to confirm the results above for the target pilot leadframe TO263-3 as shown in figure 53. Only two current densities were taken to confirm the result in the range between 30mA/cm² and 60 mA/cm² for this leadframe. In table 33 the 4 groups are shown for two different current densities of 30mA/cm² and 60mA/cm² and two different leadframe surfaces being Cu (K80, Cu-0.15Fe-0.02P) and electrochemically deposited Ni/NiP. The plating was again done by the productive plating equipment using a plating cell with anodes consisting of stainless steel (V4A) with polypropylene shields. In this case the flow guide base plate was removed and a cell geometry as shown in figure 90 cell type A was used. With this cell a better homogeneity of the A2 layer comparing the top row and the bottom row of the leadframe could be achieved. Analysis and rating was done analogous to the previous experiment above but the number of positions of FESEM analysis was increased to 6 positions on the device as shown in the picture in table 33. In addition also devices were completely assembled with the same MOSFET chip and identical stress tests as described above were performed.

Er174	Variation for A2 process		FESEM analysis on devices at various positions:					
Group #	Lead frame surface	A2 cell	A	B	C	D	E	Alu chip
A1	Cu-K80	i=30 mA/cm ² U=6.6V	2A 1B	3A	1B 2C	B	A	B
A2	NiP		3A	1A 2B	1A 2B	A	A	C
B1	Cu-K80	i=60 mA/cm ² U=10.8V	2A 1B	1A 2B	1A 2B	A	A	C
B2	NiP		2A 1B	2A 1B	3A	A	A	A

Table 33: FESEM results from er174 experiment on a TO263-3 MOSFET device at various device positions.

The FESEM result obtained for both current densities were very similar regarding the morphology of the A2 layer. For the higher current density of 60 mA/cm² there was a slight trend to a higher quality of the A2 deposit with 6x category A and 5x category B for the Cu substrate in group B1 and even better with 9x category A and only 2x category B for the NiP substrate in group B2. For the lower current density of 30 mA/cm² for example in group A1 on Cu substrate a lower grade of category C was found two times. On the leads at position E there was no difference visible. In contrast a large variation in dendrite distribution on the Al-1Si chip metallisation was found. At this time the Al metallisation of the chip was not yet conditioned with the Ar/CF₄ plasma described in chapter "4.1.5.2 Activation of Al₂O₃ with an Ar/CF₄ plasma process" and it was realized for the first time, that activation of this surface requires a specific treatment. Therefore, a further rating of the Al surface was not done in this experiment.

Stress test results of the readily manufactured devices showed no delamination after MSL1 with 2x 260°C soldering and only slight delamination on the solder after TC100 for all 4 groups in the SAT scans of the device frontside. A significant difference between the two current densities and between the two leadframe surfaces could therefore not be derived from the performed stress test. Only the FESEM shows a slightly better morphology for groups B1 and B2 at 60mA/cm². Therefore for this specific device in this experimental setup a suitable current density range between 30mA/cm² and 60mA/cm² was fixed temporarily which correlates with the results obtained in the above study on the TO220 device in er161.

Summary:

For two different leadframe geometries a range of current densities and voltages was determined for the Cu and the NiP surfaces. For the TO220 leadframe the fully achievable range was investigated limited by rectifier limitation of a maximum voltage of 16 V and a minimum controllable current density of 5 mA/cm². The obtained limits for the Cu surface were $i = 30 \text{ mA/cm}^2$ to 210 mA/cm^2 with cell voltages of $U = 4.4 \text{ V}$ to $U = 16\text{V}$ respectively. For NiP surfaces closer limits were found being $i = 60 \text{ mA/cm}^2$ to 180 mA/cm^2 with respective cell voltages of $U = 6.3 \text{ V}$ to $U = 14.2 \text{ V}$. For the TO263 leadframe only two current densities were confirmed with $i = 30 \text{ mA/cm}^2$ (U

= 6.6 V) and $i = 60 \text{ mA/cm}^2$ ($U = 10.8 \text{ V}$) leading also to positive results. In addition for both experiments the obtained A2 layer was proven through stress tests on the final product. In conclusion the current density range for the A2 deposition is very high for the Cu surface and slightly lower for the NiP surface. Also the sponge structure of the A2 layer growing on NiP is more dense with pore sizes from 0 to 60nm compared to the Cu surface growing a layer with pore sizes of 30 to 150nm at a given current density of typically $i = 90 \text{ mA/cm}^2$. The reason for the different behaviour of NiP compared to Cu might be the lower roughness of the NiP. With the smoother surface of the NiP deposition of H_2 is happening at a higher overvoltage known from Zn deposition reported for example by Graf [174]. This may lead to less H_2 development during deposition leading to reduced blocking of the surface. In consequence, deposition of Zn may not be hindered leading to a less spongy deposit. A further discussion of this effect will be given in chapter 5.3.8.

5.3.6 Hydrodynamic influence: Electrolyte flow and transport belt speed

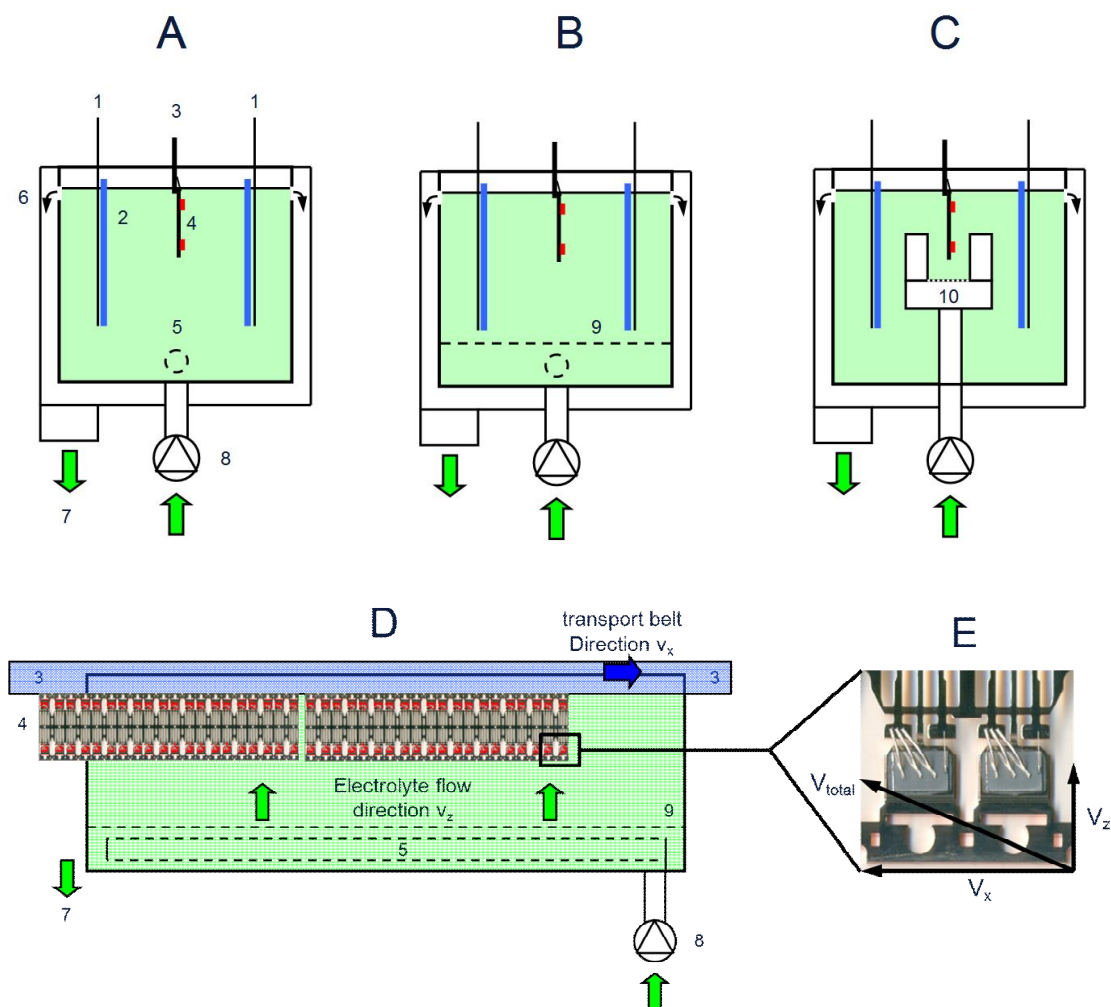
As described in the overview of process parameters in chapter 5.3.1 the electrolyte movement relative to the substrate in the deposition cell is a parameter that is linked to other parameters including for example the deposition time. Within the A2 plating cell the hydrodynamic conditions are defined through two parameters, first by the transport velocity of the leadframe within the electrolyte and second by the forced electrolyte movement perpendicular to the transport belt direction. The latter parameter is defined by the continuous pump flow of the electrolyte into the cell and the specific geometry of electrolyte guidance in the cell, i.e. the feed tube as shown in figure 91A position 5 and the base plate flow guide shown in figure 91B position 9.

The focus on investigations for electrolyte flow was first on the cell design shown in figure 91A and B consisting of two anodes of stainless steel shielded with polypropylene plates. The leadframe substrate is transported by a transport belt. The electrolyte is supplied to the plating cell by a pump leaving the cell at an overflow. The electrolyte flow is distributed along the cell with a electrolyte feed tube with holes for cell version A and with an additional flow guide plate for cell version B in figure 91 A

and B respectively. The cell material including the tubes and plates consisted of polypropylene.

Additional effort on new deposition cell features such as the cathode shield tube shown in figure 91C will be discussed later in chapter 5.3.7.

A side view of the cross-section of cell B is shown in figure 91 D. Within the cell also two substrate leadframes (TO263-3) are shown and the transport direction v_x and the electrolyte flow direction v_z is indicated. Figure 91E shows in addition the magnification of two devices of the first leadframe with the respective electrolyte flow directions v_x , v_z and the resulting flow direction v_{total} . The resulting vector \vec{v}_{total} is derived by addition of vector \vec{v}_x and \vec{v}_z . The resulting velocity is calculated with the Pythagoras equation given by $\sqrt{v_x^2 + v_z^2} = v_{total}$.



Figures 91 A-E: Cross sectional view of the drawing of three A2 cell geometries (A to C) into the transport direction and side view of cell A with two electrolyte flow directions v_z and v_y (picture D). On the right lower picture E the magnification of two devices on the leadframe and the two flow directions v_x and v_z with the resulting flow direction v_{total} is shown.

Description of the drawing positions:

- 1: Anode plates left and right, stainless steel V4A
- 2: Anode shielding, polypropylene plate with $d=5\text{mm}$
- 3: Transport belt, stainless steel V4A
- 4: Leadframe with chips
- 5: Electrolyte feed tube with holes
- 6: Electrolyte overflow left and right
- 7: Electrolyte drain into storage tank
- 8: Electrolyte pump from storage tank
- 9: Flow guide plate with holes, polypropylene
- 10: Cathode shielding tube with holes

Effect of transport belt speed variation and flow of electrolyte on A2 layer morphology on a TO220 leadframe

The first experiments on the influence of the hydrodynamics within the A2 cell were started empirically using the TO220 leadframe shown in figure 54. The A2 cell version B shown in figure 91 B was used with a flow guide plate (area of 113cm x 20cm, number of 100 x 20 = 2000 holes with a diameter of 6mm and a distance between the holes of 10mm). The two major parameters for the flow of the electrolyte relative to the leadframe were varied i.e. the volume flow of the pump and the transport speed of the product perpendicular to the volume flow as it is shown in table 34. The maximum achievable vertical flow speed was 2.5 cm/s determined by the maximum possible volume flow of the pump (5m³/h). In horizontal direction the maximum possible transport belt speed was 4.5m/min (7.5 cm/s). Both values add up to a maximum value of electrolyte movement v_{total} of 7.9 cm/s relative to the device calculated over perpendicular vectors, see figure 91E. The values obtained are listed in table 34 together with the results of the respective tape tests (see chapter 2.5) for each group done twice for each group for a Cu and a NiP plated leadframe without chip.

	Plating parameter variation						Results of tape test [%]			
	Beltspeed [m/min]	v_x (horizontal) [cm/s]	t [s]	v(pump) [m ³ /h]	V_z (vertical) [cm/s]	v (total) [cm/s]	Cu 1st	Cu 2nd	NiP 1st	NiP 2nd
er160										
1	3,6	6,0	20	5,2	2,6	6,5	100	100	100	100
2	3,6	6,0	20	2,6	1,3	6,1	100	100	100	95
3	1,8	3,0	40	2,6	1,3	3,3	100	95	85	80
4	1,8	3,0	40	5,2	2,6	3,9	95	90	100	95
er162										
1	3,6	6,0	20	5,2	2,6	6,5	100	n.a.	100	n.a.
2	4,5	7,5	16			7,9	100	100	100	95
3	2	3,3	36			4,2	100	95	100	100
4	1	1,7	72			3,1	70	60	20	10
5	0,5	0,8	144			2,7	20	20	20	<10
6	„0“	0,0	180			2,6	20	20	<10	<10
7	1	1,7	72			3,1	20	20	<10	<10

Table 34: Matrix of experiments er160 and er162 with variation of electrolyte flow and tape test results.

For the sample preparation an activation with 12wt% aqueous MSA at 25°C for 15s was used. The deposition of the A2 layer within the various groups was done at 60°C with a

current density of 45mA/cm² using the standard electrolyte as described in chapter 5.3.3.1.

The interpretation allows the conclusion that belt speed is having a much higher influence compared to the given volume flows in the cell. This trend is visible in the first 4 experiments, group er160-3 and -4 shows a reduction of the tape test value indicating a lower coverage of dendritic A2 layer over the leadframe surface compared to groups er160-1 and -2. Because of this trend in the following experiment er162 only the belt speed was varied and the volume flow of the feed pump was kept constant at 5.2 m³/h representing a vertical speed of 2.6 cm/s. In experiments er162-4 and -5 a sudden drop of the homogeneity of the dendritic layer could be observed at belt speeds ≤ 1 m/min representing a total flow speed of ≤ 3.1 cm/s. Experiment er162-6 was done by stopping the device in the electrolyte meaning only the vertical flow component of 2.6 cm/s was present bringing out the worst homogeneity. Experiment er162-7 was only a reproduction of er162-4 which confirmed the low homogeneity again. It was decided to use a belt speed of 3.6 m/min because this was also the maximum speed the automatic leadframe loading was able to achieve reliably. The pump flow was fixed to the maximum setting of 5.2 m³/h.

This settings were further used for the next experiment with the TO220 leadframe for investigating the influence of the current density as it was described above in chapter 5.3.5. within experiment er161. As described there the plating quality on leadframes carrying solder, chips and wires leaded to a systematic delamination at one side of the device during stress tests in the SAT analysis (see chapter 2.10) that was assumed to be due to unfavourable electrolyte flow in the current cell geometry cell B shown in figure 91B. In figure 92 this effect is shown with a SAT picture of devices after stress test showing respective left side delamination and the indication of the electrolyte flow direction.

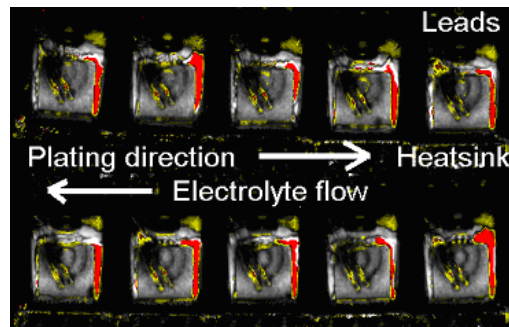


Figure 92: SAT picture of devices after stress test with "left side" delamination and correlation to the flow direction of the electrolyte during A2 deposition.

In addition in this stress test study a critical problem during molding of this leadframe was realized. For the upper part of this leadframe the strong adhesion of the molding compound led to the problem, that residuals of the molding compound could not be removed anymore at the positions of molding compound injection. This led to several issues at downstream processes, i.e. to bad electrical contacts at testing. A solution to this issue was a selective plating of the leadframe with the A2-layer being deposited only up to the area indicated as "low" position as shown in figure 93. This means only the lower part of the device carrying the chip was plated with the A2-layer.

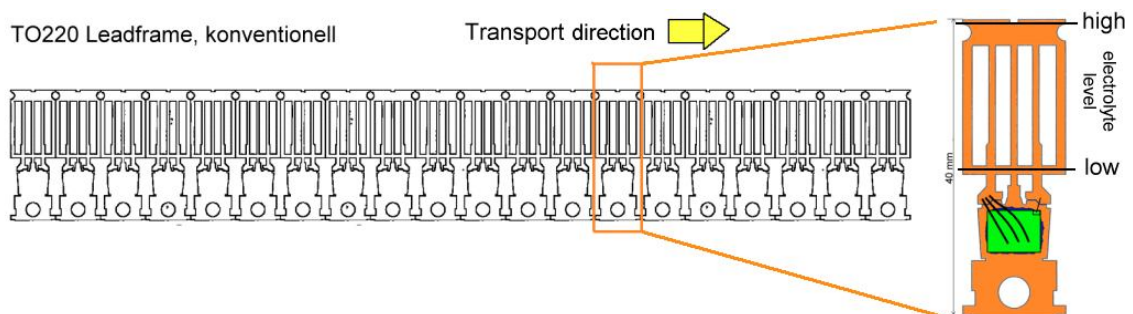


Figure 93: Definition of the border for A2 deposition for TO220 leadframe to solve the molding issue. The electrolyte level was adjusted to the "low" position and therefore only the device with the chip is getting an A2 layer.

This could be achieved by adjusting the level of the electrolyte to this limit during plating. The disadvantage of this approach was, that the device was now plated at the electrolyte surface and the control of agitation was getting more difficult there compared to the bulk electrolyte. Therefore further studies were started to develop a new cell geometry with a much better control of the electrolyte flow.

Summary:

To summarize, the influence of the belt speed for the cell B shown in figure 91B was found to be the dominating factor. The limit of belt speed was found to be 2 m/min, below this value a sudden drop of the homogeneity of the morphology of the A2 deposit was observed using a leadframe without chips. Major drawbacks with usage of leadframe with applied chips were found in terms of a systematic delamination of one side of the device and issues with molding compound residuals at the downstream processes, i.e. contact failures during the electrical testing process. Therefore the concept of this deposition cell B consisting of a base plate flow guide was not further followed. Further investigations were started to design a cell with a much better control of the hydrodynamic parameters.

5.3.7 Cell design for A2 deposition

As indicated in previous experiments the geometry of the plating cell plays an important role for the plating result. This can be seen already for example for the TO263 leadframe with two rows of devices through a slightly darker colour of the devices plated at the bottom position indicating a difference of the A2 layer forming at both positions. In this section the effort for developing an optimal deposition cell geometry for the A2 process is described for both discussed leadframes, the TO220 and the TO263 leadframe shown in figures 53 and 54. Besides the experimental results also hydrodynamic simulations were used for the design of the final plating cell considering both the fluid dynamical aspects and the aspects regarding potentials distribution in the plating cell.

5.3.7.1 Cathode shield tube: Design of geometry and flow of electrolyte for TO220 leadframe (er228).

To get an answer what cell design provides the best control of electrolyte flow the concept of direct guidance of the electrolyte to the device was tried out with a cathode shield tube shown in figure 94.

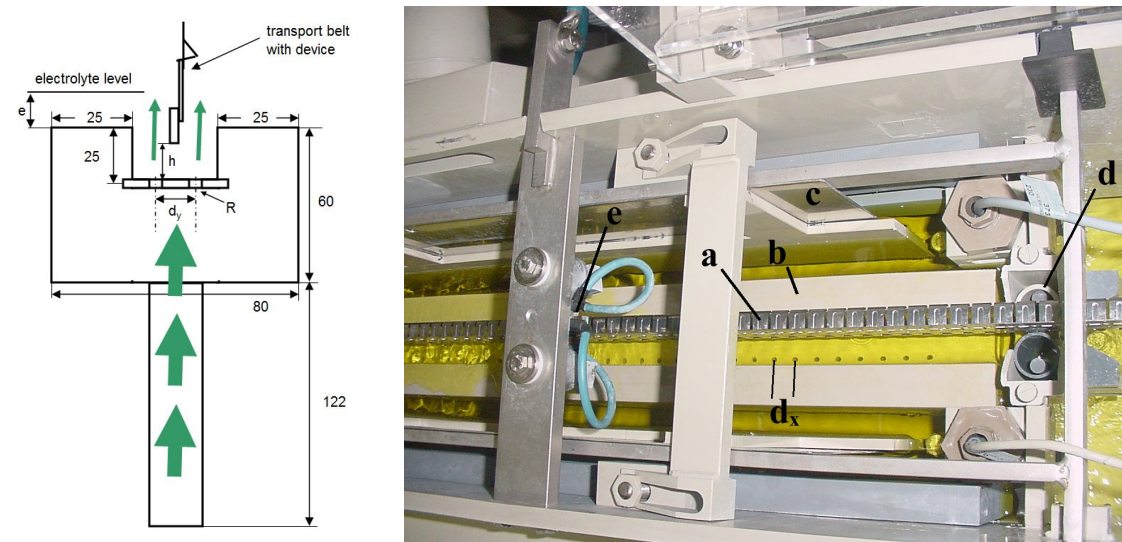


Figure 94 a+b: Geometry of the cathode shield tube (left) and photograph of the plating cell (right) with transport belt (a), cathode shield tube (b), anode (c), cell gate overflow (d), d_x inlet holes and cathodic belt contact (e).

The flow of the electrolyte in this case is guided through the tube of the cathode shield and through the holes of the base plate of the cathode shield as shown in figure 94a position R. The green arrows indicate the direction of flow of the electrolyte. The electrolyte is leaving the cathode shield tube perpendicular to the base plate at position R flowing in parallel to the device. The characteristic geometries of the cathode shield are the distance of the outlet holes d_y and d_x , the radius of the outlet holes R and the outer dimensions of the shielding tube that were fixed to the values shown in the drawing in figure 94a. A further characteristic is the distance h between the device bottom and the outlet baseplate.

To achieve a homogenous flow along the cell length of 120 cm within the cathode shield various geometries of the inlet holes were tried out. Both the radius R of the inlet holes ($R = 1$ to 2mm) and their distance d_x in x-direction ($d_x = 10$ to 20mm) was varied. Their distance d_y in y-direction was kept constant at $d_y = 16$ mm, see figure 94a. The final values after the flow optimization between a total electrolyte flow of 30 L/min to 100 L/min were $R = 2$ mm and $d_x = 15$ mm. With the values of $d_x = 15$ mm in total 74 pairs of holes have been drilled for the cell length of 120cm that adds up to a total area of $A = 1.86 \cdot 10^{-3}$ m². For the upper and lower volume flow of 30 L/min and 100 L/min this results in flow speeds in the z-direction of $v_z = 27$ cm/s and $v_z = 90$ cm/s, respectively. Compared to the cell geometry with the base plate flow guide used in the previous chapter (see figure 91B) where the flow speed was only 2.6 cm/s with the

current design a flow speed increase of at least factor 10 was possible. The total flow is represented again by adding horizontal movement of the devices in x-direction to the electrolyte flow perpendicular to this movement in z-direction. The speed in x-direction gives a value of $v_x = 6$ cm/s for the target belt speed of 3.6m/min. Compared to the high values of v_z being 27cm/s to 90cm/s the flow speed generated through the belt speed is much lower and therefore for this type of cell the dominant hydrodynamic influence is generated by the electrolyte pumping velocity v_z in contrast to the cell B (see figure 91B) discussed in chapter 5.3.6. where the transport speed of the substrate through the the electrolyte (v_x) was dominant.

Two other important measures for the flow homogeneity are the distance between the device and the cathode shield (figure 94 a: Measure h) and the electrolyte level above the cathode shielding (figure 94 a: Measure e). These values depend on the leadframe width and the dipping depth of the leadframe into the electrolyte during the deposition. After the electrolyte has passed the devices it flows over the cathode shielding walls leaving the cell.

For the case of a TO220 leadframe these two values were fixed with $e = 18$ mm and $h = 11$ mm and then the investigations on the TO220 leadframe were stopped due to other reasons.¹

However the basis of this plating cell geometry as shown in figure 94 a and b was further developed for the TO263 leadframe with an additional experiment er309 that will be discussed below.

5.3.7.2 A2-Cell: Design of geometry of plating cell for TO263 leadframe (er309).

To achieve an optimum deposition cell for the TO263-3 leadframe (see chapter 5.1 figure 53) with two rows of devices the same cell (cell length 120 cm) with anode shield and with the respective cathode shield tube for controlling the flow of electrolyte was

¹ : Activities on the TO220 leadframe were stopped due to reliability risks of the devices manufactured with an adjusted electrolyte level showing inconsistent plating result and unsolved drawbacks during electrical testing of the devices as described in chapter 5.3.6.

used as describe in the previous chapter for the TO220 leadframe. Both shields together have been leading to a homogeneous plating result and differences between the top device row and the bottom device row could be minimized as shown in the following experiment.

In total 10 experimental groups have been investigated. NiP plated TO263 leadframes with a MOSFET chip with Al-1Si-0.5Cu metallisation were used. For all cells the immersion depth of the leadframe into the electrolyte was exactly its width of 62mm. The major cell geometry variations used for the A2 deposition in this experiment were the distance between cathode shield base plate and substrate d and the length of both anodes with their shields a shown in figure 95, besides other versions described below.

Referring to figure 96 cell A0 is the standard cell only consisting of 2 stainless steel (V4A) anodes with polypropylene shielding of a thickness of 4 mm covering the complete anode area; immersion depth a of the anodes was 92mm.

For cell A1 a shortening of the anodes and shields was done to a immersion depth a of 62mm which is the same as for the leadframe.

For cells B2, B4, B5 and B7 the cathode shield tube described in figure 94 was installed accordingly. For Cell B2 and B4 the deep immersion depth of 92mm for the anodes with shields was chosen, the distance between the cathode shield base plate and the leadframe bottom d was varied with the values $d = 10\text{mm}$ for cell B2 and $d = 30\text{mm}$ for the cell B4. For the cell B5 the distance d was kept high at $d = 30\text{ mm}$ but the anode immersion depth was shortened to $a = 62\text{mm}$. Finally the geometry of cell B7 was tested removing the anode shields in comparison to the cell B5.

An overview on the various modifications of the investigated cells and the results of the FESEM analysis of the obtained deposits is summarized in table 35.

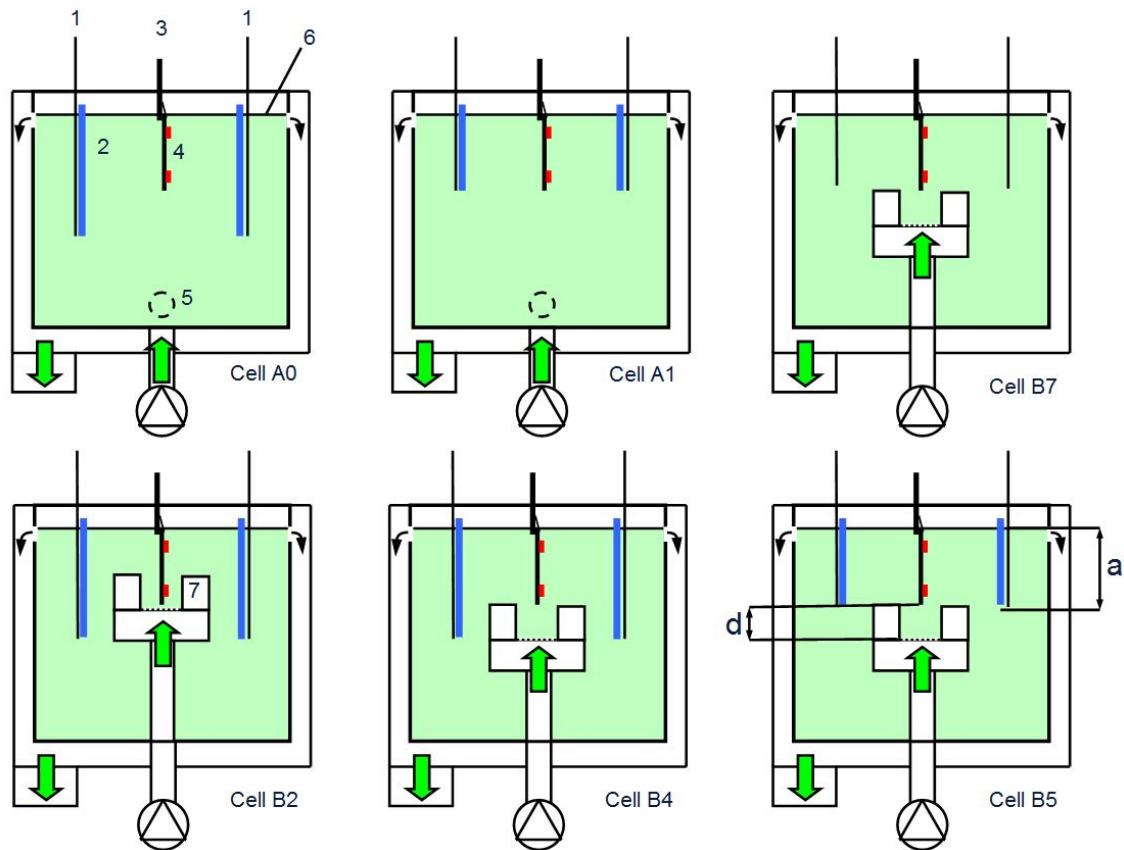


Figure 95: Cross sectional view of cell variants investigated in er309 with a TO263-3 dual row leadframe.

The sample preparation was done in the same way as in the previous experiment (activation with 12wt% aqueous MSA at 25°C for 15s; deposition of the A2 layer at 60°C with a current density of 45mA/cm² galvanostatically) using the standard electrolyte as described in chapter 5.3.3.1.

Due to the strong increase of the cell voltage for the cells with double shields a stronger pump was installed reaching an electrolyte pump flow rate of 150 L/min used throughout all experiments. With the given geometry of the cathode shield tube shown in figure 94 a flow velocity v_z of 135 cm/s was calculated at the substrate.

For all groups the rating of the deposited A2 layer was done with tape test, for specific groups a FESEM analysis was done. The rating of the obtained morphology was again done according to the morphology catalogue from chapter 2.1 with A to D for best and worst quality, respectively. For groups A1, B4 and B5 TOFSIMS depth profiles of devices from top and bottom position were recorded for the Al-0.5Cu-1Si metallisation

and the Ni/NiP surface to get information about the elemental distribution within the respective A2 layer.

Cell	Anode immersion depth ^a	Anode shield	Distance substrate to cathode shield tube d	Cell voltage U _{cell} [V]	FESEM (9 points top and bottom)	Colour of A2 plated Cu leadframe
A0	Full TO263 leadframe width (62mm) plus 30mm = 92mm	yes	n.a.	8.9	n.a.	Top: Light grey Bottom: dark grey
A1	Full TO263 leadframe frame width: 62mm	yes	n.a.	8.6	Top: 3A, 2B Bottom: 3A, 1B, 1C ¹	Top: Light grey Bottom: dark grey
B2	Full TO263 leadframe width (62mm) plus 30mm	yes	10mm	14.5	n.a.	Homogeneous grey on both top and bottom row.
B4	Full TO263 leadframe width (62mm) plus 30mm	yes	30mm	11.7	Top: 2A, 2B, 1C Bottom: 3A, 1B, 1C	Homogeneous grey on both top and bottom row.
B5	Full TO263 leadframe width (62mm)	yes	30mm	9.6	Top: 4A, 2B, 3C Bottom: 6A, 3C	Homogeneous grey on both top and bottom row.
B7	Full TO263 leadframe width (62mm)	no	30 mm	5.9	Top: 3A, 1B, 5C Bottom: 3A, 3B, 3C	Homogeneous grey on both top and bottom row.

Table 35: Overview of deposition cell variants investigated in er309 and the obtained deposition quality.

First, for all experimental groups the tape test resulted in a 100% coverage for both top and bottom row. This showed that for each cell geometry A2 deposition happened homogeneously. For the cells A0 and A1 without the cathode shield tube a strong optical difference of the obtained A2 layer was observed by using Cu leadframes in between the NiP plated samples. On Cu the grey layer can be seen more clearly compared to the NiP leadframes and therefore was used for assessment of the optical homogeneity of the deposit. The top row of the leadframe only shows a light grey colour compared to the bottom position with a dark grey colour. This indicates a difference of the A2 layer thickness and inhomogeneous deposition conditions along the leadframe width.

¹ : Only 5 FESEM positions were analysed for top and bottom position of the leadframe for group A1 and B4.

For the cells with installed cathode shield tube (cells B2, B4, B5 and B7 in figure 95) this inhomogeneity vanished. For cell B2 consisting of a very strong shielding of the cathode due to the low distance of $d = 10\text{mm}$ between leadframe and cathode shield base plate the cell voltage was increasing to the upper limit of the rectifier being 15V. Therefore this geometry was not further considered. Also for cell B4 the cell voltage was considerably high with 11.7V. Cell B7 showed the lowest cell voltage of 5.9V due to the missing anode shields.

Comparing the FESEM results of the top and bottom position of the leadframe within the 4 cells A1, B4, B5 and B7 there was no clear difference between the A2 structure at those two positions visible. Also comparing the various groups with each other did not lead to big differences of the A2 morphology analysed with FESEM. Only for the cell B7 without the anode shields there are more FESEM positions rated with category C compared to the other groups. In this group also the top position counts 5x category C which is the lowest quality found in the experiment. Therefore use of cell B7 without anode shields was not further considered.

To find out differences of the specific cells and to clarify the reason for the optical difference between top and bottom position for those groups without the cathode shielding tube TOFSIMS depth profiles were performed on three samples. Cell B4 and B5 with a comparison to cell A1 as a reference with strong difference between top and bottom A2 layer were taken and analysed for the NiP substrate and for the Al-1Si-0.5Cu chip metallisation. In figure 97 examples of the results are shown for the A2-layer on the NiP surface for top and bottom position of the leadframe, respectively.

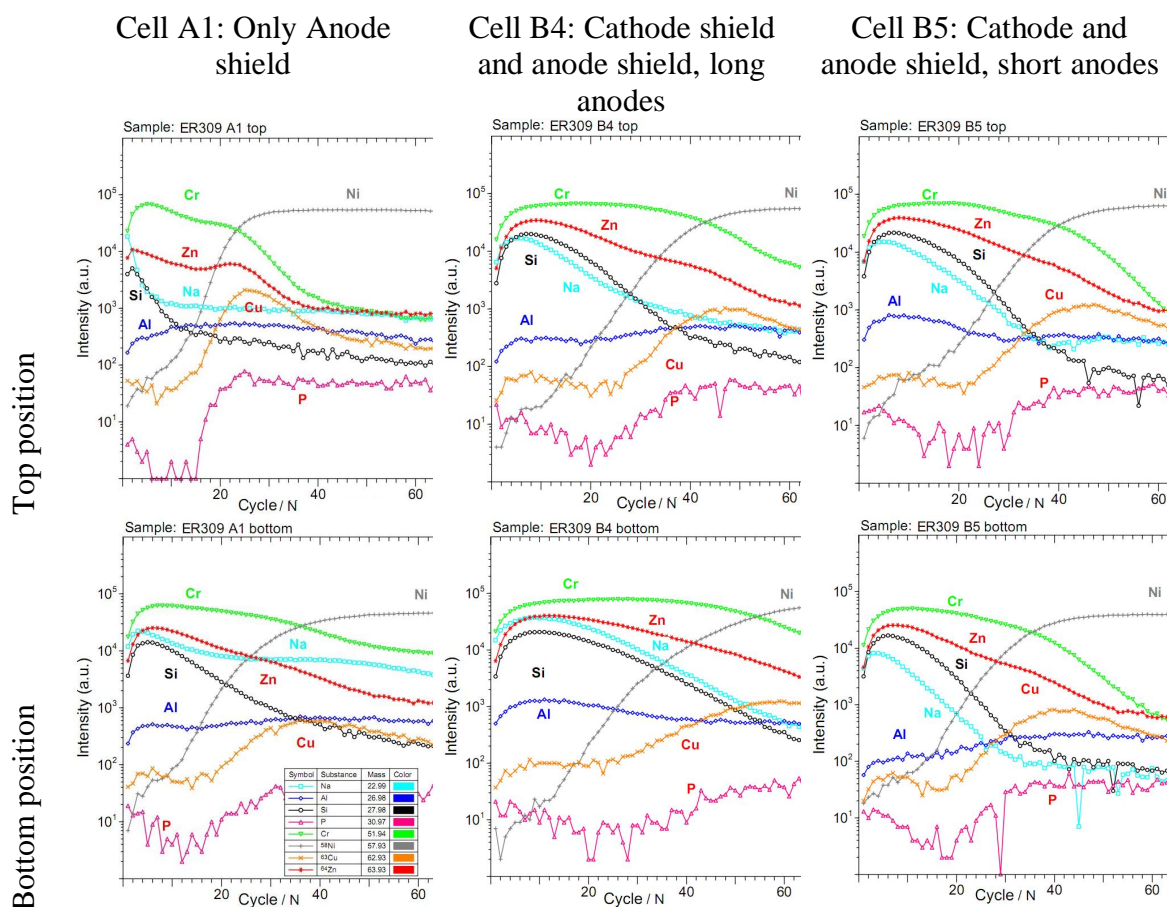


Figure 97: TOF SIMS depth profiles within experiment er309 from 6 samples plated with cell A1, B4 and B5 on a Ni/NiP leadframe surface for top and bottom position of the leadframe. The charts are numbered from a to f. Charts a to c are from top position and charts d to f are from bottom position.

The characterisation of the A2 layer with TOFSIMS shows for all depth profiles the existence of the three major partners within the A2 layer being Zn, Cr and Si. Also Na is present in low quantity as this ion is included to a certain extent during the deposition. Zn, Cr and Si intensities are dropping continuously through the layer for all groups with the exception of group A1 at the top position. It can be seen in figure 97a that the Si signal drops much more rapidly compared to the other groups.

Further differences between the various cells were i.e. for cell A1 the depth profile comparison of top and bottom position in figure 97a and d first shows a much thicker A2 layer on the bottom position by approximately factor 2 compared to the other two cells. A strong difference can be seen regarding the Zn and the Cr distribution. Especially the former one has a very pronounced peak in sample group A1 at the

interface to NiP for the top position in figure 97a which is missing for the bottom position shown in figure 97d.

Comparing the depth profile for both position of cell B4 in figure 97b and e it is obvious that the usage of the cathode shield tube entails a much more homogeneous distribution of Zn and Cr on top and bottom positions. There is no Zn or Cr peak visible at the interface to the NiP. The depth profile comparison between top and bottom position shows only a slightly thicker layer of the ZnCrSi layer at bottom position.

The result of A2 plating with cell B5 finally shows the best homogeneity regarding top and the bottom positions. Both depth profiles shown in figure 97c and f for top position and bottom position, respectively, are nearly identical.

For the TOF SIMS depth profiles obtained on the Al-1Si-0.5Cu there were no similar differences of the elemental distribution of Zn, Cr and Si found. All analysed samples show nearly identical shape. This can be interpreted through the fact that the A2 deposition on Al is a combined mechanism including chemical deposition as described in chapter "2.6 A2 dip test" and electrochemical deposition. Since the former mechanism is not dependent on current or potential a much more homogeneous deposition will occur compared to the purely electrochemical deposition mechanism on NiP.

To sum up this experiment on various plating cell geometries the cell geometry B5 resulted as the best option for homogeneous A2 plating on a TO263-3 leadframe with two rows of devices. The combination of an anode shield with a cathode shield leads obviously to much better hydrodynamic conditions and to a better homogeneity of the deposited layer.

Differences of the various groups and between top and bottom position of the leadframe could only be identified through measurement of the chemical compositions of the layers via TOFSIMS depth profile. For example cell A1 without a cathode shielding showed tree outcomes when compared to the results from other cells:

First a thickness of about factor 2 higher at bottom position compared to top position.

Secondly the Si content within the layers differs strongly.

Thirdly Zn and Cr both show two maxima in the layer at top position. This was not seen for the cells with a cathode shielding installed.

For the usage of this new plating cell in the next step a process parameter refinement was done including a variation of current density in the range of 10mA/cm² to 45mA/cm². Finally the process parameters using this new cell were fixed to a current density of 45mA/cm².

5.3.8 Summary on A2 deposition

For the A2 plating on semiconductor devices the following can be summarized: Analytical characterisation of the Zn-Cr layer obtained during A2 process results in alloy compositions between 20 to 35 at% Cr under various plating conditions. From metallurgical point of view these concentrations in the system Zn-Cr represent non-equilibrium phases ($\delta + \Gamma$) that are supersaturated solid solutions of Cr in a Zn matrix transforming partly to Zn₁₃Cr above $\Theta=170^\circ\text{C}$. The structure of the A2 layer in a cross sections shows a homogeneous alloy seed layer with a thickness of about 10-30nm and a subsequent nanostructured sponge and dendrite shaped upper layer with a thickness of 10 to 100nm. The structure of the second layer is the functional part of the adhesion promotion properties towards polymers that are filling up the nanostructured layer forming a mixture of ZnCr alloy framework and polymer. The ZnCr alloy framework is partly consisting of the respective ZnCr oxide depending on thermal treatment at the downstream processes and depending on the thickness of the structures.

The electrolyte used for the A2 deposition consists of rather low target concentration of zincate (13,8 mmol/L; 0,6 g/L Zn²⁺), of sodiumdichromate dihydrate (11,5 mmol/L; 0,6 g/L Cr⁶⁺), and of sodiummetasilicate (2,5 mmol/L; 0,07 g/L) being present as a colloid in alkaline aqueous milieu (12 g/L NaOH). The mentioned target concentrations can be increased by factor 5, but with the drawback of very limited electrolyte stability. With reducing the concentrations underneath the target concentrations the system shows up more sensitive. All three involved species Zn, Cr and Si have a major influence. A reduction of more than 50% of each species leads to a degradation of the process result, no dendritic A2 layer is obtained anymore.

Using this electrolyte at a high current density of $i=45\text{mA/cm}^2$ at high cell voltages of 5 to 8V yields a very low current efficiency of 2%, hence strong hydrogen development at the cathode occurs with some risks to the device, e.g. mechanical stress to wires and polyimide layers. The thickness of the obtained layer is independent of the current density applied in this region. Furthermore a dendritic growth is only observed above a certain limit of voltage and current density of 4,4V and 30mA/cm^2 in the investigated deposition cell. Underneath this limit only a flat layer is deposited. The obtained range for current density and cell voltage for a proper A2-layer growth were found to be $i=30\text{mA/cm}^2$ to 210mA/cm^2 and $U=4,4\text{V}$ to 16V , respectively. Within this range the layer morphology does not change significantly on Cu and on NiP substrates. In conclusion the current density factor is less sensitive compared to the concentration factor. Electrolyte flow as another factor for electrodeposition was found to have a big influence to the plating result. Best results were found at turbulent fluid dynamics. With laminar flow no homogenous dendritic morphology are possible.

Combining several factors of requirements for dendritic growth being a high cell voltage, turbulent flow and the presence of SiO_x colloid a electroporetic deposition mechanism can be concluded. Also the theoretical treatment of the deposition kinetics shows that the limiting current density at turbulent conditions is not reached and therefore a transport controlled mechanism can be excluded.

In terms of plating homogeneity on the geometrically complex device the development of a specific plating cell geometry was done. This includes the guidance of the electrolyte towards the product and some geometrical factors like the distance between anodes and the cathode as well as the size of the polymer shieldings between them. The obtained plating cell reported was the released for production.

5.4 Environmental measures for A2 technology

Usage of chromium-VI (Cr-VI) within the A2 electrolyte generates some requirements on occupational health and safety and environmental safety. Though Cr-III is an essential trace element in man and animal playing an important role e.g. in insulin metabolism, the higher oxidation state of Cr, Cr-VI is known as a very toxic substance with both acute toxicity, chronic toxicity with inhalation and skin contact and is further suspected to act teratogenic and carcinogenic [175] which was confirmed especially for inhalation of insoluble Cr-VI species [176] such as calcium chromate. Therefore tight regulations for working with those substances exist and proper and continuous training of the affected employees together with a medical monitoring is a major duty for industries using Cr-VI.

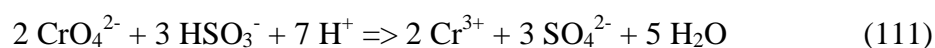
Besides the protection of employees from harm from Cr-VI exposure also environmental measures have to be taken regarding e.g. the handling of aerosols from the plating equipment and treatment of waste water. In Germany, for example, the emission of Cr-VI into rivers is limited to 0.1mg/L in general [177]. To keep this limit two possibilities exist: First the cleaning of waste water which was implemented in the first step and secondly the usage of a new electrolyte without involvement of Cr-VI, effort on both steps is described in chapter 5.4.1 and 5.4.2, respectively.

5.4.1 Wastewater treatment to prevent chromium-VI emission

For the handling of Cr-VI being emitted from the A2 plating process three major sources had to be considered: First source, Cr-VI emitted through the exhaust system of the plating equipment soaking off hydrogen that is generated during the plating carrying Cr-VI containing aerosol, second source, waste water from the rinsing sections that carry low concentrations of Cr-V continuously during production and third source, waste water from weekly electrolyte changes involving concentrations of 1g/L Cr-VI discontinuously.

The first emission of Cr-VI aerosol is captured through guiding the exhaust gas from the plating equipment through an alkaline washer column, the obtained washing solution is collected and frequently exchanged with new NaOH solution, the old solution is

combined with the third emission in a dedicated tank. The second emission, the Cr-VI containing rinsing water, is directly pumped into a reduction reactor system cascading over three reactors. Within those reactors the Cr-VI is reduced to the less toxic Cr-III via dosing a sodiumbisulfite solution ($\text{Na}_2\text{S}_2\text{O}_5$; in aqueous solution: $\text{Na}_2\text{S}_2\text{O}_5 + \text{H}_2\text{O} \Rightarrow 2 \text{NaHSO}_3$) as shown in equation (111). The correct dosing is controlled with an in situ redox electrode in each of the three reactors.



The third water emission consisting of higher concentrations of NaOH and Cr-VI combined with the frequently incoming exhaust gas washer solution is collected in a storage tank. In addition, also the strongly acidic waste water flowing from the acidic activation section of the plating equipment (methane sulfonic acid) is collected in a separate tank. From both tanks the alkaline Cr-VI solution and the acidic waste solutions are dosed into the reduction reactor with a ratio that adjusts a low pH level of $\text{pH} < 2.5$ required for a fast reduction of the Cr-VI to Cr-III according to equation (111).

The acidic Cr-III solution is finally leaving the reduction sequence into the central wastewater treatment of the factory. There all waste water is treated with hydrochloric acid (HCl) first to slightly decrease the pH if required. In a second step the pH is increased again with lime milk ($\text{Ca}(\text{OH})_2$) which leads to precipitation of heavy metal hydroxides, e.g. $\text{Cr}(\text{OH})_3$. The precipitates afterwards are filtered continuously and the slurry is moved to a repository.

Besides the complex and expensive process and equipment effort that is spend to the waste water cleaning the major risks regarding employee safety can only be fulfilled with the respective precaution of each employee. In addition, discussions with customers have aroused questioning the Cr-VI content within the A2 layer inside of the product. From chromate conversion coatings (CCCs) it is known that the deposited passivation layers are containing traces of Cr-VI [178]. To finally exclude any of those risks related to Cr-VI the only way is to completely prevent the usage of this substance in the A2 electrolyte.

5.4.2 New chromium-VI free electrolytes for A2 process in the future

To prevent the usage of Cr-VI in the A2 electrolyte three different approaches were started: I. Usage of the original A2 electrolyte without addition of any chromate. II. Usage of the original A2 electrolyte and substitution of chromate by other similar substances. III: Usage of new electrolytes formulations based on Zn-salts combined with other metal salts in a bigger pH range.

In table 36 an overview on the evaluated electrolytes is given. Electrolyte A is a simplification of the A2 electrolyte leaving out $\text{Na}_2\text{Cr}_2\text{O}_7 \times 2\text{H}_2\text{O}$. In electrolyte B, C and D instead of $\text{Na}_2\text{Cr}_2\text{O}_7 \times 2\text{H}_2\text{O}$ other oxidizing agents were used such as KMnO_4 , K_3VO_4 and K_2MoO_4 , respectively. The concentrations of the various species were kept constant for the electrolytes A-D with values identically to the species used for the A2 electrolyte (see table 36). It is also notable that for those alkaline electrolytes instead of NaOH solution KOH was used due to device specific risks regarding change of electrical parameters due to a higher mobility of Na^+ ions compared to K^+ ions in a MOSFET gate oxide [179], usually SiO_2 ¹. All these four electrolytes were prepared in the same way as for the standard A2 electrolyte as described in chapter 5.3.3.1.

In addition electrolytes E-G were evaluated over an area of concentrations in an acidic milieu as given in table 36 using the sulphate salts of Zn^{2+} , Co^{2+} , Cu^{2+} and Ni^{2+} as a basis for the deposition of binary Zn-Co, Zn-Cu and Zn-Ni alloys, respectively.

¹ : Sodium is known as a potential risk for semiconductor devices leading to shift of the threshold voltage. This phenomenon is related to the contamination of the gate oxide (SiO_2) of a semiconductor chip with sodium ions changing the dielectric properties of the SiO_2 . To minimize this risk it was an additional target of this project also to prevent the usage of sodium in the A2 electrolyte and to switch to the usage of potassium.

c_{metall} (A,B,C,D) [mmol/L]	A2 electrolyte	A	B	C	D	c (E,F,G) [mmol/L]	E	F	G
300	NaOH	KOH	KOH	KOH	KOH	10-100	ZnSO ₄ x 7H ₂ O	ZnSO ₄ x 7H ₂ O	ZnSO ₄ x 7H ₂ O
2,5	Na ₂ O:SiO ₂ (27% SiO ₂)					10-50	CoSO ₄ x 7H ₂ O	CuSO ₄ x 5H ₂ O	NiSO ₄
11,5	Na ₂ Cr ₂ O ₇ x 2H ₂ O	none	KMnO ₄	K ₃ VO ₄	K ₂ MoO ₄	0-100	K ₂ SO ₄	K ₂ SO ₄	K ₂ SO ₄
13,8	Zn(OH) ₄ ²⁻	ZnO	ZnO	ZnO	ZnO	0-70	H ₂ SO ₄	H ₂ SO ₄	H ₂ SO ₄
Experiment No.	Reference	ER222/322					ER311/ 321/32 5/335	ER393	ER394

Table 36: Overview on evaluated Cr-VI free electrolytes.

5.4.2.1 Chromium-VI free alkaline zincate electrolytes for A2 deposition

A: Identification of suitable Cr-VI substitutes

For the first electrolyte (A) the chromate was left out due to the results obtained in chapter 5.3.4 that showed that zincate and silicate are the more important species for the deposition of a suitable morphology and that chromate is most probably not required to obtain a sufficient mechanical strength of the deposited layer with a suitable morphology even though the results there show a more plate-like morphology.

For electrolyte B-D substitutes for chromate were chosen comparing various properties as shown in table 37. One of the major factors was the toxicity that is much lower for the chosen permanganate, orthovanadate and molybdate compared with chromate. In addition a minimum solubility of the salt in water is required to get a clear solution of the respective electrolyte. The solubility of potassium orthovanadate (K₃VO₄) was determined in the laboratory due to missing literature data. Within all three substances the metals that are to deposit are in their highest oxidation state similar to Cr-VI.

Species	Toxicity	Solubility in aqueous solution	Oxidation state	Anion structure in alkaline aqueous solution [45]	Metallurgical compatibility with Zn based on equilibrium phase diagram at temperatures below 200°C [139] ¹
$\text{Na}_2\text{Cr}_2\text{O}_7 \cdot x \text{H}_2\text{O}$	High, very toxic (T+, Teratogenic, cancerogenic): LD50 (rat, oral) = 50mg/kg LD50 (rat, inhalation) = 0.12mg/L in 4h [180]	731,8 g/L (20°C) [160]	+6	tetragonal coordinated oxygen in alkaline solution	Zn-Cr (see chapter): No solubility of Cr in Zn; IMPs: Zn_{17}Cr , Zn_{13}Cr
KMnO_4	Low, Irritating (Xn): LD50 (rat, oral) = 750 g/kg [181]	64 g/L (20°C) [161]	+7	tetragonal coordinated oxygen in alkaline solution	Zn-Mn: (αMn) limited at 1 at% Zn (0°C); (βMn) between 21at%<n(Zn)<50at% (0°C); IMCs: ZnMn , α' , γ_1 , δ_1 , ζ ; (Zn) limited at 0.1at% Mn (0°C)
K_3VO_4	Low, Irritating (Xn): LD50 (rat, oral) = 330 g/kg [182]	23 g/L (own measurement)	+5	tetragonal coordinated oxygen in alkaline solution	Zn-V: No solubility of Zn in V or of V in Zn; IMPs: V_4Zn_5 , VZn_3
K_2MoO_4	Very low, no specific signs required: LD50 (rat, oral) = 4233 g/kg [183]	840 g/L (20C) [163]	+6	tetragonal coordinated oxygen in alkaline solution	Zn-Mo: No solubility of Zn in Mo or of Mo in Zn; IMPs: MoZn_7 , MoZn_{22}

Table 37: Comparison of permanganate, orthovanadate and molybdate as possible substitutes for chromate.

In alkaline solution of the base A2 electrolyte also a certain similarity of the respective anions exists. Chromate anions are tetragonal coordinated with oxygen with formally two negative charges. Depending on pH level equilibrium exists as shown in equation (112) as discussed in chapter 4.2.4 already. In this equation the formal charges are assigned to two oxygen atoms, in reality all four bindings are equivalent and the two charges are delocalized [45].

1 : Description of the different phases according to Massalski [139] for the example of Mn-Zn:

(αMn): α - allotrope of Mn terminal solid solution of Zn

(βMn): β - allotrope of Mn terminal solid solution of Zn

ZnMn : IMC (intermetallic compound) with a specific stoichiometry such as ZnMn

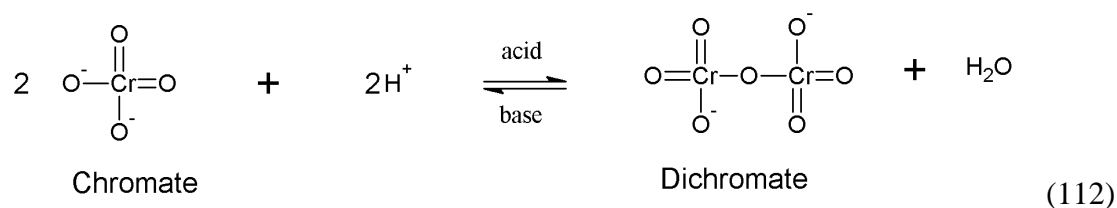
α' : MnZn_3 (low temperature phase)

γ_1 : γ -brass type structure, MnZn_4 (low temperature phase)

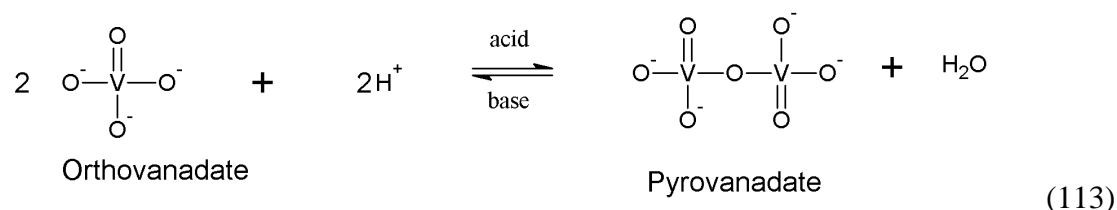
δ_1 : Phase with specific stoichiometry MnZn_9

ζ : Disorder body-centered-cubic phase MnZn_{13}

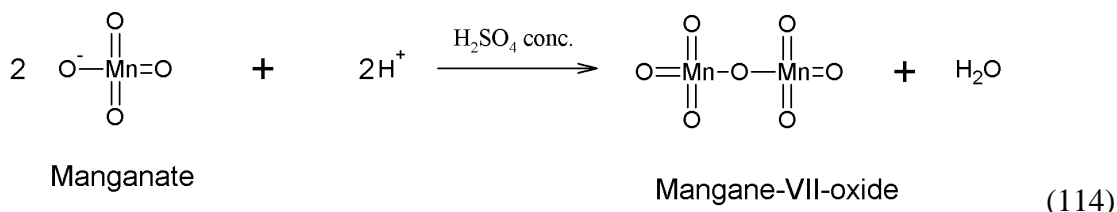
(Zn): Terminal solid solution of Mn in Zn



Orthovanadate anions behave similarly in alkaline solutions compared with chromate anions; they also form equilibrium depending on pH value and are converted to pyrovanadate upon adding acid to the solution. The structure of the orthovanadate anion also consists of a tetragonal coordination of oxygen atoms around the central V atom with three formal charges that are delocalized leading to four equivalent V-O bonds [45]. For simplification in equation (113) the charges are assigned again to three oxygen atoms.

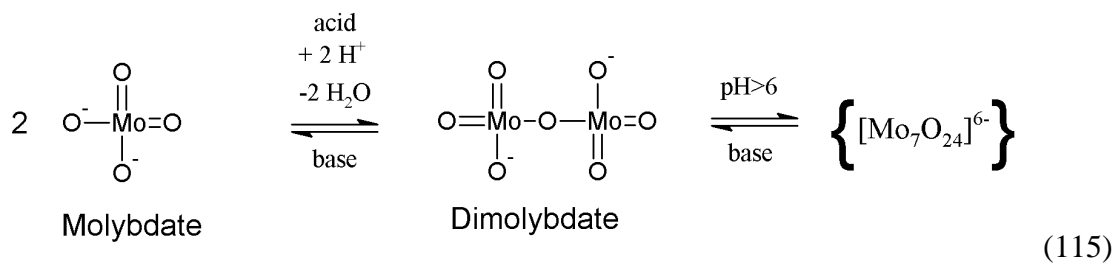


For the other two possible substitutes of chromate, the manganate and the molybdate, the similarity of the anion chemistry is less pronounced. Manganate is stable over a broad pH area and is converted to a manganese-VII-oxide via dehydration with concentrated H_2SO_4 only forming an explosive liquid (see equation (114)). There is no similar equilibrium known for manganate as it is for chromate or orthovanadate. However, also the manganate has a tetragonal coordination of oxygen atoms around the metal and also in this case the formal charge of -1 is allocated leading to four equivalent Mn-O bonds [45].



Molybdate in this row has more complex equilibria in aqueous solution. In alkaline solution also a tetragonal coordination of oxygen atoms around the central metal atom

exists, the formal charge of -2 is also delocalized in this anion leading to equivalent Mo-O bonds. However, a stable dimolybdate is only known together with bigger cations such as ammonium or tetrabutylammonium [184]. With sodium or potassium cations decreasing pH level leads to isopolymolybdates such as $[\text{Mo}_7\text{O}_{23}]^{6-}$ based on linked distorted $\{\text{MoO}_6\}$ – octahedra [184] and upon further decrease of the pH level ($\text{pH}<6$) $[\text{Mo}_8\text{O}_{26}]^{4-}$ is obtained, see equations (115) and (116). Finally at $\text{pH}<1$ precipitation of yellow molybdenum oxide hydrate ($\text{MoO}_3 \cdot n \text{H}_2\text{O}$; $n=1$ to 2) occurs. This material dissolves again in strong acidic milieu at $\text{pH}<0.1$ via formation of $[\text{MoO}_2]^{2+}$ oxo-anions [45].



To estimate the metallurgical compatibility the binary equilibrium phase diagrams were analysed. During electrodeposition possibly non-equilibrium phases are formed as in the case of the Zn-Cr alloy deposition (see chapter 4.2.6). During further downstream processes and during the lifetime of the product an additional thermal budget is applied that may lead to phase transitions and to separation of specific phases like for example for the phase transition reported for NiP deposits (see chapter 4.1.3). This metallurgical assessment was limited to phases existing below 200°C as this is the maximum temperature the product is exposed to.

In table 37 a short summary is given showing that in the Zn-Mn system the (α Mn)-phase has a limited solubility at 1 at% Zn (0°C). There is a second (β Mn)-phase in the concentration range of 21at%<n(Zn)<50at% (0°C) and several intermetallic phases (IMPs) (ZnMn, α' , γ_1 , δ_1 , ζ). On the side of high Zn concentrations a (Zn)-phase exists

that is limited at a concentration of 0.1at% Mn (0°C) [139]. In this system therefore several stable alloy compositions are possible.

In contrast to this in the Zn-V system there is no solubility of either Zn in V or of V in Zn and therefore no solid solution phase can be found. There are only two IMPs with discrete stoichiometry V_4Zn_5 and VZn_3 [139]. Therefore in the Zn-V system the orders of freedom of forming a stable alloy are low compared to the Zn-Mn system mentioned above. Formation of non-equilibrium phases during deposition with following phase transition is more likely to happen.

A similar indication is given for the Zn-Mo system that also shows no solubility of either Zn in Mo or of Mo in Zn and therefore no solid solution phase exists in equilibrium. The only stable alloys compositions are represented by the two IMPs that again have a discrete stoichiometry of $MoZn_7$ and $MoZn_{22}$ [139]. Also in the Zn-Mo system the freedom forming a stable alloy is limited to those two compositions.

B: First step of a laboratory plating evaluation and adhesion force determination

For the evaluation of the described electrolytes in the first step deposition experiments have been done in a laboratory beaker cell as shown in figure 98. On a magnetic stirrer (a) a 2 L beaker (b) was placed and two stainless steel anodes ($A = 6.6 \times 9.5 \text{ cm}^2$ each; $d = 0.5 \text{ mm}$) were placed at a distance of 10cm (d). Both anodes were covered with two polypropylene shields ($d = 1 \text{ cm}$) that were shielding the complete anodes from the substrate (c). As substrates either a Cu plate with a NiP plating (Dimensions of plate: $2 \times 10 \times 0.2 \text{ cm}^3$; $d_{\text{plate}} = 0.2 \text{ cm}$; $A_{\text{plate}} = 43 \text{ cm}^2$) or a TO263 leadframe section of 8 devices with Ni-NiP plating ($A_{\text{leadframe}} = 45 \text{ cm}^2$) were used as shown in chapter 5.1 in figure 53. To maintain continuous hydrodynamic conditions for all experiments the geometry was kept constant and the cell was filled up with 1.5 L of electrolyte, for the stirring a magnetic Teflon coated stirring rod was used ($l = 45 \text{ mm}$; $R = 3 \text{ mm}$). Mainly potentiostatic conditions were applied with a standard laboratory current source and the applied current density was recorded.

The various plating experiments were done in five steps: a) Activation at $\theta = 20^\circ\text{C}$ in 12 wt% methane sulfonic acid (MSA); b) Rinsing with deionized water for $t = 10 \text{ s}$; c) Deposition at $\theta = 60^\circ\text{C}$ for $t = 20 \text{ s}$; d) Rinsing with deionized water for $t = 10 \text{ s}$; e) Drying

with warm air. For some experimental groups purposely no activation was performed which showed no big influence in the tape test results, maybe because the used substrate were already very clean as they are taken out from the store and are without any visible sign of oxidation.

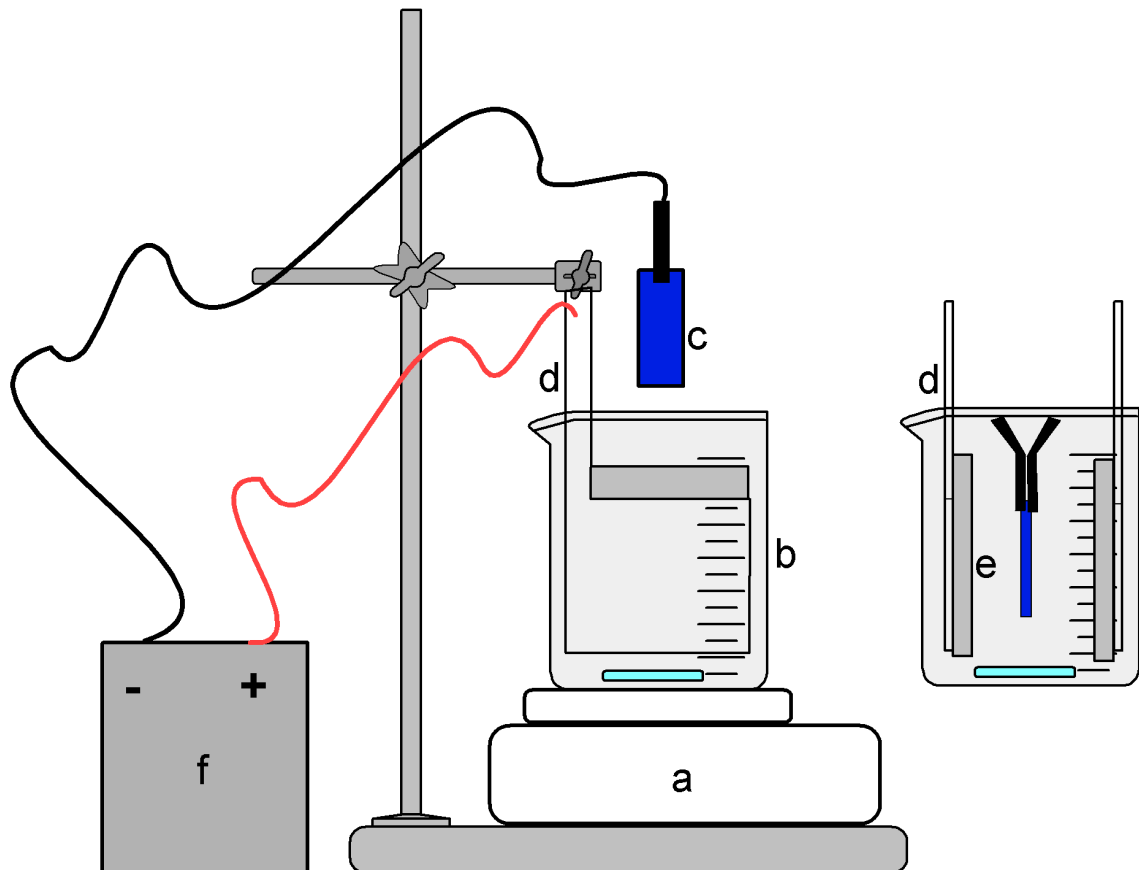


Figure 98: Sketch and description the beaker cell used for A2 deposition evaluations in the laboratory.

The various experimental groups were analysed according to table 38 in terms of the colour of the plating and via applying a tape test to assess the homogeneity of the adhesion promotion layer (as explained in chapter 2.5) and its adhesion to the substrate through observation of residuals of the plating on the tape after the tape test which was rated as “peeling”. For clarity and simplicity the tape test results $\geq 90\%$ are indicated green and $\leq 50\%$ are indicated red in table 38.

For some experimental groups a FESEM analysis of the bottom position of the sample was performed to analyse the morphology of the surface. To match the morphology obtained by FESEM to the adhesion promotion performance within a semiconductor package, i.e. a TO263-3 package, a button shear test (see chapter 2.4) was done on three experiments as defined in Table 38 using the molding compound KMC 2110-7¹ that is also used for production of devices with standard A2 plating.

First the electrolyte A described in table 36 was the standard A2 electrolyte without addition of $\text{Na}_2\text{Cr}_2\text{O}_7$ leading to a clear and colourless solution. It was tried out on a Cu/NiP plate with consistently good tape test on the bottom position of the plate, but low adhesion on the top side for two voltages. Group A1 was running with lower agitation reducing the rotation speed of the magnetic stirrer to 300 min^{-1} instead of 1000 min^{-1} for all other groups. Reproducing the result with the leadframe substrate showed good results of the tape test for both sides. For group A5 and A6 a sweep of the applied cell voltage from 6 to 12 V was tried with the same good results of the tape test indicating, that a higher voltage is favourable for certain morphology to grow. In group A7 and A8 this was confirmed with the Cu/NiP plate substrate and the conditions of $U_{\text{cell}}=10\text{V}$ were chosen for plating of four plates planned for further button shear testing. In addition samples from group A4 and A5 were separated for FESEM analysis.

The second electrolyte B evaluated in this experiment was substituting $\text{Na}_2\text{Cr}_2\text{O}_7$ by KMnO_4 as described in table 36 leading to a purple solution. Running the deposition in a row from 4, 6 and 10 V cell voltage brought out a deposit consisting of black spots that peeled off from both used substrates during the tape test. Due to the insufficient adhesion result this electrolyte was not further investigated, one sample (B3) was subjected to FESEM to analyse the morphology of those black spots, but only a flat surface was found without any sign of porosity.

The third electrolyte C looked much more promising in the first plating tests. All applied voltages 6, 8 and 10V resulted in positive tape tests on top and bottom positions for both substrates. Adhesion of the black deposit was sufficiently high after tape test, no peeling was observed, therefore group C4 was chosen for the button shear test and

¹ : KMC 2110-7 is the product name of a epoxy molding compound from the company Shin-Etsu

group C1a with identical plating conditions like group C4 was chosen for FESEM analysis.

Finally, for the fourth electrolyte D only 10V voltage was run for both substrates with reasonable good results of the tape test and sufficient adhesion of the deposit after it. Group D1 was chosen for button shear testing and D1a and D2 were taken for FESEM analysis, the latter being plated turning the leadframe substrate for 90°angle to evaluate geometrical influences of the leadframe.

Group er222	Substrate (LF=leadfram)	Electrolyte	Activation [sec]	I (A)	i [mA/cm ²]	U _{cell} [V]	Colour of plating	Tape test top	Tape test bottom	Adhesion of plating after tape test	Sample taken for shear test	FESEM bottom
A1 ¹	Plate	(Electrolyte A) Only Zn(OH) ₂	10	1,58	37	6,5	grey	0	95	ok		
A2	Plate		10	1,58	37	6,5	grey	0	95	ok		
A3	Plate		10	2,8	65	10	grey	0	90	ok		
A3a	LF			2,5	56	10	grey	100	100	ok		
A4	LF		10	1,5	33	8	grey	95	100	ok		Fig. 100
A5	LF			sweep 6 to 10 V in 20s			grey	100	100	ok		Fig. 103
A6	LF		10	sweep 6 to 10 V in 20s			grey	90	90	ok		
A7	Plate		10	sweep 6 to 10 V in 20s			grey	100	100	ok		
A8	Plate			2,8	65	10	grey	95	100	ok	4 pc	
B1	Plate	(Electrolyte B) KMnO ₄	10	3,5	82	10	black spots	0	0	peeling		
B1a	LF		10	3	67	10	black spots	0	10	peeling		
B2	LF		10	1,25	28	6	black spots	0	20	peeling		
B3	LF		10	0,5	11	4	yellow-brown	20	20	peeling		Flat
C1	Plate	(Electrolyte C) K ₃ VO ₄	10	3,5	82	10	black plating	100	100	ok		
C1a	LF			3,5	78	10	black plating	100	100	ok		Fig. 102
C2	Plate			2	47	8	black plating	100	100	ok		
C2a	LF			2,5	56	8	black plating	100	100	ok		
C3	LF			1,25	28	6	black plating	80	100	ok		Fig. 104
C4=C1a	Plate		10	3,75	87	10	black plating	100	100	ok	4 pc	
C4a	LF			3	67	10	black plating	100	100	ok		
D1	Plate	(Electrolyte D)		3,5	82	10	light blue	100	100	ok	4 pc	
D1a	LF			3	67	10	light blue	80	100	ok		Fig. 101
D2 ²	LF			3,5	82	10	light blue	90	90	ok		Fig. 105

Table 38: Overview on experiments done in a laboratory plating cell on Cr-VI free A2 electrolytes in experiment er222.

¹ : Stirring was done slowly with 300 min⁻¹ for this group whereas for all other groups stirring was done at 1000 min⁻¹.

² : Substrate turned by 90° angle compared to all other experiments.

The button shear test was performed on three different electrolytes, the bare zincate electrolyte A, the orthovanadate electrolyte C and the molybdate electrolyte D with the respective plating parameters as described above. Figure 99 shows a chart of all shear test results that were obtained after preconditioning (precon)¹, after precon plus 500 temperature cycles (TC) (-55°C to 150°C), after precon plus 1000 TC and finally after precon plus 2000 TC. The statistics varied from 5 to 10 values per measurement.

For the first reference group NiP-Ref without adhesion promoter the readouts after TC could not be obtained as the buttons were falling of the Cu/NiP plates during removing the samples from the TC oven. The second reference group on bare Cu showed an adhesion value of 8 N/mm² with a slight decrease along the TC stress.

Comparing the three adhesion promoter systems then electrolyte A (bare Zn) shows the lowest increase of adhesion at the beginning compared to the reference groups ending up with a value of 17 N/mm² after TC2000 which is by factor 2 higher compared to Cu-Ref and by factor 10 higher compared to the group NiP-Ref that had a shear value of 1.7N/mm² at the beginning only.

Adhesion forces from electrolyte C (Zn-V) and electrolyte D (Zn-Mo) show nearly identical high values of 17 N/mm² at the beginning but system D (Zn-Mo) seems to degrade less compared to system C (Zn-V) after TC2000 with 17 N/mm² and 13 N/mm², respectively. On the other hand the values after TC1000 for both groups were beyond to the limit of the shear tester (100kg; 21,5 N/mm²), therefore much higher adhesion is expected for those readouts, especially because system D after TC500 shows a high adhesion force of 25 N/mm². The big variation of shear forces especially of the plated groups can be also due to the experimental setup of the plating with limited homogeneity over various samples of plates prepared for button shear test. Comparing the first and the last readout of each group a clear degradation of the adhesion shear force during TC stress cannot clearly be concluded. But comparing the average value of adhesion forces of all groups it is seen that all three evaluated electrolyte systems are in

¹ : Preconditioning in this case was done with moisture sensitivity level 1 (MSL1) and 260°C soldering.

a range of 15-20 N/mm² and are by factor 3-4 higher compared to the Cu-Ref group and by factor 30-40 higher compared to the NiP-Ref group.

In addition by these data a rating is possible of the three electrolytes showing system D (Zn-Mo) to be the best, system C (Zn-V) to be second best followed by system A (bare Zn) as the third best. Based on this rating in the second step system D (Zn-Mo) was further refined and used for a product level evaluation on the real product.

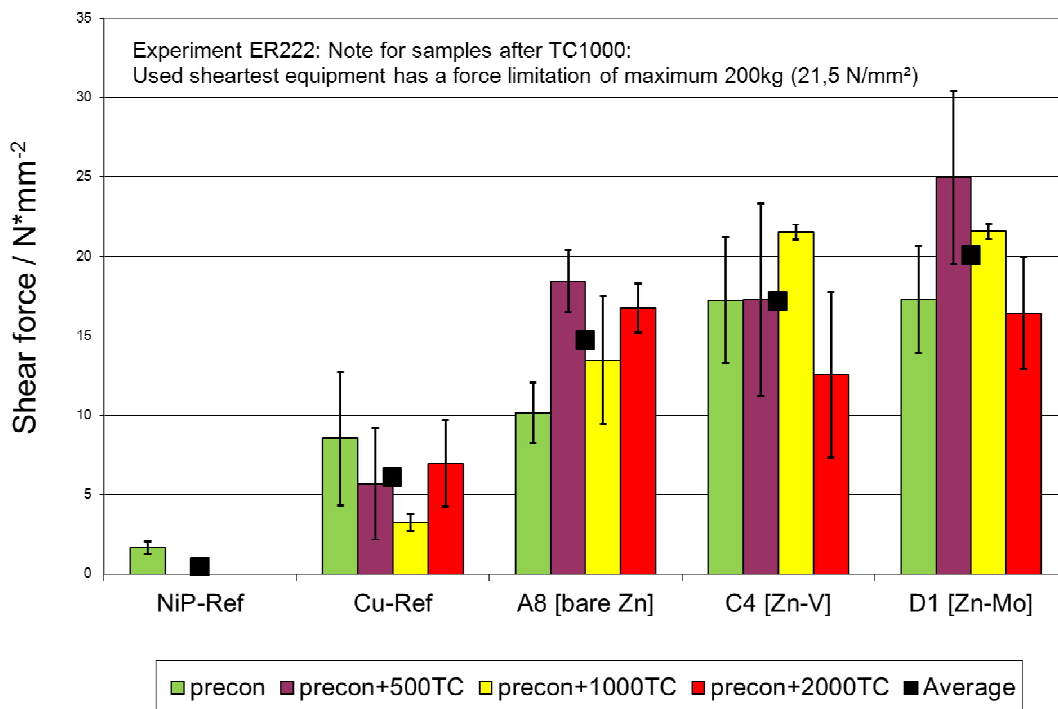


Figure 99: Button shear test results of electrolyte A, C and D including the Cu reference and the NiP reference surfaces without an adhesion promoter layer.

Comparing the surface morphology analysed with FESEM then system A (bare Zn) and D (Zn-Mo) show a similar grain structure of plate-like crystals growing mainly perpendicular to the surface with diameters ranging from 100 to 300nm and thicknesses in the range of 50 to 100nm as shown in figure 100 and 101. System C (Zn-V) shows much thinner plates and in addition needles are indicated in figure 102. Doing a voltage sweep from 6 to 10V over 20s in group A5 did not change the morphology in comparison to the deposition at a constant voltage of 10V, see figures 103) and 100,

respectively. Also using 6V instead of 10V in group C3 shows no change in morphology (figure 104 and 102).

In contrast system D (Zn-Mo) shows a more compact plate structure in group D2 where the leadframe substrate has been plated with a different orientation to the anodes and to the electrolyte movement compared to group D1 (see figure 105 and 101). System B (Zn-Mn) did not show any crystal like morphology but a flat surface known from the NiP surface and was not further evaluated.

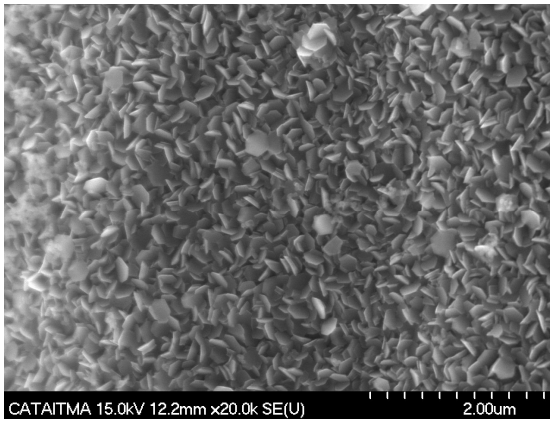


Figure 100: FESEM image of deposit from electrolyte A deposited at a voltage of 8V (experiment er222-A4, bare Zn).

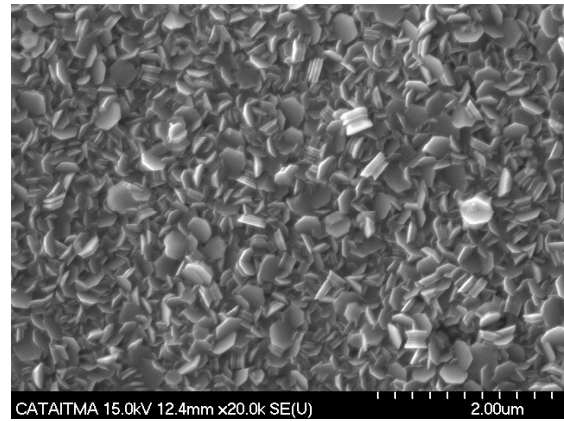


Figure 103: FESEM image of deposit from electrolyte A deposited during a voltage sweep from 6 to 10V in 20 s (experiment er222-A5, bare Zn).

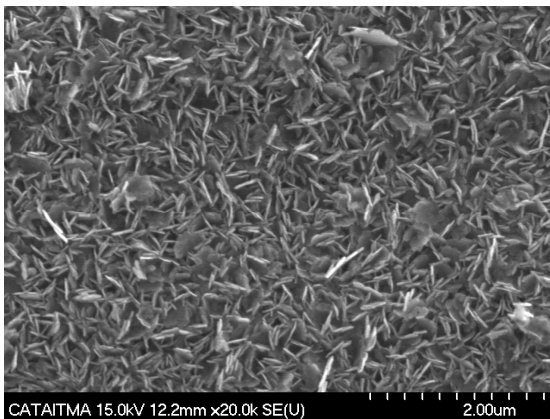


Figure 102: FESEM image of deposit from electrolyte C deposited at 10V (experiment er222-C1a, Zn-V).

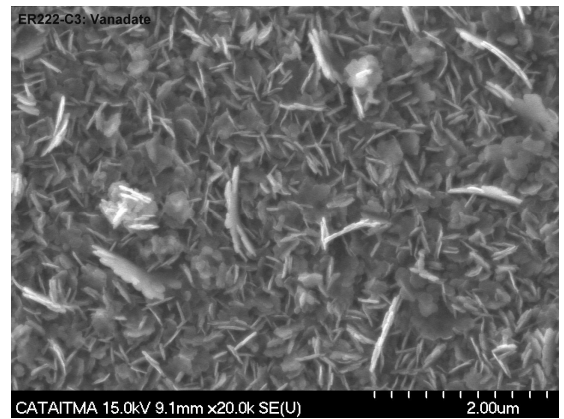


Figure 104: FESEM image of deposit from electrolyte C deposited at 6V (experiment er222-C3, Zn-V)

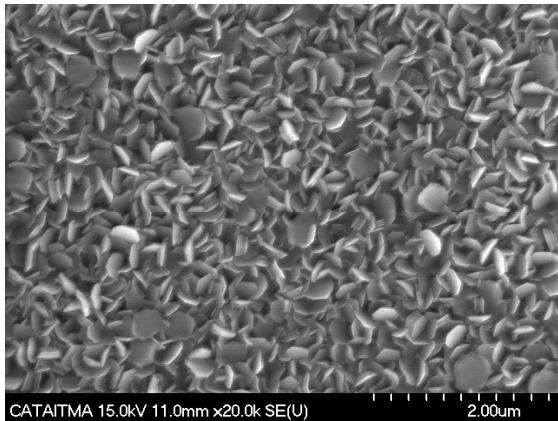


Figure 101: FESEM image of deposit from electrolyte D deposited at 10V (experiment er222-D1a, Zn-Mo).

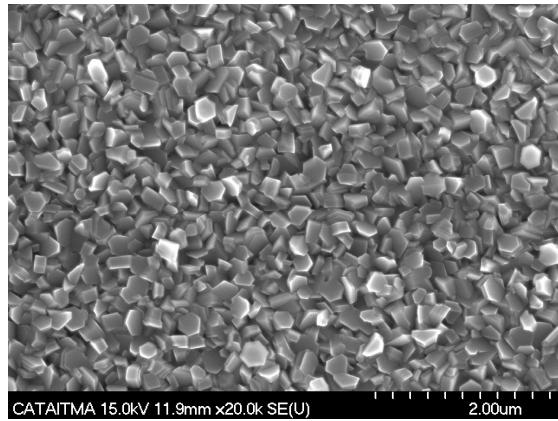


Figure 105: FESEM image of deposit from electrolyte D deposited at 10V, 90° turned substrate (experiment er222-D2, Zn-Mo).

A look at a higher magnification of the FESEM images shows that all three systems A, C and D are consisting of thin plates with thicknesses below 20nm, but for system A (bare Zn) and D (Zn-Mo) the plates are grown together at the flat crystal plane forming thicker blocks of 50-100nm thicknesses. The plate crystals in system C (Zn-V) have grown less symmetrically in much more different angles to each other leading to much more cross over and to smaller pores of <50nm between the crystals (figure 106) compared to system A or D showing pores >50nm (example given in figure 107).

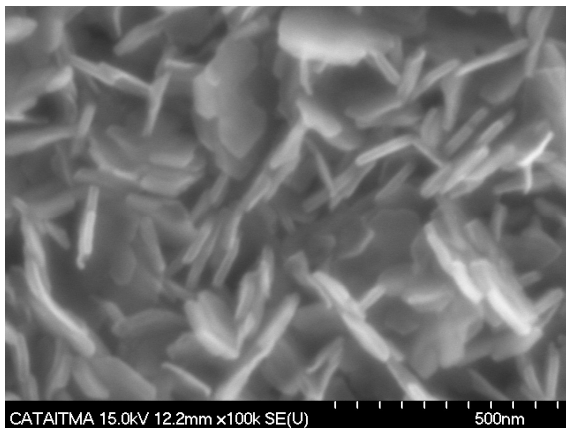


Figure 106: 100k FESEM image of deposit from electrolyte C deposited at 10V (experiment er222-C1a, Zn-V).

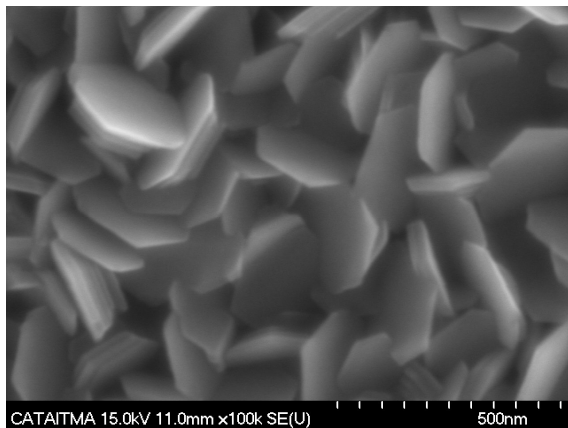
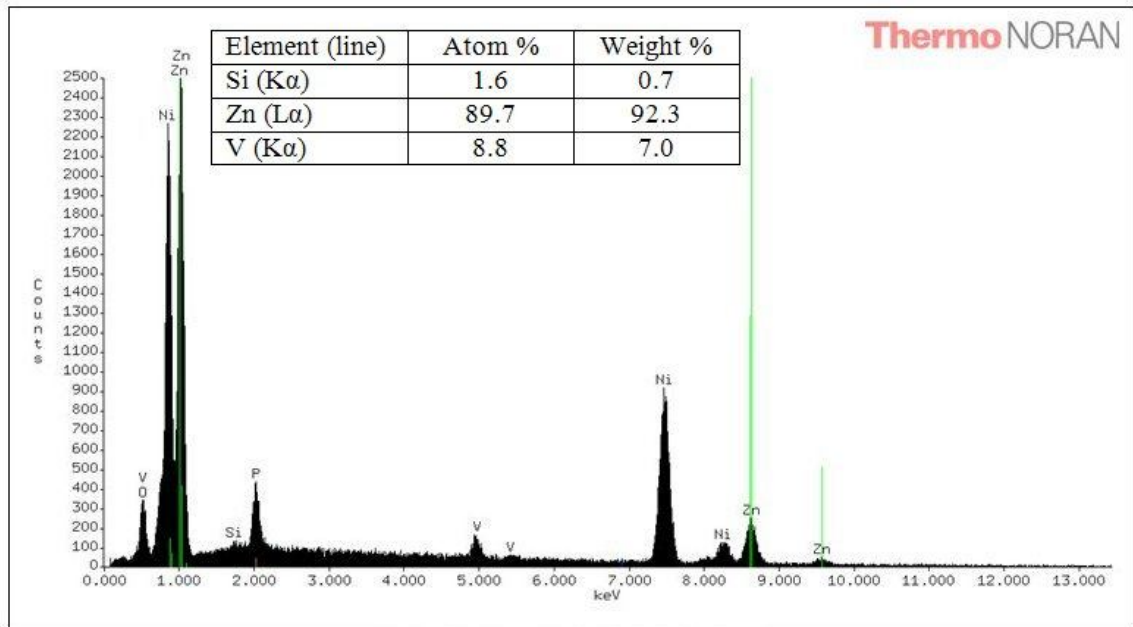


Figure 107: 100x FESEM image of deposit from electrolyte D deposited at 10V (experiment er222-D1, Zn-Mo).

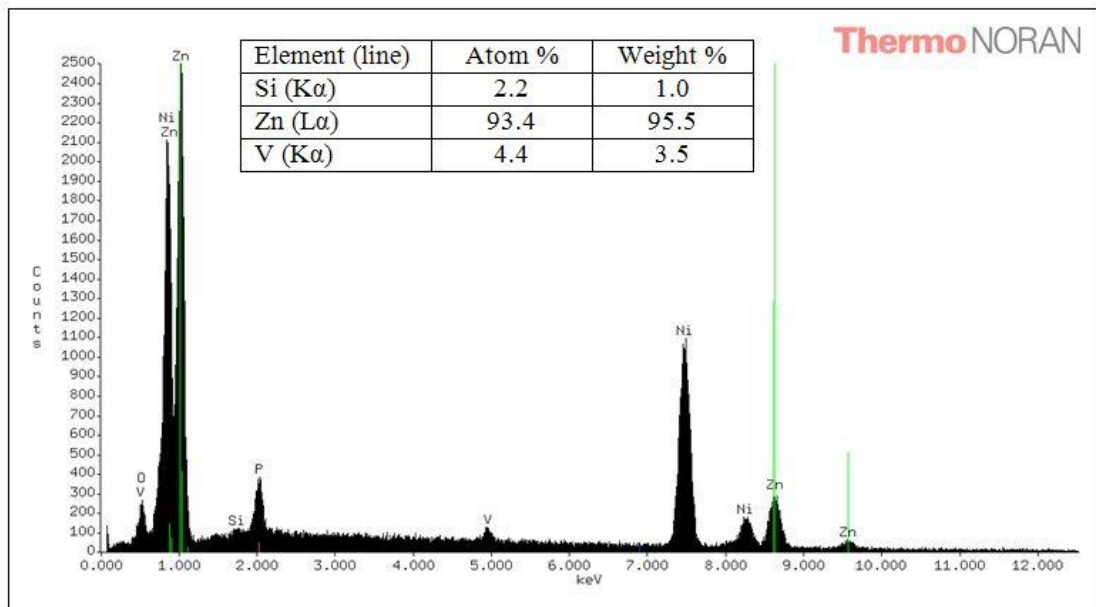
Besides the morphological assessment of the various surfaces also an EDX spot analysis was done from sample C1a and C3 (Zn-V). Both EDX spectra confirmed the co-deposition of Zn, V and Si; with spectrum of sample C1a deposited at 10 Volts an alloy composition of Zn-7V-0.7Si was quantified and with spectrum C3 deposited at 6 Volts Zn-3.5V-1Si was found, see figures 108 and 109. The signal of Ni and P within both

spectra belongs to the NiP substrate because at the 15kV acceleration voltage of the exciting electron beam also the material underneath the thin deposited layers is measured. Due to limited analysis equipment time no further samples from system D (Zn-Mo) were analysed.



C312-Riedl-ER222-C1-15kV

Figure 108: EDX spectrum of deposit from electrolyte C deposited at 10V (experiment er222-C1a; from elemental analysis: Zn-7V-0.7Si).



C312-Riedl-ER222-C3-15kV

Figure 109: EDX spectrum of deposit from electrolyte C deposited at 6V (experiment er222-C3; from elemental analysis: Zn-3.5V-1Si).

It is noteworthy that electrolyte system A, C and D lead to a homogenous coverage of the substrate with the respective plate morphology also at edges and at gaps that can be clearly seen in figure 110. At some positions, e.g. corners or sharp edges even an extreme macroscopic crystal growth with crystal sizes up to 5 μ m is observed, example given in figure 111. This indicates a transport controlled growth mechanism with crystallites growing into the Nernst diffusion layer during deposition as discussed in chapter 4.2.3 and as discussed by various authors cited there on the classical dendritic growth mechanisms for zinc, e.g. Naybour [117]. This result indicates that for those electrolytes the mechanism of morphology formation seems to be a classical diffusion controlled deposition leading to crystal sizes on the micron scale which is different from the suggested mechanism of the A2 morphology formation as discussed in chapter 5.3.8 which refers to the nanometer scale.

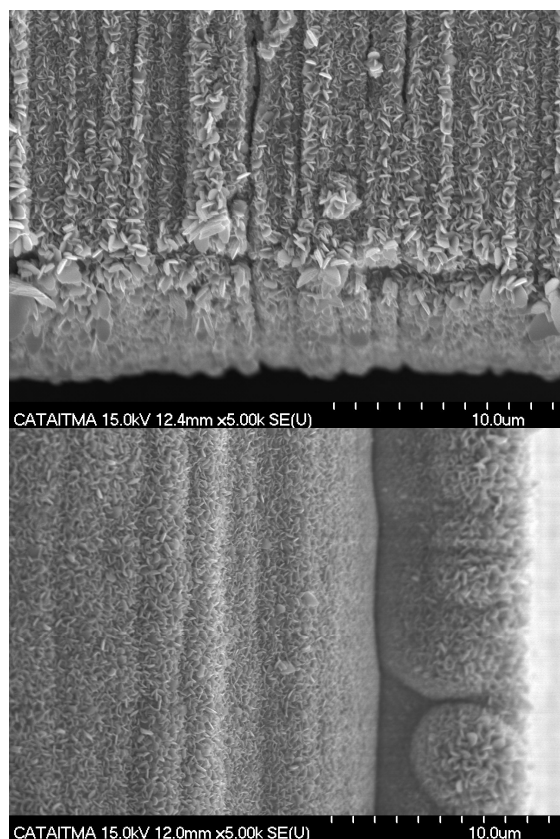


Figure 110: FESEM image of deposit from electrolyte D deposited at 10V, (experiment er222-D1, Zn-Mo). Homogeneous distribution of morphology at edge (top) and gap (bottom)

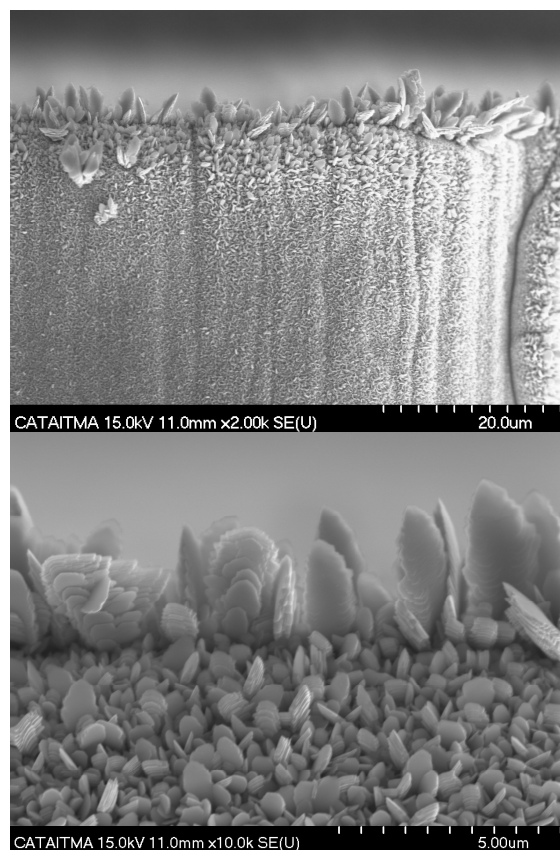


Figure 111: FESEM image of deposit from electrolyte D deposited at 10V, (experiment er222-D1, Zn-Mo). Extreme crystal growth at edge (Magnification: top 2k, bottom 10k).

For further assessment of the suitability electrolyte system C (Zn-V) and D (Zn-Mo) was chosen regarding evaluation within the product and within the production line.

C: Second step of evaluation at the product level via a pilot plant plating cell (er322)

A confirmation of the promising results of the two electrolyte systems C (Zn-V) and D (Zn-Mo) was planned by evaluation on the real product within the TO263 production line. Due to limited availability of equipment time slots in production and delivery delays of K_3VO_4 it was decided to focus on the system D (Zn-Mo) using $KMoO_4$ instead of $Na_2Cr_2O_7$. For all manufacturing processes productive equipment for this evaluation was used besides the A2 plating equipment. However, due to incalculable risks of a cross contamination of the productive A2 electrolyte and the new electrolyte based on KOH and orthovanadate it was decided not to run the plating on the productive equipment but to build a pilot plant cell for the deposition and to use a rectifier from an old plating equipment.

The size of the pilot plat cell was less than half the size compared to the productive cell, one complete TO263-3 leadframe could be plated at one time discontinuously. Figure 112 shows a sketch of this cell as top view and side view. The cell consists of an inner compartment (a) and an outer compartment (b). The electrolyte enters the cell via tube (d) flowing into the cathode shield tube (c) from where it is flowing perpendicular to the leadframe (f). This cell geometry results in a flow direction parallel to the chip surface and to the leadframe surface as shown in the magnification of one device in figure 112 (right). After passing the substrate the electrolyte reaches the overflow of compartment (a) from where it enters compartment (b) and from there finally leaves the cell over tube (e). The complete electrolyte volume of 13L is pumped around in a closed cycle. The various geometries within the cell, such as the geometry of the cathode shield tube (c) with its holes and the stainless steel anodes (h) with their polypropylene shields (g) were identically built as within the productive cell (see chapter 5.3.7, figure 95, cell No. 5)¹. The position of the leadframe inside the cell was done via the same clamps that are

¹ : The following dimensions were selected for the variables of the pump and the tubing for the pilot plant cell similar to those of the production cell: Maximum electrolyte velocity $v_z = 90 \text{ cm/s}$; Dimension of the cathode shield tube: 38 holes each with $R=2\text{mm}$; Maximum pump flow required: $\dot{V} = 26L/\text{min}$

used inside the productive equipment including a height adjustment mechanism for the leadframe. This means both the electrical connection and the dipping depth of 1 mm was exactly the same as within the productive plating cell. The main difference between the productive and the pilot plant plating process is that in production all necessary steps for activation, first rinsing, plating, second rinsing and drying are done continuously. Also the current density is ramped up automatically when a leadframe enters the cell from the side gates. During the pilot plant plating all necessary steps were done by placing the leadframe into the respective solution, i.e. the MSA solution, measuring the process times manually and removing the leadframe to move it to the next step, i.e. the rinsing. For the DC plating specifically the current was switched on only after placing the leadframe into the electrolyte. After the plating time of 20s the leadframe was taken out and at the same time the current was manually ramped down to zero depending on the dipping depth of the leadframe. This was done conformal to production in order to keep the current density constant also during removal of the leadframe which made also sure that the leadframe with the readily deposited A2 structure was not staying inside the electrolyte without any applied current. The electrolyte flow was manually adjusted through a valve after the pump and through a flow meter at the inlet (d).

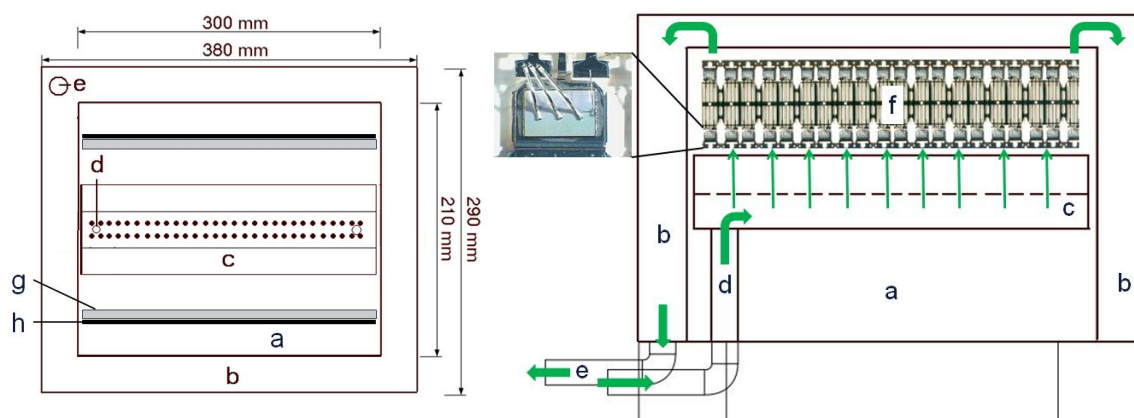


Figure 112: Sketch of the pilot plant cell from top (left) and as a side view (right). Position: (a) inner compartment, (b) the outer compartment of the cell; (c) cathode shield tube with its feeding tube (d); (e) drain tube; (f) substrate (leadframe); (g) anode shields; (h) anodes.

Due to the higher volume of electrolyte required to fill up the cell ($V=13L$) the setup of the electrolyte was done in the same way as described for the productive electrolyte in chapter 5.3.3.1. The concentrations of the four different stock solutions and the final electrolyte concentrations are summarized in table 39

Solution	Stock solutions				Molybdate A2 Electrolyte			
	Component	w [g/L]	Metal	C _{metal} mol/l	V _{concentrates} [L] for V=13L electrolyte	W _{metal} [g/L]	C _{metal} [mol/L]	
A	KOH	700	K	12,475	0,177	9,539	170,0	
B	Na ₂ O:SiO ₂ (27% SiO ₂)	128	Si	0,890	0,036	0,070	2,5	
C ¹	K ₂ MoO ₄	206	Mo(VI)	0,865	0,173	1,107	11,5	
D	ZnO	125	Zn (as zincate)	1,536	0,116	0,900	13,8	
						K (total)	16,767	299,0

Table 39: Electrolyte components and concentrations for the stock solutions and the concentrations of the electrolyte components in the final electrolyte.

For evaluation of a working process point first several settings were varied such as the current density (range: 10 - 110 mA/cm²), the plating time (10s and 20s) and the agitation (pump flow 8 L/min related to $v_z=27\text{cm/s}$; 26L/min related to $v_z=27\text{cm/s}$). NiP-plated leadframes were used for the plating and a tape test was applied to assess the homogeneity of the adhesion promoter plating. It turned out that the plating quality was differing strongly comparing top and bottom position of the leadframe. Therefore it was decided to remove the polypropylene shieldings completely which resulted in homogenous plating. Finally a parameter set was fixed for the manufacturing of those leadframes which carried chips² planned for a complete built of devices and for further reliability investigations on the final product. The major parameters for the deposition were $i=65\text{ mA/cm}^2$ (6V), $\theta=60^\circ\text{C}$, $t=20\text{s}$, $\dot{V}_{pump}=26\text{L/min}$ (related to a electrolyte velocity at the device of $v_z = 90\text{ cm/s}$) and a pilot plant cell geometry as described above, but without anode shields³. Activation, rinsing and drying was done according to the productive A2 process (see chapter 5.3.1).

After manufacturing of the devices further stress tests were applied on two experimental groups and after each stress (MSL1/260°C and TC500) a readout on 15 devices each

¹ : Potassium molybdate purchased from Riedel-de-Haen, pure, No.13304

² : Device type SPP80N06S2-09; chip size 3,8x3,8mm², AlSiCu metallisation and Pb-2Sn-2.5Ag chip solder, standard assembly of the TO263-3 linked package line (LPL).

³ : Results are referring to experiment er336 that is not explicitly described in this work, only the outcome is reported.

group was done with scanning acoustic microscopy (SAM, see chapter 2.10). The SAM was done on three levels, first the chip surfaces together with die pad, secondly the leads and thirdly the chip solder layer was scanned to find possible degradation at interfaces at those levels. Two groups were investigated, the reference group (1ref) and the group carrying the adhesion promoter of the molybdate electrolyte (2), both plated in the pilot cell.

In figure 113a and b the SAM pictures of these two groups are compared after the preconditioning stress for the chip frontside and the die pad. The devices with the standard A2 deposition show no significant delamination on all 15 devices; however the devices built with the molybdate electrolyte show slight delamination on the die pad, but no delaminated areas on the chip surface. Further stress on these devices with TC500 results in a partly die pad delamination for the group 1ref with standard A2 (see figure 113c) and for the molybdate group 2. Degradation of the interface molding compound to die pad gets worse seen in figure 113d. This weakness, which is known from the standard A2 technology regarding delamination on the die pad, is getting worse with the molybdate electrolyte. The die pad is covered mainly by chip solder and the deposition of Zn-Mo from the molybdate electrolyte in a suitable morphology seems to be insufficient on the solder surface. It is very important to note that for both electrolytes the adhesion on the chip surface is sufficient and does not show any delamination.

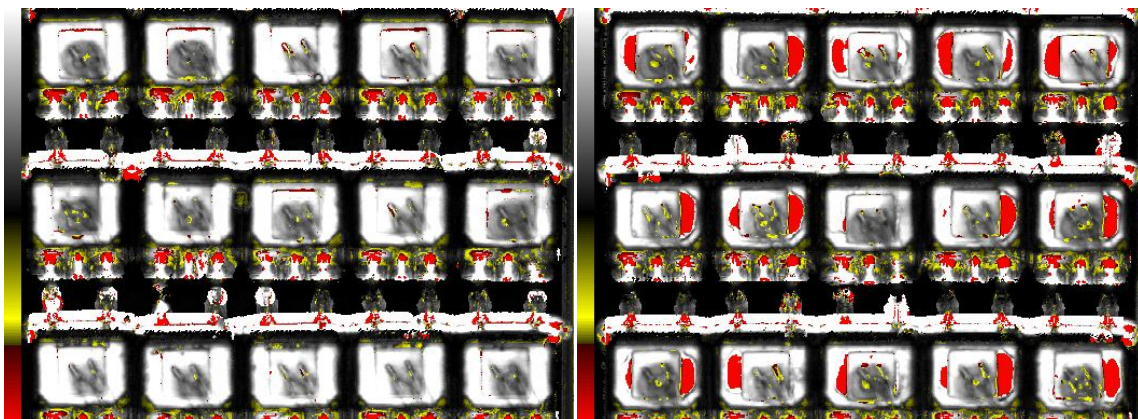


Figure 113a: Experiment 1ref, standard A2, SAM of chip frontside and die pad after preconditioning

Figure 113b: Experiment 2, molybdate electrolyte, SAM of chip frontside and die pad after preconditioning

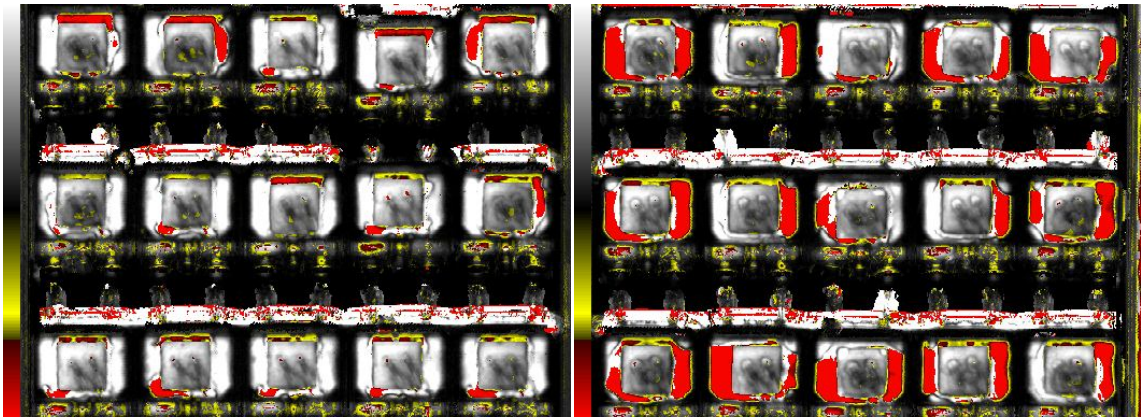


Figure 113c: Experiment 1ref, standard A2, SAM of chip frontside and die pad after TC500

Figure 113d: Experiment 2, molybdate electrolyte, SAM of chip frontside and die pad after TC500

A very impressive result was obtained on the lead surfaces where both electrolytes were leading to a complete adhesion during both stress tests. Figures 114 a and b show the comparison of both electrolytes after precon plus TC500 stress; there is no degradation visible. This position on leads is known as a critical position that suffers from delamination in all cases where no adhesion promoter is applied. The new molybdate electrolyte offers a sufficiently high adhesion on the leads which is comparable to the adhesion offered by the standard A2 electrolyte.

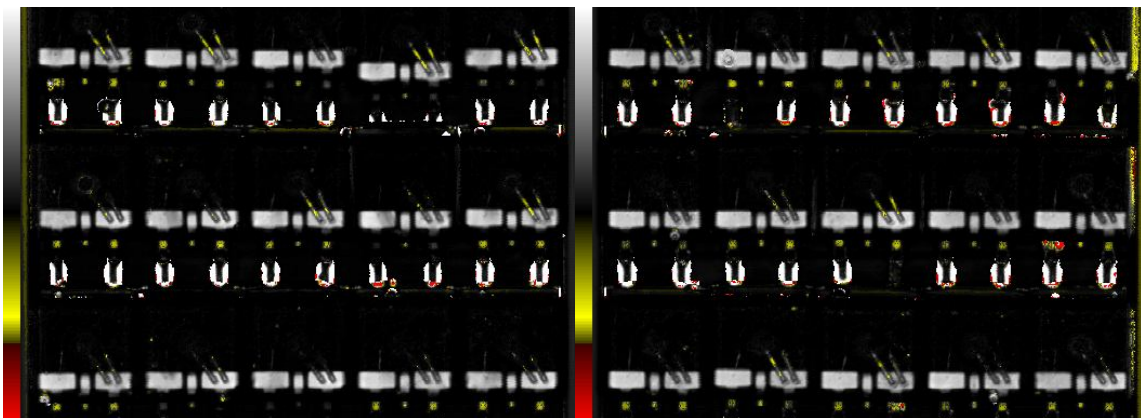


Figure 114a: Experiment 1ref, standard A2, SAM of leads after TC500

Figure 114b: Experiment 2, molybdate electrolyte, SAM of leads after TC500

A second strong indication of the high potential and the reliability of the molybdate based electrolyte can be seen in the SAM images of the chip solder layer. Also within the chip solder the device shows no degradation. After precon plus TC500 no difference between the two electrolytes can be observed (see figure 115 a and b), the molybdate electrolyte shows still the same sharp corner shapes of the chip as the standard A2 electrolyte shown in figure 115c. This allows concluding that the molybdate electrolyte offers a similar stability of the major package interfaces as the standard A2 electrolyte

as the degradation of the chip solder layer during TC stress is an indicator for interface weaknesses in a package leading to higher stress towards the chip solder and finally leading to solder degradation which first can be seen at corners.

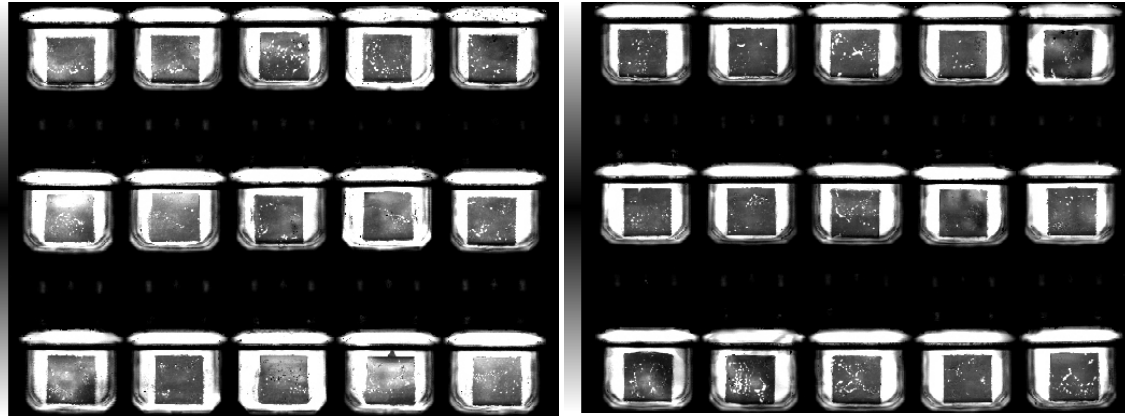


Figure 115a: Experiment 1ref, standard A2, SAM of chip solder layer after TC500

Figure 115b: Experiment 2, molybdate electrolyte, SAM of chip solder layer after TC500

D) Summary on alkaline Cr-VI free electrolytes

Summarizing the four electrolytes investigated in this section the following can be stated:

Substituting Cr-VI ($\text{Na}_2\text{Cr}_2\text{O}_7$) of the standard A2 electrolyte by Mn-VII (KMnO_4 , electrolyte B) instead of did not show promising results in the laboratory experiments and was therefore stopped early. For three other electrolytes investigations on adhesion promoting properties were showing very promising adhesion results compared to NiP and Cu substrates without adhesion promoter. Using only a zincate based electrolyte (electrolyte A) without any substitute for Cr-VI showed increased adhesion and offers a huge simplification of the bath chemistry. Evaluations based on K_3VO_4 as a Cr-VI substitute (electrolyte C) showed promising results also during laboratory experiments leading to alloy deposition such as Zn-3.5V-1Si with slightly better adhesion compared to electrolyte A. Both promising systems have still been investigated on laboratory scale and not yet been used in a manufacturing environment.

Also electrolyte D using Mo-VI (K_2MoO_4) as Cr-VI substitute showed promising adhesion results from the laboratory that were quite equivalent to electrolyte C. Furthermore, it was possible for this electrolyte to scale up the deposition process and

hardware from the laboratory to a pilot plant level and to show the excellent adhesion promoter function in the final product with promising reliability results. Using K_2MoO_4 instead of $Na_2Cr_2O_7$ within the standard A2 electrolyte has a high potential for achieving similar product reliability in a TO263-3 device with a standard MOSFET with AlSiCu metallisation. Processability of this new electrolyte is similar as for the standard electrolyte, no modification of the deposition equipment is required and most important: Toxic Cr-VI can be avoided.

A further discussion and summary on the potential of the alkaline electrolytes from this section will be given after discussion of acidic electrolyte systems in the next section to come to a more general conclusion and final outlook in chapter 5.4.3.

5.4.2.2 Chromium-VI free acidic zinc electrolytes for A2 deposition

Apart from the alkaline zincate system three different alloys obtained from zinc sulphate based solutions were evaluated for A2 deposition, such as Zn-Co, Zn-Cu and Zn-Ni as shown in table 36. Besides the substitution of Cr-VI there was a second motivation to investigate electrolytes in more neutral and acidic pH milieu: The usage of the alkaline zincate electrolytes generates fast corrosion of aluminium of the device during deposition. To minimize this corrosion a complete change of the electrolyte system was considered.

For alkaline pH value the conditions for the dendritic deposition of Zn was described (in chapter 4.2.3 ff). However, dendritic growth of Zn is also reported from acidic electrolytes. Mackinnon et al. report dendritic and flower-like deposits from a zinc chloride based electrolyte¹ [185] and even so they spend much effort to get a smooth Zn deposit by using additives, some of those additives were still leading to dendritic deposition of the Zn. Examples are animal glue [186] or commercial Zn electro winning additives (Kelex100, Sherex Chemical Co., Dublin, Ohio) [187].

Steffen and Wolfhard investigated the deposit morphology of Zn from an acidic $ZnSO_4$ electrolyte (100g/L Zn^{2+} , 75°C, pH=2.5) for steel plating for corrosion protection and

¹ : Conditions were for example 15 g/L Zn^{2+} , 0.12 mol/L HCl, $j=323A/m^2$ at 35°C.

obtained also a dendritic deposit at high current density and low electrolyte agitation [188].¹

Furthermore, dendritic deposition of zinc was also observed by Hsieh et al using zinc chloride electrolytes with applying various additives as brighteners to prevent dendrite formation [189]; however it seems to be quite difficult to obtain smooth zinc deposits in their work at high current density (100mA/cm²) and low Zn²⁺ concentration (0.44 mol/L ZnCl₂).

Dendritic growth of Zn during electrodeposition from ZnCl₂ solution was investigated to control the manufacturing of tailored nano crystalline electrodes achieving high surface areas [190, 191]. The usage of chloride containing electrolyte however is not advisable for electronic devices as several parts of the device are consisting of aluminium suffering from strong corrosion caused by presence of chloride ions in aqueous solution [227]. Therefore the first selection of suitable electrolytes for dendritic growth consisted of sulphate electrolytes.

Also from ZnSO₄ electrolytes electrochemical deposition of zinc metal leaves and fractal structures in acidic milieu is possible. Under conditions such as a high deposition current density and low zinc concentration mass transport limited deposition far away from equilibrium conditions leads to those morphologies [192, 193, 194, 195, 196] window [197]. Grier et al. investigated zinc sulphate in the concentration range 0.01 to 1.0 mole/L Zn²⁺ and at a pH of 7 at various potentials and obtained dendritic growth of zinc at high deposition potentials. These findings on the concentration window were partly confirmed from the experimental results in this work (see table 40).

Apart from the deposition of bare zinc there is the possibility of co-deposition of Zn with other metals such as Cu, Co or Ni to form alloys with adhesion promoting and corrosion preventing properties.

Zn-Cu alloy (brass) can be deposited over the complete concentration range of Cu from alkaline cyanic electrolytes what is known since the year 1844 [198] and being

¹ : Conditions were: $i=25\text{A/m}^2$ at $v_x=0$ and $i=300\text{A/m}^2$ at $v_x=1.5\text{m/s}$ (v_x is the relative velocity between substrate and electrolyte in parallel direction)

established in many industrial applications. Brass is used for example as adhesion promoter between natural rubber and steel cord within car tires [15, 199], but has corrosion risks regarding the attack of the iron core of the tire cord due to the insufficient protection of the porous brass layer. Therefore Zn-Ni (i.e. Zn-82Ni), Zn-Co (i.e. Zn-1.5Co) and dual layer systems Zn-Co/Zn-Ni alloys (Zn-Co is the layer towards the steel cord) with similar composition as given above and thicknesses of about $1\mu\text{m}$ have been developed. They show similar adhesion strength as for the traditional brass which is by a factor three higher compared to the adhesion of rubber to uncoated steel or to bare zinc [199]. For example, the morphology of electrodeposited Zn-Ni alloy is also grainy and sponge like supporting adhesion to rubber [199, 200]. In addition, these alloys show much higher corrosion resistance on steel and have excellent long term durability in tires compared to brass [201, 202, 203].

Using this previously given information from literature, experiments were done on three acidic electrolytes based on ZnSO_4 and combined with CuSO_4 , CoSO_4 and NiSO_4 , respectively. The first step of the evaluations was again done in the laboratory using the beaker lab-cell as shown in figure 98 with identical experimental setup as for the alkaline zincate experiments. As a substrate a bare Cu TO263 leadframe section of 8 devices ($A_{\text{leadframe}} = 45\text{ cm}^2$) was used as shown in chapter 5.1 in figure 53. Results are summarized in table 40 giving an overview of the evaluated ranges of concentrations and deposition parameters in one column and the final best parameters that were found for the respective electrolyte. The readout was done with tape test, FESEM and Auger analysis (see chapter 2) for specific groups out of in total 70 experiments. For most of the experiments the obtained tape test was insufficient. Especially for the deposition of Zn-Ni (electrolyte G) and Zn-Cu (electrolyte F) the best tape tests that were reached were 30% and 40%, respectively. Therefore for these deposits no further analysis was done.

Electrolyte		E (Zn-Co)		F (Zn-Cu)		G (Zn-Ni)	
Parameter		Range	Best parameters	Range	Best parameters	Range	Best parameters
c [mmol/L]	ZnSO ₄ x 7H ₂ O	10-100	37	20; 30; 50	60	20	20
	CoSO ₄ x 7H ₂ O	10-50	7; 14; 28				
	CuSO ₄ x 5H ₂ O			5; 20	20		
	NiSO ₄					5; 30	5
	K ₂ SO ₄	0-100	100	50	50	none	none
	H ₂ SO ₄	pH: 7; 3; 1	pH = 7	pH: 7; 3; 1	pH = 1	pH = 7	pH = 7
Deposition	j [mA/cm ²]	5-75	33; 33; 67	45-100	45	45; 100	45
	U [V]	3-23	3.3; 3.4; 4.5	4-14	n.a.	7; 12	7
	T [°C]	35-60	60	60	60	60	60
	t [s]	10; 20	20	10; 20	10	10; 20	10
	n [min ⁻¹]	300-1000	700	300; 700	300	300-1000	700
Readout	Tape test on Cu [%]		55; 65; 50		40		30
	FESEM		Fig. 116a-c		n.a.		n.a.
	Auger		Fig. 116d		n.a.		n.a.
Experiment	ER311/321/325/335	ER321: A10; A11; A14	ER393	ER393-15	ER394	ER394-1	

Table 40: Overview on results obtained on deposition of Zn-Co, Zn-Cu and Zn-Ni alloys.

The results of the Zn-Co alloy deposition (electrolyte E) appeared much more promising. Three parameter sets with tape test results between 50-65% were identified; the obtained deposits were further analysed with FESEM and Auger showing dendritic growth of a Zn-Co alloy. In figure 116 a, b and c the FESEM image of experiment A10, A11 and A14 plated with 7, 14 and 28 mmol/L Co²⁺, respectively, show a similar porous layer with a pore size <100nm and with needle diameters <10nm comparable to the morphology know from the A2 layer from the standard electrolyte (In figure 116 c the FESEM picture was recorded at a higher magnification of 50k).

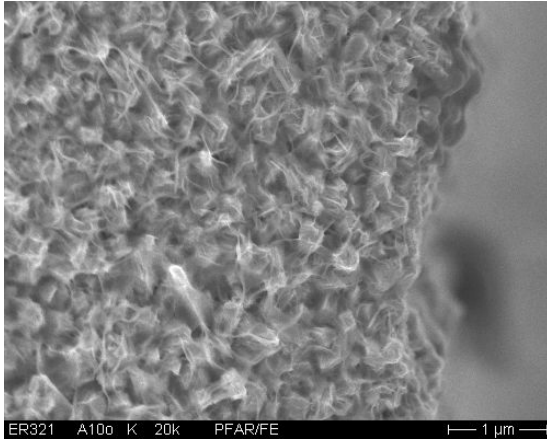


Figure 116a: FESEM (20kx) of sample A10, deposition conditions were $c(\text{CoSO}_4)=7\text{mmol/L}$ and $j=33\text{mA/cm}^2$.

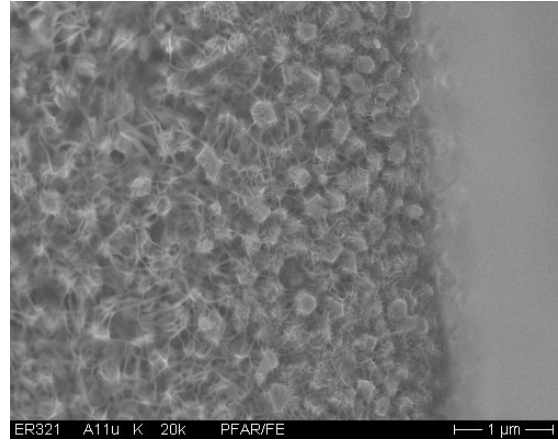


Figure 116b: FESEM (20kx) of sample A11, deposition conditions were $c(\text{CoSO}_4) = 14\text{mmol/L}$ and $j=33\text{mA/cm}^2$.

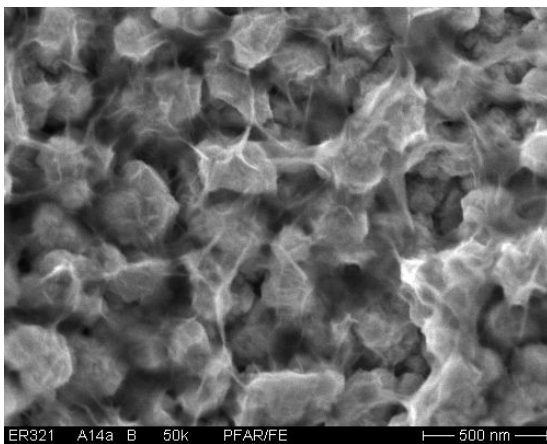


Figure 116c: FESEM (50kx) of sample A14, deposition conditions were $c(\text{CoSO}_4) = 28\text{mmol/L}$ and $j=67\text{mA/cm}^2$.

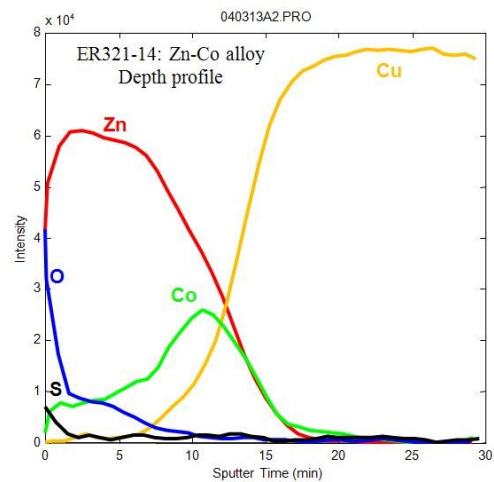


Figure 116d: Auger depth profile of sample A14, deposition conditions were $c(\text{CoSO}_4) = 28\text{mmol/L}$ and $j=67\text{mA/cm}^2$.

The Auger depth profile presented in figure 116 d for experiment A14 shows a Zn-Co alloy with increasing Co concentration starting from the surface to the Cu interface showing a peak there. The decreasing Zn-signal at the Cu interface shows, that at the beginning of the deposition dominantly Co^{2+} is deposited and after a certain deposition time a constant alloy composition is reached.

In the second step these first parameters obtained with the laboratory cell were then used for the scale up of the Zn-Co deposition in the pilot plat cell (see figure 112) similar to the alkaline molybdate electrolyte described in chapter using exactly the same hardware. Unfortunately the laboratory results could not be confirmed on the pilot plant cell and due to limited time this electrolyte was not further evaluated at that time.

In summary for the acidic and ZnSO₄ based electrolytes only the deposition of Zn-Co shows a clear potential as a substitute for the Cr-VI containing standard A2 electrolyte from laboratory experiments, co-deposition of Zn and Co was shown to be in a suitable morphology being comparable to the morphology of the standard A2 layer. The system Zn-Cu and Zn-Ni did not show any promising results as an adhesion promoter. Therefore, further work on Zn-Co alloy deposition is identified as another possible way to get a new Cr-VI free A2 electrolyte. Also more recent publications on the deposition of ternary Zn-Co-Ni and the binary Zn-Co alloy from acidic sulphate electrolytes [204, 205] or from chloride baths [206, 207, 208, 209] for highly corrosion resistant steel coating in industry motivate the further development of this alloy based on this new electrolyte for dendritic A2 deposition.

5.4.3 Summary and outlook on Cr-VI free electrolytes for A2 deposition

The usage of highly toxic and environmental hazardous Cr-VI for processing the standard A2 electrolyte requires huge industrial effort on waste treatment and working safety. In addition the motivation to exclude the risk of any Cr-VI contaminants within the semiconductor product started development activities on Cr-VI free A2 electrolytes.

Three electrolyte classes were investigated: First, a bare zincate electrolyte for deposition of bare Zn, secondly alkaline zincate electrolytes with substitution of the toxic chromate with permanganate, orthovanadate or molybdate to deposit the respective Zn-Mn, Zn-V and Zn-Mo alloys, thirdly acidic electrolytes based on zinc sulphate with additions of copper, nickel or cobalt sulphate for deposition of the respective Zn-Cu, Zn-Ni and Zn-Co alloys.

For all electrolyte systems a deposition parameter study was done on a laboratory plating cell in order to obtain a dendritic or sponge like morphology of the layer as a prerequisite for adhesion promotion towards epoxy molding compounds. After this first screening for the most promising candidates a scale up of the plating process was done to a pilot plant cell. For one electrolyte based on zincate and molybdate (electrolyte D in table 41) MOSFET products were manufactured and subjected to temperature cycling stress tests for a reliability assessment with positive results of this electrolyte and

similar reliability when compared to the use of the standard A2 electrolyte. In table 41 an overview is given on the results for the various electrolytes.

The assessment from there allows the following quality sequence of the investigated electrolytes in terms of the homogeneity and strength of their adhesion promoting function, i. e. of the potential as possible substitutes for the current standard A2 electrolyte (character in brackets gives the electrolyte shown in table 41):

Zn-Mn (B) = Zn-Cu (F) = Zn-Ni (G) < Zn-Co (E) < Zn (A) < Zn-V (C) = Zn-Mo (D)

Therefore a further development makes sense for the electrolytes D and C due to their excellent performance. Electrolyte A with a bare Zn deposition has major benefits due to its simplicity. Finally electrolyte E is worth looking at due to the potential to prevent an alkaline milieu and to minimize corrosion of aluminium in the device. Publications on this topic are summarized together with other topics in chapter 7.1.

System	Zincate electrolytes				Acid ZnSO ₄ electrolytes		
Electrolyte	A	B	C	D	E	F	G
Alloy	bare Zn	Zn-Mn	Zn-V	Zn-Mo	Zn-Co	Zn-Cu	Zn-Ni
Electrolyte components	KOH; 300 mmol/L				ZnSO ₄ ; 37 mmol/L	ZnSO ₄ ; 60 mmol/L	ZnSO ₄ ; 20 mmol/L
	Silicate; Na ₂ O:SiO ₂ 2.5 mmol/L				CoSO ₄ ; 7 to 28 mmol/L	CuSO ₄ ; 20 mmol/L	NiSO ₄ ; 5 mmol/L
		KMnO ₄ ; 11,5 mmol/L	K ₃ VO ₄ ; 11,5 mmol/L	K ₂ MoO ₄ ; 11,5 mmol/L	K ₂ SO ₄ ; 100 mmol/L	K ₂ SO ₄ ; 50 mmol/L	
	ZnO; 13.8 mmol/L				pH=7	H ₂ SO ₄ pH=1	pH=7
Adhesion of layer on substrate	high	low	high	high	medium	low	low
Layer morphology	porous and dendritic	flat	porous and dendritic	porous and dendritic	porous and dendritic		
Adhesion of molding compound [Shearforce]	medium [15 N/mm ²]		high [17 N/mm ²]	high [20 N/mm ²]			
Product reliability				similar good like standard A2			

Table 41: Overview on investigated Cr-VI free electrolytes for A2 deposition technology.

6 Addendum - Organic coatings of surfaces for prevention of copper oxidation

6.1 Applications of copper and its limitations due to oxidation

In electronics industry copper is widely used for various applications including semiconductor chip metallisations over package interconnect material to printed circuit board (PCB) wiring material. All those applications make use of the specific benefits of copper material in terms of its high electric and thermal conductivity, the broad possibilities of processing copper and of the moderate price in comparison to precious metals such as gold, silver or palladium.

Especially the second argument of broad processing possibilities shows up in the fact that copper can be electrodeposited as well as sputtered in contrast to aluminium that is only deposited via sputtering in semiconductor industry. Another example is that copper is widely used as a soldering substrate and is compatible to most of the tin-based solder alloys.

The usage of copper in semiconductor industry on the other hand brings up challenges due to specific corrosion and oxidation properties which disturb manufacturing processes and that are a risk for the reliability of a product.

For using copper as a soldering substrate in PCB industry, the protection from oxidation and corrosion in this application can be done with deposition of tin, silver or nickel phosphorous with thin gold [210]. Cheaper products use organic surface protection (OSP) mainly utilizing benzotriazolium derivatives.

For the interconnects of semiconductor chips to the package, e.g. Cu wirebonding, copper is used in combination with precious metal coatings such as silver, palladium or gold to prevent the formation of copper oxide and corrosion [211, 212, 213, 214, 215, 216]. Organic corrosion inhibitors as substitutes for precious metals offer a huge potential of lowering product cost and manufacturing complexity in this application.

Furthermore the usage of a thin film of an organic corrosion inhibitor for copper enables the direct interconnection between two copper partners such as copper wirebonding on a copper chip metallisation [217, 218]. The usage of this simple interconnect is consisting of only one metal type and this prevents any formation of intermetallic phases that are known as a reliability risk. One example is the couple of a gold wire interconnect to an aluminium metallisation leading to brittle intermetallic phases [219].

In addition, bonding copper to a copper substrate results in an interconnect without any interfaces because there is no limitation of miscibility between the two metallic partners. In contrast, at an interface between a copper substrate and a protecting precious metal, e.g. silver, always two phases (Ag) and (Cu) appear due to the miscibility limits in this system. Interdiffusion between the copper and the thin protecting precious metal film such as gold leads to a vanishing of the protection layer and to a formation of intermetallic phases like Au_3Cu , AuCu and AuCu_3 at the interface. Therefore protection of copper corrosion with a precious metal requires additional metal layers in between to minimize the interaction between the copper and the protecting metal. One example is the usage of a layer sequence of NiP, Pd and Au for copper with NiP acting as diffusion barrier [220, 221]. In this example the implementation of an additional nickel phosphorous layer is further complicating the system because this layer is recrystallizing within thermal manufacturing processes and releasing Ni_3P [222]. In addition the electroless deposition of Au on NiP is leading to an Au layer with a limited seal against Ni diffusion requiring the implementation of a further Pd protection layer. Therefore, systems get more and more complex and difficult to handle in a production.

Development of organic corrosion protection coatings for copper is a possible answer to those problems and is in focus in electronic industry to minimize complexity of Cu protection, lower cost and sustain reliability.

6.2 The Oxidation of copper

The reaction of Cu with O₂ is complex and in contrast to metals like aluminium or nickel the oxidation of copper is not self passivating. Oxidation proceeds fast and oxide thickness increases further depending on parameters like temperatures, oxygen pressure, water pressure, feature size, grain size, crystallographic direction, impurities and alloy components. The oxidation rate k_p represents the kinetic parameter that is dependent on the above mentioned conditions. In figure 117 examples of oxidation rates over the temperature range from room temperature to 1000°C are given from data of Refs. [2, 54, 41].

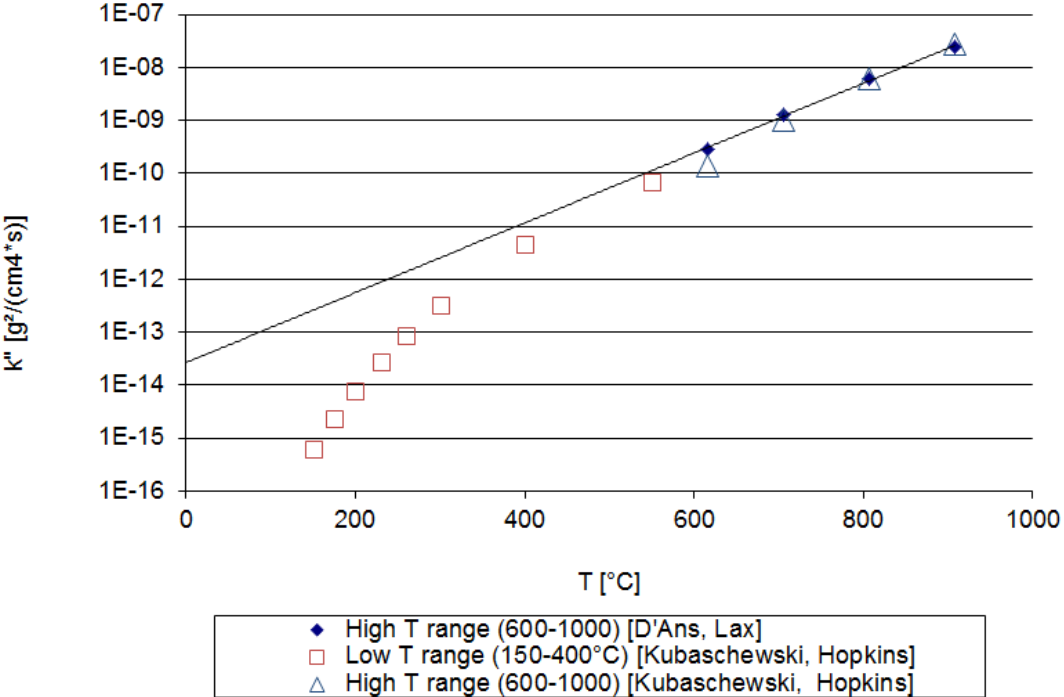


Figure 117: Diagram of corrosion rate of Cu k_p as function of temperature for the temperature range from 150°C to 1000°C from D'Ans and Lax [2] and Kubaschewski and Hopkins [41]

During oxidation of Cu the primary phase forming is Cu₂O over a surface diffusion mechanism of oxygen leading to island formation of the Cu₂O in the first phase [223, 224, 225].

After a closed layer has formed, in the second phase layer growth prolongs, at higher temperature ($\Theta > 800^\circ\text{C}$) lattice diffusion of Cu-ions through Cu_2O dominates, at a temperature below 800°C both lattice diffusion and grain boundary diffusion happens and underneath a temperature of 500°C grain boundary diffusion is the predominant oxidation mechanism [226]. Cu_2O belongs to the p-type metal oxides where the positive metal ions diffuse through the oxide layer to the oxide/gas interface to form further metal oxide [227].

Besides Cu_2O also CuO can form at lower temperatures and higher oxygen pressures, below the decomposition conditions of CuO . The reported ratio of CuO and Cu_2O varies among the different authors due to measurement methods and delay in the conversion of Cu_2O to CuO [41, 226]. Older sources report up to 90 at% CuO below 400°C and approximately zero at a temperature above 800°C . In newer work the formation of CuO from Cu_2O is only moderate with about 10 at% at 400°C (0,1 MPa O_2) and of approximately zero at a temperature above 800°C . At specific conditions (air, $\Theta \leq 250^\circ\text{C}$) an intermediate phase Cu_3O_2 was observed before the formation of CuO [228, 224].

In the temperature range around 150°C and below, a logarithmic relationship is reported including the formation kinetics of a native copper oxide at room temperature [229, 230] as shown in equation 117. For the room temperature oxidation kinetics an example and chart was given already in chapter 4.1.2. Above a temperature of 200°C the oxidation behaviour follows essentially a parabolic relationship [41, 226, 231], see equation (118)

$$\frac{\Delta m}{A} = k_p \cdot \log(a \cdot t) \quad (117)$$

$$\left(\frac{\Delta m}{A}\right)^n = k_p \cdot t; \quad n = 2 \quad (118)$$

In the equations Δm is the increase of mass of a sample during oxidation, A is the area of the sample, k_p is the oxidation rate $\left[\frac{\text{kg}}{\text{m}^2 \cdot \text{s}}\right]$, a is a factor [1/s] and n is the exponent for the specific oxidation kinetic, e.g. $n=2$ for a square root oxidation behaviour.

The oxidation rate dependency on oxygen pressure can also be differentiated into a low temperature region (around 150°C) with $k_p \sim p_{O_2}^{1/4}$ and a high temperature region ($T > 800^\circ\text{C}$) with $k_p \sim p_{O_2}^{1/7}$ which means that at high temperature the influence of O_2 pressure p_{O_2} is much lower compared to lower temperature [232, 48] (see also chapter 4.1.2). Interfering with the dependency on O_2 pressure, the dependency of the growth rate with water pressure p_{H_2O} is similar at lower temperatures ($\Theta < 800^\circ\text{C}$) with $k_p \sim p_{H_2O}^{1/4}$ [233 [234].

Especially for the lower temperature range there is a strong influence of the feature size and of the grain size distribution of Cu. At higher temperatures the Cu_2O grains are bigger compared to the lower temperatures. Therefore at lower temperature the grain boundary density is much higher due to lower grain sizes which provides more path for grain boundary diffusion [226] [235]. Also feature size plays a role, at small features size of 35nm Cu films the grain boundary density can be very high so that grain boundary diffusion mechanism is dominating. In this case this leads to a nearly linear oxidation rate relationship with $n=0,82$ (250°C) to $n=0,95$ (175°C) where n is the exponent in equation (118) [[236].

Most of the studies were prolonged on highly purified Cu to exclude any influence of impurities. At higher temperature for lattice diffusion impurities do not play a big role, in contrast at lower temperature with grain boundary diffusion becomes dominant impurities and alloy elements play a major role for the oxidation rate. Grain boundary diffusion can be hindered by impurities accumulating at grain boundaries reducing the growth rate of Cu_2O [226] [237]. Furthermore, alloy partners are known to reduce the oxidation rate of Cu tremendously, the following order can be given: $Al > Mg > Cd > Be > Sn > Zn$; e.g. addition of 5wt% Al reduces the oxidation rate of Cu by factor 120 and leads to nearly self-passivation of the alloy at a concentration of 8 wt% Al [41]. For Cu alloys used for leadframe materials the reduction of oxidation rate through alloy elements has to be considered on the one hand and on the other hand the formation of porous Cu oxide films is leading to heterogeneous oxidation mechanisms due to pore diffusion of the oxygen leading to much smaller experimental obtained activation energies compared to the oxidation of a pure copper [238].

6.3 Organic materials for copper passivation

Copper corrosion inhibitors vary over a huge field of substances. The understanding of those molecules in regards of their passivating properties towards copper is the presence of heteroatoms such as nitrogen, sulphur, phosphorous or the presence of π -electron systems like aromatic rings or carbonyl groups that are acting as electron donators interacting with the vacant d-orbitals of the Cu atoms.

Known substance classes are triazoles, azoles, amines, aminoacids, thiols and combinations thereof, a brief review is given by Antonijevic and Petrovic [32].

Due to the broad variety of organic molecules used for the passivation of Cu in this work the focus will be limited to the benzotriazole (BTA) as a well-known molecule for moderate application temperatures and poly(vinylimidazole) as possible candidates for applications where high temperature stability is required.

6.3.1 Application of benzotriazole for copper passivation of semiconductor device terminals for PCB soldering

BTA (figure 119 a) is a species out of the group of triazoles with three nitrogen heteroatoms. This material is well known in semiconductor industry and broadly investigated. For an application as final finish for package termination, investigations have been started with BTA as it has been used already to some extent on PCB surfaces. Usually package termini were plated with Pb-Sn alloy until in 2006 legislation forced industry to move to Pb-free options, the primary one then being pure Sn. However, with the drawback of carrying a reliability risk known as Sn whisker formation during lifetime of the device leading to electrical shorts. Therefore alternatives have been searched for, one being an organic Cu passivation.

The prerequisite of this application is the ability to serve as a Cu surface protection along the downstream processes of a semiconductor package manufacturing including transport and storage until the final soldering of the device onto a PCB is done, as outlined in figure 118.

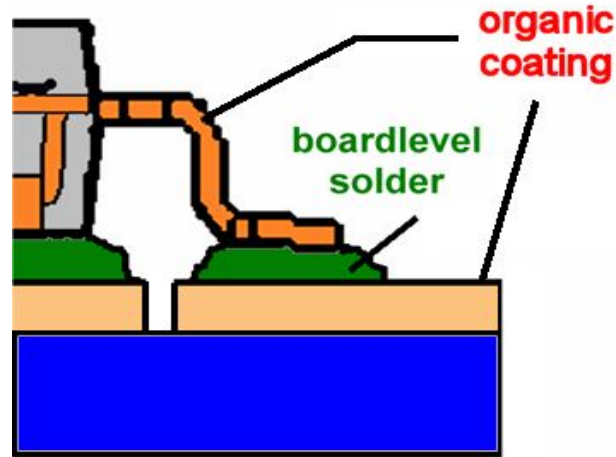
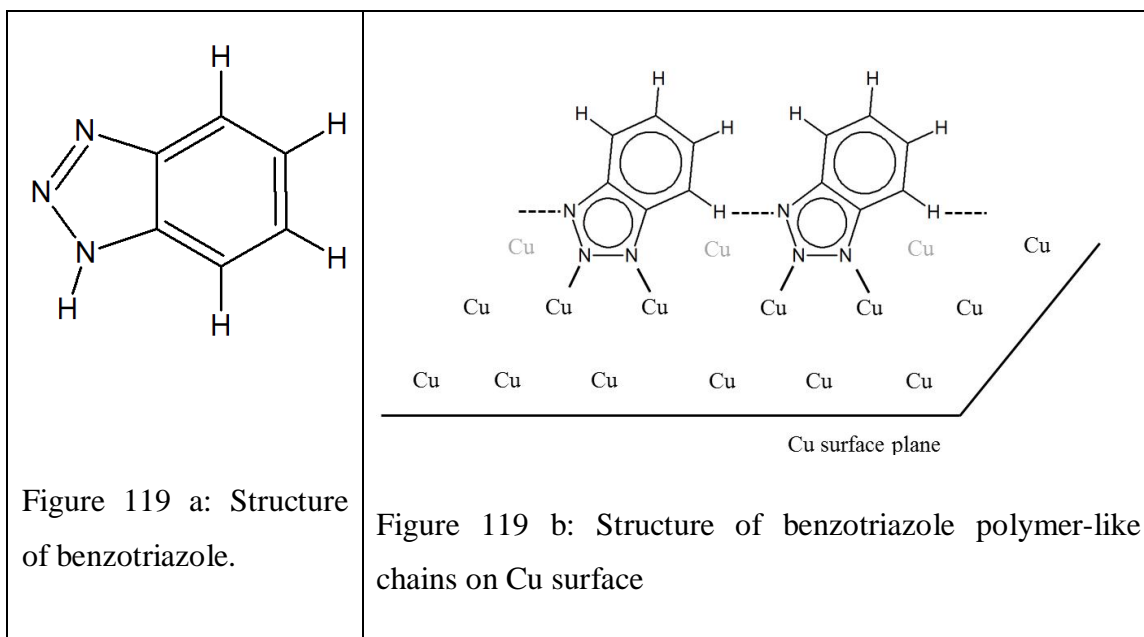


Figure 118: Semiconductor device soldered onto a PCB with both the package terminus (orange) and the PCB board Cu layer (brown) protected from corrosion with an organic coating.

During soldering on a PCB with e.g. a Sn-Ag-Cu solder paste consisting of alloy-powder within an organic flux matrix (e.g. adipic acid) the protection layer needs to be thermally desorbed or cracked via the flux components. This means the adsorption energies of suitable molecules to Cu should only be moderate and integration into a deposition process, e.g. into the plating equipment that is normally used for pure Sn plating, should be easy.

BTA shows properties that support this application. First, the deposition of BTA can be done from aqueous solution and does not require a complicated deposition process. The deposition by adsorption is well understood including its dependencies on temperature, pH and concentration. During deposition on Cu a Cu(I)-BTA complex is forming in a polymer-like chain structure [239, 32]. The mechanism of action of Cu(I)-BTA is still under discussion and needs to be further elucidated. On model is shown in figure 119 b representing a polymer-like arrangement of the BTA molecules attached to the Cu surface over a nitrogen complex bond. A brief review on BTA interaction with a copper surface is given by Finsgar and Milosev [240].



Thickness growth follows three phases, first a fast formation of Cu(I)-BTA followed by a slower growth of the layer due to diffusion of Cu^+ ions through the initially built up layer. Finally in the third phase layer growth asymptotically comes to its final thickness mainly due to physical adsorption [241]. The velocity of layer growth and the final layer thickness depends on typical parameters such as temperature, pH and concentration of BTA in solution, foreign ions (e.g. chloride) or oxygen in solution.

Temperature has a strong influence on the final thickness. For example at pH=7 and a concentration of 0,05 mole/L in aqueous solution at $\Theta = 20^\circ\text{C}$ a stable thickness of 8nm was found increasing to 22nm at $\Theta = 80^\circ\text{C}$. The dependency on pH is also high showing an increase of thickness from 7nm (pH=7 to 9) to 90nm (pH=2) and to 30nm (pH=12) in both directions along the pH scale. Addition of foreign ions such as chloride or bromide achieves thicknesses in the range of 130-160nm [242, 243]. During deposition O_2 is required for the formation of the Cu(I)-BTA complex, in O_2 -free solutions only very thin layers are forming (<90 ppb O_2 : 4nm; ambient air conditions: 30nm after 4h) [244].

For the free adsorption energy ΔG_{ads} of BTA on copper out of aqueous solutions a value of $(-39 \pm 4) \text{ kJ} \cdot \text{mol}^{-1}$ was found within our own work [245] which is in good agreement to Milic and Antonijevic [246] who found $\Delta G_{\text{ads}} = -35.4 \text{ kJ} \cdot \text{mol}^{-1}$.

The thermal stability of Cu(I)-BTA layers is moderate and depends on the atmosphere it is exposed to. According to Christensen [247] in normal air destruction of the passivation layer starts at 150°C, at 180°C after 5 minutes no BTA can be found on the Cu anymore. The passivation efficiency is deteriorating with addition of H₂S or SO₂, with 100ppb H₂S after a few hours at 40°C BTA is completely gone from the Cu surface, using SO₂ this happens already at room temperature. In contrast, in N₂ atmosphere or under high vacuum BTA coating resists thermal stress of up to 200°C until decomposition occurs; it is worth noting that under these conditions any underlying Cu₂O layer may also decompose already.

Within this work for evaluation of BTA as a possible molecule for package termination finishing, several deposition conditions have been tried out. The deposition experiments were done on Silicon wafer with a sputtered Ti-50W barrier (300nm), a sputtered Cu seed layer (300nm) and a final 10µm Cu layer electrodeposited. Stripes (10cm · 3cm) were cut from the wafers for deposition and usage for solderability test (solder dip-and-look¹). In addition Cu wires² (diameter 2mm, length 20mm) were used for the solder wetting balance measurement (see chapter 2.11). Furthermore XPS spectra were collected from specific sample to verify the presence of BTA. For the application mentioned above it is necessary to test beside the initial solderability also the solderability after an aging of 16h at 150°C as this is the requirements that are also fulfilled from the current pure Sn final finish technology.

¹ : Solder dip-and-look is a standard test optical assessment of the solderability of various surfaces in semiconductor industry. The test stripes are dipped into a SnAgCu solder for 3 seconds at 245°C and afterwards assessed optically for voids or non-wetted areas.

² : Cu wires were obtained from Goodfellow (Cu007905), 99.99% Cu

The parameter ranges are given in table 120 together with the four major experimental groups (experiment er800) out of 20.

Deposition of BTA						Initial: Analytical readouts				150°C/16h aging: Analytical readouts		
	Agitation	c [mmol /L] BTA	T [°C]	pH	time [sec]	Optical appearance	Solder dip and look (on Cu-plates)	Solder wetting balance (on Cu wire; t0_x value)	XPS	Optical appearance	Solder dip and look (on Cu-plates)	Solder wetting balance (on Cu wire)
Range	calm - strong	1, 10, 100	RT, 60°C	1, 7, 13	10, 180							
Ref1	n.a.	n.a.	n.a.	n.a.	n.a.	Cu colour	good wetting	normal (9.5s)	no BTA detected	brown Cu ₂ O colour	no wetting	no wetting
A2	calm	1	RT	pH7	180	same as Ref 1	good wetting	fast (5.6s)	n.a.	brown similar to ref1	no wetting	no wetting
A16	calm	100	60	pH1	180	white film	bad wetting	fast (17.9s)	BTA present	Cu colour	no wetting	no wetting
A20	strong	10	60	pH1	180	white coating	no wetting	no wetting	n.a.	cancelled	cancelled	cancelled

Table 120: Overview on the deposition conditions used for BTA deposition (samples for soldering tests). Surface preparation was done for all runs with acetone dip, activation in 40wt% H₃PO₄ both at room temperature. Solder dip-and-look was done with Cu plates. Solder wetting balance was done with a ST60 from Metronelec company. For the experiments Ref1, A2, A16 the value t_{0_x} from solder wetting balance measurement is given as an indicator for the wetting velocity.

Comparing the pure untreated Cu (experiment Ref1) with the BTA coated Cu (experiment A2) the optical wetting behavior during solder dip-and-look was identical. The solder wetting balance measurement showed a faster wetting of the surface in experiment A2 which can also be seen in figures 121 a and b and 122 a and b. The XPS measurement unfortunately was only done on the reference sample Ref1 and not on sample A2 and confirmed that there was no BTA present. The reason for the faster wetting of sample A2 might be the low concentration of BTA of only 1 mmol/L and the low temperature during deposition (room temperature) leading to a very thin protection coating that is easily removed during soldering.

In contrast to this sample A16 shows a typical N signal in the XPS spectrum at 400eV indicating a much thicker layer, see figure 125. The soldering results were different from the first two groups, solder dip-and-look showed a bad wetting and also the solder wetting balance measurement indicates a very slow wetting behavior of this sample at the initial stage, see figures 123 a and b, respectively. Obviously the high deposition temperature (60°C) and the high concentration of BTA (100mmol/L) led to a much thicker protection layer that cannot be removed fast during soldering.

Therefore sample A20 was deposited at a concentration of 10mmole/L at the same conditions, but incidentally a very strong stirring of the solution was applied. The optical appearance of this sample was showing a white coating and there was no wetting possible, even not after more than 20 second exposure to the solder (see figure 124). Further analysis with this group was not done.

After all the samples have been subjected to the aging for 16h at 150°C the solder dip result showed no wetting of any sample anymore, examples given in figure 126. Further analysis therefore was not done.



Figure 121 a: Pure Cu reference (Ref1), solder dip and look results.

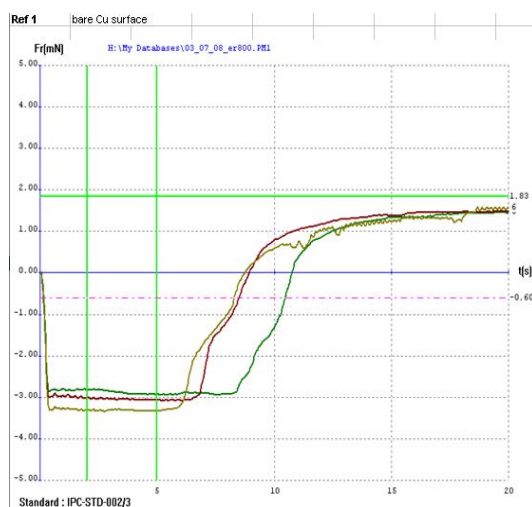


Figure 121 b: Pure Cu reference (Ref1), solder wetting balance measurement.

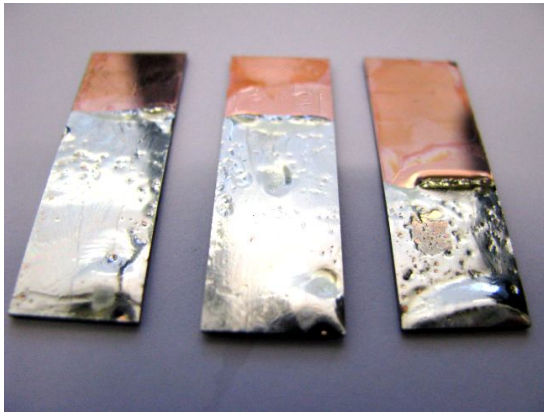


Figure 122 a: Experiment A2 with 1mmol/L BTA, RT, pH7, 180s; solder dip and look results.

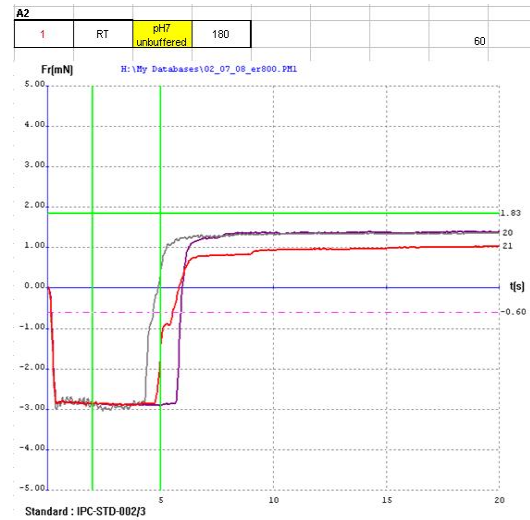


Figure 122 b: Experiment A2, solder wetting balance measurement.

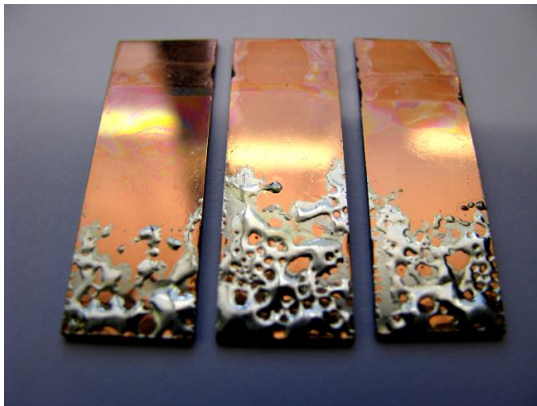


Figure 123 a: Experiment A16, 100mole/L BTA, 60°C, pH1, 180s.

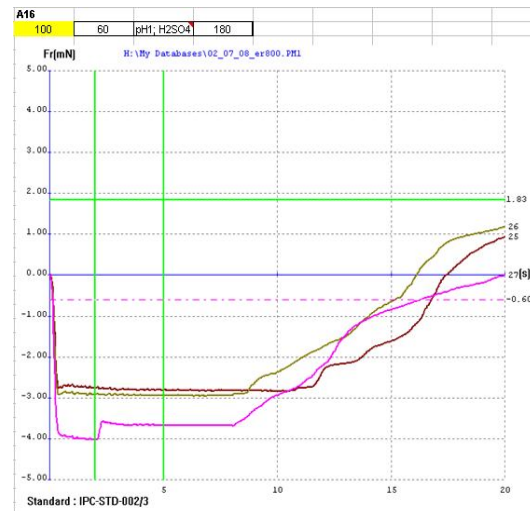


Figure 123 b: Experiment A16, solder wetting balance measurement.

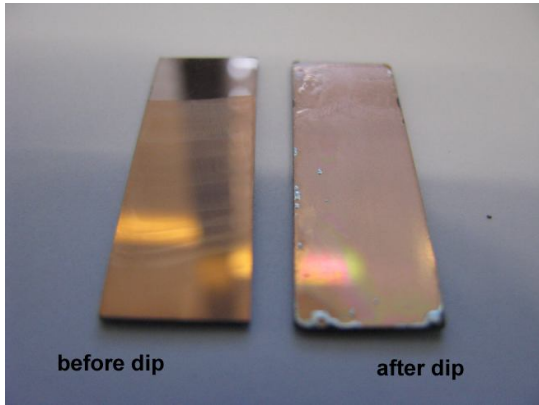


Figure 124 : Experiment A20: 10mmol/L, 60°C, pH1, 180s + strong stirring of solution

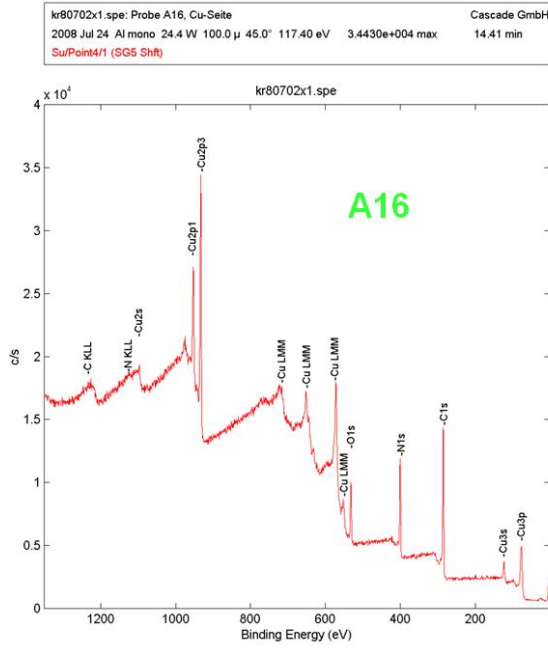


Figure 125.: XPS spectrum of sample A16 with pronounced N-signal of the BTA molecule.

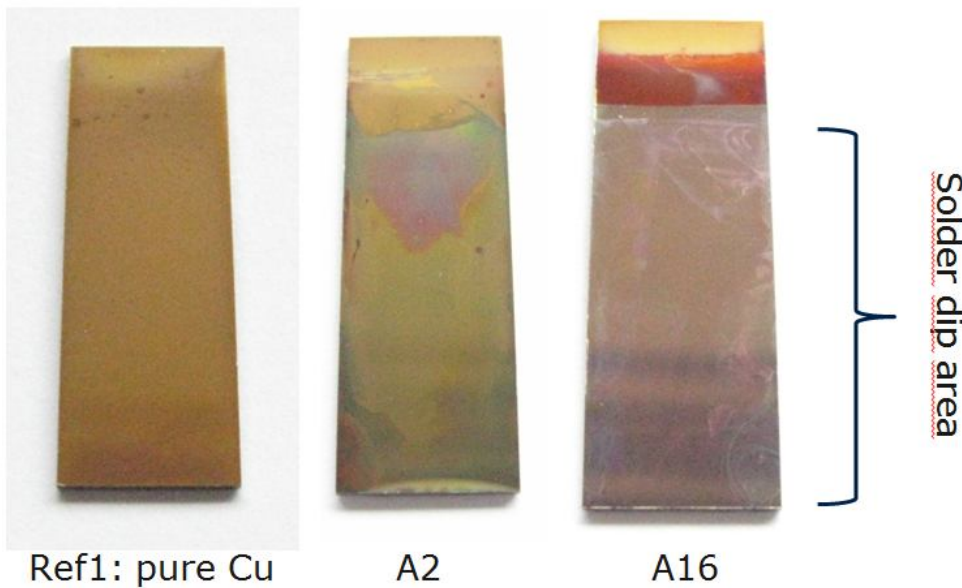


Figure 126: Solder dip-and-look results of sample Ref1, A2 and A16 after storage at 150°C for 16h. No wetting of solder was possible after this aging step.

Due to these insufficient results and due to the change of priorities in the project further investigations on BTA as final finish for package termini were not done. The focus

changed to another application to use organic passivations for Cu wirebonding. This topic is reported in the next section.

6.3.2 Application of poly(vinylimidazole) for copper passivation for copper wirebonding on copper metallisation

The trend of semiconductor industry to use copper for chip metallisations and for interconnect materials between chip and package was also driving the copper wirebonding technology. As described above already, some development has been done to move towards copper wirebonding technology without applying precious metals for protecting copper from corrosion. One way is to apply organic passivating agents to the Cu pads of the chip and to the Cu areas of the leadframe as outlined in figure 127. The chip is attached to the leadframe with glue or solder, the chip pads and the leadframe leads are protected with an organic passivation coating. The deposition of the organic passivation is done at wafer manufacturing and at leadframe manufacturing. During the downstream processes the organic layer has to withstand several processes at elevated temperature, e.g. during chip attachment to the leadframe with glue. Glue curing at temperatures in the range of 150-200°C is required. Furthermore, soldering of the chip requires a temperature up to 350°C.

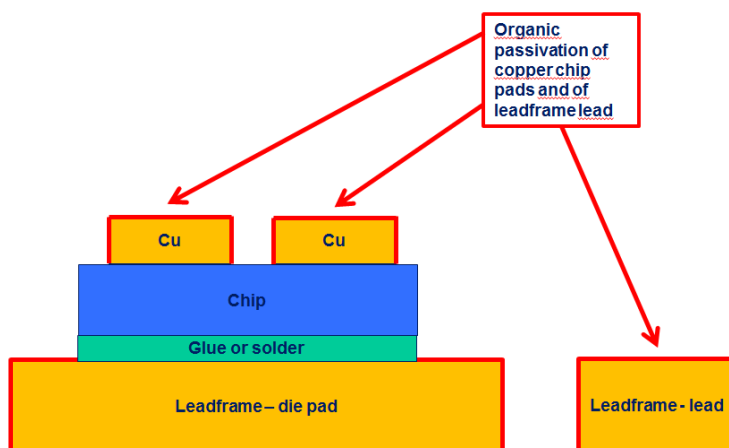


Figure 127: Semiconductor device with organic passivation layer on all relevant copper surfaces, here symbolized by redlines at some surfaces.

In addition, also during copper ball-wedge wirebonding, see figures 128a-d, higher temperatures in the range of 150 to 200°C are applied in air that lead to oxidation of

unprotected copper. Any organic passivation has also to overcome this thermal budget without leaving the copper unprotected. In figure 128 the process principle of a copper ball-wedge bonding is outlined. The protective coating has to be soft and thin enough to be penetrated from the copper ball on the chip pad bond position and from the copper wire on the lead bond position, see figure 128 b and c, respectively.

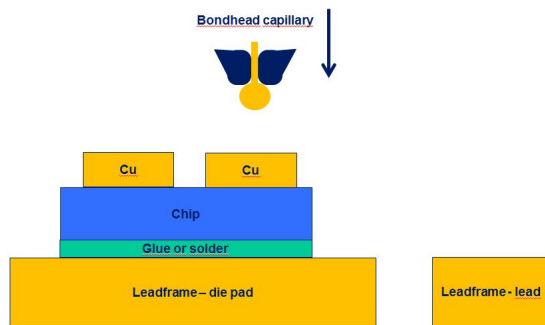


Figure 128 a: Cu ball-wedge wirebonding process principle; a Cu ball is formed from the Cu wire by an electric torch.

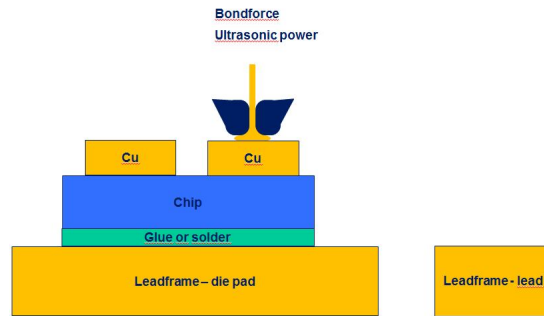


Figure 128 b: Cu ball-wedge wirebonding process principle; Cu ball is bonded onto the chip pad with a Cu metallisation by application of bondforce and ultrasonic energy.

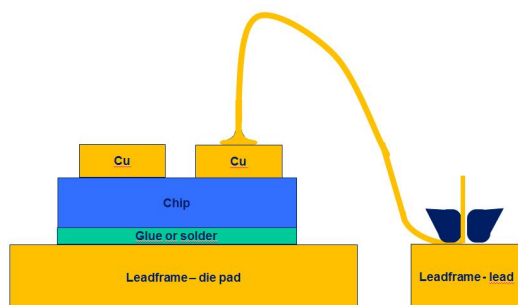


Figure 128 c: Cu ball-wedge wirebonding process principle; the Cu wire loop is formed and the bond head capillary performs the second bond on the lead.

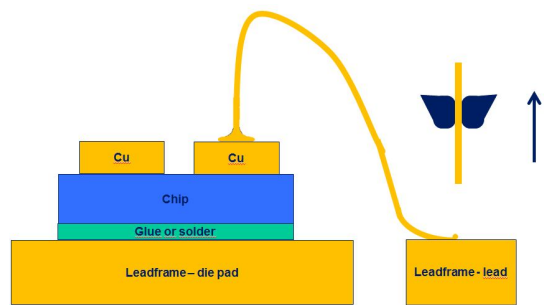


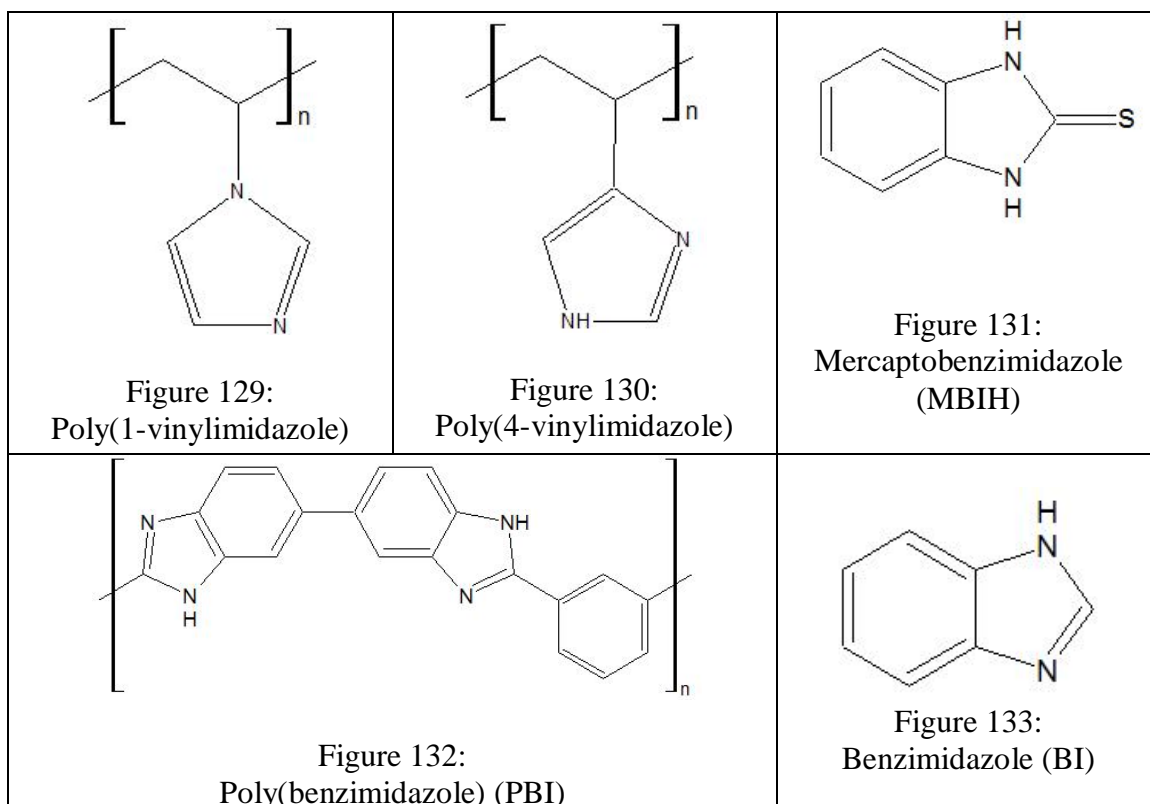
Figure 128 d: Cu ball-wedge wirebonding process principle; bond head capillary moves away from second bond position to the initial position where a new Cu ball is formed, as shown in figure 128 a.

Besides the influence of the various process parameters of this complex process, it is known that prevention of Cu oxide formation is a key for a successful process result with proper metallurgical interconnect at both bonds [248, 249].

Usage of 1-decanethiol (C10-SH) as a copper passivation agent was found to improve bonding quality of copper on copper substrates [249]. In wire bonding experiments Whelan et al [250] found that application of C10-SH on Cu in comparison to a pure Cu

surface decreases the non-stick-on-pad rate (NSOP)¹ from 100% to 3% with C10-SH protected Cu. In another study this result was confirmed by a reduction of NSOP from 71% to zero with C10-SH protected Cu surfaces [251]. In addition an increase of the ball shear strength of 10-30% was reported. The thickness of the C10-SH layer used was 1.8nm and its thermal stability on the copper surface was found to be limited to the temperature range of 175°C to 200°C. Besides this limitation, the protection time is only 5 days [249] under normal room temperature conditions in air. The same potential and in contrast similar limitations apply when using other passivating molecules of small size, such as benzotriazole and benzylthiole [250].

These results encouraged us to focus investigations to organic passivating molecules which have the properties of forming a polymeric film on the Cu in addition to the formation of a complex towards the Cu. Two polymers were chosen that are poly(1-vinylimidazole) (PVI-1) (fig.129) and poly-(benzimidazole) (PBI) (fig. 132).



¹ : Non-stick-on-pad (NSOP) is the amount of ball-bonds during a wirebonding process that are separating after the ball placement. This number indicates a very low adhesion between substrate and ball already at the bonding process.

PBI is known to form strong coatings if it is applied together with a smaller molecule, such as mercaptobenzimidazole (MBIH) (fig.131). MBIH is closing open areas on the surface that are not covered by the polymeric PBI due to steric limitations. With this synergetic effect resistance to Cu oxidation can be achieved up to 200°C for a time of 10 hours [252]. This coating was also used for improving adhesion of polyimides or epoxy resins on copper being resistive to a temperature of 250°C for 30 minutes. [253].

For poly(vinylimidazoles) a synergetic effect is known, as well. For example, together with benzimidazole (BI) (fig.133) poly(4-vinylimidazole) (PVI-4) (fig.130) forms a passivation layer on copper that prevents formation of any copper oxide up to 250°C for a time of 15 minutes [254]. The layer thickness used in this work was estimated to be about 60nm. Eng and Ishida [255] found that both PVI-1 and PVI-4 form complexes with Cu surfaces that can prevent the formation of Cu oxide up to a temperature of 400°C for a time of 15 minutes. They applied polymeric films with thicknesses around 150nm and an average molecule mass of 55-1300 kDalton without additional help of a smaller second molecule. This shows the potential of using (poly)vinylimidazoles as single substance to achieve copper passivation. The higher temperature stability and the much easier application of a single coating process without requirement for a second molecule entailed a further investigation of PVI-1. In contrast to PVI-4, PVI-1 can be deposited at room temperature. As PVI-4 has one proton attached to the nitrogen atom in the imidazole ring, hydrogen-bridge bonds can form in solution that lead to a steric hindrance of the imidazole rings towards the Cu surface, as described by Eng and Ishida [255]. Therefore PVI-4 has to be deposited at a temperature of 60°C or higher to achieve a polymer layer with identical protection strength as PVI-1 deposited at room temperature.

In order to get an indication about the protection efficiency of PVI-1 coatings as single substance coating or together with a synergetic second molecule, deposition experiments and tempering of coated samples at 150°C was done for periods from 20 to 420 minutes in air. In addition the passivation effect of the smaller second molecule was included to have a comparison to the behaviour together with PVI-1. Figure 42 gives an overview on the results, including deposition and tempering experiments and the used molecules. The deposition experiments were simultaneously to the experiments

described in the previous section 6.3.1. Assessment of the samples after specific time of tempering was done with optical appearance of the copper surface.

Substrates:

Silicon wafer with a sputtered Ti-50W barrier (300nm), a sputtered Cu seed layer (300nm) and a final 10 μ m Cu layer electrodeposited, stripes (10cm · 3cm) were cut from the wafers.

Deposition:

1. Cleaning and activation: Pre-cleaning in acetone (RT, 1 min); activation in 40wt% H₃PO₄ (RT, 1 min)
2. Deposition of PVI-1: Solvent MeOH, w=10wt%, deposition temperature variation as shown in table 42, dipping time 5 minutes.
3. Deposition of second molecule: Solvent MeOH, concentration 840 mmole/L, T variation as shown in table 42, dipping time 5 minutes. For some experiments the second deposition was done with a mixture of both PVI-1 (w=10wt%) and the second molecule.

Tempering conditions:

150°C, air, time ranging from 20 minutes to 420 minutes simultaneously to the experiment described in the previous chapter.

Sample	Substance	Deposition temperature (T1: PVI-1; T2: 2nd molecule)		Tempering of Samples at 150°C for a time [min] in air									
		T1 [°C]	T2 [°C]	20	38	60	90	120	180	240	300	360	420
Ref1	no			purple	purple	blue metallic	silver						
A1	PVI-1	55		no change									Light brown
A2	BTA		55	no change			Light brown	Light brown	brown /orange			dark brown/orange	
A3	MBIH		55	white layer on surface						layer turns grey, underlying Cu turns brown/orange			
A4	C10-SH		55	Light brown	Light brown	Light brown	Light brown	reddish/brown	purple blue	blue	quite silver	silver	silver/blue
B1	PVI-1 + BTA	RT	RT	no change									Light brown
B2		55	55	no change						Light brown	Light brown	light brown	
B3		RT	RT*	no change						Light brown			
B4		55	55*	no change						Light brown			
C1	PVI-1 + MBIH	RT	RT	no change									Light brown
C2		55	55	no change					Light brown	brown			
C3		RT	RT*	no change						Light brown			
C4		55	55*	no change						Light brown			
D1	PVI-1 + C10-SH	RT	RT	no change			light brown	light brown	brown /orange		purple/blue/silver		
D2		55	55	no change	Light brown	Light brown	red / brown		purple/blue		purple/silver		
D3		RT	RT*	no change				brown/orange			purple/silver		
D4		55	55*	Light brown			reddish/brown		purple		purple / silver		silver/blue

Table 42: Results of the tempering experiment on discolouration of copper surfaces after a tempering time from 20 to 420 minutes. T1 is the temperature used for the first deposition step with PVI-1. T2 is the temperature used for deposition of the 2nd molecule. In some groups marked with an asterisk the second deposition was done with a mixture of PVI-1 and the respective 2nd molecule.

After the deposition step (either PVI-1 or the second molecule or both in a sequence) the surface of all samples optically shows no changes to the bright mirror-like copper surface as it looked directly after activation. One exemption was experiment A3 showing a white layer on the surface due to unknown reason.

During tempering sample A1, B1 and C1 showed no optical change of the surface until a annealing time of 360 minutes, even after 420 minutes the surface still was shiny showing slightly brown colour. This shows that PVI-1 alone and together with BTA and

with MBIH shows similar protection strength under these conditions. Increase of deposition temperature or running the second deposition step with a mixture of PVI-1 and BTA or MBIH did not show any improvement but instead even a reduction of protection time, see experiments B2-B4 and C2-C4.

The oxidation protection of the single non-polymeric molecules shows a significant lower oxidation protection as seen in experiments A2-A4. In addition, also combination of PVI-1 and C10-SH showed no promising results. Therefore, the deposition of PVI-1 as shown in experiment A1 was chosen for further experiments due to a much simpler deposition method and lower complexity.

Further experiments were done within a wirebonding study for Cu ball-wedge wirebonding with a 22 μ m thick wire on standard wirebonding equipment¹. For each sample ball and wedge bonds were placed on the same substrate plates that have been used for the previous experiments, an example shown in figure 134 a and b.

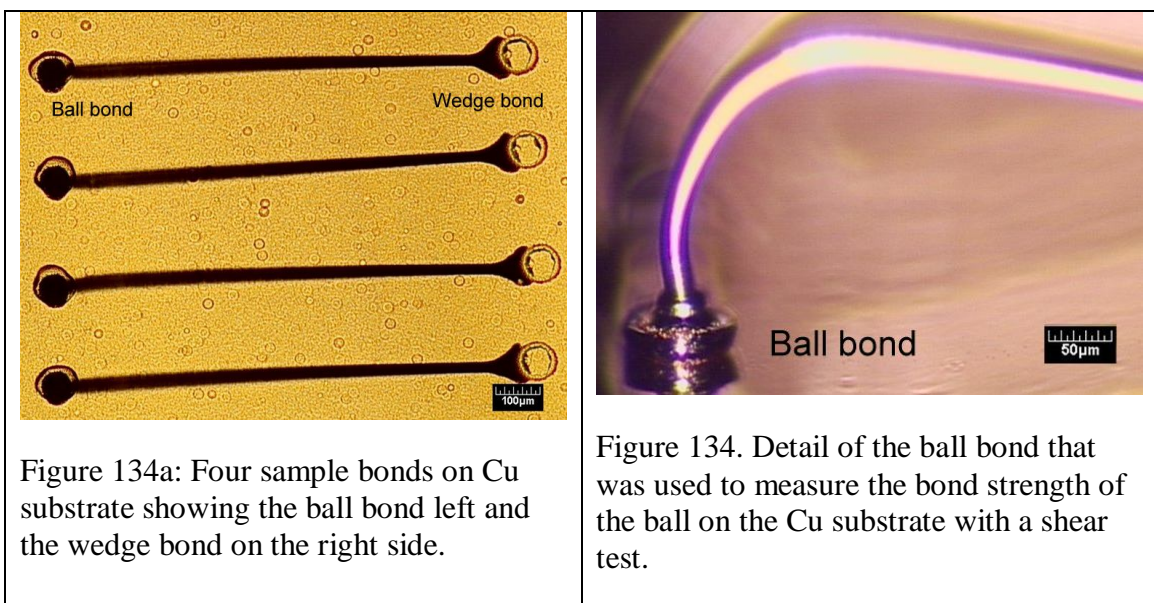


Figure 134a: Four sample bonds on Cu substrate showing the ball bond left and the wedge bond on the right side.

Figure 134. Detail of the ball bond that was used to measure the bond strength of the ball on the Cu substrate with a shear test.

In table 43 some of the many experiments are summarized that have been performed. Three organic substances were used, PVI-1, BTA, and C10-SH. BTA and C10-SH were

¹ : An ASM Eagle Xpress thermosonic wirebonding equipment was used for the bonding experiments. The basic parameter setting for the ball bond was as following: Ultrasonic time = 10 ms, ultrasonic power = 350 AU (arbitrary unit, ASM specific), bond force = 1N, force time = 10ms. For free air ball formation the parameters were: Current time = 0.85ms, current = 60 mA. For the wedge bond parameters were: Ultrasonic time = 20 ms, ultrasonic power = 350 AU, bond force = 1N, force time = 20ms. A 22 μ m Cu wire from MEM was used.

used as reference substances to reproduce the results reported from Whelan et al [251] at the same concentration being 10wt% BTA and 14.6wt% C10-SH in methanole. Also the deposition at room temperature was identical to the conditions used from this team. Only the deposition time was reduced to 5 minutes in contrast to the results published by Whelan et al [251] with deposition times in the range of 0,25 to 24 hours. The third substance PVI-1 was deposited at identical conditions with 2 concentrations being 0,05 wt%, 5 wt% and 10 wt%. The deposition time of 5 minutes was kept as well. In a study of the kinetics of adsorption of PVI-1 onto Cu surfaces with our novel fis-QCM [256] we found that after 5 minutes the equilibrium thickness of PVI-1 is achieved and no significant further increase of the layer thickness can be expected [257].

The wirebonding was done at room temperature and some experiments were run at $\Theta = 150^{\circ}\text{C}$ with an exposure time of 45 minutes to show the passivation by the organic coating in the respective experiment. Only experiment F1 with C10-SH could be performed successfully at 150°C , experiment A1 with PVI-1 did not yield enough ball bonds due to bad wedge bonds and process issues. As wedge bonds are required for getting the next ball bond in the sequence, as explained in figure 128 a-d, this experiment was therefore discarded.

No	Cu surface	W1 [wt%]	Wirebond temp. [$^{\circ}\text{C}$]	Exposure time [$^{\circ}\text{C}$]	Results of wirebonding
Ref0-9	cleaned Cu		25		16 bonds performed
A1	PVI-1	5	150	45	no bonds due to bad wedge bond; discarded
B1	PVI-1	0,05	25		12 bonds performed
E1	BTA	10	25		15 bonds in one series
F1	C10SH	14.6	150	45	8 bonds performed
F4	C10SH	14.6	25		8 bonds performed
H*	PVI-1	10	25		9 bonds performed

Table 43: Extract of experiments run on Cu wirebonding on Cu substrates passivated with organic substances. *: Experiment H was running within a second wave of evaluations.

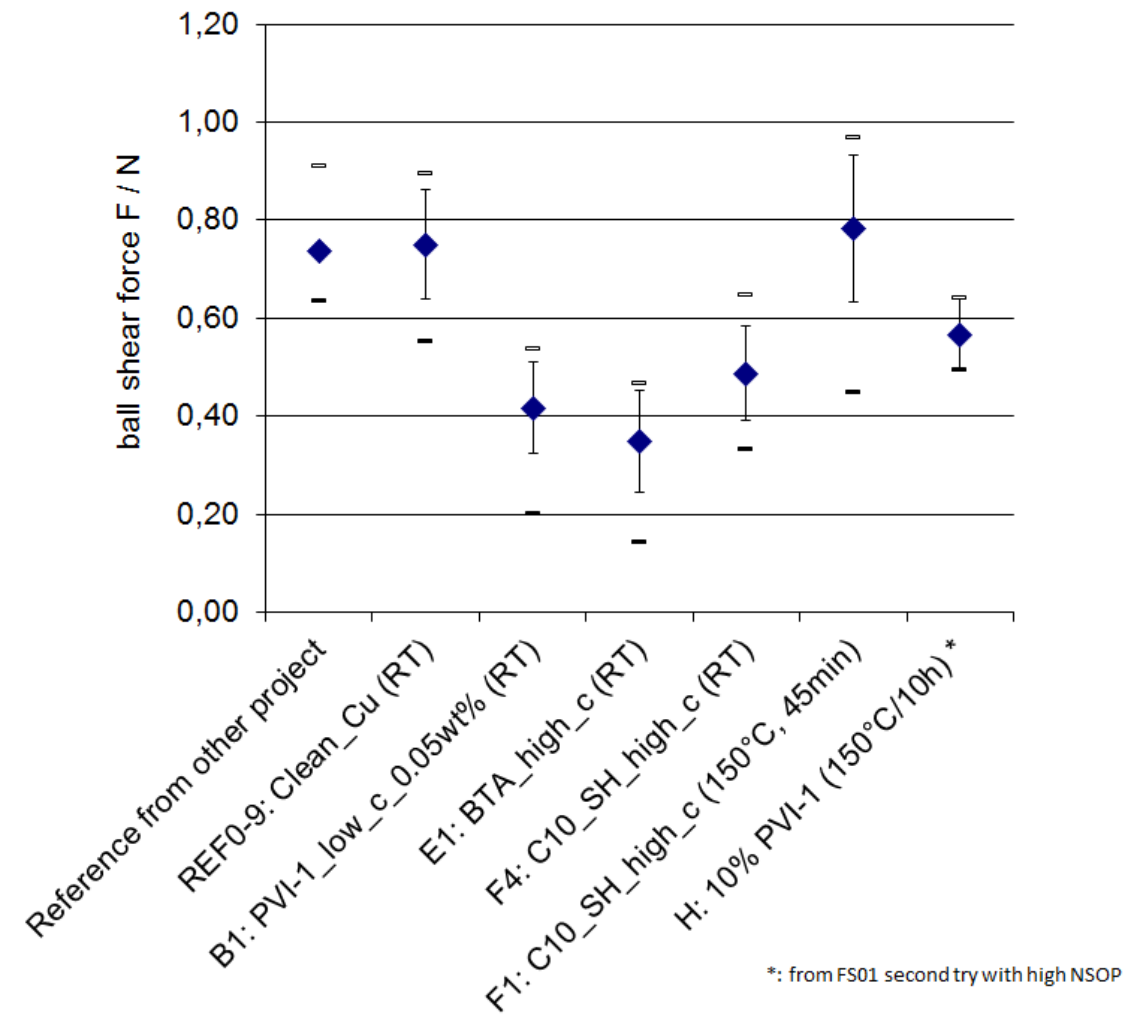


Figure 135 Wirebonding ball shear test results from experiment FS01. First try of Cu surfaces for Cu wirebonding passivated with different organic species.

The data of the ball shear measurement obtained with a standard shear tester can be seen in figure 135. The reference Ref0-9 fits to the value of another project that is shown here for comparison and verification. The coated samples all show lower bond strength at this condition.

Experiment F1 with C10-SH bonded at a temperature of 150°C shows similar bond strength as the reference even with a 45 minutes thermal budget in air. This shows that the thiole coating shows a protection enabling bonding at this condition. Unfortunately no data could be obtained for the PVI-1 coated substrate at higher temperatures in the first set of experiments. In a second set, experiment H was prepared with coating at a concentration of 10 wt% PVI-1. After application of a thermal budget of 150°C for 10h the sample did still show a typical Cu colour and bonding was possible for a few bonds,

but the obtained ball shear force was again lower compared to the reference values Ref0-9.

To sum up, application of organic passivations shows no trend of improvement during Cu wirebonding. The Cu surface is protected from oxidation, but the coating itself probably acts as a barrier during the ball bond formation and especially during the wedge bond formation. A specific optimization of the wirebonding parameters to such new inert surfaces would be necessary to obtain better results. Within the running project the focus changed towards the application of inorganic passivations such as Al_2O_3 or silicon nitride that are not included in this work. From the work with organic passivations in the area of usage as soldering surfaces a patent was published showing the potential of these molecules in this region. The work on organic passivations was stopped at this point but can and should be reassumed and extended in future.

7 Summary, publications and outlook

7.1 Main part: Nanoporous adhesion promoter in semiconductor packages - A2 technology

In semiconductor industry various technologies were developed to address the increasing demand on reliability. This was achieved in many cases via the minimization of interface degradation between the device functions like chip and interconnects and the encapsulation materials.

A fundamentally new approach was started in Infineon from 2005 onwards to do a deposition of a nanostructured, dendritic sponge of a ZnCr alloy in an electrochemical process inside the assembly production line in a cleanroom environment. To run a galvanic deposition on open devices with thin wire interconnects down to 25 μ m of Au wires was a novum and dedicated to Infineon power semiconductors.

Due to the fact that the deposition has been established on Al chip metallisations and on the rest of the device metal surfaces like Cu, NiP, solder, and wires an activation concept was installed addressing both the chip and the package. It was another shift of paradigm to integrate wafer processes and package processes into one optimized process flow. The result was a chip conditioning plasma etch process on wafer scale using Ar/CF₄ and later Ar/O₂ combined with a galvanic deposition process directly after the wirebonding process at the package assembly.

This galvanic process called A2-plating was consisting of activation with methanesulfonic acid and hydrofluoric acid and a specific electrolyte consisting of zincate, chromate and silicate optimized for this application.

Specifically for the activation of Al basic work was done and has been published [258] regarding wet chemical methods to activate Al.

For the discussion of the A2 deposition, a comparison of the A2 electrolyte to common electrolytes for Zn, Cr or ZnCr alloy plating was performed. Very low similarity was found as the applied concentrations of the used metals are about one magnitude lower in

the A2 electrolyte compared to other known electrolytes. The obtained surface structure and deposition mechanism also differ significantly.

First a nanoscopic structure appears on all investigated surfaces suggesting a transport controlled mechanism. Calculation of limiting current densities and comparison to typical process currents shows that the deposition is not transport controlled. Therefore a further mechanism must be present leading to dendrite growth. This assumption is supported by experimental results showing that high cell voltages, turbulent fluid dynamic conditions and the presence of a SiO_x colloid are required for dendritic growth.

The suggested mechanism is an electrophoretic deposition via SiO_x colloids. It is based on the following arguments:

- a. Over SiO_2 colloids a co-deposition of Zn and Cr with excess Zn content is possible. Usually under normal aqueous conditions without additive this binary behaves anomalously with excess Cr content deposits. The colloids are acting as a carrier for Zn and Cr ions.
- b. The silicate content in the electrolyte is of major importance for the dendritic growth on nanoscale under process conditions.
- c. Besides the Zn and Cr content the A2-layer also consists of Si through incorporation of these colloid particles into the deposit.
- d. Deposition conditions are not reaching the theoretical limiting current density.
- e. High cell voltages are required to obtain dendritic growth of the ZnCr alloy.

Besides the theoretical and experimental work carried out in this work a major focus was the industrial realization of this adhesion promoter technology at Infineon. A vertical plating equipment was used and adapted to the process requirements of plating on a sensitive device in highly reactive chemicals under high current density. This includes also the industrial usage of Cr^{6+} requiring high standards in terms of wastewater treatment and safety.

The success of this development is proven by the obtained outstanding reliability Infineon is delivering with various robust products that carry this technology in

different kinds of markets and applications, e.g. automotive and industrial areas, at a significantly high production volume.

With the motivation of substituting Cr^{6+} from the process and to further improve the deposition process, basic work has been done to develop new electrolytes for deposition of nanostructured layers serving as an adhesion promoter. Electrolytes using molybdate or vanadate as potential substitutes for the chromate ion have been proven to work also in this industrial process. The work has been published [259] [260].

In addition for specific other applications the deposition of selective A2 was developed and reported [261].

The basic principle of the deposition of nanostructured metals and alloys was further extended to other metals and alloys such as Ag or Au and its alloys and its application was extended from adhesion promoters to layers that can be used for metallurgical interconnects in semiconductor industry. This work has also been published, see reference [262].

Using nanostructured surfaces as an adhesion promoter was also done via gas phase processes by either oxidizing a Cu surface with final reduction in H_2/N_2 mixtures to obtain sponge-like surfaces called “Reduced Nanopor”, published in references [263] and [264].

Finally also with a gas phase deposition of nanostructured SiO_2 remarkable adhesion promoting results were obtained. This work has been published as well [265], [266], and [267].

As an outlook for the A2 technology several steps are seen in the future including refinement of pulse plating technology for further improvement of the process, the implementation of an electrolyte without any Cr(VI) content to save the effort on waste water treatment, and the integration of latest semiconductor technologies into this technology. Especially the latter work on new device technologies will be a challenge in the future to integrate the A2 technology in process flows of newer semiconductor technologies that carry new metallisations such as palladium or gold.

The summary of this work shows that the basic principle of an adhesion promoter acting on morphological adhesion functions has broad application fields also outside semiconductor industry.

List of publications in this section:

[258] E. Riedl, S. Jordan, C. M. Schilz, F. H. Wendy: Semiconductor package and method of assembling a semiconductor package; patent application WO2007/129132 A1 (2007)

[259] E. Riedl, W. Schober: Verfahren zum Abscheiden einer porösen Haftvermittlungsschicht auf einer Oberfläche eines elektrisch leitenden Körpers sowie Verwendung des Verfahrens; Patent DE 103 30 192 B4 (2008)

[260] E. Riedl, W. Schober: Electrically conductive body including an adhesion promoter layer, and process for depositing an adhesion promoter layer; patent US7540950B2 (2009)

[261] M. Weber, R. Sewald, E. Riedl: Elektronische Bauteile mit Halbleiterchips und Systemträger und Verfahren zur Herstellung derselben; Offenlegungsschrift DE 101 24 047 A1 (2002)

[262] E. Riedl, I. Nikitin, J. Lodermeier, R. Bergmann, K. Guth: Method of fabricating a semiconductor device; patent application US2010/0059857 A1 (2010)

[263] E. Riedl, W. Schober: Metal article intended for at least partially coating with a substance and a method for producing the same; patent US7384698 B2 (2008)

[264] E. Riedl, W. Schober: Method for producing a metal article intended for at least partially coating with a substance; patent US8147621 B2 (2012)

[265] J. Mahler, R. Wombacher, D. Lachmann, B. Betz, S. Paulus, E. Riedl: Systemträger mit in Kunststoffmasse einzubettenden Oberfläche, Verfahren zur Herstellung eines Systemträgers und Verwendung einer Schicht als Haftvermittler; Patent DE 10 2005 061 248 B4 (2007)

[266] J. Mahler, R. Wombacher, D. Lachmann, B. Betz, S. Paulus, E. Riedl: Semiconductor device with semiconductor device components embedded in a plastic housing composition; patent US7705472 B2 (2010)

[267] A. Kessler, J. Mahler, E. Riedl: Halbleiterbauteil mit in Kunststoffgehäusemasse eingebetteten Halbleiterbauteilkomponenten; Offenlegungsschrift DE 10 2004 047 510 A1 (2006)

7.2 Addendum: Organic coatings of surfaces for prevention of copper oxidation

Organic molecules are used in various applications in semiconductor and metal industry. Two new types of application specifically in semiconductor package manufacturing were investigated. The first application uses nitrogen containing organic molecules to protect the package terminations that are made from copper and copper alloys. The use of these molecules in this region enables substitution of metals such as lead-tin alloys or pure tin due to environmental reasons and due to technical risks, respectively. In addition the copper package terminations can be protected at lower manufacturing cost due to a less complex deposition process. Experiments with benzotriazole as a molecule known in other applications showed the general potential of using an organic copper passivation on package terminations for soldering devices onto printed circuit boards. In addition, a couple of other molecules can be used. In this work the experimental focus stayed at benzotriazole due to limited time. A study of the adsorption kinetics of benzotriazole on copper with the fast impedance scanning quartz crystal microbalance [256] was published and the respective free adsorption energy ΔG_{ads} was reported to be 35,4 kJ/mole [245]. Due to the potential seen in using this substance, further studies led to a patent for nitrogen containing molecules for this application [268].

As an outlook, organic agents for protection of package termini for soldering especially may have a potential in new packages where the package termini are not mechanically processed as this leads to a damage of the protection coating. This is beside other risks one of the major drawback in this application which can be overcome by new package technologies, e.g. chip embedding platforms such as DRBLADETM.

Furthermore, usage of copper protecting agents was investigated for the application of copper wirebonding on copper surfaces. Poly(1-vinylimidazole) (PVI-1), poly(4-vinylimidazole) (PVI-4), poly(benzimidazole) (PBI) were chosen as agents forming complexes to copper in addition to their strong polymeric properties. This combination generates a high temperature stability of the respective coatings, e.g. PVI-1 protects up to 15 minutes at 400°C. Further small molecules were combined with the polymeric coatings to investigate the synergistic effect between big polymeric domains closed by

smaller molecules adsorbed to the copper. But the usage of benzotriazole (BTA), mercaptobenzimidazole (MBIH) or decanethiole (C10-SH) revealed no difference to the protection of copper with using the single polymeric coatings. Because of the moderate temperature for the application at copper wirebonding in the range of 150-200°C the protection of copper in air at 150°C was investigated with annealing experiments and PVI-1 was finally derived as the agent to be used for substrates used for Cu wirebonding. Even though a copper corrosion protection was observed the improvement for copper wirebonding could not be shown, instead even a drop of the wirebonding quality was observed as the protecting coating also acts as a barrier for wirebonding as it is known from copper oxide.

For investigation of the deposition conditions of PVI-1 on copper a study on the deposition kinetics of PVI-1 was published [257] also performed with the fast impedance scanning quartz crystal microbalance. In this study the equilibrium thickness during deposition of PVI-1 from aqueous solutions was found to be reached after 5 minutes already. Besides the understanding of the deposition conditions reported there it is necessary for future investigations in this application to adapt the copper wirebonding parameters to this new surface or to apply a cleaning process prior to the copper wirebonding process that opens the protected copper surface right before the bond happens.

As an outlook the application of organic protecting coatings for copper wirebonding can be combined with for example plasma cleaning processes that open the copper surface at bonding. This would offer a very reproducible surface as the protected copper is not exposed to corrosive environment at all prior downstream processes.

List of publications in this section:

[257] Simbeck T., Hammer M. M., Thomaier S., Stock Ch., Riedl E., Gores H. J.: Kinetics of adsorption of poly(vinylimidazole) (PVI) onto copper surfaces investigated by quartz crystal microbalance studies; *Journal of solid state electrochemistry*, 16, 3467-3472 (2012)

[245] Simbeck T., Thomaier S., Stock Ch., Riedl E., Gores H. J.: Measurement of adsorption kinetics of benzotriazole on copper surfaces via impedance scanning quartz crystal microbalance studies; *Electrochemistry communications*, 13 (8), 803-805 (2011)

[268] E. Riedl, J. Mahler, J. Lodermeier, M. Vaupel, S. Jordan: Semiconductor package; patent US7989930 B2 (2011)

8 Abbreviations and acronyms

MOSFET:	Metal oxide semiconductor field effect transistor
RoHS:	Restriction of hazardous substances, EU law to restrict heavy metals (Pb, Cd, Cr, Hg) and brominated flame retardant substances in electronic devices and components.
WEEE:	Waste of electrical and electronic equipment, European Community directive 2002/96/EC on waste electrical and electronic equipment (WEEE) which, together with the RoHS Directive 2002/95/EC, became European Law in February 2003, setting collection, recycling and recovery targets for all types of electrical goods.
PCB:	Printed circuit board
NiP:	Nickelphosphorus, NiP alloy commonly used in semiconductor industry for leadframe surfaces, NiP is deposited electroless, (3-5 μ m thickness ; 5<wt%-P<11).
NiNiP:	Leadframe surface used in semiconductor industry, electrochemical deposition of Ni (1-2 μ m thickness) and NiP (0,1-0,3 μ m thickness; 5<wt%-P<11)
CTE:	Coefficient of linear thermal expansion α [10^{-6} K^{-1}]
T _g :	Glass transition temperature of polymers.
SiN:	Siliconnitride
DVSD:	Delta V _{SD} , source-drain voltage characteristic of the inverse diode within a MOSFET. This parameter is often used to measure the thermal connection of the device to specific heatsinks in the package to detect weaknesses of the chip interconnects.
OCN:	Orthocresol novolac resin
SiON:	Silicon oxy nitride
RIE:	Reactive ion etching
FESEM:	Field effect scanning electron microscope
MSL:	Moisture sensitivity level for packages and semiconductor device qualification
MSA	Methanesulfonic acid
BPSG	Boron-phosphorous-silicon-glass
SAM	Scanning acoustic microscopy

FIB	Focus ion beam
CE	Current efficiency
Re	Reynolds number
CCC	Chromate conversion coatings
BET	Brunnauer-Emmett-Teller surface adsorption kinetics
PEG	Polyethyleneglycole
TC	Temperature cycling stress test for semiconductor devices, usually from -55°C to 150°C within a period of 30 minutes. Usual stress levels are TC500 and TC1000
MSL	Moisture sensitivity level. A level of moisture conditioning of devices prior to the soldering on PCB that is applied for device qualification in semiconductor industry. (e.g. MSL1 is level 1)

9 Curriculum Vitae

Name: Edmund Martin Riedl

Birth: 15.09.1968 in Regensburg, married, 2 daughters

Address: Sandorf 5, 93192 Wald

Contact: Edmund.martina@web.de; Edmund.martina@t-online.de

Period	Stage
1978-1986	Gymnasium Neutraubling, Werner-von-Siemens Gymnasium Regensburg
1986-1989	Vacational training Squibb - Von Heyden GmbH, Regensburg, pharmaceutical industry.
1989-1990	Technical College of Regensburg (FOS)
1991-1996	Study at Georg-Simon-Ohm University of Applied Sciences, Technical Chemistry Engineering; center of gravity: Applied Chemistry
1996-1997	Research and development at Bristol-Myers Squibb GmbH on chemical synthesis and analysis of pharmaceutical substances.
1996-1998	Scientific assistant at University of Bayreuth, departement of crystallography. Synthesis and X-ray analysis of inorganic single crystals.
Since 1999	Cooperation projects University of Regensburg and Infineon Technologies AG (see separate table below)
2005 – 2007	Exams for PhD qualification: Electrochemistry; Inorganic Chemistry; Organic Chemistry. Seminars on electrochemical methods, Laplace transformation, Energy transformation and storage devices.
2007	Start of PhD work at University of Regensburg, Departement “Solution chemistry”, Prof. Kunz

Cooperations within the University of Regensburg:

The following ten projects have been accomplished together with the workgroup “Electrochemistry and Electrolytes” at the University of Regensburg, Institute of Physical and Theoretical Chemistry, chair Prof. Dr. W. Kunz. For four of the projects an industrial realization of the technology was reached.

Start	Topic	Basic R+D	Development	Implementation milestone T8-T9	Massproduction milestone T10
2004	A2 electrolyte Cr-VI free	Several new Cr-VI free electrolytes	Feasibility	Planned	
2004	Nanoflame	Characterisation of deposition and layer.	Feasibility on DSO and TO platform		
2005	A2-process with minimum wireetching	Identification of suitable process conditions and etching influences.	Feasibility on DSO300mil	Implementation of short A2-cell and modified concentrations in Batam (T9)	Massproduction since 2006
2006	HF activation for A2	Identification of chemicals for Alu activation.	Feasibility on TO263 and DSO300mil	Implementation of Ar/O ₂ + HF/A2 in MAL and BAT for SMART5 (T9)	Massproduction since 2007
2007	Pulplating process for A2	Research on puls conditions and very short A2-cell.	Feasibility on TO263	Implementation on TO263 (T9 in 2010)	Massproduction since 2012
2008	Organic final finish	Development of organic molecules for PCB soldering	Feasibility		
2008	Organic coating for Cu-to-Cu interconnect	Development of organic molecules for Cu-to-Cu interconnect	Feasibility		
2008	Noble metal plating for final finish	Development of noble metal coatings as substitute for Sn plating as solderable package surface for powerpackages.	Feasibility		
2009	Surfaces for Cu-to-Cu interconnect	Basic Cu wirebonding on bare Cu surfaces	Feasibility		
2010	Development of a anisotropic Cu etch chemistry and process for package sawing.	Deep trench etching for Cu leadframes for package separation.	Package process freeze T7 reached by 2010	Implementation on Blade3x3 (T9 in 2012)	Massproduction since 2012

10 Literature

- [1] Neul R.: From Micro/Nanosystems Technologies to Smart Systems Integration; Robert Bosch GmbH, High level conference on nanotechnologies, 20-21.11.2007, Braga; link: http://www.fct.mctes.pt/hlc/Talks/Reinhard_Neul.pdf
- [2]: D'Ans, Lax: Taschenbuch für Chemiker und Physiker; 4.Auflage, Springer, Berlin (1998), ISBN 3 540 60035 3
- [3]: Shin-Etsu Electronics (M) Sdn Bhd: Technical Data of KMC-180-7, KMC-2110G-7 and KMC-2110G-7X molding compounds, TD-03-0336 (2003)
- [4]: K. Tada, H. Fujioka: Properties of molding compounds to improve package reliability of SMD's, IEEE transactions on components and packaging technology, **22**, no.4, 534 (1999)
- [5] M. Huang, Z. Suo: Thin film cracking and ratcheting caused by temperature cycling, J. Mater. Res., **15**, 1239-1242 (2000)
- [6] G. Harman: Wire Bonding in Microelectronics, 3rd edition, McGraw Hill Professional, New York (2010), ISBN 0071476237, 9780071476232
- [7] P. Alpern, K. C. Lee, R. Dudek, R. Tilgner: A simple model for the mode I popcorn effect for IC packages, Microelectronics Reliability, **40**, 1503-1508 (2000)
- [8]: B. Plikat: "Packaging für Hochtemperatur Applikationen"; Systemintegration in der Mikroelektronik, Messe + Kongress, ISBN 3-8007-2761-7, (2003)
- [9] Technical specification of Hitachi SU9000 XHR SEM, <http://www.hht-eu.com/cms/5149.html>, Hitachi High-Technologies Europe GmbH (2010)
- [10] Technical specification of Hitachi SU-70 FESEM, http://www.hht-eu.com/cms/Hitachi_SU-70_07_2006.html, Hitachi High-Technologies Europe GmbH (2010)
- [11] H. Schumann, H. Oettel: Metallografie, 14. Auflage, Wiley-VCH Verlag GmbH & Co KG, Weinheim (2005), ISBN 3-527-30679-4
- [12] Lee M. R.: Transmission electron microscopy (TEM) of earth and planetary materials: A review: Mineralogical Magazine, Vol 74 (1), 1-27 (2010)
- [13] T. W. Jelinek: Oberflächenbehandlung von Aluminium, 1. Auflage, Eugen G. Leuze Verlag, Saulgau (1997), ISBN 3-87 480-115-2
- [14] J. F. Watts, J. Wolstenholme: An Introduction to surface analysis by XPS and AES, John Wiley & Sons Ltd., West Sussex (2003), ISBN 0470847123
- [15] J.W. Martin: The Local Chemical Analysis of Materials; Pergamon Materials Series Vol.9, Elsevier Ltd., Kidlington, Oxford (2003), ISBN: 0080439365

- [16] J. Grams: New trends and potentialities of TOF-SIMS in surface studies, Nova Science Publishers, Inc., New York 2007, ISBN 1-60021-635-8
- [17] <http://www.iontof.com>, ION-TOF GmbH, Münster 2011
- [18] J. C. Vickerman, D. Briggs: TOF-SIMS: Surface analysis by mass spectrometry, IM Publications LLP, 2001, ISBN 1901019039
- [19] Briggs A., Kolosov O.: Acoustic Microscopy, second edition, Oxford University Press, Oxford 2010, ISBN 978-0-19-923273-4
- [20] S.-J. Cho, K.-W. Paik: The effect of oxidation of Cu-base leadframe on the interface adhesion between Cu metal and epoxy molding compound, IEEE transactions on components, packaging and manufacturing technology - part B, **20**, 167-175 (1997)
- [21] P. W. K. Chung, M. M. F. Yuen, P. C. H. Chan, N. K. C. Ho, D. C. C. Lam.: Effect of copper oxide on adhesion behaviour of epoxy molding compound - copper interface, Electronic Components and Technology Conference 52nd proceedings, 1665-1670 (2002)
- [22] M. Lebbai, J.-K. Kim, M. M. F. Yuen: Effects of dimple and metal coating on interfacial adhesion in plastic packages, Journal of electronic materials, **32**, 564-573 (2003)
- [23] J. Fauty, J. Knapp, J. Yoder: Mold compound adhesion to bare copper leadframes - effect of laser texturing, The international journal of microcircuits and electronic packaging, **25**, 51-79 (2002)
- [24] M. Lebbai, J.-K. Kim, W. K. Szeto, M. M. F. Yuen, P. Tong: Optimization of black oxide coating thickness as an adhesion promoter for copper substrate in plastic integrated-circuit packages, Journal of electronic materials, **32**, 558-563 (2003)
- [25] C. V. Bishop, G. S. Bokisa, R. J. Durante, J. R. Kochilla: US patent 6284309, Atotech, <http://www.atotech.com/en/products/electronics/surface-treatment/bonding-enhancement/bondfilm.html>, (2001)
- [26] C. V. Bishop, G. S. Bokisa, R. J. Durante, J. R. Kochilla: US patent 6579591, Atotech, (2003)
- [27] C. V. Bishop, G. S. Bokisa, R. J. Durante, J. R. Kochilla: US patent 6602440, Atotech, (2003)
- [28] D. Ferrier, F. Durso: US patent 6020029, MacDermid, (2000)
- [29] M. Carano, L. Burger, A. Kucera, R. Bernards: Building Strong Bonds, www.circuitree.com, 26-32 (2004)
- [30] S. Nolte: Haftvermittler auf Basis von 1H-Benzotriazol für Aluminium- und Kupferklebungen, Dissertation, Universität Bielefeld (2002)

- [31] H. Y. Lee, G. S. Park: Failure paths at copper-base leadframe/epoxy molding compound interfaces, *Journal of materials science*, **37**, 4247-4257 (2002)
- [32] M. M. Antonijevic, M. B. Petrovic: Copper Corrosion Inhibitors: A review. *Int. J. Electrochem. Sci.*, **3**, 1-28 (2008)
- [33] L. Lin, C.-Y. Chao: US patent 5022968A, Olin corp., (1991)
- [34] L. Lin, C.-Y. Chao: US patent 5098796A, Olin corp., (1992)
- [35] S. F. Chen, N. Yukov, L. Lin, C.-Y. Chao: 5230932A, Olin corp. (1993)
- [36] M. Lebbai, J.-K. Kim, M. M. F. Yuen: Effects of moisture and elevated temperature on reliability of interfacial adhesion in plastic packages, *Journal of electronic materials*, **32**, 574-582 (2003)
- [37] M. Lebbai, M. Naina: Improvement of interfacial adhesion in plastic packages - dimples, metallic coating and black oxide, dissertation thesis, The Hongkong University of Science and Technology (2002)
- [38] Product information of Surachemicals GmbH, Bucha, Germany;
http://www.surachemicals.de/produkte/surasil_technik.html
- [39] J. A. Rodriguez, J. Y. Kim, J. C. Hanson, M. Perez, A. I. Frenkel: Reduction of CuO in H₂: In Situ Time-Resolved XRD Studies, *Catalysis Letters*, **85**, 247-254 (2003)
- [40] J. Y. Kim, J. A. Rodriguez, J. C. Hanson, A. I. Frenkel, P. L. Lee: Reduction of CuO and Cu₂O with H₂: H embedding and kinetic effects in the formation of suboxides, *J. Am. Chem. Soc.*, **125**, 10684-10692 (2003)
- [41] O. Kubaschewski, B. E. Hopkins: Oxidation of metals and alloys, second edition, Butterworth & Co, London (1962)
- [42] T. A. Utigard, M. Wu, G. Plascencia, T. Marin: Reduction kinetics of Goro nickel oxide using hydrogen, *Chemical Engineering Science*, **60**, 2061-2068, (2005)
- [43] J. A. Rodriguez, J. C. Hanson, A. I. Frenkel, J.-Y. Kim, M. Perez: Experimental and theoretical studies of the reaction of H₂ with NiO: role of O vacancies and mechanism for oxide reduction, *J. Am. Chem. Soc.*, **124**, 346 (2002)
- [44] G. Humpston, D. M. Jacobson: Principles of Soldering, ASM International, (2004) ISBN 9780871707925
- [45] A. F. Hollemann, E. Wieberg, N. Wieberg: Lehrbuch der anorganischen Chemie, 91.-100. Auflage, Walter de Gruyter, Berlin (1985), ISBN 3110075113
- [46] H. H. Kung: Transition metal oxides - surface chemistry and catalysis, Elsevier, Amsterdam, (1989) ISBN 0-444-87394-5
- [47] E. Fromm: Kinetics of metal-gas interactions at low temperatures - hydriding, oxidation, poisoning, Springer, Heidelberg, (1998), ISBN 3-540-63975-6

- [48] J. E. Boggio: The room temperature oxidation of Cu (111): Pressure effects, *J. Chem. Phys.* **70**, 5054-5058 (1979)
- [49] J. Iijima, J.-W. Lim, S.-H. Hong, S. Suzuki, K. Mimura, M. Isshiki: Native oxidation of ultra high purity Cu bulk and thin films, *Applied Surface Science* **253**, 2825–2829, (2006)
- [50] W. H. Casey: On the relative dissolution rates of some oxide and orthosilicate minerals, *Journal of colloid and interface science*, **146**, 586-589 (1991)
- [51] H. Majima, T. Awakura, T. Yazaki, Y. Chikamori: Acid Dissolution of Cupric Oxid, *Metall. Trans. B*, **11**, 209 (1980)
- [52] V. V. Danilov, N. M. Sorokin, A. A. Ravdel, *Zh. Prikl. Khim.*, **49**, 1006 (1976)
- [53] M. D. Gernon, M. Wu, T. Buszta, P. Janney: Environmental benefits of methanesulfonic acid: Comparative properties and advantages, *Green chemistry*, **1**, 127-140 (1999)
- [54] D. R. Lide: *CRC Handbook of Chemistry and Physics*, 87th edition, (2006 - 2007)
- [55] F. Winkler, M. Guttman: Galvanisch-Nickel-Phosphor – alternatives Material zur Beschichtung von Bauteilen oder zum Einsatz in der Mikrosystemtechnik? Teil I: Eine Literatur und Industrierecherche, *Galvanotechnik*, **8**, 1948-1954 (2005)
- [56] F. Winkler, M. Guttman: Galvanisch-Nickel-Phosphor – eine Alternative zur stromlosen Beschichtung von Bauteilen oder ein Material für die Mikrosystemtechnik? Teil II: Eine Literatur und Industrierecherche, *Galvanotechnik*, **93**, 2260–2274 (2004)
- [57] C.-C. Hu, A. Bai: Composition control of electroplated nickel-phosphorus deposits, *Surface and coatings technology*, **137**, 181-187 (2001)
- [58] R. Bmgger: *Die galvanische Vernicklung*, 2. Auflage, Eugen G. Leuze Verlag, Saulgau/Württ. (1984), ISBN 3-87-480-009-1
- [59] ASM International: *Binary alloy phase diagrams*, second revised edition, ASM International, (1997), ISBN 0871705621
- [60] H.-C. Huang, S.-T. Chung, S.-J. Pan, W.-T. Tsai, C.-S. Lin: Microstructure evolution and hardening mechanisms of Ni-P electrodeposits, *Surface and coatings technology*, **205**, 2097–2103 (2010)
- [61] C. S. Lin, C. Y. Lee, F. J. Chen, W. C. Li: Structural Evolution and Internal Stress of Nickel-Phosphorus Electrodeposits, *Journal of The Electrochemical Society*, **152**, C370-C375 (2005)
- [62] D. J. Siconolfi, R. P. Frankenthal: Air Oxidation of a Ni-P Alloy, *J. Electrochem. Soc.*, **136**, 2475-2480 (1989)

- [63] C. F. Jones, R. L. Segall, R. St.-C. Smart, P. S. Turner: Semiconducting oxides: Effects of electronic and surface structure on dissolution kinetics of nickel oxide, *J. Chem. Soc. Faraday Trans. 1*, **74**, 1615 (1978)
- [64] J. W. Diggle: Dissolution of oxide phases, in oxide and oxide films, ed. J. W. Diggle (Marcel Dekker, New York, 1973), vol. 2, p. 281 ff
- [65] B. Beverskog, I. Puigdomenech: Revised pourbaix diagrams for nickel at 25-300°C, *Corrosion Science*, **39**, 969-980 (1997)
- [66] G. Wolf: Specific heat of nickel hydride from 10 to 200K, *J. Phys. Chem. Solids*, **32**, 1649-1655 (1971)
- [67] E. M. Relitz: Method of obtaining bright chromium deposits on bright nickel deposits, Canadian patent 378303 (1938)
- [68] N. V. Mandich, D. L. Snyder: Electrodeposition of chromium in modern electroplating, 4th edition, p.289, John Wiley & Sons Inc., New York (2000), ISBN 0471168246
- [69] N. V. Mandich: Toward understanding nickel activation and chromium reverse etching, *Plating surf. finish.*, **85**, 91-96 (1998)
- [70] L. J. Durney: Electroplating engineering handbook, 4th edition, Chapman and Hall, London (1984, reprinted 1998), ISBN 0412741105
- [71] W. Gruhl, U. Gruhl: The oxidation of liquid tin, *Metall*, **6**, 177 (1952)
- [72] M. Nagasaka, H. Fuse, T. Yamashina: Oxidation of vacuum-evaporated films of tin and stannous oxide, *Thin Solid Films*, **29**, L29-L32 (1975)
- [73] Gmelin: Handbuch der anorganischen Chemie, Zinn, Band 32, 8.Auflage, Verlag Chemie GmbH, Weinheim (1971)
- [74] Römpp Online - Version 3.5, Georg Thieme Verlag, Stuttgart (2009)
- [75] C. I. House, G. H. Kelsall: Potential - pH diagrams for the Sn / H₂O - Cl system, *Electrochimica acta*, **29**, 1459-1464 (1984)
- [76] G. S. Forbes, H. H. Anderson: Rearrangements in compounds of carbon, silicon, germanium and tin containing halogens, isocyanate and thiocyanate, *Journal of the American chemical society*, **67**, 1911-1914 (1945)
- [77] B. N. Stirrup, N. A. Hampson: Electrochemical reactions of tin in aqueous electrolytic solutions, *Surface Technology*, **5**, 429 - 462 (1977)
- [78] R. H. Carter: Solubilities of some inorganic fluorides in water at 25°C, *Industrial and engineering chemistry*, **20**, 1195-1195 (1928)

- [79] G. M. Scamans, E. P. Butler: In situ observations of crystalline oxide formation during aluminum and aluminum alloy oxidation, *Metallurgical Transactions A*, **6**, 2055-2063 (1975)
- [80] D. J. Field, G. M. Scamans, E. P. Butler: The high temperature oxidation of Al-4.2 wt pct Mg alloy, *Metallurgical Transactions A*, **18**, 463-472 (1987)
- [81] I. Olefiord, A. Nylund: Surface analysis of oxidized aluminium, *Surface and interface analysis*, **21**, 290-297 (1994)
- [82] R. S. Bailey: Effects of target microstructure on aluminum alloy sputtered thin film properties, *Journal of vacuum science and technology A*, **10**, 1701-1705 (1992)
- [83] G. A. Walker, C. C. Goldsmith: Precipitation and solid solution effects in aluminum-copper thin films and their influence on electromigration, *Journal of applied physics*, **44**, 2452-2455 (1973)
- [84] A. Nylund, K. Mizuno, I. Olefiord: Influence of Mg and Si on the oxidation of aluminum, *Oxidation of Metals*, **50**, 309-325 (1998)
- [85] W. Hufnagel: *Aluminium Taschenbuch*, 3. datenaktualisierter Druck, Aluminium Verlag, Düsseldorf (1988), ISBN 3-87017-169-3
- [86] S. Wernick, R. Pinner, P. G. Sheasby: *The surface treatment and finishing of aluminium and its alloys*, 5th edition, reprinted 1996, ASM International, Metal Park (1996), ISBN 0-904477-09-6
- [87] R. W. Revie, H. H. Ulig: *Corrosion and corrosion control*, 4th edition, John Wiley & Sons, Inc., Hoboken New Jersey (2008), ISBN 978-0-471-73279-2
- [88] W. Vedder, D. A. Vermilyea: Aluminium + water reaction, *Transactions of the Faraday society*, **65**, 561-584 (1968)
- [89] J. W. Diggle, T. C. Downie, C. W. Goulding: The dissolution of porous oxide films on aluminium, *Electrochimica acta*, **15**, 1079-1093 (1970)
- [90] J. A. Dyer, N. C. Scrivner: A practical guide for determining the solubility of metal hydroxides and oxides in water, *Environmental progress*, **17**, 1-8 (1998)
- [91] R. Ramos, G. Cunge, B. Pelissier, O. Joubert: Cleaning aluminum fluoride coatings from plasma reactor walls in SiCl₄/Cl₂ plasmas; *Plasma sources sci. technol.*, **16**, 711-715 (2007)
- [92] G. Cunge, B. Pelissier, O. Joubert, R. Ramosand, C. Maurice: New chamber walls conditioning and cleaning strategies to improve the stability of plasma processes, *Plasma sources sci. technol.*, **14**, 599-609 (2005)
- [93] S. Alberici, D. Coulon, P. Joubin, Y. Mignot, L. Oggioni, P. Petruzza, D. Piumi, L. Zanotti: Surface treatment of wire bonding metal pads, *Microelectronic engineering*, **70**, 558-565 (2003)

- [94] K. H. Ernst, D. Grman, R. Hauert: Fluorine-induced corrosion of aluminium microchip bond pads: An XPS and AES analysis, *Surface and interface analysis*, **21**, 691-696 (1994)
- [95] J. H. Thomas, C. E. Bryson, T. R. Pampalone: X-ray photoelectron spectroscopy and surface charge build-up used to study residue on aluminium contacts on integrated circuits, *Surface and interface analysis*, **14**, 39-45 (1989)
- [96] I. Yamai, H. Saito: Vapor phase growth of alumina whiskers by hydrolysis of aluminium fluoride, *Journal of crystal growth*, **45**, 511-516 (1978)
- [97] Technical specification for "Aluminiumbeize AL-B", BAD 01022, Schloetter Galvanotechnik, Geislingen (1998)
- [98] R. Grauer, W. Stumm: Die Koordinationschemie oxidischer Grenzflächen und ihre Auswirkung auf die Auflösungskinetik oxidischer Festphasen in wässriger Lösungen, *Colloid and polymer science*, **260**, 959-970 (1982)
- [99] V. Zutic, W. Stumm: Effect of organic acids and fluoride on the dissolution kinetics of hydrous alumina. A model study using rotating disc electrode, *Geochimica et cosmochimica acta*, **48**, 1493-1503 (1984)
- [100] G. Wedler: *Lehrbuch der Physikalischen Chemie*, 3. durchgesehene Auflage, VCH Verlagsgesellschaft, Weinheim (1987), ISBN 3-527-26702-6
- [101] C. Hamann, W. Vielstich: *Elektrochemie II, Elektrodenprozesse, angewandte Elektrochemie*, Verlag Chemie, Weinheim (1981), ISBN 3-527-21081-4
- [102] M. Paunovic, M. Schlesinger: *Fundamentals of electrochemical deposition*, John Wiley & Sons, Inc, New York (1998), ISBN 0-471-16820-3
- [103] A. C. Fisher: *Electrode dynamics*, Oxford University Press, Oxford (1996), ISBN 019 855690 X
- [104] C. Hamann, W. Vielstich: *Elektrochemie I, Leitfähigkeit, Potentiale, Phasengrenzen*, 2. überarbeitete Auflage, Verlag Chemie, Weinheim (1985), ISBN 3-527-21100-4
- [105] A. J. Bard, L. R. Faulkner: *Electrochemical methods - Fundamentals and Applications*, 2nd edition, John Wiley and Sons, Inc, Brisbane 2001, ISBN 13-978-0-471-04372-0
- [106] Bockris A. K., N. Reddy, M. Gombao-Aldeco: *Modern Electrochemistry Part 2A*, second ed. Plenum, New York, 2000
- [107] J. Tafel: Über die Polarisation bei kathodischer Wasserstoffentwicklung, *Zeitschrift für physikalische Chemie*, **41**, 642-712 (1905)
- [108] A. T. Vagramyan: Mechanism of simultaneous reduction of metal ions, published in V. A. Averkin: *Electrodeposition of alloys*, Israel Program for Scientific Translations, Jerusalem 1964

- [109] I. Epelboin, M. Ksouri, R. Wiart: On a model for the electro crystallisation of zinc involving an autocatalytic step, *Journal of the Electrochemical Society*, **122**, 1206-1214 (1975)
- [110] A. R. Despic, Dj. Jovanovic, T. Rakic: Kinetics and mechanism of deposition of zinc from zincate in concentrated alkali hydroxide solutions, *Electrochimica Acta*, **21**, 63-77 (1976)
- [111] C. Cachet, U. Ströder, R. Wiart: The kinetics of zinc electrode in alkaline zincate electrolytes, *Electrochimica Acta*, **27**, 903-908 (1982)
- [112] J. O'M. Bockris, Z. Nagy, A. Damjanovic: On the deposition and dissolution of zinc in alkaline solutions, *Journal of the Electrochemical Society*, **119**, 285-295 (1972)
- [113] J. Hendrikx, A van der Putten, W. Visscher, E Barendrecht: The electrodeposition and dissolution of zinc and amalgamated zinc in alkaline solutions, *Electrochimica Acta*, **29**, 81-89 (1984)
- [114]: M. Schlesinger, M. Paunovic: *Modern electroplating*, 4th edition, John Wiley & Sons, New York 2000, ISBN 0-471-16824-6
- [115]: T. W. Jelinek: *Galvanisches Verzinken*, Eugen G. Leuze Verlag, Saulgau 1982, ISBN 3-87480-010-5
- [116] V. Danciu, V. Cosoveanu, I. C. Ladiu: Vergleichende Untersuchungen an cyanidfreien Zinkelektrolyten mit Natrium- oder Kaliumhydroxid, *Galvanotechnik*, **91**, 3364-3371 (2000)
- [117] R. D. Naybour: Morphologies of zinc electrodeposited from zinc-saturated aqueous alkaline solutions, *Electrochimica Acta*, **13**, 763-769 (1968)
- [118] R. D. Naybour: The effect of electrolyte flow on the morphology of zinc electrodeposited from aqueous alkaline solution containing zincate ions, *Journal of the Electrochemical Society*, **116**, 520-524 (1969)
- [119] G. Cerbe, H. J. Hoffmann: *Einführung in die Wärmelehre*, 9. Verbesserte Auflage, Hanser Verlag, München (1990), ISBN 3-446-15952-5
- [120] J. W. Diggle, A. R. Despic, J. O'M. Bockris: The mechanism of dendritic electrocrystallization of zinc, *Journal of the Electrochemical Society*, **116**, 1503-1514 (1969)
- [121] I. N. Justinijanovic, A. R. Despic: Some observations on the properties of zinc electrodeposited from alkaline zincate solutions, *Electrochimica Acta*, **18**, 709-717 (1973)
- [122] K. I. Popov, N. V. Krstajic: The mechanism of spongy electrodeposits formation on inert substrate at low overpotentials, *Journal of Applied Electrochemistry*, **13**, 775-782 (1983)

- [123] R. Y. Wang, D. W. Kirk, G. X. Zhang: Effects of deposition conditions on the morphology of zinc deposits from alkaline zincate solutions, *Journal of the Electrochemical Society*, **153**, C357-C364 (2006)
- [124] R. Weiner: Die galvanische Verchromung, 2. Auflage, Eugen G. Leutze Verlag, Saulgau (1974)
- [125] O. Bernhauser: Electroplating of articles with chromium, US patent, US 1 985 308, (1934)
- [126] W. Roggendorf: Electrodeposition of chromium and duplex micro-crack chromium coatings, US patent, US 3 418 220, (1968)
- [127] B. Kerle, M. Opper, S. Volk: Sechswertige Chromverfahren, SurTec GmbH, <http://www.surtec.de/Vortraege/Chromverfahren.pdf>, Mai 2000
- [128] G. A. Lausmann, J. N. Unruh: Die galvanische Verchromung, 2. Auflage, Eugen G. Leutze Verlag, Bad Saulgau (2000), ISBN 3-87480-216-7
- [129] N. M. Martyak: Internal stress in zinc-chromate coatings, *Surface and Coatings Technology*, **88**, 139-146 (1996)
- [130] X. Zhang, C. van den Bos, W. G. Sloof, A. Hovestad, H. Terryn, J. H. W. de Wit: Comparison of the morphology and corrosion performance of Cr(VI)- and Cr(III)-based conversion coatings, *Surface and Coatings Technology*, **199**, 92-104 (2005)
- [131] T. Watanabe, S. Ando, T. Urakawa: Method of manufacturing plated steel sheet with Zn-Cr alloy plating, EU patent, EP 0 638 668 A1 (1994)
- [132] H. Nakamaru, T. Fujimura, H. Ohnuma, K. Mochizuki, N. Morito, M. Katayama: Rust proof steel sheet excellent in various characteristics including corrosion resistance, EU patent, EP 0 607 452 A1 (1993)
- [133] M. Abe, T. Watanabe, S. Ando, T. Urakawa: Method of manufacturing plated steel sheet with Zn-Cr composite plating, EU patent, EP 0 643 157 A1 (1994)
- [134] T. Kanamaru, M. Nakayama, K. Arai, S. Suzuki, R. Naka: Corrosion resistant plated steel strip and method for producing same, EU patent, EP 0 285 931 A1 (1988)
- [135] L. Guzman, M. Adami, W. Gissler, S. Klose, S. De Rossi: Vapour deposited Zn-Cr alloy coatings for enhanced manufacturing and corrosion resistance of steel sheets, *Surface and Coatings Technology*, **125**, 218-222 (2000)
- [136] T. Boiadjeva, D. Kovacheva, K. Petrov, S. Hardcastle, M. Monev: Effect of anodic treatment on the composition and structure of electrodeposited Zn-Cr alloy coatings, *Corrosion Science*, **46**, 681-695 (2004)
- [137] A. Watson, Y. J. Su, M. R. el-Sharif, C. U. Chrisholm: The electrodeposition of zinc chromium alloys and the formation of conversion coatings without the use of chromate solutions, *Transactions of the Institute of Metal Finish*, **71**, 15-20 (1993)

- [138] H. Kronberger, A. Tomandl: Korrosionsschutz auf Zink-Legierungsbasis, Offenlegungsschrift, DE 10 2009 045 076 A1 (2011)
- [139] T. B. Massalski, H Okamoto: Binary alloy phase diagrams, 2nd edition, ASM international, Materials Park Ohio (1990), ISBN 087170403X
- [140] N. Y. Tang, X. B. Yu: Study of the zinc-rich corner of the Zn-Fe-Cr system at galvanizing temperatures, Journal of Phase Equilibria and Diffusion, **26**, 50-54 (2005)
- [141] G. Reumont, P. Perrot: Thermodynamic assessment of the zinc-rich part of the Cr-Zn system, Journal of Phase Equilibria and Diffusion, **24**, 50-54 (2003)
- [142] Z. Moser, L. A. Heldt: The Cr-Zn (chromium-zinc) system, Journal of Phase Equilibria, **13**, 172-176 (1992)
- [143] C. Scott, C. Olier, A. Lamande, P. Choquet, D. Chaleix: Structural evolution of co-deposited Zn-Cr coatings produced by vacuum evaporation, Thin Solid Films, **436**, 232-237 (2003)
- [144] T. Boiadjieva, M. Monev, A. Tomandl, H. Kronberger, G. Faflek: Electrochemical studies on Zn deposition and dissolution in sulphate electrolyte, Journal of Solid State Electrochemistry, **13**, 671-677 (2009)
- [145] T. Boiadjieva, K. Petrov, H. Kronberger, A. Tomandl, G. Avdeev, W. Artner, T. Lavric, M. Monev: Composition of electrodeposited Zn-Cr alloy coatings and phase transformations induced by thermal treatment, Journal of Alloys and Compounds, **480**, 259-264 (2009)
- [146] T. Boiadjieva, D. Kovacheva, L. Lyutov: Deposition of Zn-Cr alloy coatings from sulfate electrolyte: Effect of polypropylene glycol 620 and glycine and combinations thereof, Journal of Applied Electrochemistry, **38**, 1435-1443 (2008)
- [147] T. Boiadjieva, D. Kovacheva, K. Petrov, S. Hardcastle, A. Sklyarov, M. Monev: Electrodeposition, composition and structure of Zn-Cr alloys, Journal of Applied Electrochemistry, **34**, 315-321 (2004)
- [148] A. T. Vagramyan: Codeposition of chromium with other metals, published by V. A. Averkin: Electrodeposition of alloys, Israel Program for Scientific Translations, Jerusalem 1964
- [149] T. Akiyama, S. Kobayashi, J. Ki, T. Ohgai, H. Fukushima: Role of polyethylene glycol in electrodeposition of zinc-chromium alloys, Journal of Applied Electrochemistry, **30**, 817-822 (2000)
- [150] A. Ledin, S. Karlsson, B. Allard: Effects of pH, ionic strength and fulvic acid on size distribution and surface charge of colloidal quartz and hematite; Applied Geochemistry, **8**, 409-414 (1993)
- [151] A. Düker, A. Ledin, S. Karlsson, B. Allard: Adsorption of zinc on colloidal (hydr)oxides of Si, Al and Fe in the presence of a fulvic acid; Applied Geochemistry, **10**, 197-205 (1995)

- [152] A. Kozawa: Ion-exchange adsorption of zinc and copper ions on silica; *Journal of Inorganic Nuclide Chemistry*, **21**, 315-324 (1961)
- [153] B. Cabot, A. Foissy: Reversal of the surface charge of a mineral powder: Application to electrophoretic deposition of silica for anticorrosion coatings, *Journal of Materials Science*, **33**, 3945-3952 (1998)
- [154] A. Takahashi, Y. Miyoshi, T. Hada: Effect of SiO₂ colloid on the electrodeposition of zinc-iron group metal alloy composites, *Journal of the Electrochemical Society*, **141**, 954-957 (1994)
- [155] T. J. Tuaweri, G. D. Wilcox: Behaviour of Zn-SiO₂ electrodeposition in the presence of N,N-dimethyldodecylamine, *Surface and Coatings Technology*, **200**, 5921-5930 (2006)
- [156] T. A. Witten, Jr.: Diffusion-limited aggregation, a kinetical critical phenomenon; *Physical Review Letters*, **47**, 1400-1403 (1981)
- [157] F. Sagues, M. Q. Lopez-Salvans, J. C. Claret: Growth and forms in quasi-two-dimensional electrocrystallization; *Physics Reports*, **337**, 97-115 (2000)
- [158] J. N. Chazalviel: Electrochemical aspects of the generation of ramified metallic electrodeposits; *Physical Review A*, **42**, 7355-7367 (1990)
- [159] B. R. Scharifker, J. Mostany: Three dimensional nucleation and diffusion controlled growth: Part 1. Number density of active sites and nucleation rates per site; *Journal of Electroanalytical Chemistry*, **177**, 13-23 (1984)
- [160] M. E. Hyde, R. G. Compton: A review of the analysis of multiple nucleation with diffusion controlled growth; *Journal of Electroanalytical Chemistry*, **549**, 1-12 (2003)
- [161] L. Heerman, A. Tarallo: Theory of the chronoamperometric transient for electrochemical nucleation with diffusion-controlled growth; *Journal of Electroanalytical Chemistry*, **470**, 70-76 (1999)
- [162] M. V. Mirkin, A. P. Nilov: Three-dimensional nucleation and growth under controlled potential; *Journal of Electroanalytical Chemistry*, **283**, 35-51 (1990)
- [163] M. Y. Abyaneh: Modelling diffusion controlled electrocrystallisation processes; *Journal of Electroanalytical Chemistry*, **586**, 196-203 (2006)
- [164] P. Ferrin, S. Kandoi, A. U. Nilekar, M. Mavrikakis: Hydrogen adsorption, absorption and diffusion on and in transition metal surfaces; *Surface Science*, **606**, 679-689 (2012)
- [165] H. M. Wang, S. F. Chen, T. J. O'Keefe, M. Degrez, R. Winand: Evaluation of mass transport in copper and zinc electrodeposition using tracer methods; *Journal of Applied Electrochemistry*, **19**, 174-182 (1989)

- [166] G. Trejo, H. Ruiz, R. Ortega Borges, Y. Meas: Influence of polyethoxylated additives on zinc electrodeposition from acidic solutions; *Journal of Applied Electrochemistry*, **31**, 685-692 (2001)
- [167] P. Neogi: Length scales and rough ness on a growing solid surface: A review; *Journal of Electroanalytical Chemistry*, **595**, 1-10 (2006)
- [168] K. Kondo, A. Ohgishi, Z. Tanaka: Electrodeposition of zinc-SiO₂ composite, **147**, 2611-2613 (2000)
- [169] M. Hiramatsu, H. Kawasaki, Y. Nakayama, T. Omi: Surface morphology and polymer adhesion of electroplated zinc/silica composite, *Plating and Surface Finishing*, **47**, 48-51 (1987)
- [170] B. Hoppe: *Mikroelektronik 2*, 1. Auflage, Vogel Fachbuch, Würzburg (1998), ISBN 3-8023-1588-X
- [171] XPS and AES spectroscopy databank, National Institute of Standards and Technology, USA (NIST), <http://srdata.nist.gov/xps/index.htm>
- [172] J. Loder Meyer: Elektrochemische Abscheidung von Metallen und Legierungen aus nichtwässrigen Systemen und Aktivierung von passivierten Metalloberflächen zur Abscheidung nanoporöser Schichten aus wässrigen Lösungen, Dissertation, University Regensburg (2006)
- [173] T. Schedlbauer: Bestimmung und Charakterisierung eines Infineon A2-Elektrolyten, Bachelorarbeit im Rahmen des Bachelorstudiengangs Chemie an der Universität Regensburg, (2008)
- [174] G. G. Graf: Zinc, Ullmann's encyclopaedia of industrial chemistry, Wiley-VCH Verlag GmbH & Co. KGaA, Weinheim (2005)
- [175] R. von Burg, D. Liu: Toxicology update; *Journal of Applied Toxicology*, **13 (3)**, 225-230 (1993)
- [176] S. A. Katz, H. Salem: The toxicology of chromium with respect to its chemical speciation: A review; *Journal of Applied Toxicology*, **13 (3)**, 217-224 (1993)
- [177] Bundesministerium für Umwelt, Naturschutz und Reaktorsicherheit: Verordnung über Anforderungen an das Einleiten von Abwasser in Gewässer – AbwV (vom 17. Juni 2004, BGBl. I S. 1108, zuletzt geändert am 31. Juli 2009, BGBl. I S. 2585 (Inkrafttreten am 01.03.2010)
- [178] C. S. Jeffcoate, et al.: Chromate in conversion coatings: A XANE study of its concentration and mobility; *Journal of the Electrochemical Society*, **147 (2)**, 540-547 (2000)
- [179] G. Greeuw, J. F. Verwey: The mobility of Na⁺, Li⁺, and K⁺ ions in thermally grown SiO₂ films; *Journal of Applied Physics*, **56**, 2218-2224 (1984)

- [180] Merck Safety Datasheet according to EC Directive 91/155/EEC: Sodium dichromate, $\text{Na}_2\text{Cr}_2\text{O}_7 \times 2 \text{H}_2\text{O}$, CAS-No: 7789-12-0, Merck KGaA Darmstadt, www.chemdat.info (2004)
- [181] Merck Sicherheitsdatenblatt gemäß Verordnung (EG) Nr. 1907/2006: CAS Nr.: 7722-64-7, Kaliumpermanganat, KMnO_4 , Merck KGaA Darmstadt, www.merck-chemicals.com (2010)
- [182] Alfa Aesar Sicherheitsdatenblatt gemäß Verordnung (EG) Nr.1907/2006, Artikel 31: Kaliumorthovanadate, K_3VO_4 , CAS-Nr.: 14293-78-8; Alfa Aesar GmbH & Co.KG Karlsruhe, www.alpha.com (2007)
- [183] Merck Sicherheitsdatenblatt gemäß Verordnung (EG) Nr. 1907/2006: CAS-Nr.:10102-40-6, Natriummolybdat-Dihydrat, $\text{Na}_2\text{MoO}_4 \times 2 \text{H}_2\text{O}$, Merck KGaA Darmstadt, www.merck-chemicals.com (2011)
- [184] R. F. Sebenik, et al.: Molybdenum and Molybdenum compounds; Ullmann's Encyclopedia of Industrial Chemistry; Wiley-VCH Verlag GmbH & Co KGaA, Weinheim 2012
- [185] D. J. Mackinnon, J. M. Brannen: Evaluation of organic additives as levelling agents for zinc electrowinning from chloride electrolytes; Journal of Applied Electrochemistry, 12, 21-31 (1982)
- [186] D. J. Mackinnon, J. M. Brannen: Zinc deposit structures obtained from synthetic zinc chloride electrolyte; Journal of Applied Electrochemistry, 9, 603-613 (1979)
- [187] D. J. Mackinnon, J. M. Brannen, V. I. Lakshmanan: The effects of chloride ion and organic extractants on electrowon zinc; Journal of Applied Electrochemistry, 10, 321-334 (1980)
- [188] R. Steffen, D. Wolfhard: Einfluss von Stromdichte und Strömung auf die Zinkkristallisation bei der elektrolytischen Hochleistungs-Bandverzinkung; Galvanotechnik, 86, 756-763 (1995)
- [189] J. C. Hsieh, C. C. Hu, T. C. Lee: The synergistic effects of additives on improving the electroplating of zinc under high current densities; Journal of the Electrochemical Society, 155 (10), D675-D681 (2008)
- [190] Y. Oren: Growth of zinc dendrites in acidic zinc chloride solutions; Electrochimical Acta, 27, 739-748 (1982)
- [191] C. M. Lopez, K. S. Choi: Electrochemical synthesis of dendritic zinc films composed of systematically varying motif crystals; Langmuir, 22, 10625-10629 (2006)
- [192] M. Matsushita M. Sano, Y. Hayakawa, H. Honjo, Y. Sawada: Fractal structures of zinc metal leaves grown by electrodeposition; Physical Review Letters, 53, 286-290 (1984)
- [193] Y. Sawada, A. Dougherty, J. P. Gollub: Dendritic and fractal patterns in electrolytic metal deposition; Physical Review Letters, 56, 1260-1265 (1986)

- [194] F. Argoul, A. Kuhn: The influence and reaction processes on the morphology of a metal electrodeposit in thin gap geometry; *Physica A*, 213, 209-231 (1995)
- [195] F. Argoul, E. Freysz, A. Kuhn, C. Leger, L. Potin: Interferometric characterization of growth dynamics during dendritic electrodeposition of zinc; *Physical Review E*, 53, 1777-1788 (1996)
- [196] T. R. N. Mhiochain, G. Hinds, A. Martin, E. Z. Y. Chang: Influence of magnetic field and gravity on the morphology of zinc fractal electrodeposits; *Electrochimica Acta*, 49, 4813-4828 (2004)
- [197] D. Grier, E. Ben-Jacob, R. Clarke, L. M. Sander: Morphology and microstructure in electrochemical deposition of zinc; *Physical Review Letters*, 56, 1264-1269 (1986)
- [198] V. I. Lainer: Brass plating, published by V. A. Averkin: Electrodeposition of alloys, Israel Program for Scientific Translations, Jerusalem 1964
- [199] J. Giridhar: Adhesion and corrosion properties of a new Ni-Zn/Zn-Co-coated steel tire cord; *Surface and Coatings Technology*, 53, 243-255 (1992)
- [200] S. O. Pagotto Jr., C. M. de Alvarenga Freire, M. Ballester: Zn-Ni alloy deposit obtained by continuous and pulse electrodeposition process; *Surface and Coatings Technology*, 122, 10-13 (1999)
- [201] J. Giridhar, W. J. van Ooij: Study of Zn-Ni and Zn-Co alloy coatings electrodeposited on steel strips. II: Corrosion, dezincification and sulfidation of the alloy coatings; *Surface and Coatings Technology*, 53, 35-47 (1992)
- [202] R. Fratesi, G. Roventin, C. Branca, S. Simoncini: Corrosion resistance of Zn-Co alloy coatings; *Surface and Coatings Technology*, 63, 97-103 (1994)
- [203] R. Fratesi, G. Roventin: Corrosion resistance of Zn-Ni alloy coatings in industrial production; *Surface and Coatings Technology*, 82, 158-161 (1996)
- [204] M. M. Abou-Krishna, H. M. Rageh, E. A. Matter: Electrochemical studies on the electrodeposited Zn-Ni-Co ternary alloy in different media; *Surface and Coatings Technology*, 202, 3739-3746 (2008)
- [205] B. Szczygiel, A. Laszczynska, W. Tylus: Influence of molybdenum on properties of Zn-Ni and Zn-Co alloy coatings; *Surface and Coatings Technology*, 204, 1438-1444 (2010)
- [206] Z. F. Lodhi, J. M. C. Mol, A. Hovestad, H. Terryn, J. H. W. de Wit: Electrodeposition of Zn-Co and Zn-Co-Fe alloys from acidic chloride electrolytes; *Surface and Coatings Technology*, 202, 84-90 (2007)
- [207] J. B. Bajat, S. Stankovic, B. M. Jokic, S. I. Stevanovic: Corrosion stability of Zn-Co alloys deposited from baths with high and low Co content – The influence of deposition current density; *Surface and Coatings Technology*, 204, 2745-2753 (2010)

- [208] A. C. Hegde, K. Venkatakrishna, N. Eliaz: Electrodeposition of Zn-Ni, Zn-Fe and Zn-Ni-Fe alloys; *Surface and Coatings Technology*, 205, 2031-2041 (2010)
- [209] N. Eliaz, K. Venkatakrishna, A. C. Hegde: Electroplating and characterization of Zn-Ni, Zn-Co and Zn-Ni-Co alloys; *Surface and Coatings Technology*, 205, 1969-1978 (2010)
- [210] Vianco P. T.: An overview of surface finishes and their role in printed circuit board solderability and solder joint performance; *Circuit World* 25/1, 6-24 (1998)
- [211] Murata A, Shimada T (1990), US patent no. 4,894,752
- [212] Abbott D, Moehle PR (2001), US patent no. 6,194,777
- [213] Chang CA, Koopman NG, Roldan JM, Strickman S, Srivastava K, Yeh HL (1991), US patent no. 5,048,744
- [214] Takahashi S, Masukawa S, Futatsuka R, Sugimoto T, Suzuki T, Azuma C, Kanda Y, Fukatami T (1996), US patent no. 5,510,197
- [215] Ramsey TH, Alfaro RC (1995), US patent no. 5,455,195
- [216] Yang JC, Lee KC, Tan AC (1999), *Electronic components and technology conference, 1999 Proceedings* 49th: 842-847
- [217] Whelan CM, Kinsella M, Ho HM, Maex K (2004) *J Electrochem Soc* 151: B33-B38
- [218] Ho HM, Lam W, Stoukatch S, Ratchev P, Vath CJ, Beyne E (2003) *Microelectron Reliab* 43: 913-923
- [219] Breach CD, Wulff F (2004) *Microelectron Reliab* 44: 973-981
- [220] Romm D, Lange B, Donald A (2001) *Texas Instruments Application Report SZZA026* July 2001; <http://www.ti.com/lit/an/szza026/szza026.pdf>
- [221] Abbott D, Romm D, Lange B (2001) *Texas Instruments Application Report SZZA031* December 2001; <http://www.ti.com/lit/an/szza031/szza031.pdf>
- [222] Peeters P, Hoorn G, Daenen T, Kurowski A, Staikov G (2001) *Electrochim Acta* 47: 161-169
- [223] Yang J. C., Bhardwaj M. D., Tropa L., Gibson J. M.: The surface kinetics of the initial stages of copper as investigated by in situ ultra-high vacuum transmission electron microscopy; *Materials Science Forum*, vols. 369-372, 133-140 (2001)
- [224] Honkanen M., Vippola M., Lepistö T.: Low temperature oxidation of copper alloys – AEM and AFM characterisation; *Journal of material science*, 42, 4684-4691 (2007)

- [225] Zhou G., Yang J. C.: Formation of quasi-one-dimensional Cu₂O structures by in situ oxidation of Cu(100); *Physical review letters*, 89 (10), 106101-1 to -4 (2002)
- [226] Zhu Y, Mimura K, Lim J.-W., Isshiki M., Jiang Q.: Brief review of oxidation kinetics of copper at 350°C to 1050°C; *Metallurgical and materials transactions A*, **37A**, 1231-1237 (2006)
- [227] V. S. Sastri, E. Ghali, M. Elboujdaini: *Corrosion prevention and protection practical solutions*, John Wiley and Sons Ltd, New York (2007), ISBN 10 047002402X(HB)
- [228]: Lefez B., Kartouni K., Lenglet M., Rönnow D., Ribbing C. G.: Application of reflectance spectrophotometry to the study of copper (I) oxides (Cu₂O and Cu₃O₂) on metallic substrate; *Surface and interface analysis*, 22, 451-455 (1994)
- [229]: Iijima J., Lim J.-W., Hong S.-H., Suzuki S., Mimura K., Isshiki M.: Native oxidation of ultra high purity Cu bulk and thin films; *Applied surface science*, 253, 2825-2829 (2006)
- [230] Boggio J. E.: The room temperature oxidation of Cu (111): Pressure effects; *Journal of chemical physics*, 70 (11), 5054-5058 (1978)
- [231] Tylecote M. A.: Review of published information on the oxidation and scaling of copper and copper-base alloys; *Journal of the institute of metals*, 78, no. 1280, 259-300 (1950)
- [232] Roy S. K., Bose S. K., Sircar S. C.: Pressure dependencies of copper oxidation for low and high temperature parabolic laws; *Oxidation of metals*, 35, 1-18 (1991)
- [233] Haugrud R.: The influence of water vapour on the oxidation of copper at intermediate temperatures; *Journal of the electrochemical society*, 149 (1), B14-B21 (2002)
- [234] Hu Y. Z., Sharangpani R., Tay S.-P.: Kinetic investigation of copper film oxidation by spectroscopic ellipsometry; *Journal of vacuum science and technology*, A18 (5), 2527-2532 (2000)
- [235] Zhong C., Jiang Y. M., Luo Y. F., Deng B., Zhang L., Li J.: Kinetics characterization of the oxidation of Cu thin films at low temperature by using sheet resistance measurement; *Applied physics A*, 90, 263-266 (2008)
- [236] Njeh A., Wieder T., Fuess H.: Reflectometry studies of the oxidation kinetics of thin copper films; *Surface and interface analysis*, 33, 626-628 (2002)
- [237] Zhu Y., Mimura K., Isshiki M.: Purity effect on oxidation kinetics of copper at 800-1050°C; *Journal of the electrochemical society*, 151 (1), B27-B32 (2004)
- [238] Lahiri S. K., Waalib Singh N. K., Heng K. W., Ang L., Goh L. C.: Kinetics of oxidation of copper alloy leadframes; *Microelectronics journal*, 29, 335-341 (1998)

- [239] Xu C., He Z., Ng W. Y.: Investigation in the morphology of adsorbed benzotriazole film on copper surface by scanning tunneling microscopy; Chinese Journal of chemical engineering, 10 (4), 450-453 (2002)
- [240] M. Finsgar, I. Milosev: Inhibition of copper corrosion by 1,2,3-benzotriazole: A review; Corrosion science, 52, 2737-2749 (2010)
- [241] Al Kharafi M. F., Abdullah A. M., Ateya B. G.: A quartz microbalance study of the kinetics of interaction of benzotriazole with copper; Journal of applied electrochemistry, 37, 1177-1182 (2007)
- [242] Steward K. L., Zhang J., Li S., Carter P. W., Gewirth A. A.: Anion effects on Cu-benzotriazole film formation – implications for CMP; Journal of the electrochemical society, 154 (1), D57-D63 (2007)
- [243] Xue G., Ding J., Cheng P.: Growth of a surface film on copper from benzotriazole solutions; Applied surface science, 89, 77-82 (1995)
- [244] Mansikkamaeki K., Johans C., Kontturi K.: The effect of oxygen on the copper corrosion with benzotriazole; journal of the electrochemical society, 153 (1), B22-B24 (2006)
- [245] Simbeck T., Thomaier S., Stock Ch., Riedl E., Gores H. J.: Measurement of adsorption kinetics of benzotriazole on copper surfaces via impedance scanning quartz crystal microbalance studies; Electrochemistry communications, 13 (8), 803-805 (2011)
- [246] Milic S. M., Antonijevic M. M.: Some aspects of copper corrosion in presence of benzotriazole and chloride ions; Corrosion science, 51, 28-46 (2009)
- [247] T. M. Christensen, N. R. Sorensen: Thermal stability of benzotriazole on copper during atmospheric corrosion, Surface and interface analysis, **17**, 3-6 (1991)
- [248] Harmann G., Johnson C. E.: Wire bonding to advanced copper, low-K integrated circuits, the metal/dielectric stacks, and materials considerations; IEEE Transactions on components and packaging technologies, 25 (4), 677-683 (2002)
- [249] Ho H. M., Lam W., Stoukatch S., Ratchev P., Vath III C. J., Beyne E.: Direct gold and copper wires on copper; Microelectronics reliability, 43, 913-923 (2003)
- [250] Whelan C. M., Kinsella M., Ho H. M., Maex K.: In-situ cleaning and passivation of oxidized Cu surfaces by alkanethiols and its application to wirebonding; Journal of electronic materials, 33 (9), 1005-1011 (2004)
- [251] Whelan C.M., Kinsella M., Ho, H. M., Maex K.: Corrosion inhibition by thiole-derived SAMs for enhanced wirebonding on Cu surfaces; Journal of the electrochemical society, 151 (2), B33-B38 (2004)
- [252] Carron K. T., Lewis M. L.: Surface enhanced rRahmen scattering and cyclic voltammetry studies of synergetic effects in the corrosion inhibition of copper by polybenzimidazole and mercaptobenzimidazole at high temperature; Journal of materials science, 28, 4099-4103 (1993)

- [253] Guo S., Xue G., Qian Y.: Interfacial modification of polymer / metal joints by a two-component coupling system of polybenzimidazole and 2-mercaptobenzimidazole; *Applied surface science*, 84, 351-356 (1995)
- [254] Xue G., Lu Y., Shi G.: SERS studies of synergetic effect in corrosion inhibition for Cu by a two-component inhibitor system of polyvinylimidazole and benzimidazole; *Applied Surface Science*, 74, 37-41 (1994)
- [255] Eng F. P., Ishida H.: Fourier transform infrared studies on the thermal degradation of polyvinylimidazoles – part I; *Journal of Applied Polymer Science*, 32, 5021-5034 (1986)
- [256] Wudy, F.; Multerer, M.; Stock, C.; Schmeer, G.; Gores, H. J.: Rapid impedance scanning QCM for electrochemical applications based on miniaturized hardware and high-performance curve fitting, *Electrochimica Acta*, 53(22), 6568-6574 (2008)
- [257] Simbeck T., Hammer M. M., Thomaier S., Stock Ch., Riedl E., Gores H. J.: Kinetics of adsorption of poly(vinylimidazole) (PVI) onto copper surfaces investigated by quartz crystal microbalance studies; *Journal of solid state electrochemistry*, 16, 3467-3472 (2012)
- [258] E. Riedl, S. Jordan, C. M. Schilz, F. H. Wendy: Semiconductor package and method of assembling a semiconductor package; patent application WO2007/129132 A1 (2007)
- [259] E. Riedl, W. Schober: Verfahren zum Abscheiden einer porösen Haftvermittlungsschicht auf einer Oberfläche eines elektrisch leitenden Körpers sowie Verwendung des Verfahrens; Patent DE 103 30 192 B4 (2008)
- [260] E. Riedl, W. Schober: Electrically conductive body including an adhesion promoter layer, and process for depositing an adhesion promoter layer; patent US7540950B2 (2009)
- [261] M. Weber, R. Sewald, E. Riedl: Elektronische Bauteile mit Halbleiterchips und Systemträger und Verfahren zur Herstellung derselben; Offenlegungsschrift DE 101 24 047 A1 (2002)
- [262] E. Riedl, I. Nikitin, J. Loder Meyer, R. Bergmann, K. Guth: Method of fabricating a semiconductor device; patent application US2010/0059857 A1 (2010)
- [263] E. Riedl, W. Schober: Metal article intended for at least partially coating with a substance and a method for producing the same; patent US7384698 B2 (2008)
- [264] E. Riedl, W. Schober: Method for producing a metal article intended for at least partially coating with a substance; patent US8147621 B2 (2012)
- [265] J. Mahler, R. Wombacher, D. Lachmann, B. Betz, S. Paulus, E. Riedl: Systemträger mit in Kunststoffmasse einzubettenden Oberfläche, Verfahren zur Herstellung eines Systemträgers und Verwendung einer Schicht als Haftvermittler; Patent DE 10 2005 061 248 B4 (2007)

[266] J. Mahler, R. Wombacher, D. Lachmann, B. Betz, S. Paulus, E. Riedl: Semiconductor device with semiconductor device components embedded in a plastic housing composition; patent US7705472 B2 (2010)

[267] A. Kessler, J. Mahler, E. Riedl: Halbleiterbauteil mit in Kunststoffgehäusemasse eingebetteten Halbleiterbauteilkomponenten; Offenlegungsschrift DE 10 2004 047 510 A1 (2006)

[268] E. Riedl, J. Mahler, J. Lodermeier, M. Vaupel, S. Jordan: Semiconductor package; patent US7989930 B2 (2011)

Eidesstattliche Erklärung

(1) Ich erkläre hiermit an Eides statt, dass ich die vorliegende Arbeit ohne unzulässige Hilfe Dritter und ohne Benutzung anderer als der angegebenen Hilfsmittel angefertigt habe; die aus anderen Quellen direkt oder indirekt übernommenen Daten und Konzepte sind unter Angabe des Literaturzitats gekennzeichnet.

(2) Bei der Auswahl und Auswertung folgenden Materials haben mir die nachstehend aufgeführten Personen in der jeweils beschriebenen Weise unentgeltlich geholfen:

(siehe „Danksagung“)

(3) Weitere Personen waren an der inhaltlich-materiellen Herstellung der vorliegenden Arbeit nicht beteiligt. Insbesondere habe ich hierfür nicht die entgeltliche Hilfe eines Promotionsberaters oder anderer Personen in Anspruch genommen. Niemand hat von mir weder unmittelbar noch mittelbar geldwerte Leistungen für Arbeiten erhalten, die im Zusammenhang mit dem Inhalt der vorgelegten Dissertation stehen.

(4) Die Arbeit wurde bisher weder im In- noch im Ausland in gleicher oder ähnlicher Form einer anderen Prüfungsbehörde vorgelegt.

Regensburg, den 18. Juni 2014..... (Edmund Riedl)